U.S.NRC
United States Nuclear Regulatory Commission
*Protecting People and the Environment*

NUREG/CR-7184
ANL-12/56

# Crack Growth Rate and Fracture Toughness Tests on Irradiated Cast Stainless Steels

Office of Nuclear Regulatory Research

# AVAILABILITY OF REFERENCE MATERIALS IN NRC PUBLICATIONS

**NRC Reference Material**

As of November 1999, you may electronically access NUREG-series publications and other NRC records at NRC's Library at www.nrc.gov/reading-rm.html. Publicly released records include, to name a few, NUREG-series publications; *Federal Register* notices; applicant, licensee, and vendor documents and correspondence; NRC correspondence and internal memoranda; bulletins and information notices; inspection and investigative reports; licensee event reports; and Commission papers and their attachments.

NRC publications in the NUREG series, NRC regulations, and Title 10, "Energy," in the *Code of Federal Regulations* may also be purchased from one of these two sources.

1. **The Superintendent of Documents**
   U.S. Government Publishing Office
   Mail Stop IDCC
   Washington, DC 20402-0001
   Internet: bookstore.gpo.gov
   Telephone: (202) 512-1800
   Fax: (202) 512-2104

2. **The National Technical Information Service**
   5301 Shawnee Rd., Alexandria, VA 22312-0002
   www.ntis.gov
   1-800-553-6847 or, locally, (703) 605-6000

A single copy of each NRC draft report for comment is available free, to the extent of supply, upon written request as follows:

Address: **U.S. Nuclear Regulatory Commission**
Office of Administration
Publications Branch
Washington, DC 20555-0001
E-mail: distribution.resource@nrc.gov
Facsimile: (301) 415-2289

Some publications in the NUREG series that are posted at NRC's Web site address www.nrc.gov/reading-rm/doc-collections/nuregs are updated periodically and may differ from the last printed version. Although references to material found on a Web site bear the date the material was accessed, the material available on the date cited may subsequently be removed from the site.

**Non-NRC Reference Material**

Documents available from public and special technical libraries include all open literature items, such as books, journal articles, transactions, *Federal Register* notices, Federal and State legislation, and congressional reports. Such documents as theses, dissertations, foreign reports and translations, and non-NRC conference proceedings may be purchased from their sponsoring organization.

Copies of industry codes and standards used in a substantive manner in the NRC regulatory process are maintained at—

**The NRC Technical Library**
Two White Flint North
11545 Rockville Pike
Rockville, MD 20852-2738

These standards are available in the library for reference use by the public. Codes and standards are usually copyrighted and may be purchased from the originating organization or, if they are American National Standards, from—

**American National Standards Institute**
11 West 42nd Street
New York, NY 10036-8002
www.ansi.org
(212) 642-4900

Legally binding regulatory requirements are stated only in laws; NRC regulations; licenses, including technical specifications; or orders, not in NUREG-series publications. The views expressed in contractorprepared publications in this series are not necessarily those of the NRC.

The NUREG series comprises (1) technical and administrative reports and books prepared by the staff (NUREG–XXXX) or agency contractors (NUREG/CR–XXXX), (2) proceedings of conferences (NUREG/CP–XXXX), (3) reports resulting from international agreements (NUREG/IA–XXXX), (4) brochures (NUREG/BR–XXXX), and (5) compilations of legal decisions and orders of the Commission and Atomic and Safety Licensing Boards and of Directors' decisions under Section 2.206 of NRC's regulations (NUREG–0750).

U.S.NRC
United States Nuclear Regulatory Commission
*Protecting People and the Environment*

NUREG/CR-7184
ANL-12/56

# Crack Growth Rate and Fracture Toughness Tests on Irradiated Cast Stainless Steels

Manuscript Completed: March 2015
Date Published: July 2015

Prepared by:
Y. Chen, B. Alexandreanu, and K. Natesan

Nuclear Engineering Division
Argonne National Laboratory

A. S. Rao, NRC Project Manager

Office of Nuclear Regulatory Research

## ABSTRACT

Cast austenitic stainless steel, which has a ferrite-austenite duplex microstructure, is used in the cooling system of light water reactors for components with complex shapes, such as pump casings, valve bodies, and coolant piping. In the present study, crack growth rate and fracture toughness J-R curve tests were performed on irradiated cast stainless steels and unirradiated control samples in low-corrosion-potential environments (high-purity water with low dissolved oxygen or simulated pressurized water reactor) at 320°C. Both as-received and thermally aged materials were included to investigate the combined effect of thermal aging and irradiation embrittlement on the fracture behavior of cast stainless steels. The samples were irradiated to approximately 0.08 dpa at the Halden reactor. Good resistance to corrosion fatigue and stress corrosion cracking was observed for all cast stainless steel specimens. Thermal aging had little effect on the crack growth behavior at 0.08 dpa. Cleavage-like fracture was the dominant cracking morphology during the crack growth rate tests, and the ferrite phase was deformed to a lesser extent compared with the surrounding austenite phase. The fracture toughness results showed a dominant effect of neutron irradiation, and the fracture resistances were decreased considerably for all cast specimens regardless of their thermal aging. The reduction in fracture toughness was more significant in the unaged than thermally aged specimens. Nonetheless, the fracture toughness values of thermally aged specimens were 20-30% lower than their unaged counterparts, suggesting a combined effect of thermal aging and neutron irradiation in cast stainless steel.

## FOREWORD

Cast austenitic stainless steel (CASS) is used in the cooling system of light water reactors for components with complex shapes, such as pump casings, valve bodies, coolant piping, control rod guide tubes and housing, etc. The ferrite phase in this type of steel is vulnerable to thermal aging embrittlement after long-term exposure to reactor coolant. In addition, neutron irradiation can decrease the fracture resistance of CASS significantly. It has been postulated that a combined effect of thermal aging and irradiation embrittlement could reduce the fracture resistance even further to a level neither of these degradation mechanisms can impart alone.

In the early 1990s, the NRC conducted research on the long term embrittlement of cast duplex stainless steels used in LWR systems. Under those programs, experimental data were collected on the microstructure and the mechanical properties of commercial and experimental cast steels (such as CF-3, CF-8 and CF-8M) that were thermally aged in laboratories or in reactors. These tests concluded that the chemical composition of the steels and the ferrite morphology strongly affect the kinetics of the embrittlement of steels. For example, the low carbon cast steels (CF-3) are most resistant to embrittlement, and the high carbon cast steels with molybdenum (CF-8M) are the most susceptible to embrittlement. The delta ferrite content of these steels ranged between 3 to 30%, and the morphologies of ferrite are either lacy or vermicular in the steels containing > 5% ferrite . The embrittlement in these steels was found to occur when the failure is dominated by brittle fracture that is associated with either cleavage of ferrite and/or the separation of ferrite/austenite phase boundaries.

While the thermal aging embrittlement of CASS had been studied extensively, the irradiation-induced embrittlement in CASS had not been investigated thoroughly. There was no data available on irradiated CASS alloys either with or without thermal aging. Thus, the present research was initiated to investigate the combined effects of thermal aging and irradiation damage on the fracture resistance of CASS.

Crack growth rate (CGR) and fracture toughness J-R curve tests were conducted on three grades of CASS (CF-3, CF-8 and CF-8M) containing high levels of delta ferrite (>23%). These samples were irradiated at the Halden test reactor to a low dose of 0.08 displacements per atom (dpa). Both as-received (labeled as un-aged) and thermally aged specimens were investigated to determine the combined effects of thermal aging and irradiation embrittlement. The CGR tests were conducted at 320 °C in low-corrosion-potential environments. Following the CGR tests, the fracture toughness J-R curve tests were performed on the same samples in these test environments.

The CASS materials showed good resistance to both corrosion fatigue and stress corrosion cracking (SCC) at the 0.08 dpa dose level. Trans-granular cleavage-like cracking was the dominant fracture mode during the CGR tests, and it was found that the extent of deformation of ferrite phase was significantly lesser than the surrounding austenite phase of the steel. The neutron irradiation even at low dose of 0.08 dpa significantly affected the fracture toughness of both aged and un-aged CASS.

The report presents a focused research concentration for a better understanding of the embrittlement of CASS components. The results of this study enable the agency's regulatory technical basis development efforts, such as the screening criteria of neutron fluence and upper bound value of delta ferrite in CASS components with acceptable fracture toughness properties.

Brian Thomas, Director (Acting)
Division of Engineering
Office of Nuclear Regulatory Research
U.S. Nuclear Regulatory Commission

**TABLE OF CONTENTS**

**LIST OF FIGURES**

## LIST OF TABLES

## EXECUTIVE SUMMARY

Cast austenitic stainless steel (CASS) is used in the cooling system of light water reactors for components with complex shapes, such as pump casings, valve bodies, coolant piping, and control rod guide tube spacers. In contrast to a fully austenitic microstructure of wrought stainless steel (SS), CASS consists of a ferrite-austenite duplex microstructure. A certain amount of the delta ferrite phase is intentionally designed into CASS and SS weld metals to engineer against hot cracking. However, the ferrite phase is vulnerable to thermal aging embrittlement after long-term exposure to reactor coolant. In addition, neutron irradiation can decrease the fracture resistance of CASS significantly. It was suspected that a combined effect of thermal aging and irradiation embrittlement could reduce the fracture resistance even further to a level neither of these degradation mechanisms can impart alone. While the thermal aging embrittlement of CASS has been studied extensively, no data were available with regard to the combined effect of thermal aging and irradiation embrittlement. A test program was been initiated to investigate the joint effect of thermal aging and irradiation damage on the cracking susceptibility and fracture resistance of CASS.

Crack growth rate (CGR) and fracture toughness J-integral resistance (J-R) curve tests were conducted on three grades of CASS (CF-3, CF-8, and CF-8M) containing high levels of delta ferrite (>23%). The samples were irradiated at the Halden reactor to a low dose of 0.08 displacements per atom (dpa) or $5.56 \times 10^{19}$ n/cm$^2$ (E > 1 MeV). Both as-received and thermally aged specimens were included to determine the combined effect of thermal aging and irradiation embrittlement. The CGR tests were conducted at ~320°C on the irradiated and unirradiated control samples in either a high purity water environment with low dissolved oxygen (DO) or a pressurized water reactor (PWR) environment. Following the CGR tests, the fracture toughness J-R curve tests were performed on the same samples in the test environments.

Cyclic CGRs and constant-load CGRs were measured to evaluate the corrosion fatigue and stress corrosion cracking (SCC) response of the CASS specimens. In the cyclic CGR tests, environmental enhanced cracking was more difficult to establish in the CASS specimens when compared to wrought SSs. In SCC CGR tests, only moderate CGRs, in the range of $10^{-11}$ m/s, were recorded in most of the CASS specimens regardless of their thermal aging history. In general, the CASS materials showed good resistance to both corrosion fatigue and SCC without irradiation and at 0.08 dpa. Transgranular cleavage-like cracking was the dominant fracture mode during the CGR tests, and the ferrite phase was often deformed to a less extent compared with its surrounding austenite phase. This observation supports the hypothesis that the beneficial effect of ferrite for SCC resistance arises, in part, from the low plastic deformation of ferrite phase compared to austenite.

Neutron irradiation did significantly affect the fracture toughness of CASS. At 0.08 dpa, the fracture toughness values of unaged specimens were much lower than their initial unirradiated values. Fracture toughness was also reduced by 20-30% for thermally aged specimens after irradiation. This observation suggests an interaction between thermal aging and irradiation damage. When both conditions of thermal aging and irradiation damage are present, the combined effect is not a simple addition of both degradations. The interaction between thermal aging and irradiation damage can lead to different microstructural evolutions in CASS materials

(viz. by prompting G-phase formation through radiation-induced segregations of minor elements), reducing the fracture resistance to a higher extent than either one of them can achieve alone. Neutron irradiation appears to affect not only the kinetics of thermal aging embrittlement, but also the lower bound values of fracture toughness (i.e., the saturation state). For this reason, the effects of neutron irradiation should be considered when the degree of embrittlement is evaluated for CASS components.

**ACKNOWLEDGEMENTS**

The authors would like to thank Drs. O. K. Chopra and W. J. Shack for their invaluable contribution to this project. Our special thanks go out to Ms. T. M. Karlsen, OECD Halden Reactor Project, Halden, Norway, for reactor irradiation experiments and sample transfer. L. A. Knoblich, E. E. Gruber, R. Clark, and E. J. Listwan of Argonne, Y. Yang of University of Florida, and J. Pakarinen and Y. Huang of University of Wisconsin-Madison are acknowledged for their contributions to the experimental effort. We are also grateful to Drs. R. Tregoning and W. J. Shack for their careful reviews and comments on the manuscript. This work is sponsored by the Office of Nuclear Regulatory Research, U.S. Nuclear Regulatory Commission, under Job Code N6519 and V6454; Program Manager: A. S. Rao.

## ACRONYMS AND ABBREVATIONS

| | |
|---|---|
| ASTM | American Society for Testing and Materials |
| BWR | Boiling Water Reactor |
| CASS | Cast Austenitic Stainless Steels |
| CGR | Crack Growth Rate |
| CT | Compact Tension |
| DCPD | Direct Current Potential Drop |
| DO | Dissolved Oxygen |
| ECP | Electrochemical Potential |
| HWC | Hydrogen Water Chemistry |
| IASCC | Irradiation-Assisted Stress Corrosion Cracking |
| IGSCC | Intergranular Stress Corrosion Cracking |
| IML | Irradiated materials Laboratory |
| J-R | J-Integral Resistance |
| LVDT | Linear Voltage Displacement Transducer |
| LWR | Light Water Reactor |
| NWC | Normal Water Chemistry |
| PPU | Periodical Partial Unloading |
| PWR | Pressurized Water Reactor |
| SCC | Stress Corrosion Cracking |
| SEM | Scanning Electron Microscopy |
| SS | Stainless Steel |
| TG | Transgranular |

**UNITS of MEASURE**

| | |
|---|---|
| °C | degrees centigrade |
| cm | centimeter |
| dpa | displacement per atom |
| hr | hour |
| J | joule |
| m | meter |
| mm | millimeter |
| MPa | megapascal |
| ppb | part per billion |
| ppm | part per million |
| psig | pound per square inch gauge |
| s | second |
| μ | micron |

## 1. INTRODUCTION

Stainless steel is an important class of engineering materials used in light water reactors (LWRs). While the main structure of reactor core internals is constructed from wrought stainless steels (SSs), components with complex shapes, such as pump casings, valve bodies, coolant piping, elbows, and control rod guide tube spacers, are often made of cast austenitic stainless steels (CASS).[1] The CF grades of CASS whose compositions are similar to those of 300-series austenitic SSs are the most widely used corrosion-resistant CASS. The CF-3 and CF-8 grades contain nominal 19% Cr and 9% Ni and are the cast equivalents of Types 304L and 304 SSs, respectively. In addition, the CF-3M and CF-8M grades are the molybdenum-containing cast versions of 316L and 316 SSs, respectively. Like their wrought equivalents, the CF grades of CASS possess excellent corrosion resistance and mechanical properties,[2] and, thus, are ideal for LWR applications in aqueous environments. The strength and ductility of CF grades are comparable to those of wrought SSs. At room temperature, the yield and tensile strengths of CF-3 and CF-8 grades are greater than 200 MPa and 480 MPa,[3] respectively, similar to those of solution-annealed SSs. A good combination of strength and ductility also gives rise to excellent fracture toughness. Stable tearing occurs in CASS samples well above their yield strength before final fracture. Chopra and Sather [4] showed that the crack initiation toughness of CF-3 and CF-8 CASS varies from ~200 kJ/m$^2$ to over 1000 kJ/m$^2$ at room temperature; these values are comparable to those of wrought SSs reported by Mills.[5]

In contrast to the fully austenitic microstructure of wrought SSs, CASS consists of a ferrite-austenite duplex microstructure. It is common that a certain amount of δ ferrite is present along with austenite (γ) in the solidification microstructure such as CASS or weld metals. The precise fractions of ferrite and austenite phases depend on the chemical composition and casting thermal history. Experimental methods, such as quantitative metallography and ferromagnetic measurement, can be used to determine the ferrite content in CASS or weld metals.[6,7] Empirical models have also been developed to predict and control phase content with alloy composition. Based on the phase-stabilizing effects of Cr and Ni in Fe-Cr-Ni systems, several constitution diagrams have been established to estimate phase content.[8,9,10] The contributions of minor alloying elements are incorporated with Cr and Ni equivalent numbers and computed with empirical equations. The applicable range of composition, incorporated alloying elements, and weighing factors vary in these models, and thus the predicted phase contents differ among them to some extent.[11] For steel castings of CF grades, use of the Scheofer diagram, which is a modified version of the Schaeffler diagram[8], is recommended by the American Society for Testing and Materials (ASTM) for estimating ferrite content.[12]

The ferrite phase is critical for the mechanical properties and corrosion resistance of CASS and weld metals. Since hardening mechanisms by thermal-mechanical treatments cannot be easily implemented in castings, the strength of CASS mainly relies on the ferrite-austenite duplex microstructure. Beck et al. [13] showed that the tensile and yield strengths of CASS increase with δ ferrite content up to 40% at both room and elevated temperatures. The strengthening effect of ferrite phase is attributed to ferrite-austenite boundaries and can be explained with the Hall-Petch model.[14] Ferrite phase is also crucial for the soundness and weldability of steel castings. A minimum ferrite content is often specified for SS welds to reduce the tendency of hot cracking. In addition, the presence of ferrite phase can improve the resistance to sensitization and stress

corrosion cracking (SCC).[15] In susceptible environments, CASS tends to be more resistant to SCC than the same grade of wrought SS. This beneficial effect of ferrite was clearly demonstrated by Hughes et al.[16] in boiling water reactor (BWR) environments. Using slow strain rate tests, they showed that CF-3, CF-3A, and CF-8 have an exceptional resistance to intergranular SCC (IGSCC) in high-purity (HP) water containing 6-8 ppm dissolved oxygen (DO).

While the presence of δ ferrite in CASS is mostly beneficial, ferrite phase can also exert a detrimental effect on the fracture resistance of CASS under certain conditions. Exposed to temperatures of 300-500°C, ferrite phase is vulnerable to a low-temperature thermal aging phenomenon known as "475°C embrittlement." [17,18] The consequences of the thermal aging embrittlement are an increased tensile strength and reduced ductility.[19,20] The upper-shelf impact energy is also reduced, and the ductile-to-brittle transition temperature shifts higher.[20]

Because of thermal aging embrittlement, the long-term performance of CASS materials at elevated service temperatures is of concern. The degradation of CASS components resulting from thermal aging embrittlement has been recognized as a potential issue for aging reactors.[21] Several research programs have been conducted to assess Charpy impact properties and JR resistance curves of thermally aged CASS.[22,23] It was found that thermal aging at 290-450°C up to 30,000 hr leads to a significant deterioration in the fracture properties of CASS. The lower bound of impact energy and fracture toughness ($J_{IC}$) can be as low as 20 J/cm$^2$ and 25 kJ/m$^2$, respectively, at room temperature. The ductile-to-brittle transition temperature of CASS is also shifted to around 0°C for the thermally aged CASS. The extent of the thermal aging embrittlement increases with ferrite content and is sensitive to ferrite morphology.[22]

The mechanism of thermal aging of duplex SSs has been studied extensively.[17-20, 22-28] It is widely accepted that embrittlement is caused by the instability of the ferrite phase under thermal aging. The main reasons of the hardening and loss of toughness are (1) the formation of Cr-rich α' phase through spinodal decomposition, and (2) the precipitation and growth of carbides and G-phase at ferrite-austenite phase boundaries. Obviously, these microstructural changes are thermally activated and are fundamentally controlled by solid-state diffusion. Therefore, the thermal aging time for a given extent of degradation (e.g., an increase in hardness or decrease in toughness) follows an Arrhenius-type relationship.[24]

Besides thermal aging, neutron irradiation can also affect the microstructural evolution of CASS profoundly. Under fast neutron bombardment, lattice atoms in a crystalline material are displaced from their original sites by cascade damage. An avalanche of lattice displacements gives rise to point defect supersaturation, which does not exist under thermal equilibrium.[29,30] These point defects evolve at irradiation temperatures to form irradiation defects, giving rise to irradiation hardening and embrittlement. The irradiation embrittlement can generate further degradation in the ferrite phase, leading to an additional loss of fracture toughness. Furthermore, the presence of nonequilibrium point defects in irradiated microstructures can enhance the transportation of solutes in materials by radiation-enhanced diffusion.[30] The elevated diffusivity under neutron irradiation could certainly affect the kinetics of thermal aging. Thus, a combined

effect of irradiation embrittlement and thermal aging could not only produce a higher degree of embrittlement, but also affect the rate of degradation development.

While the thermal aging embrittlement of CASS has been studied extensively, very limited data exist in the open literature for neutron-irradiated CASS.[5,31,32] Two tests conducted on thermally aged and irradiated CF-8M showed a higher degree of embrittlement in the CASS material than wrought SSs.[31] It is not clear, however, if the simultaneous exposure to irradiation and thermal aging would reduce the fracture resistance to a lower level than either of the degradation mechanisms can impart alone. If so, the combined effect is not only important for internal components made of CASS, but also for SS weld metals that possess a similar austenite-ferrite duplex microstructure. While weld metals may contain less ferrite phase than that in CASS materials, a minimum ferrite content is usually specified for weld metals to engineer against hot cracking. Thus, weld metals may be subjected to the same type of degradation as CASS. A better understanding of the combined effect of thermal aging and irradiation would also be helpful to address issues concerning SS weld metals.

In the current study, several CF grades of CASS were irradiated to approximately 0.08 displacements per atom (dpa). Both as-received and thermally aged specimens are included. Fracture toughness J-integral resistance (J-R) curve tests were conducted on the irradiated and unirradiated control samples to assess the extent of embrittlement resulting from neutron irradiation and thermal aging. Additionally, crack growth rate (CGR) tests were carried out prior to the fracture toughness tests in low electrochemical potential (ECP) environments to evaluate their SCC performance. At 0.08 dpa, irradiation embrittlement of ferrite phase is anticipated to some extent, but little effect either on embrittlement or stress corrosion susceptibility would be expected for austenite phase. Thus, the current work is focused on the effects of thermal aging and irradiation on the ferrite phase. At higher irradiation levels, additional effect would occur due to embrittlement and increased SCC susceptibility of austenite phase. Since elevated susceptibility to irradiation-assisted stress corrosion cracking (IASCC) is unlikely at this low dose, the SCC CGR test durations were kept relatively short in the present study. Still, the CGR tests could provide corrosion fatigue starter cracks for the subsequent fracture toughness J-R curve tests, so that any environmental contribution to the fracture behavior of CASS could be detected.

## 2. EXPERIMENTAL

### 2.1 Materials and Specimens

Three experimental heats of corrosion-resistant CASS (CF-3, CF-8, and CF-8M) were obtained from a previous ANL research program.[4] The CASS heats are static cast slabs with dimensions of 610 x 610 x 76 mm. A ferrite scope measurement on these heats showed that the CF-3 and CF-8 heats contained approximately 24% and 23% delta ferrite, respectively, and the CF-8M heat had 28% delta ferrite. Table 1 gives the compositions of these materials. Both as-received (or unaged) and thermally aged specimens were prepared from these heats. The thermal aging conditions are given in Table 2. Figure 1 shows metallurgical images of the CASS materials used in this study. The samples were polished with SiC papers up to 1200 grit. After a final finish with 1 μm diamond slurry, the polished surfaces were etched with ferric chloride. Both the unaged and thermally aged microstructures are similar, as shown in Fig. 1. Note that a slight decline in ferrite content was reported for all grades of CASS after thermal aging.[4] For the aging conditions used in the current study (10,000 hr at 400°C), the decrease in ferrite content is insignificant. Thus, the average ferrite contents were considered unchanged after thermal aging.

Table 1. Chemical compositions of the cast stainless steels examined in this study.

| Cast Grade | Ferrite Content | | Heat ID | Composition (wt. %) | | | | | | | | |
|---|---|---|---|---|---|---|---|---|---|---|---|---|
| | Measured [a] | Calculated [b] | | Mn | Si | P | S | Mo | Cr | Ni | N | C |
| CF-3 | 24% | 21% | 69 | 0.63 | 1.13 | 0.015 | 0.005 | 0.34 | 20.18 | 8.59 | 0.028 | 0.023 |
| CF-8 | 23% | 14% | 68 | 0.64 | 1.07 | 0.021 | 0.014 | 0.31 | 20.46 | 8.08 | 0.062 | 0.063 |
| CF-8M | 28% | 25% | 75 | 0.53 | 0.67 | 0.022 | 0.012 | 2.58 | 20.86 | 9.12 | 0.052 | 0.065 |

a. Measured with a ferrite scope, Ref. [4].

b. Calculated with Hull's equations, Ref. [4]

Table 2. Thermal aging conditions for the cast stainless steels in this study.

| Cast Grade | Ferrite [a] | Spec. Code | Heat ID | Thermal Aging Condition |
|---|---|---|---|---|
| CF-3 | 24% | A | 69 | Unaged |
| | | B | 69 | 10,000 hr at 400°C |
| CF-8 | 23% | E | 68 | Unaged |
| | | F | 68 | 10,000 hr at 400°C |
| CF-8M | 28% | I | 75 | Unaged |
| | | J | 75 | 10,000 hr at 400°C |

a. Measured with a ferrite scope, Ref. [4].

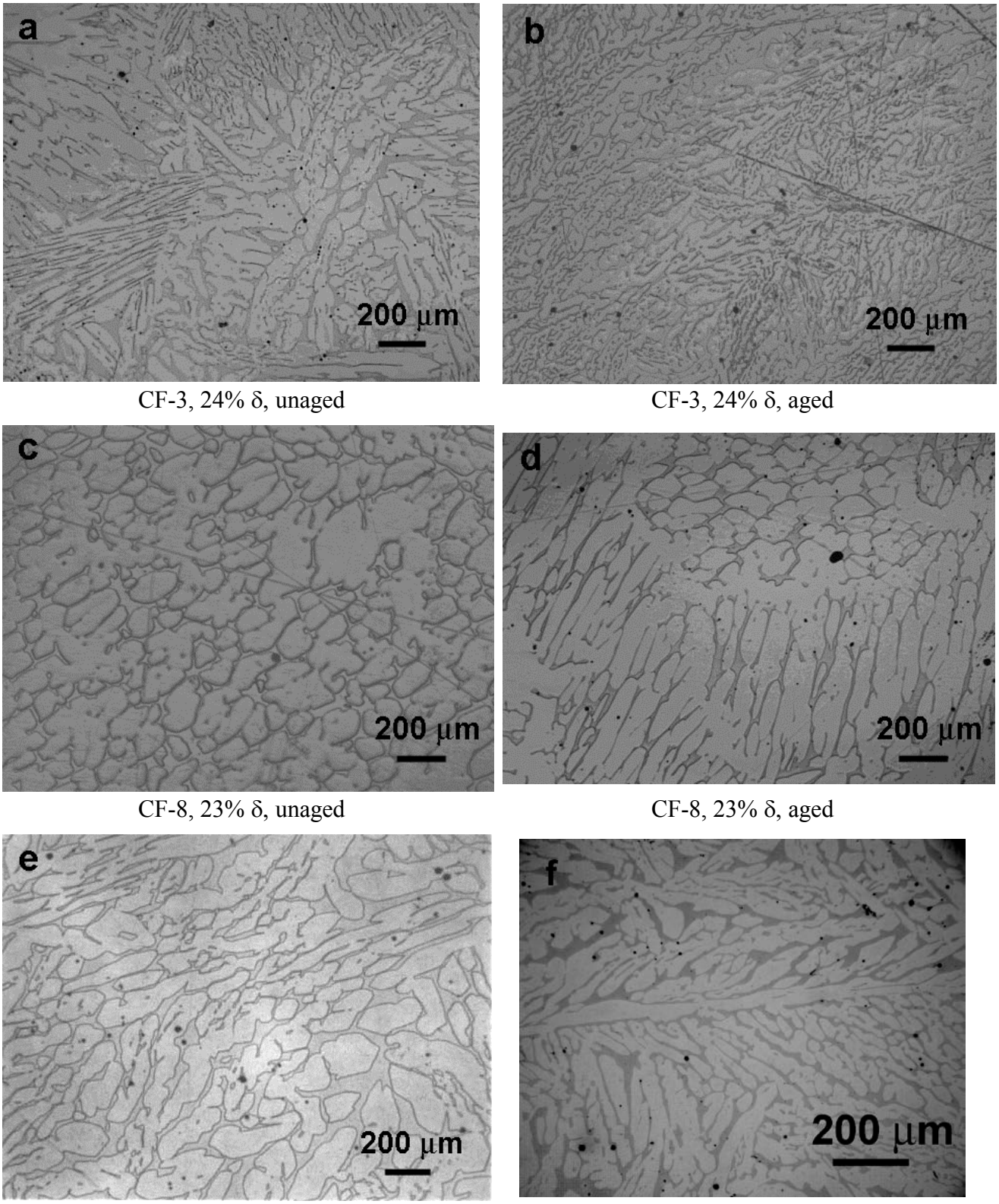


CF-3, 24% δ, unaged

CF-3, 24% δ, aged

CF-8, 23% δ, unaged

CF-8, 23% δ, aged

CF-8M, 28% δ, unaged (from ref. [4] )

CF-8M, 28% δ, aged

Figure 1. Metallurgical images of the unaged and thermally aged CASS materials.

Constrained by irradiation space, sub-sized compact tension (CT) specimens were used in this study. The sample was about 6.5-mm thick (i.e., 1/4T-CT) and 14-mm high. The starter notch size was about 6 mm. To ensure an in-plane crack growth, side grooves approximately 5% of the thickness were machined on both sides of the sample. Figure 2 is a schematic of the sample used in this study. The red lines in the figure are electrical leads spot-welded on the specimen.

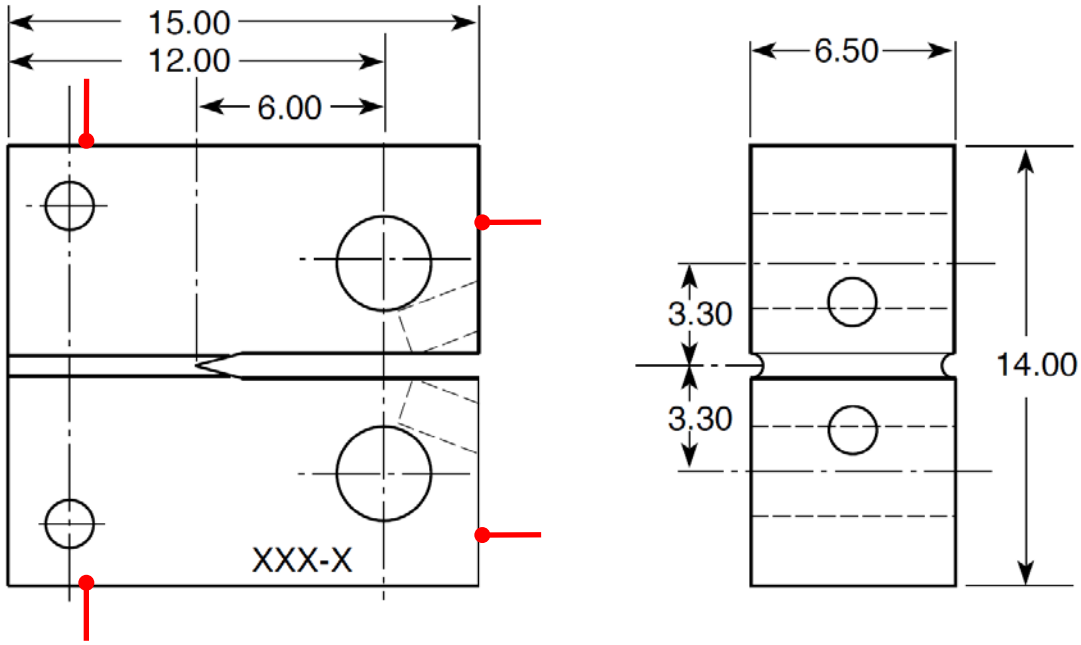


Figure 2. Schematic of 1/4T-CT specimen used in this study (red lines represent electrical leads).

## 2.2 Irradiation

The CASS specimens were irradiated in a helium-filled capsule in the Halden reactor, a boiling heavy water reactor in Norway. Figure 3 shows the assembly of the irradiation capsule. Some disk-shaped samples for transmission electron microscopy analyses were also included in a cylindrical container in the irradiation capsule (item 7 in Fig. 3). The irradiation temperature was ~315°C, and two sets of melting alloy temperature monitors (item 5) were installed in the irradiation assembly.

During the irradiation experiment, three fluence monitor wires (Fe, Ni, and Al/Co alloy) were placed outside the irradiation capsule. After the irradiation, dosimetry was performed by the Halden researchers on these wires. Using the activation cross sections determined previously, they estimated the accumulated neutron fluence for the irradiation capsule. The obtained fast neutron fluence (E > 1MeV) was about 5.56 x $10^{19}$ n/cm$^2$, which corresponds to a displacement damage of 0.08 dpa for the samples.

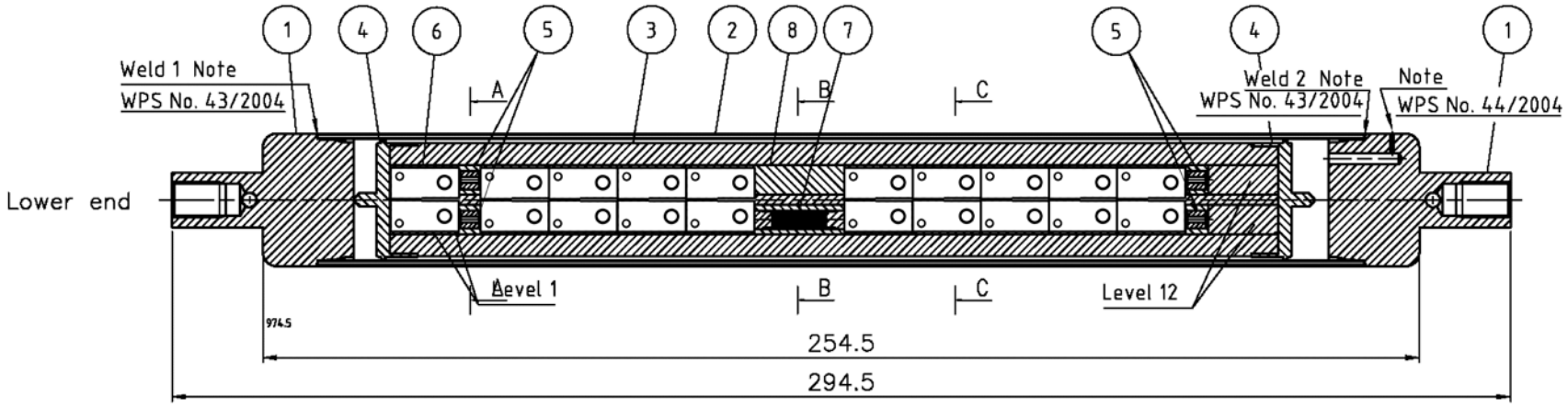


1. End Plug
2. Outer Capsule
3. Heat Transfer Body
4. End Guide Sleeve
5. Melting Alloy Assembly
6. CT Specimens
7. TEM Specimens Container
8. Spacer

Figure 3. Irradiation capsule of low-dose Halden irradiation.[33]

## 2.3 Test Facility

Two servo-hydraulic mechanical test systems located in the Irradiated Materials Laboratory (IML) at Argonne National Laboratory were used in this study. The IML is a radiological facility equipped with four air-atmosphere beta-gamma hot cells. The hot cells are maintained at a negative pressure with respect to the surroundings to maintain a proper radiological barrier. The two test systems are installed in separate hot cells. Each of the hot cells is equipped with its own loading frame, autoclave, load cell, linear voltage displacement transducer (LVDT), Instron control console, and data acquisition system.

In the current study, the tests were performed either in a simulated pressurized water reactor (PWR) environment or in a low-DO high-purity water environment. Both environments have low corrosion potentials, which are known to reduce the sensitivity of SSs to IASCC.[34] The simulated PWR water contained ~2 ppm lithium, ~1000 ppm boron, and ~2 ppm hydrogen. The conductivity was about 20 μS/cm. The low-DO high-purity water contained less than 10 ppb dissolved oxygen, and the conductivity was kept below 0.07 μS/cm during the tests. The test environments were provided by two water recirculation loops, and a schematic diagram of loop #1 is shown in Fig. 4. Each loop consists of a storage tank, a high pressure pump, a regenerative heat exchanger, an autoclave, an ECP cell, a back-pressure regulator, two ion-exchange cartridges, and several heaters. The high-pressure section of the loop extends from the high-pressure pump (item 13 in Fig. 4) through the back-pressure regulator (item 10 in Fig. 4). The rest of the loop is kept at low pressure. Over-pressurization of the high-pressure portion of the system is prevented by two rupture disks (items 3 and 15 in Fig. 4) located at the downstream of the high-pressure pump. The autoclaves are one-liter Type 316 stainless steel autoclaves and rated to 2900 psig for 350°C. The loop for hot cell #1 is a PWR water system, and hydrogen is used as cover gas. A hydrogen leak detection/alarm unit (items 36 - 38 in Fig. 4) is installed. For the hot cell #2 loop, a low-corrosion-potential environment is simulated in high-purity water using a mixture of nitrogen with 4% hydrogen as cover gas. For both systems, water is circulated at a rate of 20-30 mL/min through the autoclaves. The water conductivity and pH can be monitored with inline sensors. During the tests, the temperature and pressure of the autoclaves were kept at ~320°C and ~1800 psig, respectively.

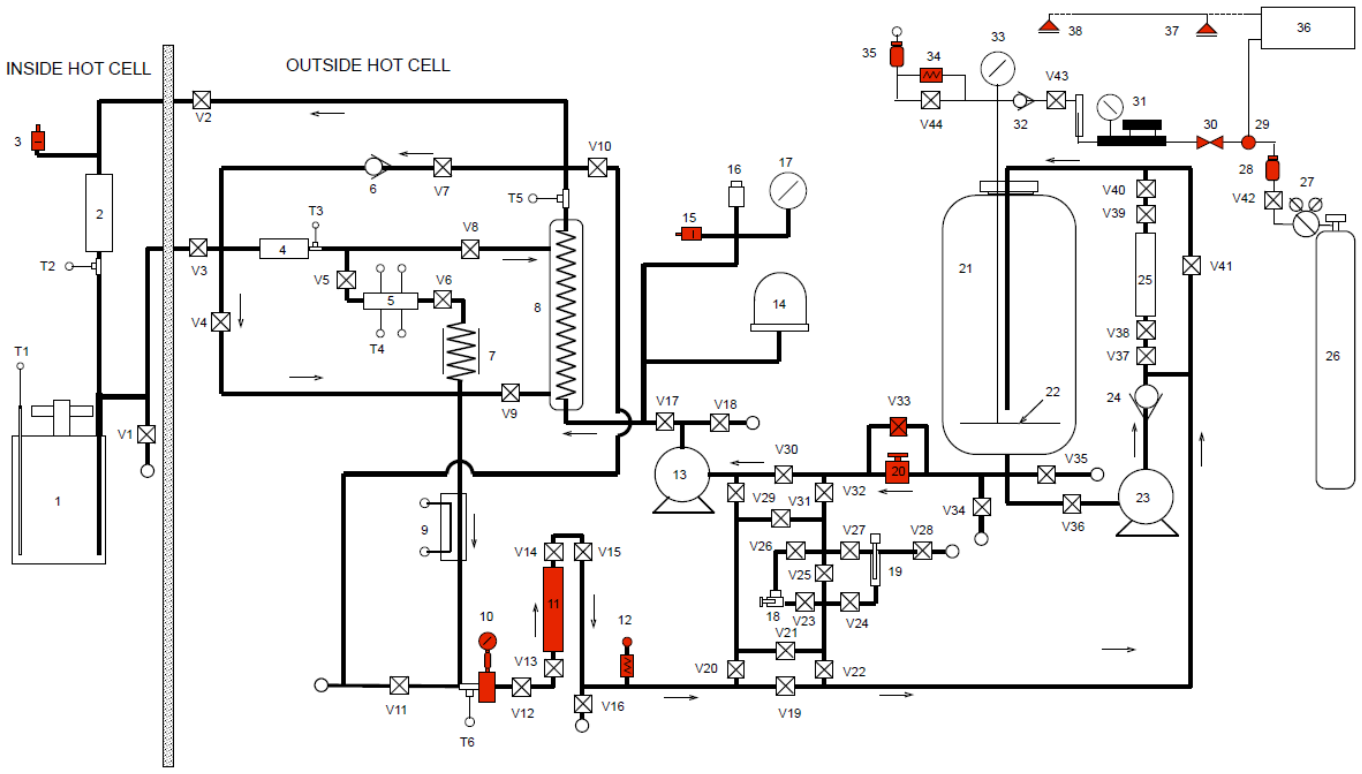


1. Autoclave
2. Autoclave preheater
3. Rupture disk
4. ECP preheater
5. ECP cell
6. Check valve
7. Air Cooled Coil
8. Heat exchanger
9. Chilled block
10. Back-pressure regulator
11. Ion exchange cartridge
12. Pressure relief valve
13. High-pressure pump
14. Accumulator
15. Rupture disk
16. Pressure transducer
17. High pressure gauge
18. Conductivity sensor
19. pH sensor
20. Solenoid valve
21. Feedwater storage tank
22. Sparge tube
23. Tank recirculation pump
24. Check valve
25. Ion exchange cartridge
26. Cover gas supply cylinder
27. High-pressure regulator
28. Flash arrestor
29. Solenoid valve
30. Excess flow valve
31. Low-pressure regulator
32. Check valve
33. Vacuum & pressure gauge
34. Pressure relief valve
35. Flash arrestor
36. Hydrogen alarm control panel
37. Hydrogen leak sensors
38. Hydrogen leak sensors
V = Valve
T = Thermocouples

Figure 4. Recirculation water loop for Cell 1 of the IML (items in red are safety significant components)

## 2.4 Crack Growth Rate and Fracture Toughness J-R curve Tests

### *2.4.1 Crack Growth Rate Test*

All CGR tests in this study were performed on the 1/4T-CT samples described above. Crack extensions were monitored with the direct current potential drop (DCPD) method during the tests. With this method, four electrical leads were spot welded on the CT sample (red lines shown in Fig. 2). A constant current was passed through the sample, and the potential drop across the crack mouth was measured and related to the crack extension of the CT sample with a calibrated correlation curve.

The CGR tests were carried out in either a simulated PWR water environment or a low-DO high-purity water environment.

A typical CGR test is started with cyclic loading to pre-crack the sample in the test environment. A load ratio around 0.2-0.3, frequency of 1-2 Hz, and maximum stress intensity factor ($K_{max}$) between 10 and 16 MPa $m^{1/2}$ are used for pre-cracking. The objective of this step is to generate a sharp fatigue crack and to advance the crack tip passing beyond the area close to the machine notch. The properties at this area may have been altered by machining and do not represent the material's intrinsic behavior.

The stress intensity factor $K$ for a CT specimen is calculated by:

$$K = \frac{P}{(B \cdot B_N \cdot W)^{1/2}} \cdot \frac{(2 + a/W)}{(1 - a/W)^{3/2}} \cdot f(\frac{a}{W}) \quad (1)$$

where $P$ is applied load; $B$ is the specimen thickness; $B_N$ is the net specimen thickness (or distance between the roots of the side grooves); $a$ is crack length; and $W$ is specimen width (measured from the load line to the back edge of the specimen). The geometry factor [f(a/W)] for a CT specimen is:

$$f(\frac{a}{W}) = 0.886 + 4.64\left(\frac{a}{W}\right) - 13.32\left(\frac{a}{W}\right)^2 + 14.72\left(\frac{a}{W}\right)^3 - 5.60\left(\frac{a}{W}\right)^4 \quad (2)$$

Once a fatigue crack is initiated, a series of test steps is carried out with gradually increased rise times and load ratios. The measured CGRs in these test steps include the contributions from both mechanical fatigue and corrosion fatigue. With the change in loading conditions, the contribution of mechanical fatigue is gradually reduced while the environmental effect is enhanced. Figure 5 illustrates the principle of introducing environmentally assisted cracking in a test. The changes in test conditions should produce cyclic CGRs along the green line. The cyclic CGR test is transitioned to a SCC CGR test when a significant environmental enhancement is observed.

Because of the beneficial effects of ferrite and the reduced sensitivity to IASCC in low-corrosion-potential environments, relatively low CGRs are expected for the CASS specimens even after irradiation to 0.08 dpa. To measure SCC CGRs at such low growth rates, a considerable amount of time is needed to collect data for adequate measurements. Since the focus of this study was on embrittlement (i.e., loss of facture toughness), a limited amount of time was spent on collecting SCC CGR data.

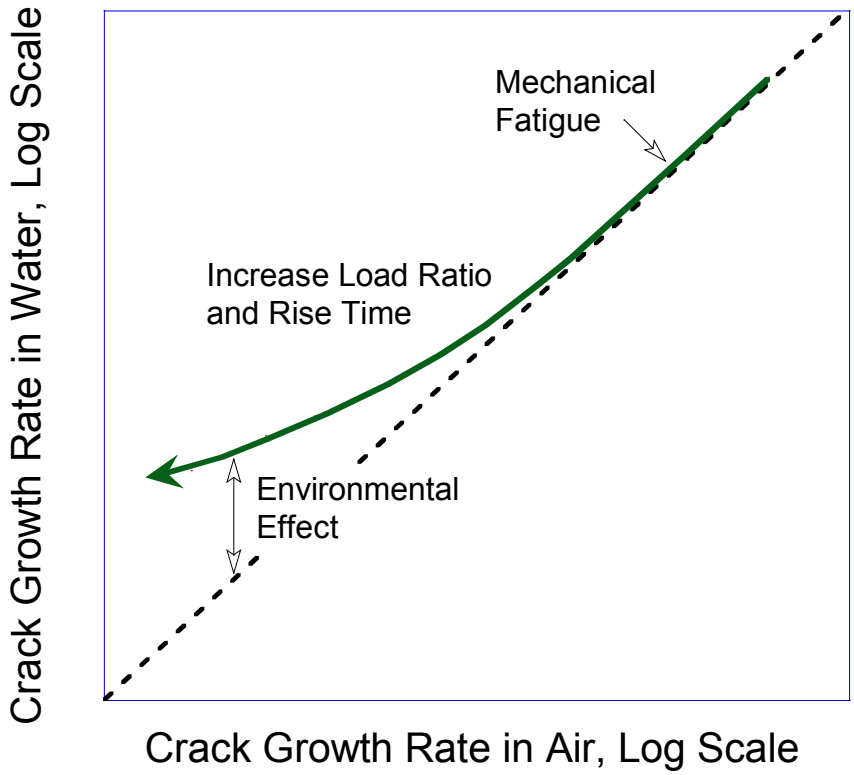


Figure 5. Schematic for inducing environmentally assisted cracking in test environment.

*2.4.2 Fracture Toughness J-R curve Test*

After each SCC CGR test, a fracture toughness J-R curve test was conducted on the same sample in the test environment. This test was performed with a constant stain rate of 0.43 μm/s, and the load and sample extension were recorded continuously outside the autoclave. The load-line displacement at load points was determined by subtracting the extension of the load train, which had been measured prior to the test. During the test, the loading was interrupted periodically, and the specimen was held at a constant extension to measure crack length with the DCPD method. Before each DCPD measurement, the sample stress was allowed to relax at a constant displacement for 30 s.

The J-integral was calculated from the load ($P$) vs. load-line displacement ($v$) curve according to ASTM Specification E 1820-8a.[35] The $J$ is the sum of the elastic and plastic components,

$$J = J_{el} + J_{pl} \tag{3}$$

At a hold point $i$ corresponding to a crack length $a_i$, as well as $v_i$ and $P_i$ on the load vs. load-line displacement curve, the elastic component $J_{el(i)}$ is given by:

$$J_{el(i)} = \frac{(K_{(i)})^2 (1-\nu)^2}{E} \tag{4}$$

where $\nu$ is Poisson's ratio, and the stress intensity $K_{(i)}$ is calculated from Eqs. 1 and 2. The plastic component $J_{pl(i)}$ is given by:

$$J_{pl(i)} = \left[ J_{pl(i-1)} + \left( \frac{\eta_{(i-1)}}{b_{(i-1)}} \right) \frac{A_{pl(i)} - A_{pl(i-1)}}{B_N} \right] \left[ 1 - \gamma_{(i-1)} \frac{a_{(i)} - a_{(i-1)}}{b_{(i-1)}} \right] \quad (5)$$

where $b_{(i-1)}$ is the remaining ligament at point *i-1*; $A_{pl(i)}$ is the area under the load vs. load-line displacement curve; and $B_N$ is the net specimen thickness. In addition, $\gamma_{(i)}$ and $\eta_{(i)}$ are factors that account for the crack growth effects on $J$ during the test and are expressed as:

$$\eta_{(i-1)} = 2.0 + 0.522 \frac{b_{(i-1)}}{W} \quad (6)$$

$$\gamma_{(i-1)} = 1.0 + 0.76 \frac{b_{(i-1)}}{W} \quad (7)$$

The quantity $A_{pl(i)} - A_{pl(i-1)}$ is the increment of the plastic area under the load vs. load-line displacement curve between lines of constant plastic displacement at points *i - 1* and *i*. The plastic area under the load vs. load-line displacement curve is given by

$$A_{pl(i)} = A_{pl(i-1)} + \frac{\left[ P_i + P_{i-1} \right] \left[ v_{pl(i)} - v_{pl(i-1)} \right]}{2} \quad (8)$$

where the plastic components of the load-line displacement, $v_{pl(i)}$, are:

$$v_{pl(i)} = v_{(i)} - P_i C_{LL(i)} \quad (9)$$

In the above, $v_{(i)}$ is the total load-line displacement, and $C_{LL(i)}$ is the compliance required to give the current crack length $a_i$ and can be determined as follows:

$$C_{LL(i)} = \frac{\left[ 1.62 + 17.80(a_i / W) - 4.88(a_i / W)^2 + 1.27(a_i / W)^3 \right]}{E' B_e [1 - (a_i / W)^2]} \quad (10)$$

where $B_e$ is the specimen effective thickness given by $B - (B - B_N)^2/B$, and $E' = E/(1 - \upsilon^2)$.

A J-R curve is constructed by fitting the calculated J values and corresponding crack lengths to a power law relationship. The J value at the intersection of the power law curve and the 0.2-mm offset blunting line are reported. Note that a blunting line of four times flow stress ($4\sigma_f$) is recommended by Mills [5] for materials with high strain hardening coefficients, and has been used in the previous thermal aging studies on unirradiated CASS.[4] To be consistent with the previous analyses, the same blunting line (i.e., $J/4\sigma_f$) was also used in the current work.

In this study, the estimated flow stresses are approximately 280-340 MPa and 420-520 MPa for unirradiated and irradiated CASS materials, respectively. This relatively low strength allows a maximum J value of 280-360 kJ/m$^2$ for a typical 1/4T-CT specimen. The maximum crack extension is limited below ~1.3 mm in most cases. Because of the low strength and high fracture toughness of CASS materials, the required crack tip constraint and upper limit of J integral are often invalid with the 1/4T-CT specimen. This is especially true for the unirradiated CASS samples since the strength is even lower without irradiation hardening. For this reason, the J values determined from this study normally cannot be validated for $J_{IC}$ per ASTM E182-8a.

*2.4.3 Fractographic Examination*

After each CGR/JR test, the final crack size was marked by fatigue cycling in an air atmosphere at room temperature. The specimen was then fractured, and the fracture surface was examined by scanning electron microscopy (SEM). Since the irradiated sample was highly radioactive, a two-step replication technique was developed for the fractographic examination. After cleaning the tested sample remotely using manipulators, we used a two-part synthetic compound to produce a negative replica of the fracture surface inside the hot cell. The negative replica was then removed from the hot cell and transferred to a radiological fume hood for decontamination. The second step of casting was to apply a low-viscosity epoxy on the surface of the negative replica. The cast was kept at approximately 70°C for several days to harden the epoxy replica. The negative replica was then removed. The obtained epoxy replica was coated with a layer of gold before it was transferred for SEM examination.

The CGR test and JR test regions were identified on the SEM images, and their fracture morphologies were analyzed. The physical crack length was also measured on the images, and a 9/8 averaging technique was used to account for the uneven extensions at the crack front. With this technique, nine measurements were taken along the crack front spaced across the width of the sample at equal intervals. The two near-surface measurements were averaged, and the resultant value was averaged with the remaining seven measurements to obtain the average crack length. All crack extensions determined from the DCPD method were scaled proportionately to match the final SEM-measured crack length.

## 3. RESULTS

Seven irradiated and four unirradiated control specimens from three heats of CASS were tested in the current study. The test matrix is shown in Table 3. The specimens were unaged and thermally aged pairs. The irradiated samples received a displacement dose of ~0.08 dpa. The CF-3 specimens were tested in either low-DO high-purity water or PWR water, and all CF-8 and CF-8M specimens were tested in low-DO high-purity water.

Table 3. Test matrix of unirradiated and irradiated low-dose CASS specimens.

| Sample ID | Dose (dpa) | Heat ID | Materials | Test Environment | Facility | CGR | JR | SEM |
|---|---|---|---|---|---|---|---|---|
| A-N1 | - | 69 | CF-3, 24% δ, unaged | Low-DO high-purity | Cell 2 | √ | √ | √ |
| A-1 | 0.08 | 69 | CF-3, 24% δ, unaged | PWR | Cell 1 | √ | - | √ |
| A-2 | 0.08 | 69 | CF-3, 24% δ, unaged | Low-DO high-purity | Cell 2 | √ | √ | √ |
| B-N1 | - | 69 | CF-3, 24% δ, aged | PWR | Cell 1 | √ | √ | √ |
| B-1 | 0.08 | 69 | CF-3, 24% δ, aged | PWR | Cell 1 | √ | √ | √ |
| E-N1 | - | 68 | CF-8, 23% δ, unaged | Low-DO high-purity | Cell 2 | √ | √ | √ |
| E-1 | 0.08 | 68 | CF-8, 23% δ, unaged | Low-DO high-purity | Cell 2 | √ | √ | √ |
| F-N1 | - | 68 | CF-8, 23% δ, aged | Low-DO high-purity | Cell 2 | √ | √ | √ |
| F-1 | 0.08 | 68 | CF-8, 23% δ, aged | Low-DO high-purity | Cell 2 | √ | √ | √ |
| I-1 | 0.08 | 75 | CF-8M, 28% δ, unaged | Low-DO high-purity | Cell 2 | √ | √ | √ |
| J-1 | 0.08 | 75 | CF-8M, 28% δ, aged | Low-DO high-purity | Cell 2 | √ | √ | √ |

### 3.1 CF-3 Cast Stainless Steel

#### *3.1.1 Unaged CF-3 CASS*

##### *3.1.1.1 Unirradiated specimen A-N1 tested in low-DO high-purity water*

Crack growth rate test

Specimen A-N1 was an unirradiated control sample tested in low-DO high-purity water. The material was an unaged CF-3 CASS with ~24% ferrite (Heat 69). The objective of this test was to provide a baseline for the irradiated tests. The test conditions and results are summarized in Table 4, and a crack-length history plot is shown in Fig. 6.

Fatigue pre-crack was initiated at ~15.4 MPa $m^{1/2}$ with a triangular waveform of 1 Hz and a load ratio of ~0.16. A cyclic CGR slightly below the fatigue growth rate in air was readily obtained in this sample. After ~220-μm crack extension, the load ratio and rise time were increased slowly to induce environmentally assisted cracking. The environmental effect on CGR was difficult to establish, and the crack stalled several times in the following test periods. Nonetheless, elevated crack growth rates were observed for this CASS sample under cyclic

loading in the low-DO high-purity water. The cyclic CGR data obtained from this test are plotted against the fatigue CGRs in air in Fig. 7. The fatigue CGRs are estimated based on James and Jones[37] with the load ratios and rise times given in Table 4. A corrosion fatigue curve proposed by Shack and Kassner[38] for unirradiated SSs in 0.2-ppm DO water at 290°C is also included in the figure as a reference. Note that the data point above the reference line (from test period *z*) was due to a temperature increase in the autoclave during that test period. After the temperature was stabilized, a much lower CGR was measured in the next test period. It is clear that the corrosion fatigue response of this CASS sample is better than that of typical SSs in low-DO high-purity water.

After a total of ~900-μm crack extension, the test was set to a constant load with periodical partial unloading (PPU) every 2 hr. The SCC CGR was negligibly low and was below the detection limit of the DCPD measurement. The SCC behavior of this sample will be discussed at the end of this section along with the other CGR data obtained from the same heat.

Table 4. Crack growth rates of specimen A-N1 (unirradiated and unaged CF-3 with 24% δ ferrite) in low-DO high-purity water.

| Test Period | Test Time, h | Test Temp., °C | Load Ratio | Rise Time, s | Return Time, s | Hold Time, s | Kmax, MPa $m^{1/2}$ | ΔK, MPa $m^{1/2}$ | CGR in Env., m/s | CGR in Air, m/s | Crack Length, mm |
|---|---|---|---|---|---|---|---|---|---|---|---|
| Start | 0.3 | | | | | | | | | | 5.978 |
| A | 3.2 | 317 | 0.16 | 0.39 | 0.39 | 0.11 | 15.4 | 12.9 | 5.94E-08 | 5.68E-08 | 6.204 |
| B | 5.1 | 317 | 0.29 | 0.36 | 0.36 | 0.14 | 14.5 | 10.3 | 1.98E-08 | 3.36E-08 | 6.257 |
| C | 9.1 | 317 | 0.40 | 0.69 | 0.69 | 0.31 | 14.3 | 8.6 | 1.01E-09 | 1.11E-08 | 6.265 |
| D | 21.8 | 317 | 0.21 | 0.38 | 0.38 | 0.12 | 16.0 | 12.6 | 7.14E-08 | 5.72E-08 | 6.419 |
| E | 24.5 | 317 | 0.30 | 0.74 | 0.74 | 0.26 | 16.5 | 11.6 | 3.02E-08 | 2.49E-08 | 6.528 |
| F | 29.4 | 317 | 0.45 | 0.68 | 0.68 | 0.32 | 16.8 | 9.3 | 1.35E-08 | 1.50E-08 | 6.611 |
| G | 43.2 | 317 | 0.60 | 3.04 | 3.04 | 1.96 | 16.6 | 6.7 | 3.02E-10 | 1.30E-09 | 6.618 |
| H | 50.7 | 317 | 0.50 | 1.65 | 1.65 | 0.85 | 16.9 | 8.5 | 5.37E-09 | 4.87E-09 | 6.664 |
| I | 66.6 | 317 | 0.50 | 6.57 | 1.31 | 3.43 | 16.8 | 8.4 | 6.07E-10 | 1.18E-09 | 6.685 |
| J | 80.2 | 317 | 0.49 | 9.91 | 3.30 | 5.09 | 16.9 | 8.5 | 6.25E-10 | 8.24E-10 | 6.702 |
| K | 97.4 | 317 | 0.49 | 19.9 | 3.31 | 10.1 | 17.0 | 8.6 | 3.28E-10 | 4.25E-10 | 6.713 |
| L | 118.2 | 317 | 0.49 | 39.7 | 7.94 | 20.3 | 17.1 | 8.7 | 2.68E-10 | 2.16E-10 | 6.728 |
| M | 145 | 317 | 0.49 | 99.7 | 7.98 | 50.3 | 17.3 | 8.8 | 1.57E-10 | 9.04E-11 | 6.737 |
| N | 170.5 | 317 | 0.49 | 199.8 | 7.99 | 100.2 | 17.3 | 8.9 | 7.96E-11 | 4.59E-11 | 6.742 |
| O | 196.2 | 317 | 0.48 | 333.6 | 8.01 | 166.4 | 17.3 | 8.9 | 1.51E-10 | 2.80E-11 | 6.751 |
| P | 236.1 | 318 | 0.48 | 667.8 | 8.01 | 332.2 | 17.3 | 8.9 | negligible | 1.42E-11 | 6.750 |
| Q | 285.6 | 318 | 0.49 | 133.3 | 8.00 | 66.7 | 17.4 | 8.9 | 6.58E-11 | 7.06E-11 | 6.758 |
| R | 308.1 | 318 | 0.49 | 66.6 | 7.99 | 33.4 | 17.5 | 8.9 | 8.93E-11 | 1.40E-10 | 6.763 |
| S | 316.7 | 318 | 0.44 | 34.2 | 8.21 | 15.8 | 17.4 | 9.7 | 3.90E-10 | 3.46E-10 | 6.769 |
| t [a] | 332.2 | 318 | 0.44 | 68.5 | 8.22 | 31.5 | 17.7 | 9.8 | 5.06E-10 | 1.81E-10 | 6.795 |
| U | 355.8 | 319 | 0.49 | 133.1 | 7.99 | 66.9 | 17.6 | 9.0 | 6.71E-11 | 7.25E-11 | 6.799 |
| V | 363.7 | 319 | 0.45 | 13.6 | 3.41 | 6.4 | 17.6 | 9.8 | 1.36E-09 | 8.90E-10 | 6.814 |
| W | 379.4 | 319 | 0.47 | 33.7 | 8.09 | 16.3 | 17.8 | 9.5 | 6.68E-10 | 3.33E-10 | 6.837 |
| X | 403.6 | 318 | 0.48 | 66.4 | 7.97 | 33.6 | 17.4 | 9.1 | 1.62E-10 | 1.48E-10 | 6.846 |
| Y | 430.8 | 318 | 0.49 | 133.2 | 8.00 | 66.8 | 17.8 | 9.2 | 8.67E-11 | 7.69E-11 | 6.851 |
| z [b] | 452.8 | 317 | 0.49 | 333.8 | 8.01 | 166.2 | 18.1 | 9.3 | 3.74E-10 | 3.19E-11 | 6.872 |
| aa | 500.3 | 319 | 0.48 | 669.5 | 8.03 | 330.5 | 18.1 | 9.4 | 3.65E-11 | 1.64E-11 | 6.876 |
| 1 | 811.3 | 318 | 0.50 | 12 | 12 | 7200 | 18.0 | 9.0 | negligible | 1.37E-12 | 6.880 |

[a] The CGR value was obtained from the later part of the test period.

[b] The autoclave temperature was unstable in the test period.

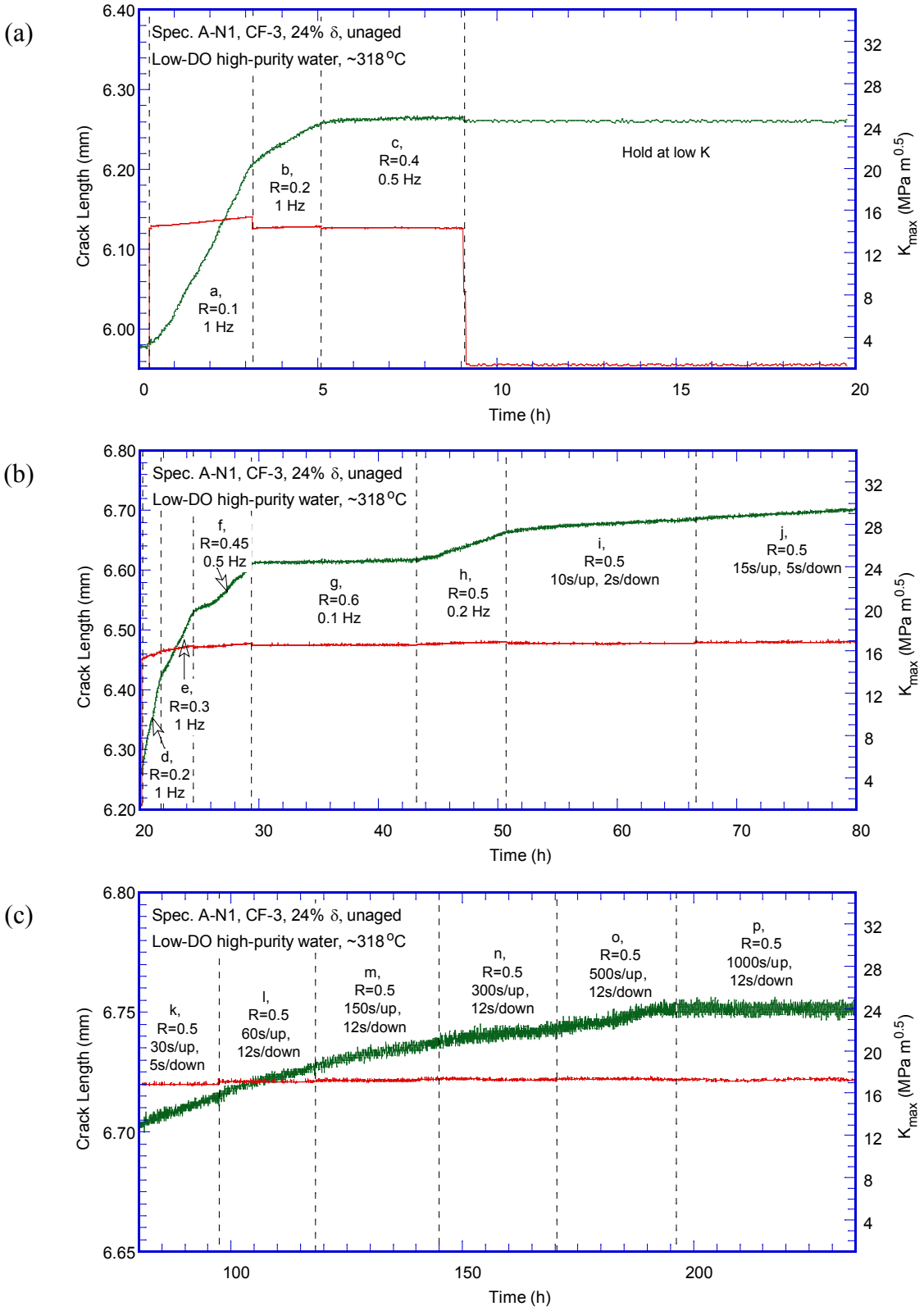


Figure 6. Crack-length-vs.-time plot for specimen A-N1 (unirradiated and unaged CF-3 with 24% ferrite): test periods (a) a-c, (b) d-j, (c) k-p, (d) q-u, (e) v-aa, and (f) 1.

(d)

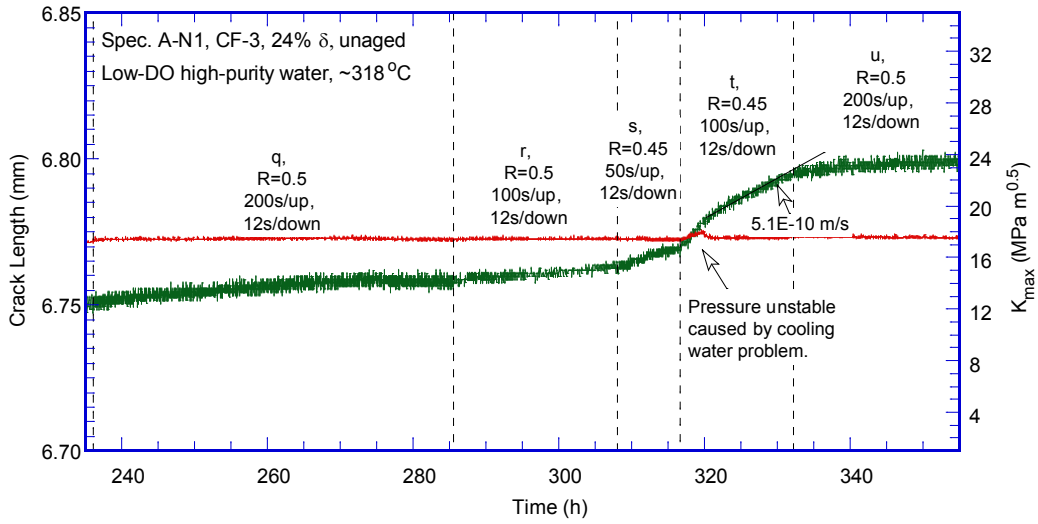


(e)

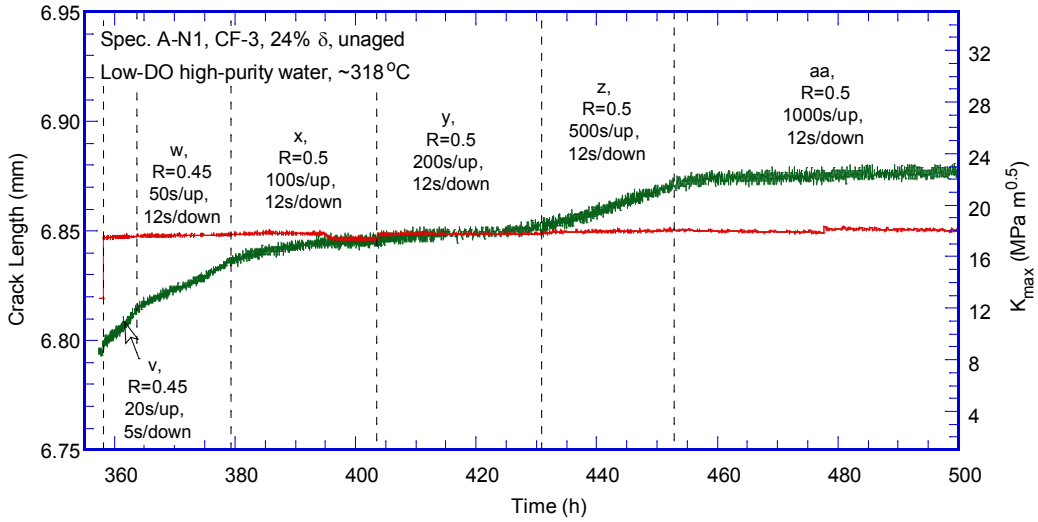


(f)

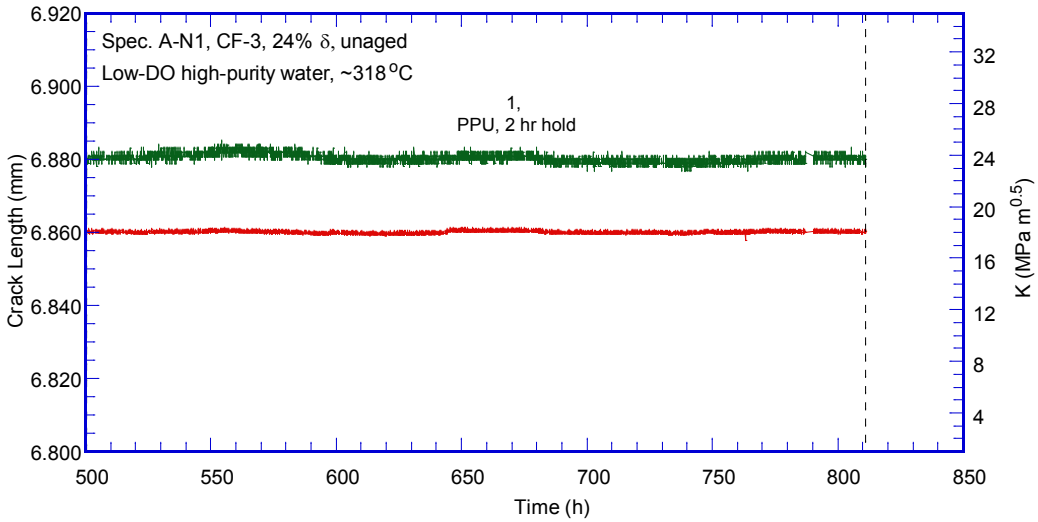


Figure 6. (Contd.)

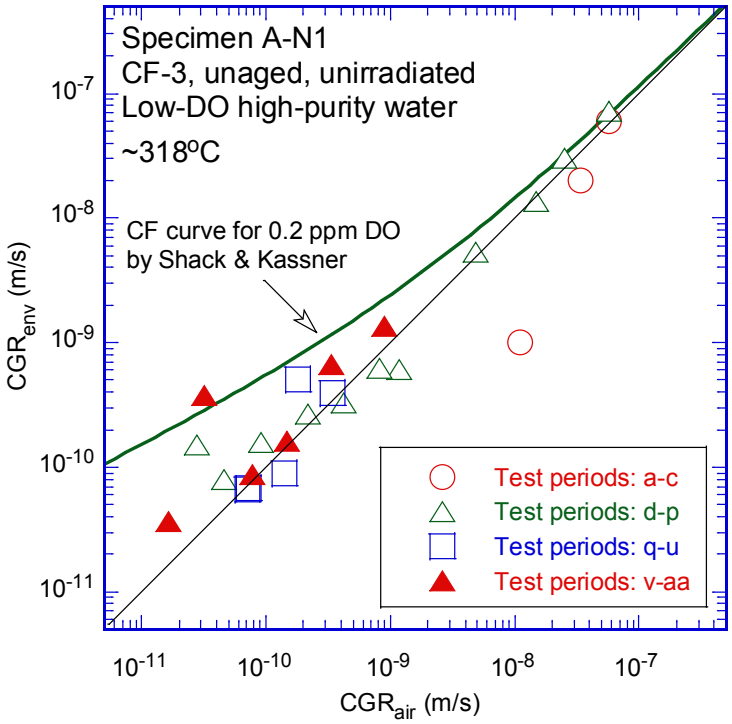


Figure 7. Cyclic CGRs of specimen A-N1.

Fracture toughness J-R curve test

A fracture toughness J-R curve test was conducted on the sample in the low-DO high-purity water environment. The sample was loaded at a constant extension rate of 0.43 μm/s while the load and load-line displacement were recorded. During the test, loading was interrupted periodically to measure the crack extension by DCPD. The obtained J and crack extension data are plotted in Fig. 8. Note that the measurement capacity of 1/4T-CT samples is significantly lower than the fracture toughness anticipated for the CASS materials, and thus a validated J-R curve test is not possible for this sample. Nonetheless, the available data points fit to a power-law relationship, and the estimated J value at the 0.2-mm offset line is about 320 kJ/m$^2$. The straightness of the crack extension and the $J_{max}$ requirement are not met in this analysis due to lack of constraint at the crack tip.

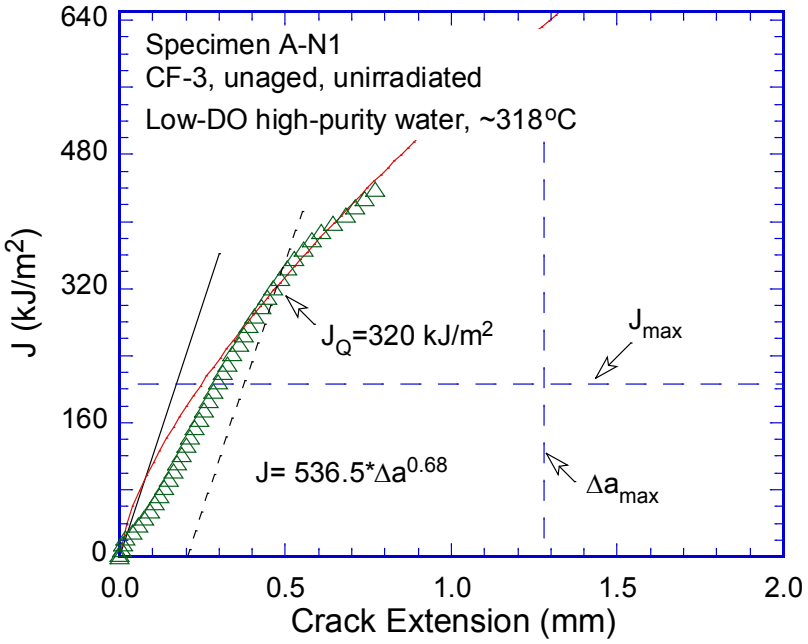


Figure 8. The J-R curve for specimen A-N1.

Fractographic examination

After the J-R curve test, the sample was fatigued and broken open at room temperature in an air atmosphere. The fracture surface was examined with SEM (Fig. 9). While the CGR test region shows a transgranular (TG) morphology, the entire JR test region is covered with ductile dimples. A major secondary crack that covers nearly a half of the width of the sample can be seen at the machined notch. This large secondary crack may affect the crack propagation, leading to a curved crack front in the CGR test. Consequently, the final crack size of the JR test is also affected with a significantly higher crack extension on the right-hand side of the SEM image. Figure 10 shows an enlarged view of the fracture surface along the sample central line. More details of the CGR and JR test regions can be seen in Figs. 11 and 12, respectively.

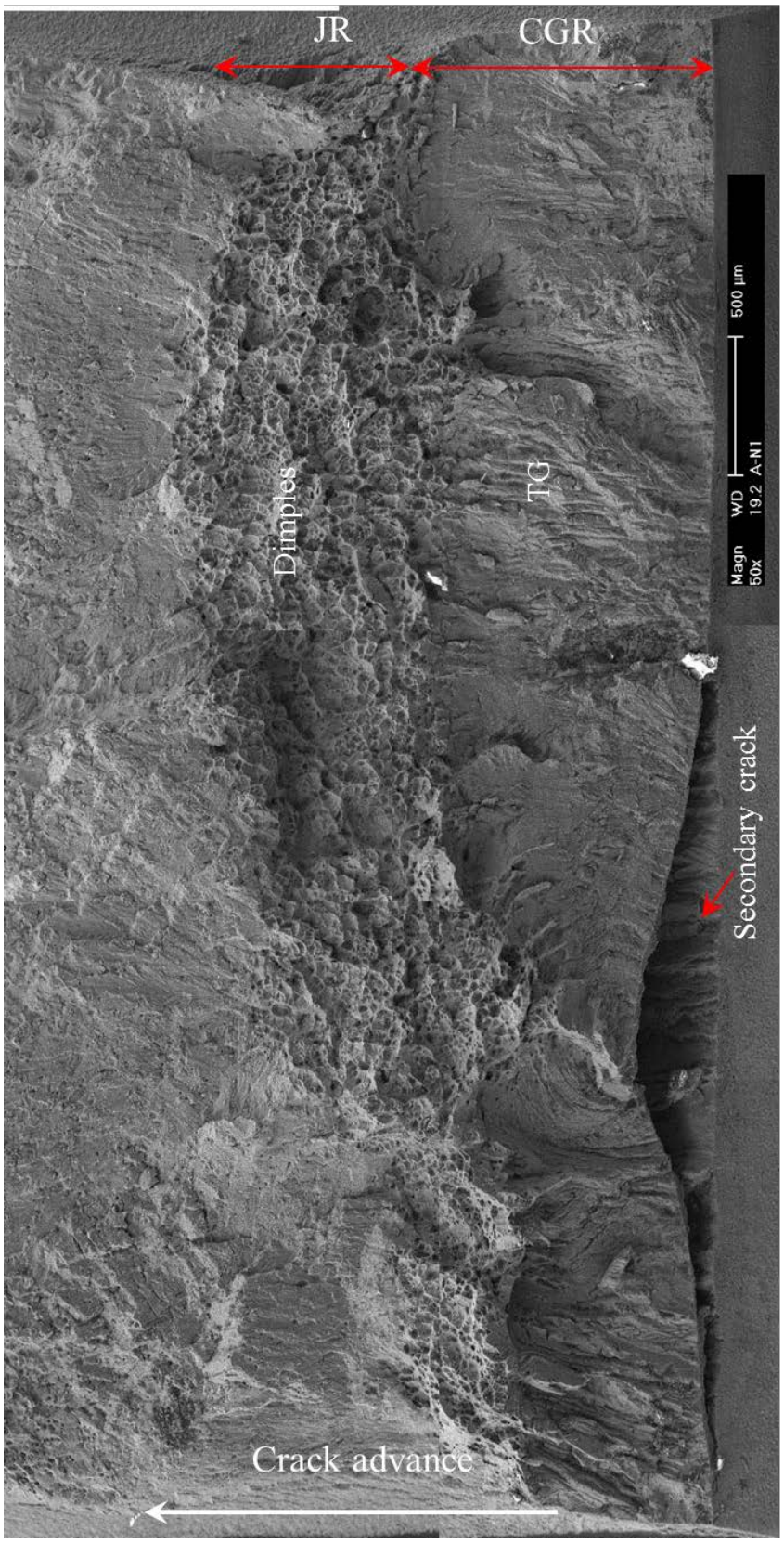


Figure 9. Fracture surface of specimen A-N1 tested in low-DO high-purity water.

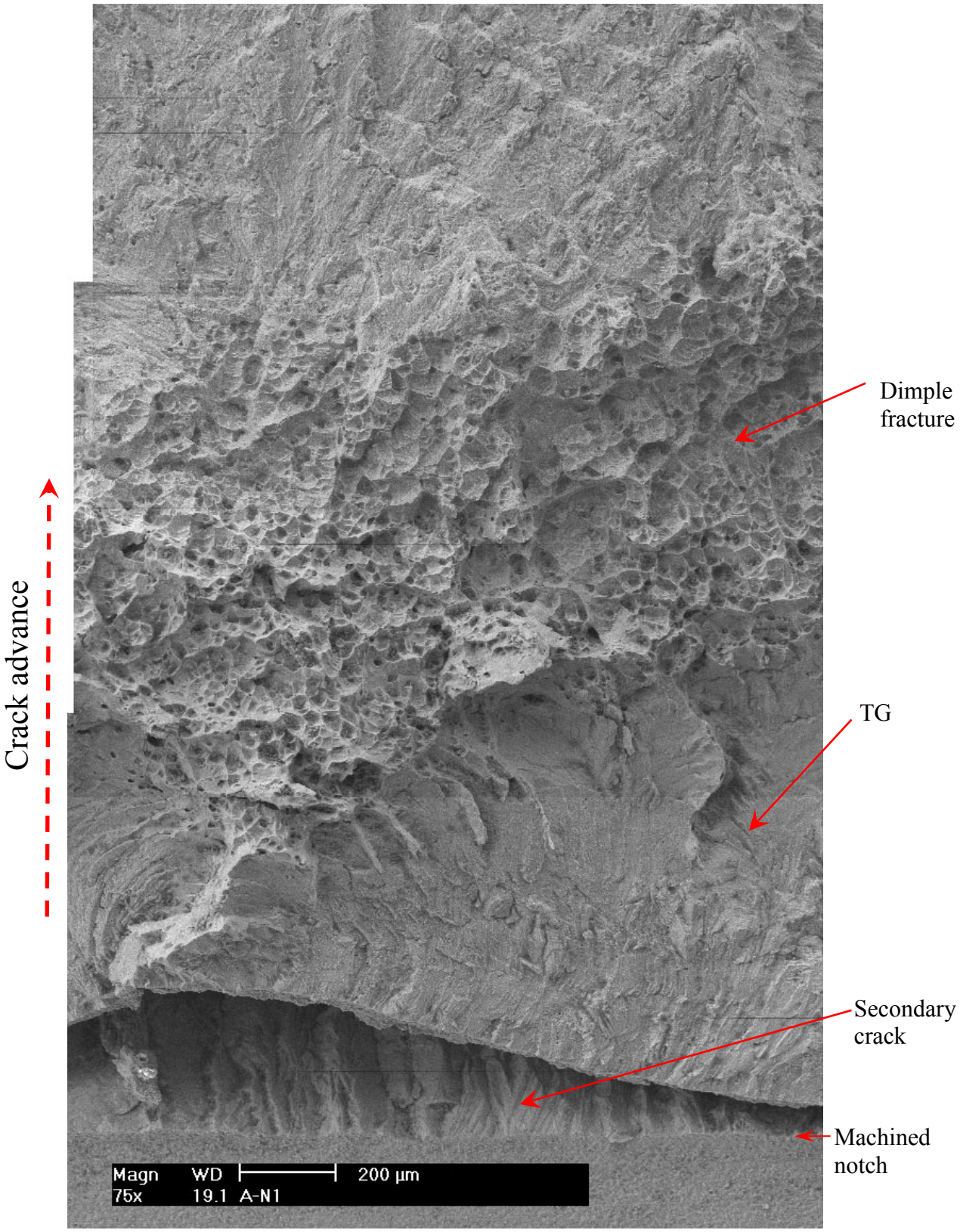


Figure 10. Fracture surface of specimen A-N1 along the sample central line.

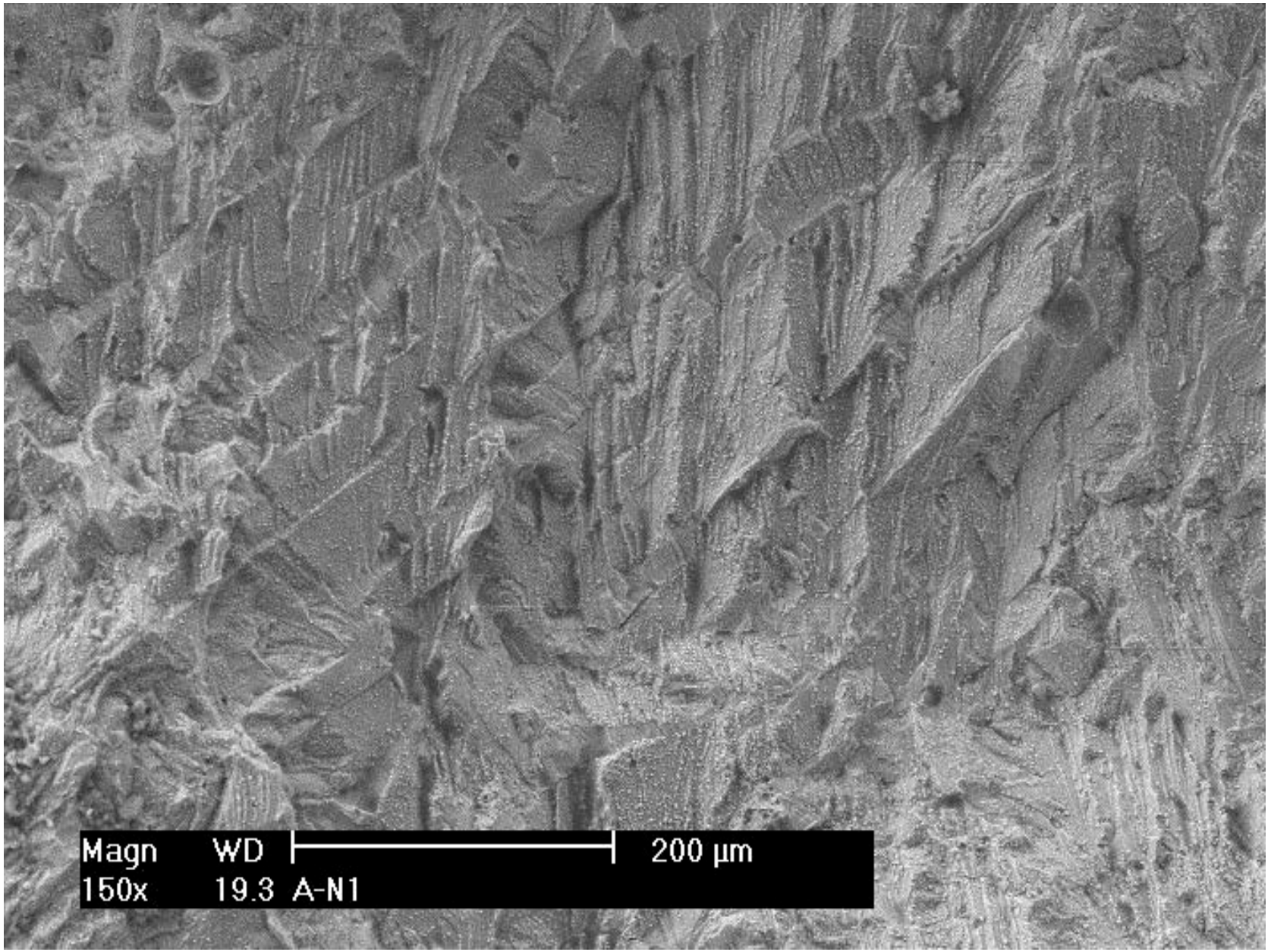


Figure 11. Transgranular fracture in the precracking region of specimen A-N1.

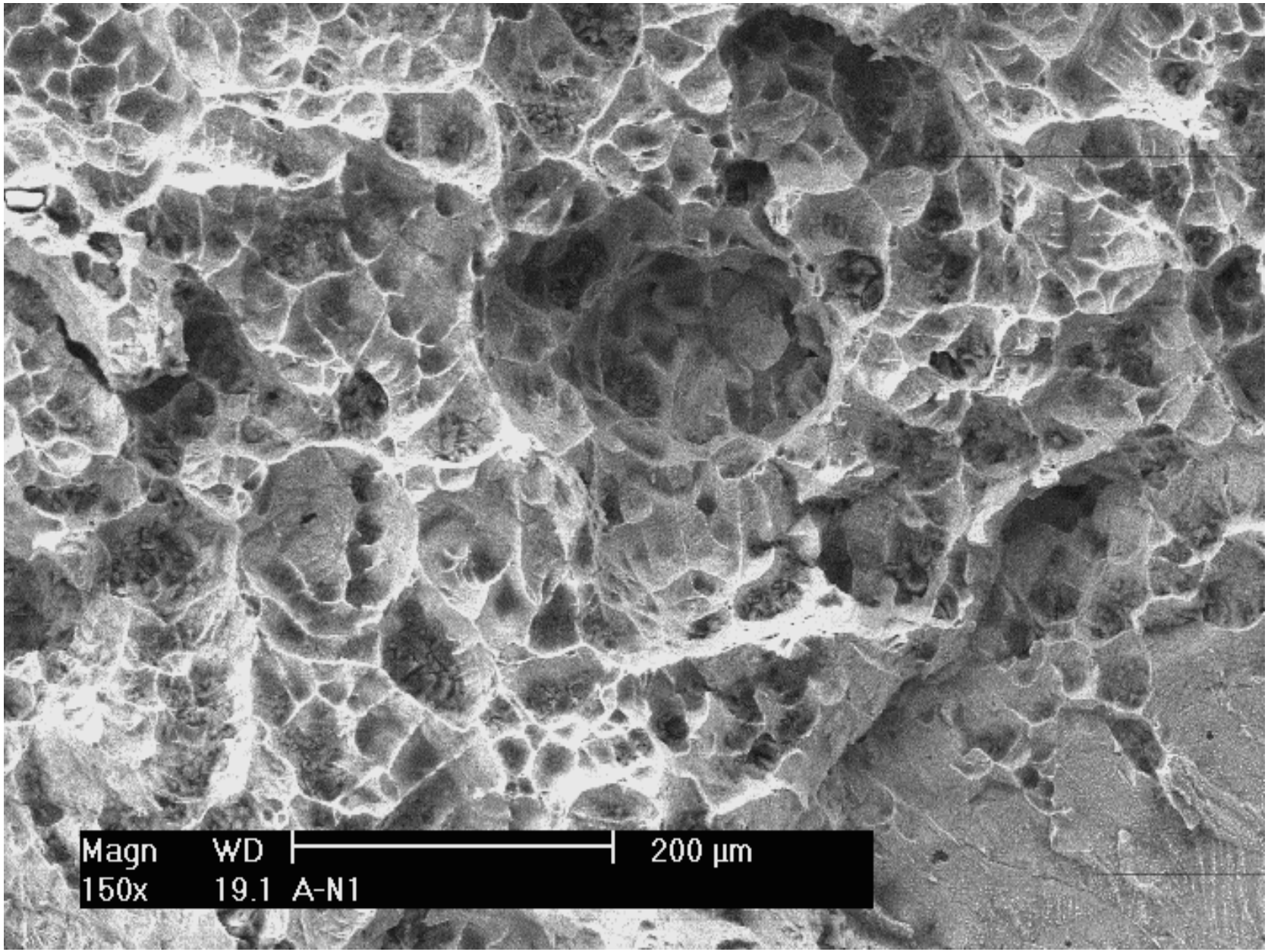


Figure 12. Ductile dimple fracture in JR test region of specimen A-N1.

*3.1.1.2 Irradiated specimen A-1 tested in simulated PWR water*

Crack growth rate test

Specimen A-1 was an irradiated CF-3 CASS sample (Heat 69) tested in the simulated PWR water environment. The specimen had ~24% ferrite and was in the as-cast condition. The objective of this test was to compare the results with those from an identical test performed in low-DO high-purity water. Also, the CGR results of this sample were compared with those obtained from its thermally aged equivalent. The test conditions and results are summarized in Table 5, and a crack-length history plot is shown in Fig. 13. Note that the starting crack length for this sample was about 1 mm longer than that of a typical 1/4T-CT specimen. This larger-than-normal initial crack length was due to a restart of the pre-cracking to correct a loose DCPD lead. The initial crack size reported in Table 5 was determined with SEM images on the fracture surface after the test.

Table 5. Crack growth rates of specimen A-1 (0.08-dpa unaged CF-3 sample with 24% δ ferrite) in PWR water.[a]

| Test Period | Test Time, h | Test Temp., °C | Load Ratio | Rise Time, s | Return Time, S | Hold Time, s | Kmax, MPa $m^{1/2}$ | ΔK, MPa $m^{1/2}$ | CGR in Env., m/s | CGR in Air, m/s | Crack Length, mm |
|---|---|---|---|---|---|---|---|---|---|---|---|
| Start | 63.9 | | | | | | | | | | 6.802 [b] |
| a | 64.8 | 319 | 0.21 | 0.43 | 0.43 | 0.07 | 24.3 | 19.2 | 1.58E-07 | 2.04E-07 | 7.009 |
| b | 66 | 319 | 0.31 | 0.41 | 0.41 | 0.09 | 23.8 | 16.4 | 1.17E-07 | 1.43E-07 | 7.218 |
| c | 68.6 | 319 | 0.41 | 0.78 | 0.78 | 0.22 | 23.1 | 13.6 | 3.21E-08 | 4.47E-08 | 7.340 |
| d | 72.3 | 319 | 0.41 | 1.54 | 1.54 | 0.46 | 21.9 | 12.8 | 9.77E-09 | 1.89E-08 | 7.395 |
| e | 87.6 | 319 | 0.46 | 2.96 | 1.48 | 1.04 | 20.3 | 11.0 | 2.89E-10 | 6.18E-09 | 7.403 |
| f | 91 | 319 | 0.41 | 3.08 | 1.54 | 0.92 | 22.2 | 13.1 | 9.46E-09 | 1.01E-08 | 7.462 |
| g | 94.1 | 320 | 0.41 | 7.69 | 1.54 | 2.31 | 22.4 | 13.2 | 5.67E-09 | 4.17E-09 | 7.503 |
| h | 103 | 320 | 0.46 | 22.6 | 3.76 | 7.42 | 22.6 | 12.2 | 1.51E-09 | 1.16E-09 | 7.535 |
| i | 114.3 | 320 | 0.46 | 45.1 | 3.76 | 14.9 | 22.7 | 12.3 | 7.63E-10 | 5.86E-10 | 7.558 |
| j | 118.7 | 319 | 0.41 | 15.3 | 3.83 | 4.66 | 23.0 | 13.6 | 4.61E-09 | 2.27E-09 | 7.602 |
| k | 127.9 | 319 | 0.41 | 46.0 | 3.83 | 14.0 | 23.0 | 13.7 | 1.25E-09 | 7.72E-10 | 7.632 |
| l | 150.3 | 318 | 0.40 | 114.9 | 9.19 | 35.1 | 23.0 | 13.7 | 3.90E-10 | 3.13E-10 | 7.655 |
| m | 168.7 | 319 | 0.40 | 385.6 | 9.25 | 114.4 | 23.9 | 14.3 | 3.56E-10 | 1.05E-10 | 7.673 |
| 1 | 209 | 318 | 0.40 | 12 | 12 | 7200 | 23.9 | 14.4 | 4.83E-11 | 5.75E-12 | 7.684 |

[a] Simulated PWR water with 2 ppm Li and 1000 ppm B. DO<10 ppb. Conductivity ~20 μS/cm.

[b] Determined from the SEM image after the test.

The specimen was pre-cracked in the PWR environment with a triangular waveform at 1 Hz, a maximum stress intensity factor of ~24 MPa $m^{1/2}$, and load ratio of 0.2. After about 200 μm extension, the load ratio was increased while the stress intensity factor and cyclic frequency were reduced gradually. The measured CGRs in the initial stage of the pre-cracking (test periods *a-d*) followed closely with the fatigue growth rates in air. Next, several test periods were carried out with saw-tooth waveforms and increased rise times to stimulate environmentally assisted cracking. The environmental enhancement of CGRs started to appear and became stabilized after some additional crack extension. The cyclic CGR data obtained from this test are plotted against the estimated fatigue CGRs in air as shown in Fig. 14. The corrosion fatigue curve proposed by Shack and Kassner is also included in the figure as a reference. Obviously, the

corrosion fatigue response of this sample is lower than that of typical SSs, suggesting good IASCC resistance of CASS in PWR water.

After the cyclic CGR test, the specimen was subjected to a constant stress intensity factor of ~24 MPa $m^{1/2}$ with PPU every 2 hours. The measured SCC CGR was about $4.8 \times 10^{-11}$ m/s, a factor of four lower than that of the NUREG-0313 curve,[36] a SCC disposition curve based on unirradiated SSs tested in a high-DO environment. The SCC response of this sample will be discussed at the end of this section along with the other CGR data obtained from the same heat.

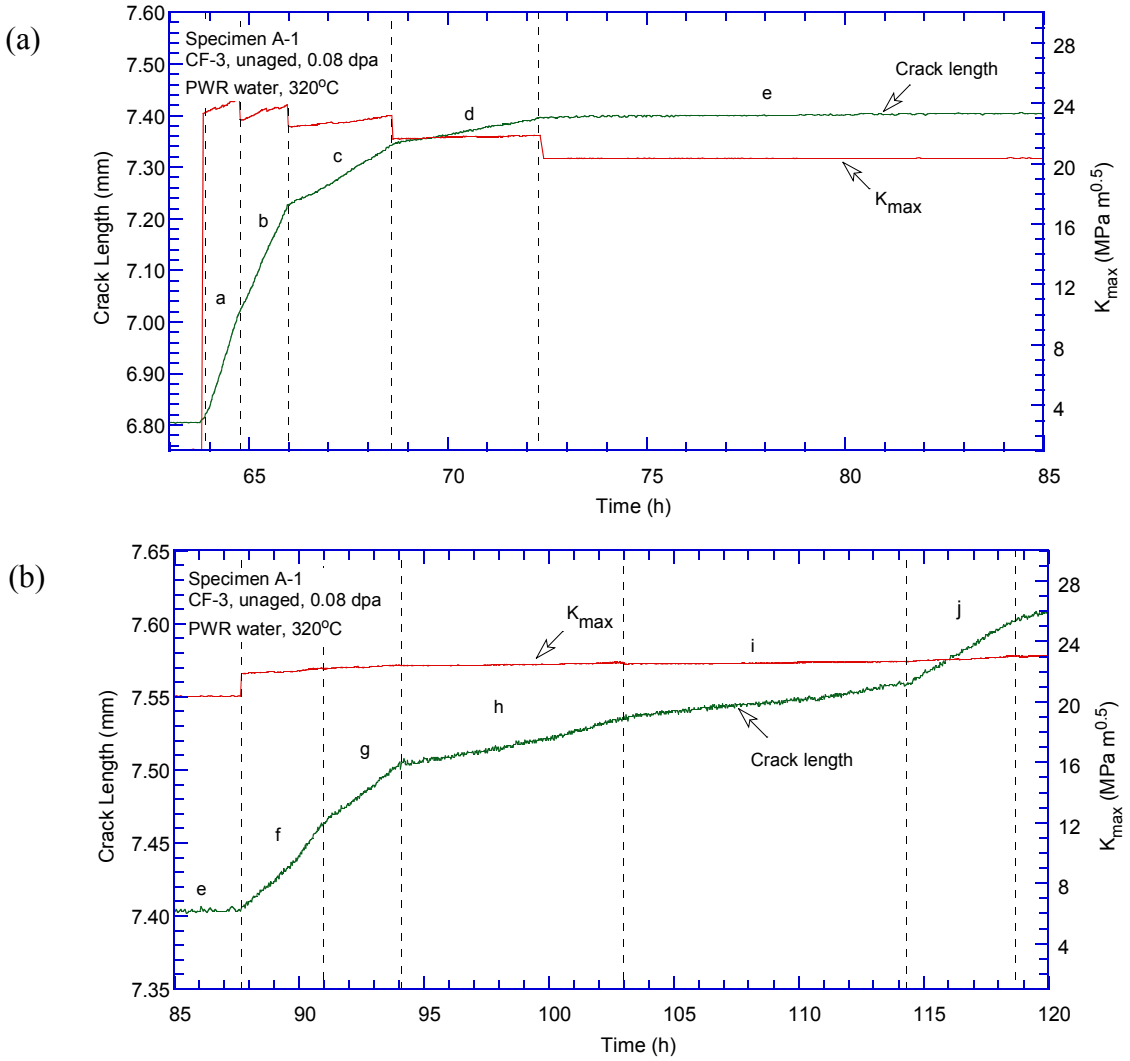


Figure 13. Crack-length-vs.-time plot for specimen A-1 (0.08-dpa unaged CF-3 with 24% ferrite): test periods (a) a-e, (b) f-j, (c) k-m, and (d) 1.

(c)

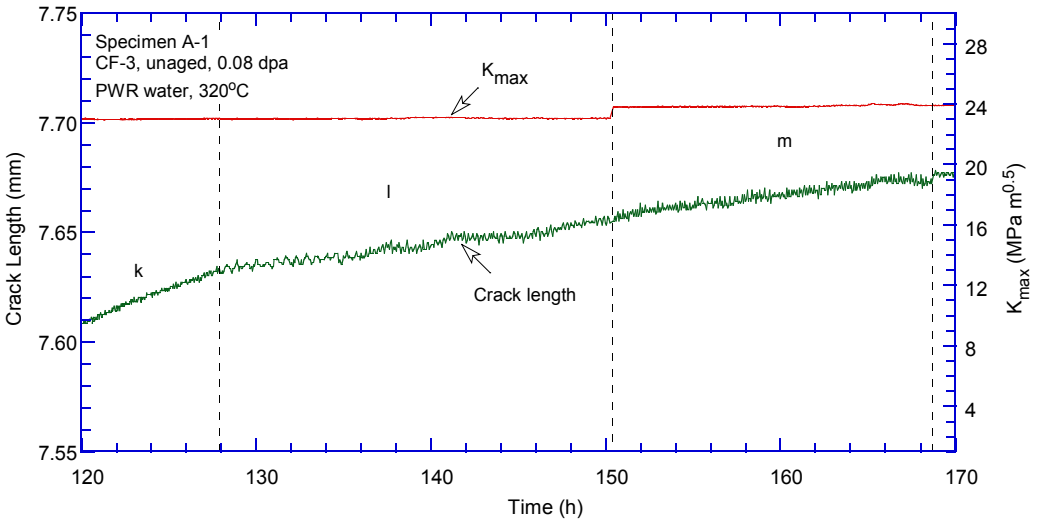


(d)

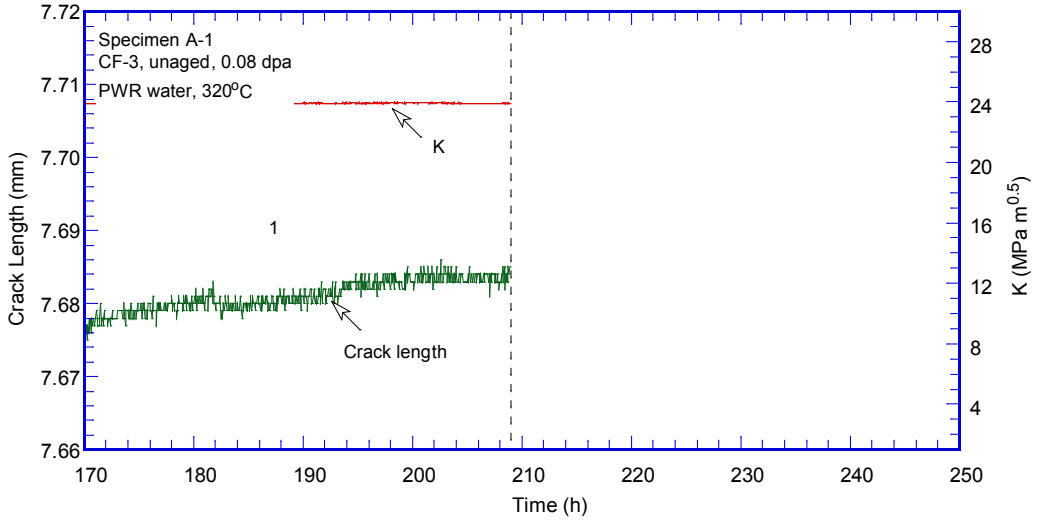


Figure 13. (Contd.)

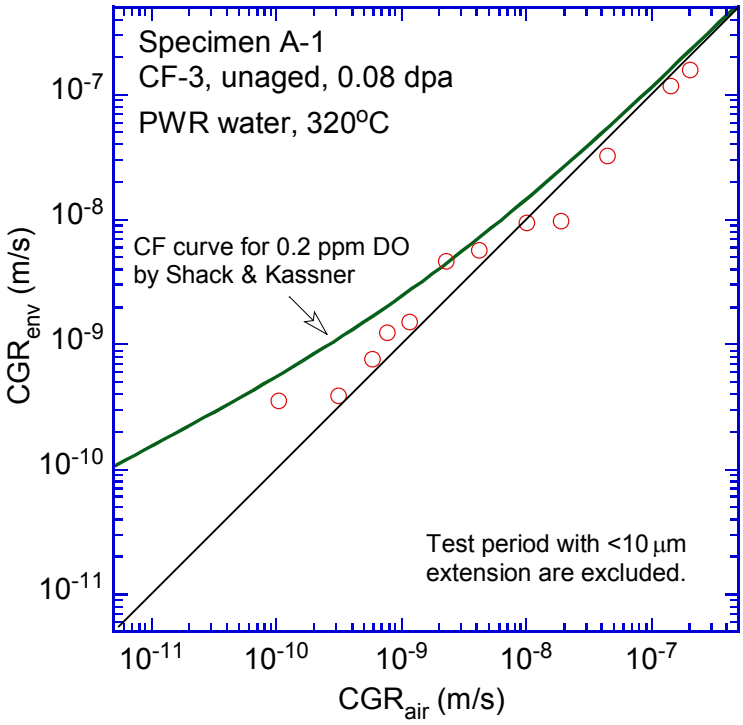


Figure 14. Cyclic CGRs of specimen A-1.

Fractographic examination

After the test, the specimen was pulled apart in an air atmosphere at room temperature, and the fracture surface was examined with SEM. Figure 15 shows the entire crack front of specimen A-1. The straight line in the middle of the picture corresponds to the restart of the pre-cracking. Figure 16 is an enlarged view along the central section of the specimen. Transgranular cleavage-like fracture is the dominant morphology throughout the CGR region. Figure 17 shows the typical river pattern of cleavage cracking at the beginning and the end of the CGR test region. Vermicular ferrite at dendrite cores can also be seen in a few places on the fracture surface. As shown in Fig. 18, fewer slip ledges can be seen within ferrite, suggesting that the ferrite dendrite core might be deformed to a lesser extent than the surrounding austenite. Beyond the CGR test, the dominant fracture mode is ductile dimples resulting from microvoid coalescence.

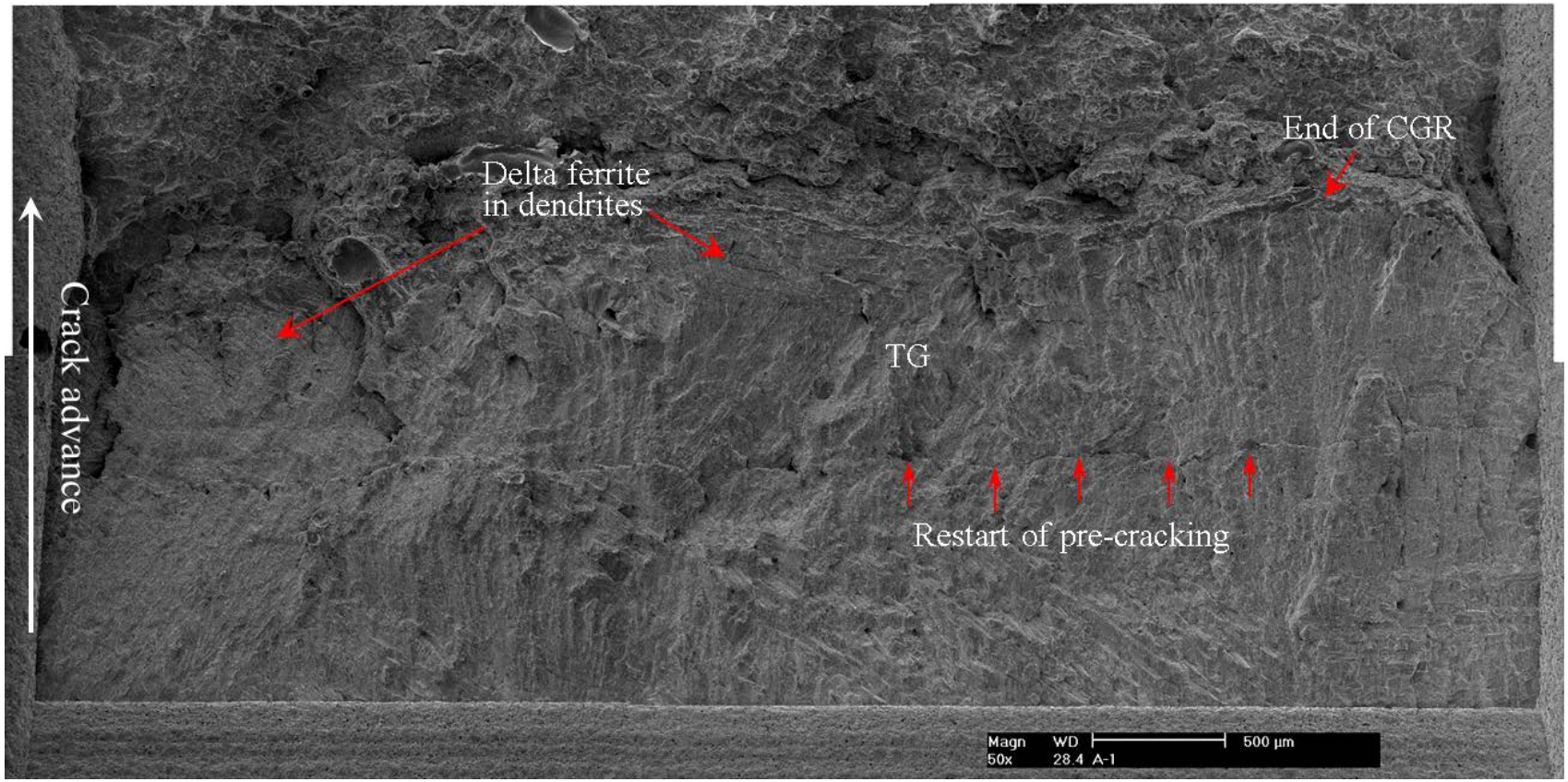


Figure 15. Fracture surface of specimen A-1 tested in PWR water.

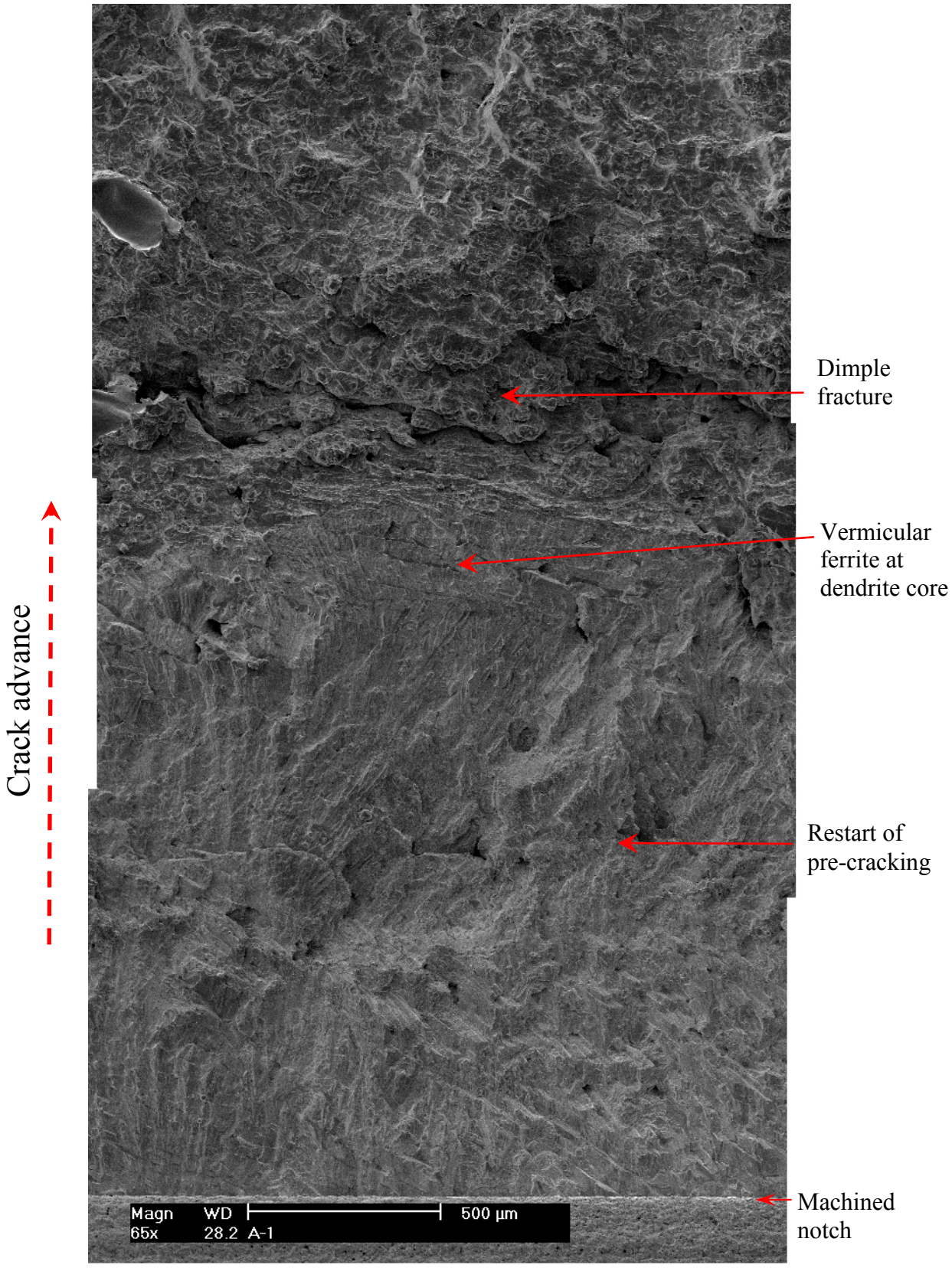


Figure 16. Fracture surface of specimen A-1 along the sample central line.

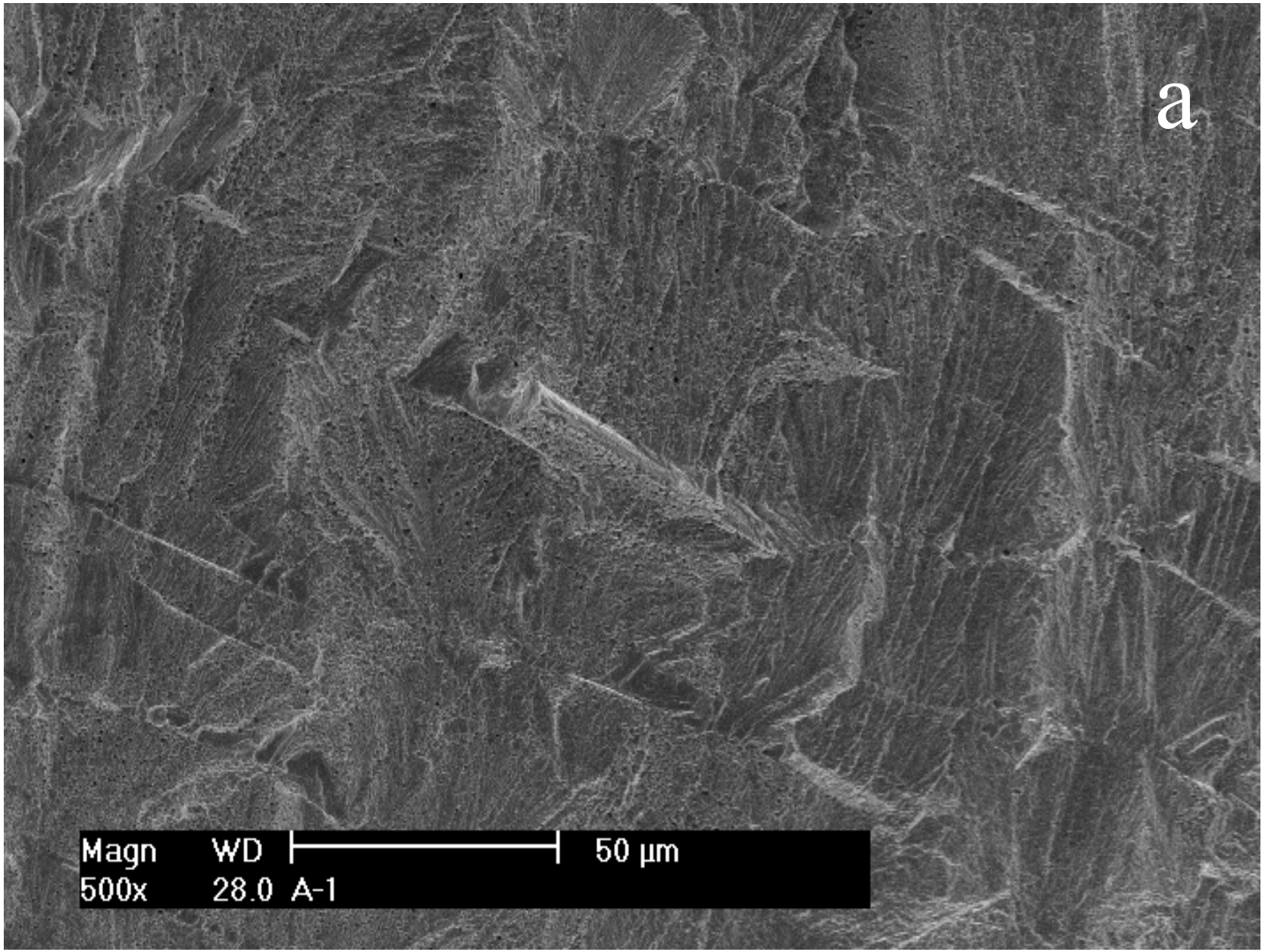


Figure 17. Cleavage-like fracture in specimen A-1: (a) pre-cracking, and (b) end of the CGR test. Crack propagation from bottom to top.

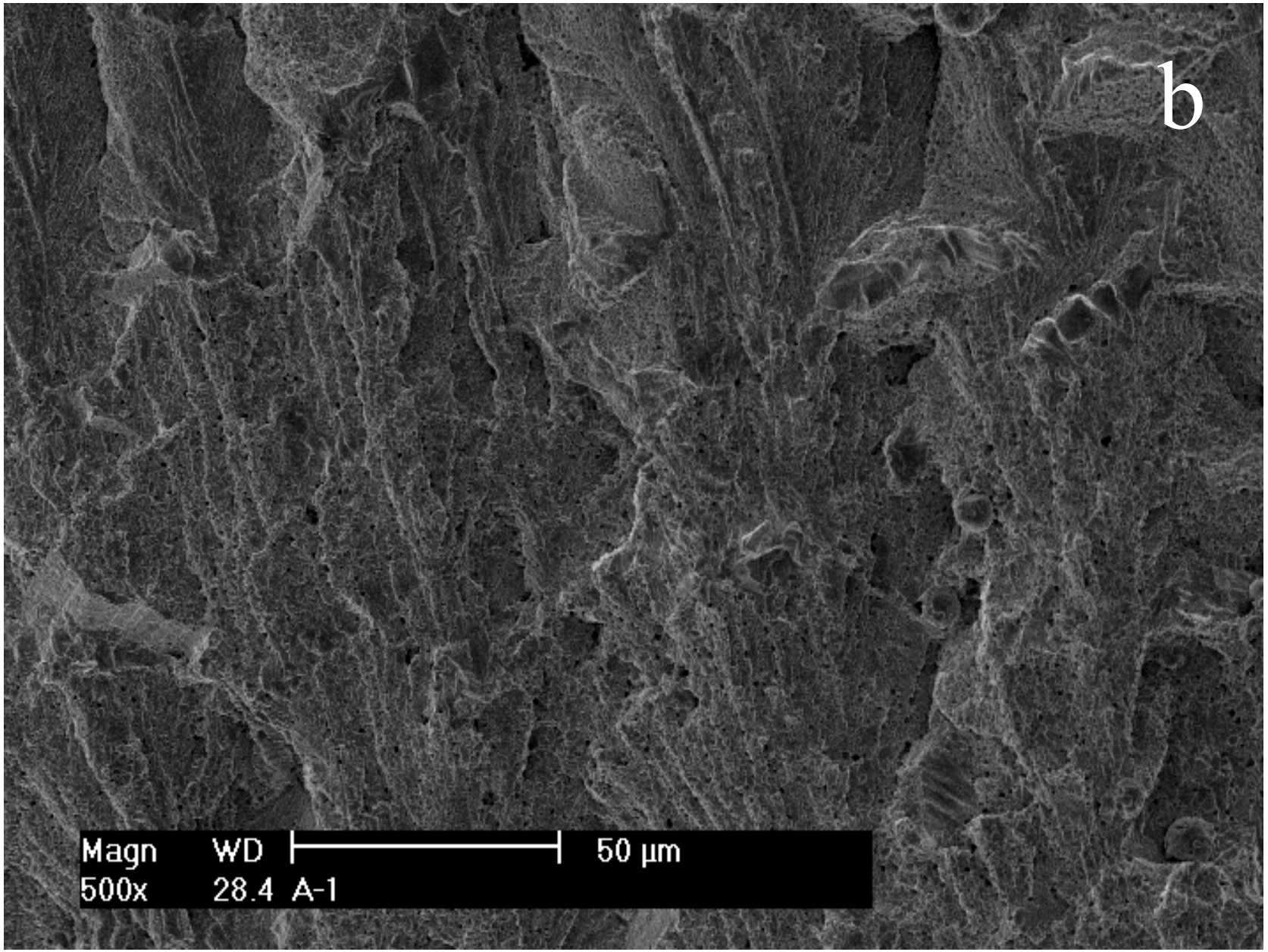


Figure 17. (Contd.)

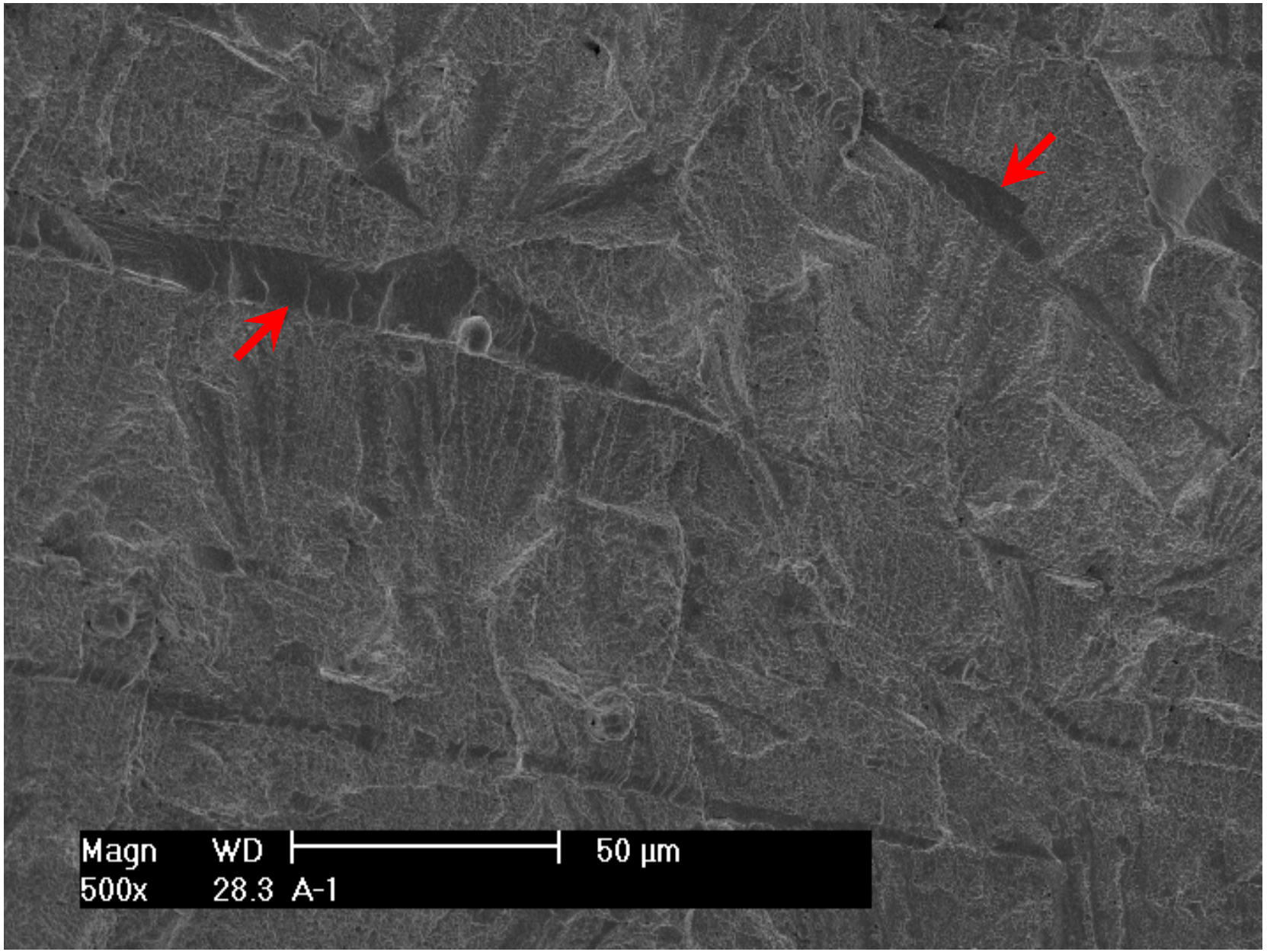


Figure 18. Fracture surface of specimen A-1 showing that delta ferrite deformed to a lesser extent than austenite. Crack propagation from bottom to top.

*3.1.1.3 Irradiated specimen A-2 tested in low-DO high-purity water*

Crack growth rate test

Specimen A-2 was an irradiated unaged CF-3 CASS with ~24% ferrite (Heat 69) tested in high-purity water with low DO. The objective of this test was to compare the irradiated specimen A-1 tested in PWR water. Also, the fracture toughness of this specimen was compared with that of thermally aged CF-3 CASS. The CGR test conditions and results are summarized in Table 6, and a crack-length history plot is shown in Fig. 19.

Table 6. Crack growth rates of specimen A-2 (0.08-dpa unaged CF-3 with 24% δ ferrite) in low-DO high-purity water environment.

| Test Period | Test Time, h | Test Temp., °C | Load Ratio | Rise Time, s | Return Time, s | Hold Time, s | Kmax, MPa $m^{1/2}$ | ΔK, MPa $m^{1/2}$ | CGR in Env., m/s | CGR in Air, m/s | Crack Length, mm |
|---|---|---|---|---|---|---|---|---|---|---|---|
| Start | 14.9 | | | | | | | | | | 5.899 |
| a[a] | 18.1 | 319 | 0.34 | 0.45 | 0.45 | 0.05 | 17.3 | 11.4 | 4.09E-08 | 4.04E-08 | 6.041 |
| b | 20 | 319 | 0.41 | 0.45 | 0.45 | 0.05 | 17.1 | 10.1 | 3.21E-08 | 2.96E-08 | 6.141 |
| c | 21.6 | 319 | 0.50 | 0.43 | 0.43 | 0.07 | 15.7 | 7.8 | 1.94E-09 | 1.43E-08 | 6.151 |
| d[a] | 24.3 | 319 | 0.45 | 0.44 | 0.44 | 0.06 | 16.5 | 9.1 | 2.27E-08 | 2.16E-08 | 6.219 |
| e | 30.4 | 319 | 0.45 | 0.88 | 0.88 | 0.12 | 16.0 | 8.8 | 5.26E-09 | 9.85E-09 | 6.274 |
| f | 39.3 | 319 | 0.50 | 1.74 | 1.74 | 0.26 | 15.9 | 8.0 | 1.80E-09 | 3.82E-09 | 6.304 |
| g | 40.4 | 319 | 0.40 | 0.45 | 0.45 | 0.05 | 17.2 | 10.4 | 5.87E-08 | 3.21E-08 | 6.410 |
| h | 42.4 | 319 | 0.45 | 0.44 | 0.44 | 0.06 | 16.3 | 9.0 | 1.25E-08 | 2.13E-08 | 6.453 |
| i | 44.6 | 319 | 0.45 | 0.88 | 0.88 | 0.12 | 16.6 | 9.2 | 1.29E-08 | 1.14E-08 | 6.497 |
| j | 49.0 | 319 | 0.45 | 1.75 | 1.75 | 0.25 | 16.8 | 9.2 | 9.20E-09 | 5.84E-09 | 6.564 |
| k | 62.2 | 319 | 0.45 | 4.38 | 4.38 | 0.62 | 17.0 | 9.4 | 3.07E-09 | 2.45E-09 | 6.627 |
| l | 74.2 | 319 | 0.46 | 8.73 | 4.37 | 1.27 | 17.2 | 9.4 | 2.37E-09 | 1.23E-09 | 6.686 |
| m | 88.4 | 319 | 0.45 | 26.2 | 4.37 | 3.79 | 17.2 | 9.5 | 7.77E-10 | 4.25E-10 | 6.719 |
| n | 110.6 | 319 | 0.44 | 52.5 | 10.5 | 7.52 | 17.2 | 9.7 | 6.45E-10 | 2.24E-10 | 6.756 |
| o | 135.7 | 319 | 0.43 | 105.0 | 10.5 | 15.0 | 17.0 | 9.7 | 3.77E-10 | 1.13E-10 | 6.780 |
| p | 184.3 | 319 | 0.43 | 262.6 | 10.5 | 37.4 | 17.3 | 9.8 | 8.72E-11 | 4.69E-11 | 6.795 |
| q | 232.7 | 319 | 0.43 | 525.9 | 10.5 | 74.1 | 17.6 | 10.0 | 1.29E-10 | 2.49E-11 | 6.815 |
| r | 278.6 | 320 | 0.43 | 876.3 | 10.5 | 123.7 | 17.6 | 10.1 | 1.73E-10 | 1.52E-11 | 6.840 |
| s | 326.7 | 319 | 0.48 | 865.9 | 10.4 | 134.1 | 17.6 | 9.2 | 1.27E-10 | 1.21E-11 | 6.860 |
| 1 | 423.9 | 319 | 0.50 | 12 | 12 | 7200 | 17.6 | 8.8 | 2.33E-11 | 1.27E-12 | 6.875 |
| 2-a | 575.3 | 320 | 0.50 | 12 | 12 | 7200 | 19.6 | 9.8 | 4.89E-11 | 1.80E-12 | 6.907 |
| 2-b | 687.3 | 321 | 1 | - | - | - | 19.8 | - | 4.94E-12 | - | 6.912 |
| 2-c | 784 | 321 | 0.50 | 12 | 12 | 3600 | 19.8 | 9.9 | 4.26E-11 | 3.73E-12 | 6.924 |

[a] The CGR value was obtained from the later part of the test period.

Pre-cracking in this sample was started with a triangle waveform at 1 Hz. The applied maximum stress intensity factor and load ratio were ~17 MPa $m^{1/2}$ and ~0.35, respectively. The initial cyclic CGRs were comparable to fatigue growth rates but were quickly diminished as the load ratio was increased to 0.5. After lowering the load ratio of 0.4 and increasing the frequency to 1 Hz, the high growth rate was re-established in test period *g* over a 100-μm crack extension. Next, the rise time was increased gradually while the maximum stress intensity factor and load ratio were kept approximately the same. In the following test periods, environmentally enhanced cracking started to appear and became evident with further increases in rise time and load ratio. By the end of test period *s*, the measured CGR was more than one order of magnitude higher than the fatigue growth rate in air. All cyclic CGRs obtained from this sample are plotted in

Fig. 20 along with the corrosion fatigue curve for unirradiated SSs in water with 0.2 ppm DO. A comparison between Figs. 14 and 20 shows that the cyclic CGRs of specimen A-1 is slightly lower than that of specimen A-2.

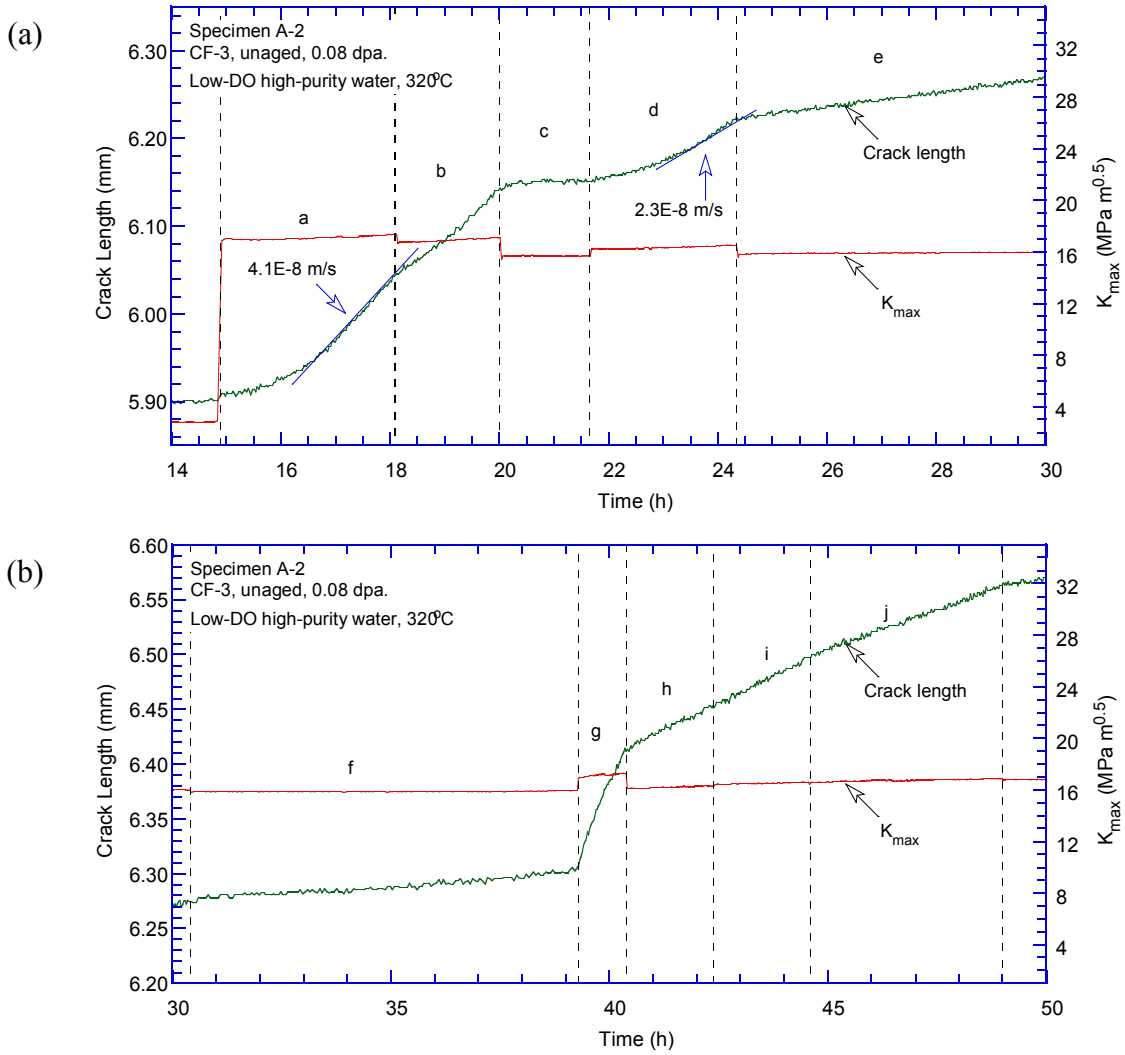


Figure 19. Crack-length-vs.-time plot for specimen A-2 (0.08-dpa unaged CF-3 with 24% ferrite) tested in low-DO high-purity water environment: test periods (a) a-e, (b) f-j, (c) k-o, (d) p-s, and (e) 1-2.

(c)

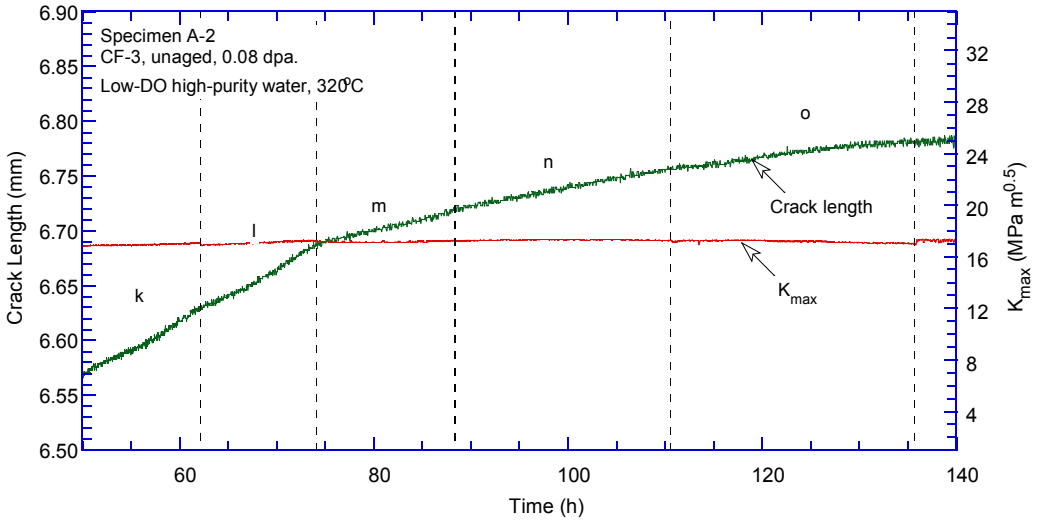


(d)

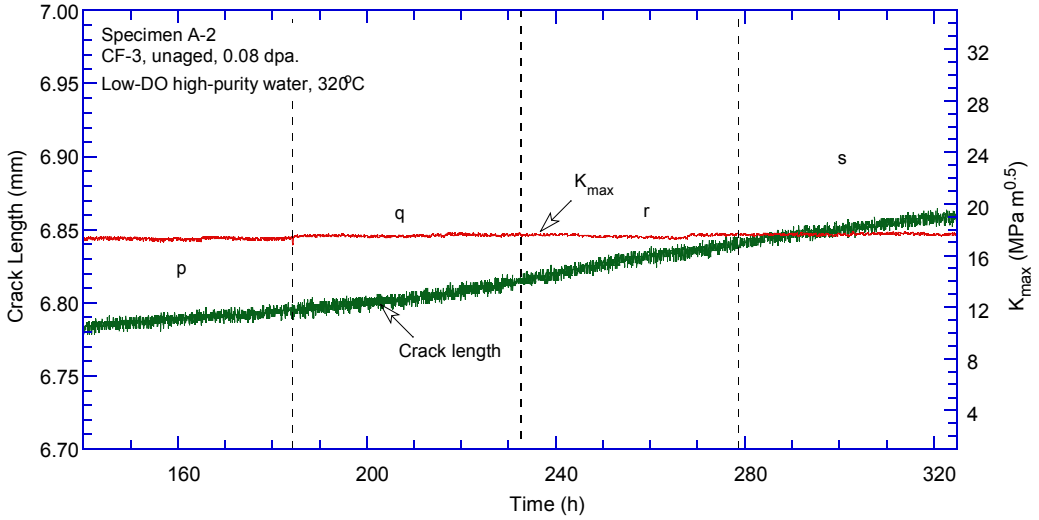


(e)

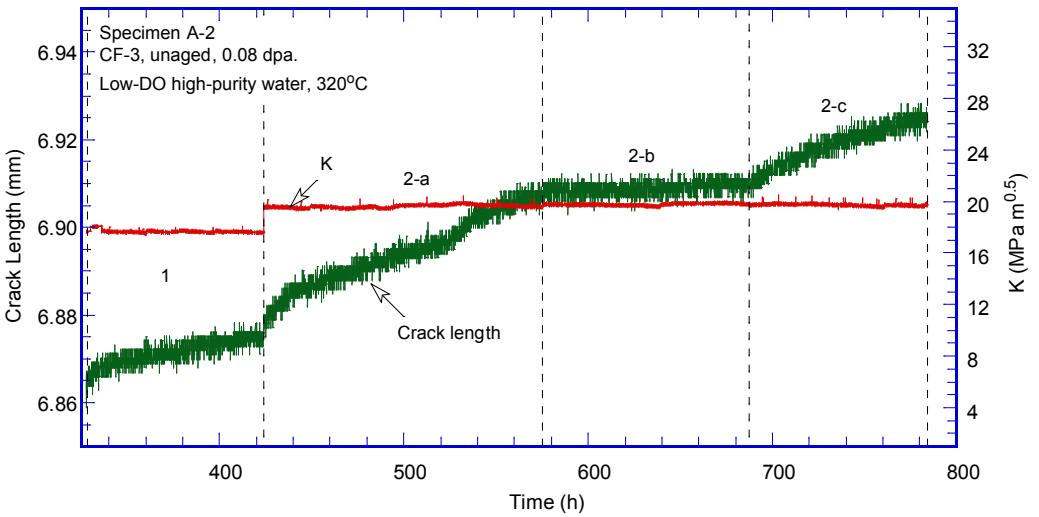


Figure 19. (Contd.)

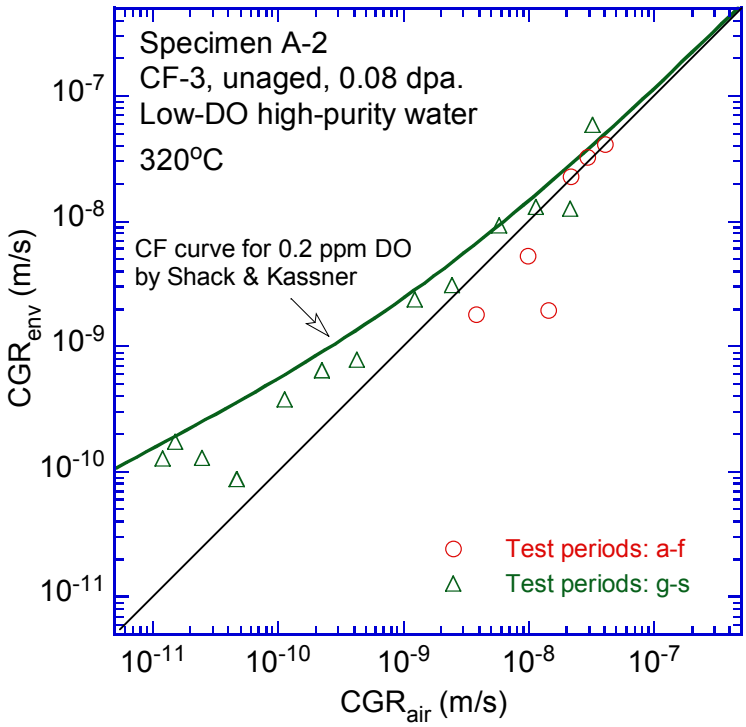


Figure 20. Cyclic CGRs of specimen A-2.

The first constant-load test period was conducted at 17.6 MPa $m^{1/2}$ with PPU every 2 hr (test period *1*). After nearly 100 hr, a CGR of 2.3 x $10^{-11}$ m/s was measured over ~15-μm crack extension. The load was increased to 19.6 MPa $m^{1/2}$ for the second constant-load test period. Again, PPU was applied every 2 hr. A CGR of 4.9 x $10^{-11}$ m/s was obtained over 150 hr. After the PPU was removed in test period *2-b*, the measured CGR decreased one order of magnitude. Constrained by test time, only 5-μm crack extension was accumulated for this test period. In test period *2-c*, the PPU was re-introduced but with 1-hour interval. The measured CGR was nearly identical to that obtained in test period *2-a*. It appears that the hold time between PPU does not affect the SCC response of CF-3 at this stress intensity level.

Fracture toughness J-R curve test

After the crack growth test, a fracture toughness J-R curve test was conducted on this sample in the low-DO high-purity water environment. The sample was loaded at a constant extension rate of 0.43 μm/s while the load and load-line displacement were recorded. During the test, loading was interrupted periodically to measure the crack extension by DCPD. The obtained J and crack extension data are plotted in Fig. 21. A power-law curve fitting of the data gives a relationship of $J = 430\Delta a^{0.64}$. The estimated J value at the 0.2-mm offset line is about 204 kJ/$m^2$. Note that the J-R curve data cannot be validated for this sample because one of the nine measurements of the final crack size was above the limit, and the $J_{max}$ requirement was omitted in this analysis.

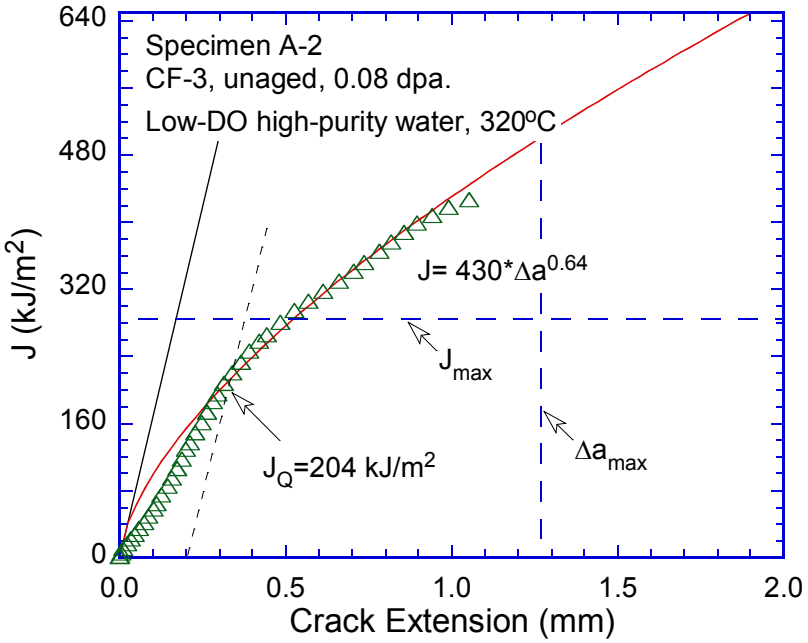


Figure 21. The J-R curve for specimen A-2.

Fractographic examination

After the J-R curve test, the sample was cyclically loaded at room temperature in an air atmosphere to break the ligament. The fracture surface was then examined with the replication technique using SEM. Figure 22 shows the entire fracture surface of specimen A-2. Note that the round smooth areas on the SEM image are air bubbles trapped during replication, not the original morphology of the fracture surface. Both the CGR and post-JR fatigue regions are relatively flat, clearly contrasting with the heavily deformed JR region. The crack front of the CGR test is straight, indicating a well-controlled loading condition during the CGR test. A curved crack front due to a non-constant constraint can be seen for the JR test region.

Figure 23 shows an enlarged view of specimen A-2 along its central line. Similar to specimen A-1, which was tested in PWR water, transgranular cleavage-like fracture was also the dominant morphology during the CGR test. Figure 24 shows the cleavage-like cracking at the initial part of the CGR test, and deformation steps resulting from brittle fracture can be seen in some places. An area of delta ferrite at the dendrite cores can be seen close to the end of the CGR test (see Fig. 25). Similar to that found in the specimen A-1, less plastic deformation activities were observed in the ferrite phase. Beyond the CGR test, ductile dimples were the only fracture morphology on the fracture surface, as shown in Fig. 26.

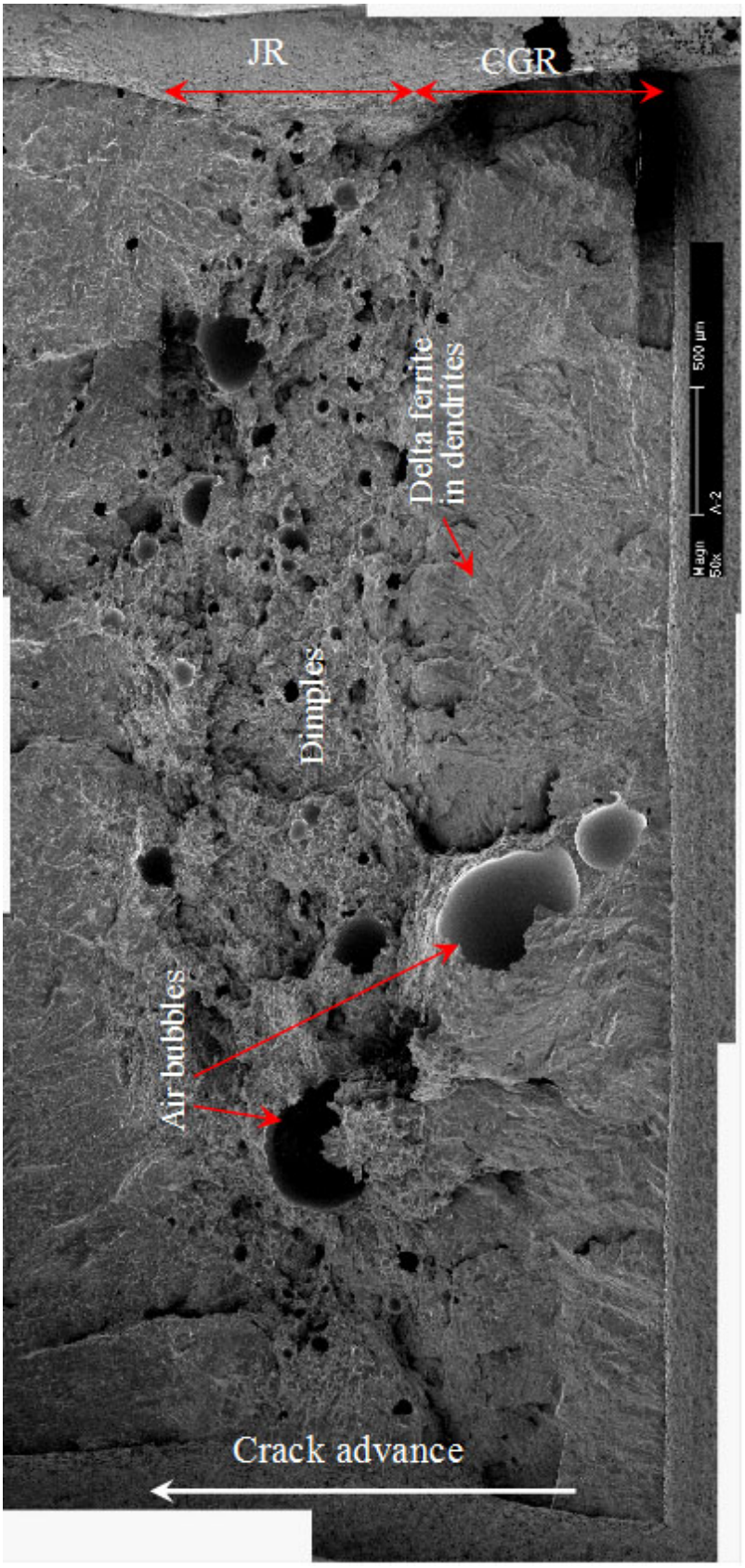


Figure 22. Fracture surface of specimen A-2 tested in low-DO high-purity water.

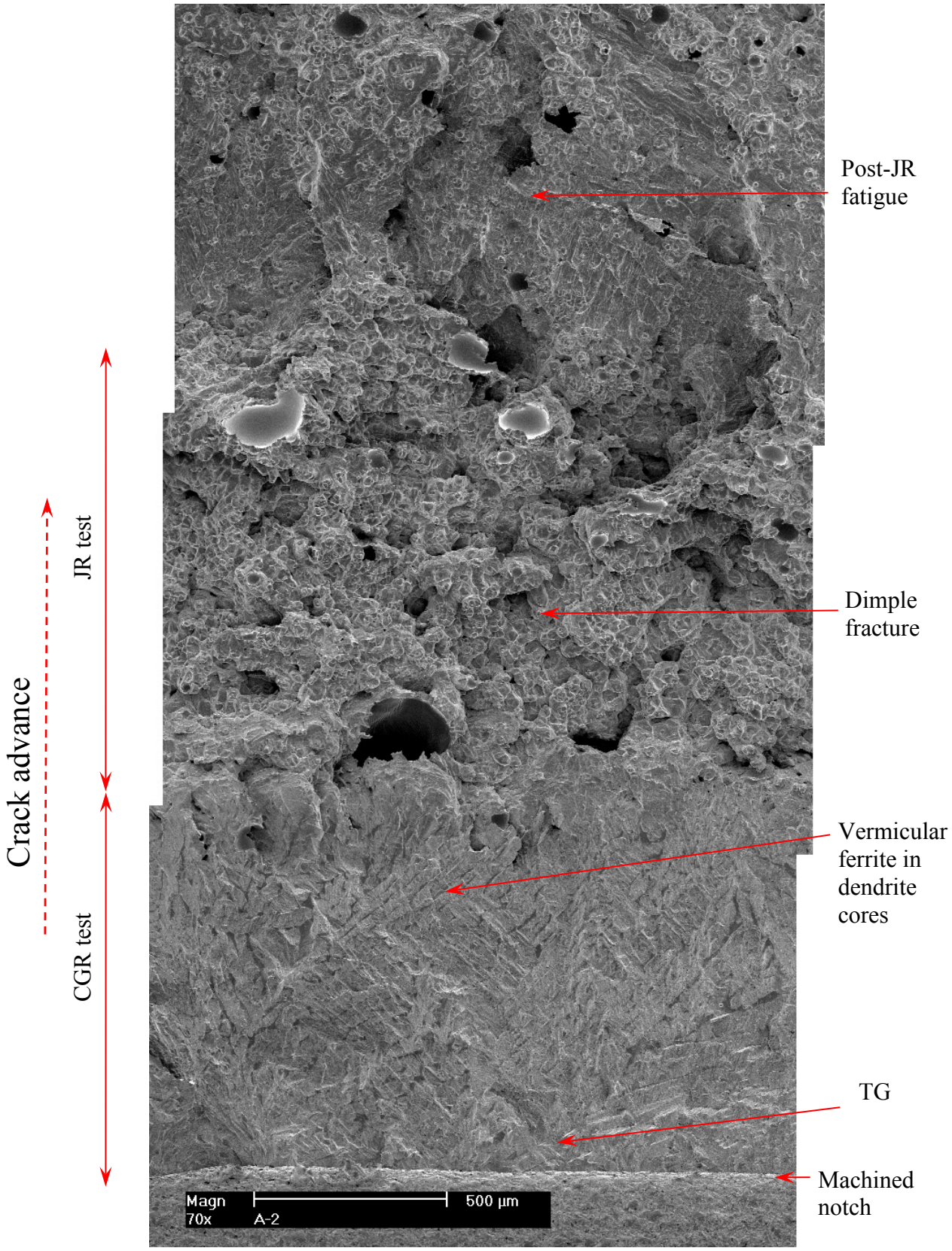


Figure 23. Fracture surface of specimen A-2 along the sample central line.

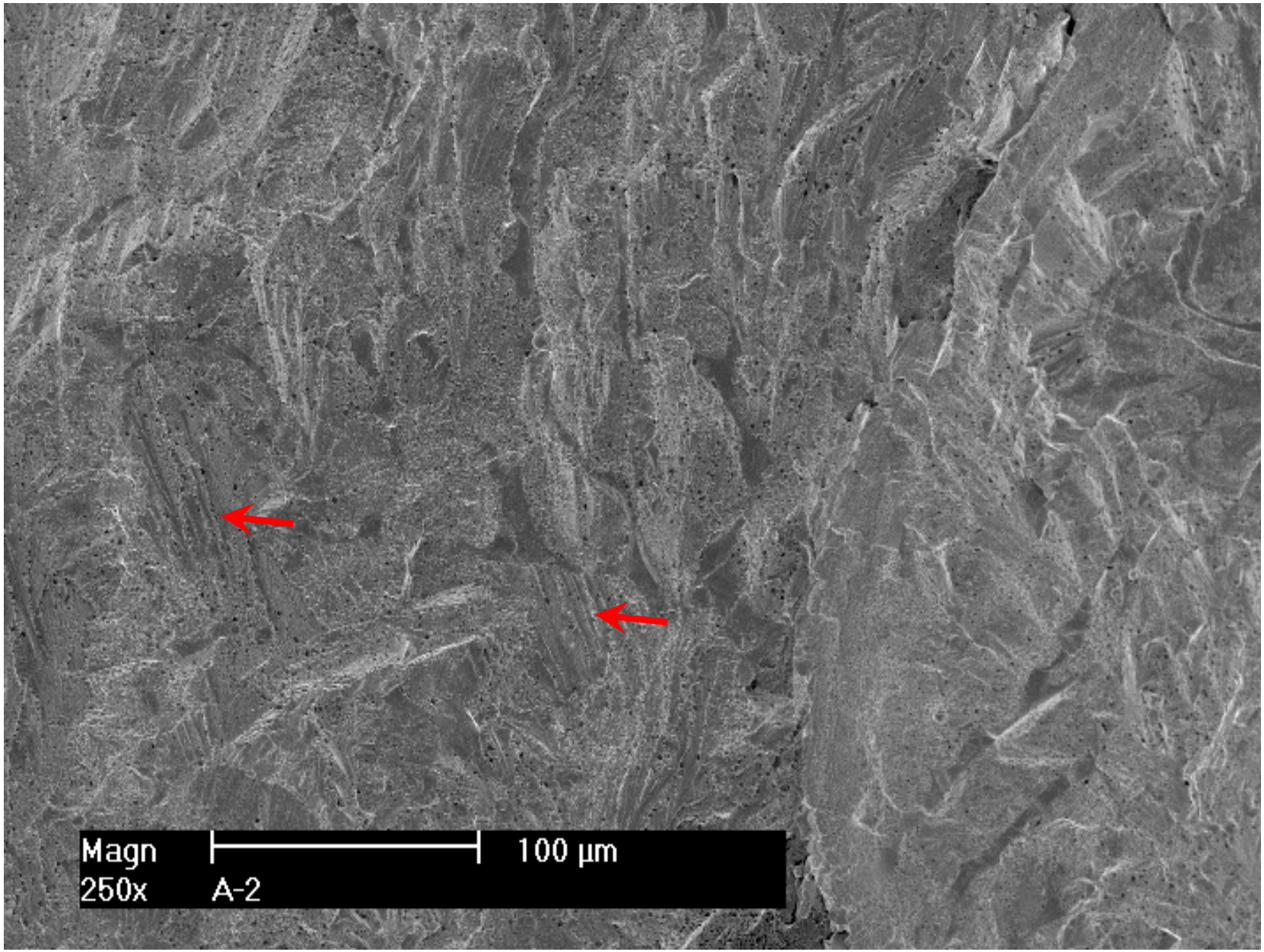


Figure 24. Cleavage-like steps at the beginning of CGR test of specimen A-2. Crack propagation from bottom to top.

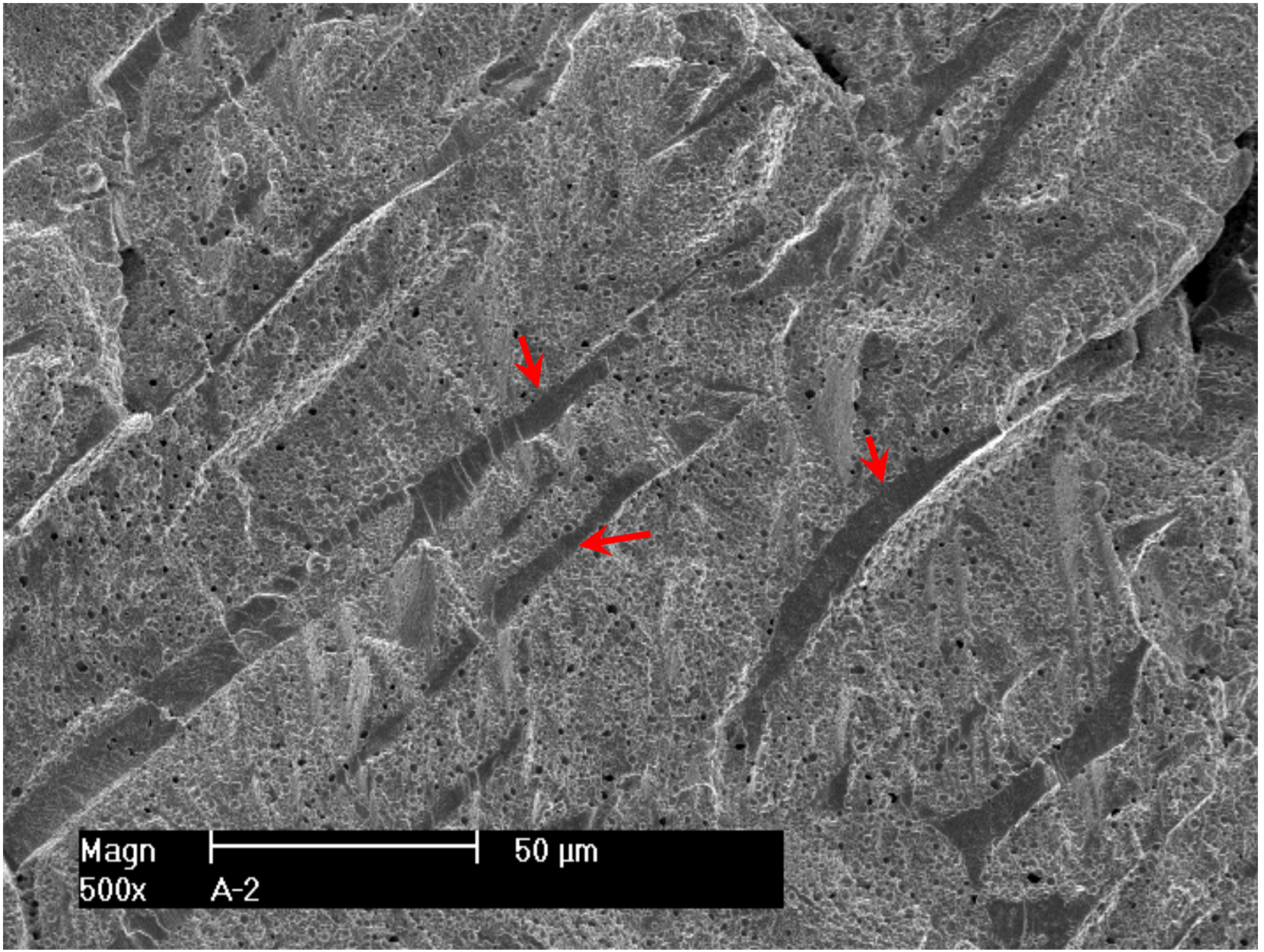


Figure 25. Fracture surface of specimen A-2 showing that ferrite deformed to a lesser extent than austenite. Crack propagation from bottom to top.

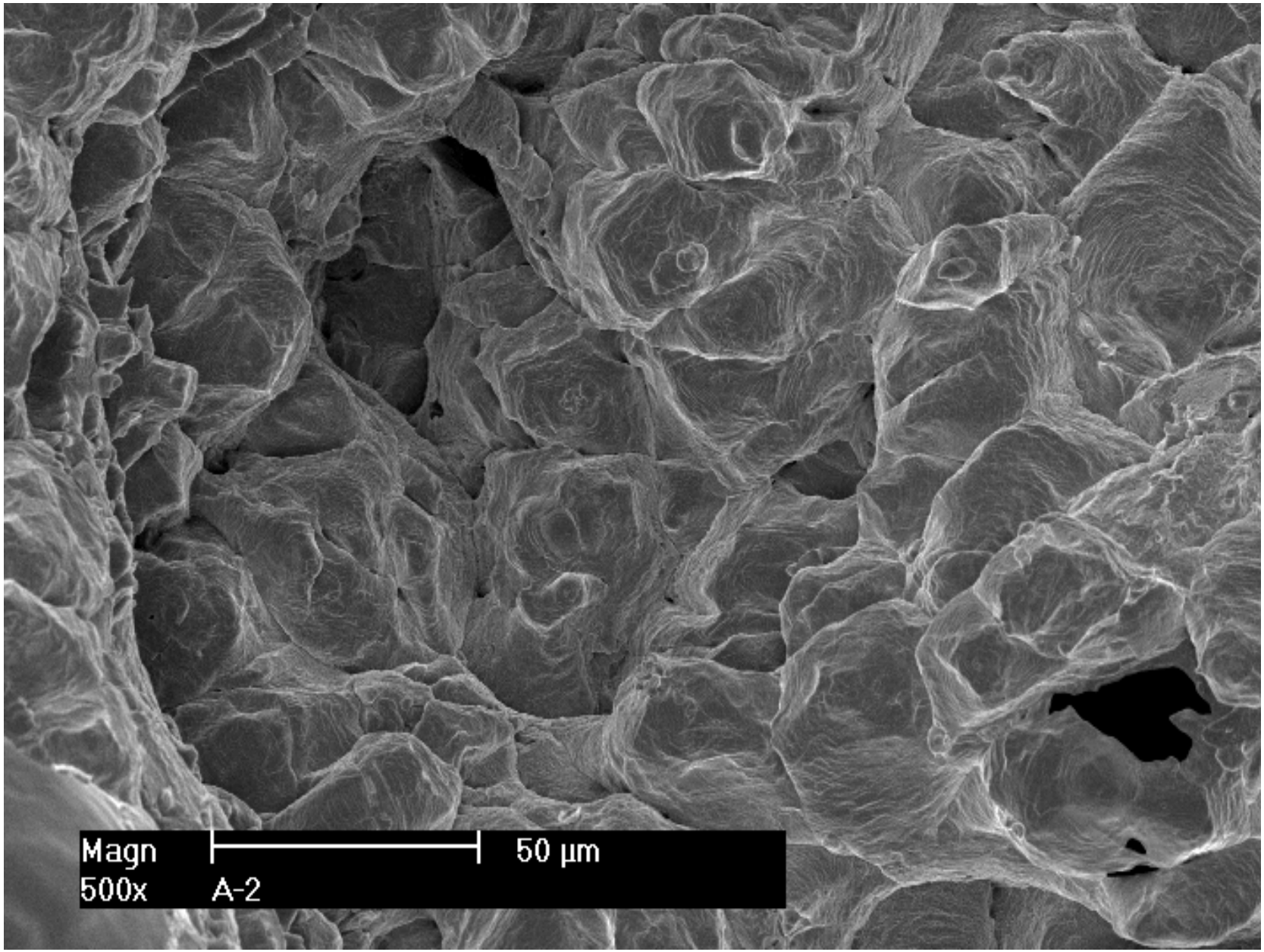


Figure 26. Ductile dimple morphology in the JR test region of specimen A-2. Crack propagation from bottom to top.

*3.1.2 Thermally Aged CF-3 CASS*

*3.1.2.1 Unirradiated specimen B-N1 tested in PWR water*

Crack growth rate test

Specimen B-N1 was an unirradiated control sample tested in PWR water. The material was a thermally aged CF-3 with ~24% ferrite. The objective of the test was to provide a baseline for irradiated tests on thermally aged specimens. The CGR test conditions and results of this sample are summarized in Table 7, and a crack-length history plot is shown in Fig. 27.

Table 7. CGR test of specimen B-N1 (unirradiated, thermally aged CF-3 with 24% δ ferrite) in PWR water.[a]

| Test Period | Test Time, h | Test Temp., °C | Load Ratio | Rise Time, s | Return Time, s | Hold Time, s | Kmax, MPa $m^{1/2}$ | ΔK, MPa $m^{1/2}$ | CGR in Env., m/s | CGR in Air, m/s | Crack Length, mm |
|---|---|---|---|---|---|---|---|---|---|---|---|
| Start | 0.3 | | | | | | | | | | 5.997 |
| a [b] | 3.0 | 319 | 0.20 | 0.43 | 0.43 | 0.07 | 14.8 | 11.9 | 5.57E-08 | 4.04E-08 | 6.182 |
| b [b] | 7.2 | 319 | 0.35 | 0.42 | 0.42 | 0.08 | 15.0 | 9.8 | 3.25E-08 | 2.67E-08 | 6.353 |
| c [b] | 13.3 | 319 | 0.49 | 0.40 | 0.40 | 0.10 | 15.1 | 7.7 | 2.19E-08 | 1.45E-08 | 6.474 |
| d | 23 | 319 | 0.54 | 0.77 | 0.77 | 0.23 | 15.0 | 6.9 | 4.85E-09 | 5.50E-09 | 6.538 |
| e | 47 | 319 | 0.54 | 1.92 | 1.92 | 0.58 | 15.0 | 6.9 | 1.63E-09 | 2.24E-09 | 6.597 |
| f | 71.2 | 319 | 0.54 | 3.82 | 1.53 | 1.18 | 15.0 | 6.8 | 1.53E-10 | 1.07E-09 | 6.608 |
| g [b] | 76.9 | 319 | 0.54 | 0.77 | 0.77 | 0.23 | 15.3 | 7.0 | 4.78E-09 | 5.77E-09 | 6.641 |
| h | 101.8 | 319 | 0.55 | 2.29 | 0.76 | 0.71 | 15.1 | 6.8 | 1.64E-10 | 1.79E-09 | 6.649 |
| i | 123.9 | 319 | 0.54 | 3.83 | 3.83 | 1.17 | 15.3 | 7.0 | 7.97E-11 | 1.14E-09 | 6.652 |
| j | 143.8 | 319 | 0.52 | 1.93 | 1.93 | 0.57 | 15.3 | 7.3 | 1.76E-09 | 2.64E-09 | 6.690 |
| k [c] | 152.8 | 320 | 0.53 | 3.85 | 1.54 | 1.15 | 15.2 | 7.2 | 5.86E-10 | 1.25E-09 | 6.701 |
| l | 192.1 | 320 | 0.52 | 7.72 | 1.54 | 2.28 | 15.3 | 7.3 | 1.77E-10 | 6.60E-10 | 6.714 |
| m | 200.2 | 319 | 0.49 | 1.96 | 1.96 | 0.54 | 15.6 | 7.9 | 2.31E-09 | 3.22E-09 | 6.744 |
| n | 215 | 320 | 0.49 | 3.91 | 3.91 | 1.09 | 15.7 | 7.9 | 2.54E-09 | 1.66E-09 | 6.794 |
| o | 224 | 320 | 0.49 | 7.81 | 1.56 | 2.19 | 15.7 | 7.9 | 8.81E-10 | 8.30E-10 | 6.813 |
| p | 241.5 | 319 | 0.49 | 15.6 | 3.91 | 4.37 | 15.8 | 8.0 | 7.40E-10 | 4.27E-10 | 6.841 |
| q | 270.9 | 319 | 0.49 | 23.4 | 3.91 | 6.56 | 15.8 | 8.0 | 1.21E-10 | 2.87E-10 | 6.850 |
| r | 289.5 | 319 | 0.49 | 46.9 | 3.91 | 13.1 | 15.7 | 8.1 | 3.27E-11 | 1.45E-10 | 6.852 |
| s | 311.3 | 319 | 0.49 | 11.7 | 3.90 | 3.30 | 15.7 | 8.0 | 7.10E-11 | 5.65E-10 | 6.855 |
| t | 316.3 | 320 | 0.32 | 12.4 | 4.14 | 2.59 | 16.5 | 11.1 | 9.66E-09 | 1.33E-09 | 6.957 |
| u | 320 | 319 | 0.35 | 24.6 | 4.10 | 5.37 | 16.5 | 10.7 | 2.99E-09 | 6.14E-10 | 6.983 |
| v | 334.4 | 319 | 0.37 | 48.9 | 4.08 | 11.1 | 16.8 | 10.5 | 1.35E-09 | 2.98E-10 | 7.037 |
| w | 347.5 | 319 | 0.42 | 96.3 | 9.63 | 23.7 | 16.8 | 9.7 | 4.65E-10 | 1.23E-10 | 7.054 |
| x | 368.1 | 320 | 0.42 | 241.0 | 9.64 | 59.0 | 16.9 | 9.8 | 2.09E-10 | 5.02E-11 | 7.065 |
| y | 383.7 | 319 | 0.41 | 401.9 | 9.65 | 98.1 | 16.8 | 9.9 | 1.26E-10 | 3.05E-11 | 7.071 |
| z | 408.5 | 319 | 0.42 | 804.3 | 9.65 | 195.7 | 17.1 | 9.9 | 1.43E-10 | 1.57E-11 | 7.083 |
| aa | 436.2 | 319 | 0.42 | 1206.2 | 9.65 | 293.8 | 17.2 | 10.0 | 7.73E-11 | 1.05E-11 | 7.090 |
| 1a | 512.5 | 319 | 0.50 | 12 | 12 | 7200 | 17.2 | 8.6 | 2.72E-11 | 1.17E-12 | 7.106 |
| 1b | 647.5 | 319 | 1.00 | - | - | - | 17.1 | - | 2.29E-13 | - | 7.107 |

[a] Simulated PWR water with 2 ppm Li and 1000 ppm B. Conductivity ~20 μS/cm.

[b] The CGR of the later part of the test period is reported.

[c] The CGR of the initial part of the test period is reported.

Fatigue pre-cracking was started at ~15 MPa $m^{1/2}$ with a triangle waveform of 1 Hz and a load ratio of 0.2. A CGR close to the fatigue growth rate in air was quickly established in this sample after about 1-hr cycling. After about 180-μm crack extension, the load ratio was increased in the next two test periods. The observed CGRs decreased as expected with the reduced contribution of mechanical fatigue (as shown in Fig. 28). However, the crack stalled in test period *f* after the triangle waveform was replaced with a saw-tooth waveform. After the crack was re-activated, several attempts were made to induce environmentally assisted cracking. The environmental effect became evident after a CGR of ~1.4 x $10^{-9}$ m/s was established in test period *v*. The load ratio and rise time were then increased simultaneously to stabilize the environmentally enhanced cracking. By the end of the cyclic loading test, the observed CGR in water was about a factor of seven higher than the fatigue growth rate in air. All cyclic CGRs obtained from this sample are plotted in Fig. 28 along with the corrosion fatigue curve for SSs in high-purity water with 0.2 ppm DO.

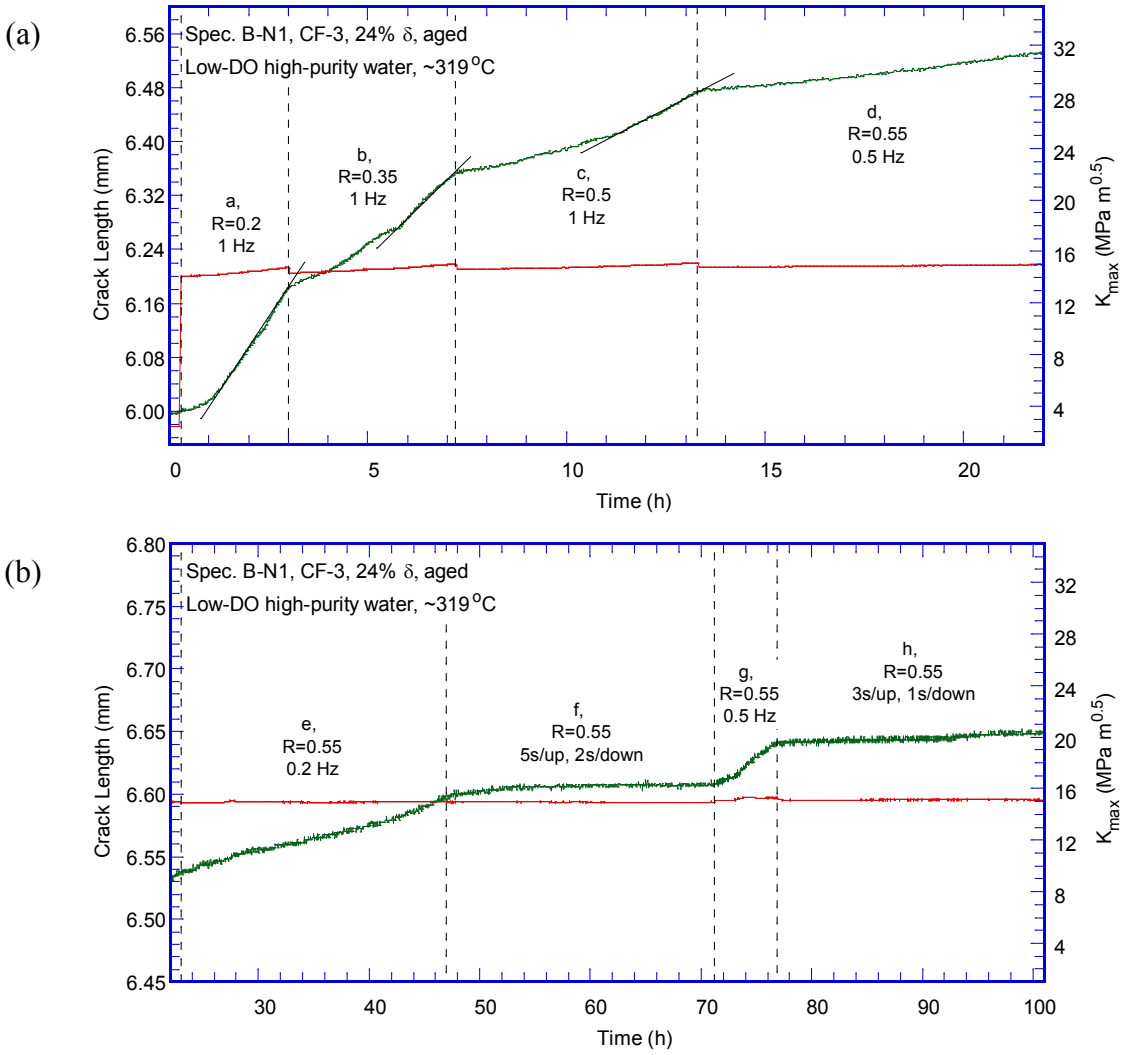


Figure 27. Crack-length-vs.-time plot for specimen B-N1 (unirradiated, aged CF-3 with 24% ferrite) in PWR water: test periods (a) a-d, (b) e-h, (c) i-n, (d) o-s, (e) t-w, (f) x-aa, and (g) 1a-1b.

(c)

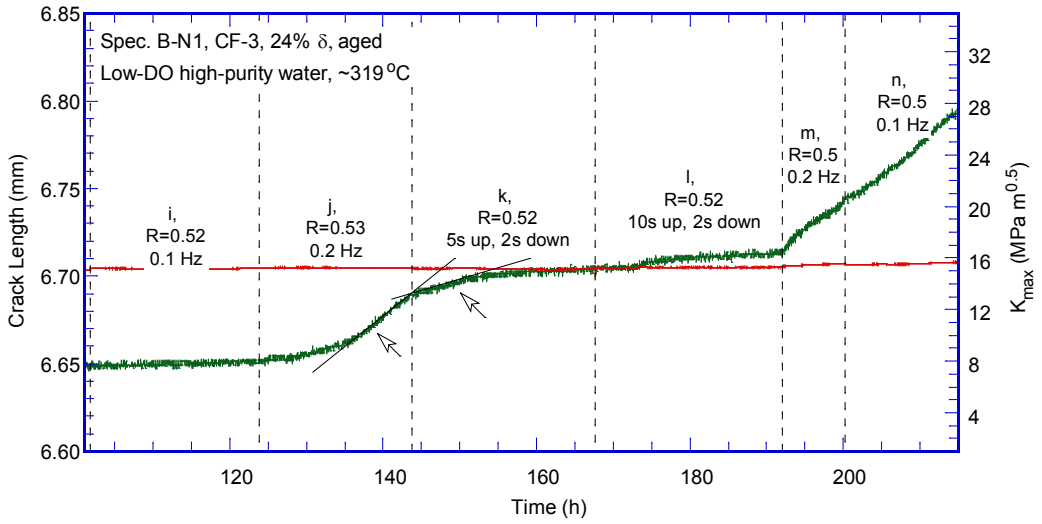


(d)

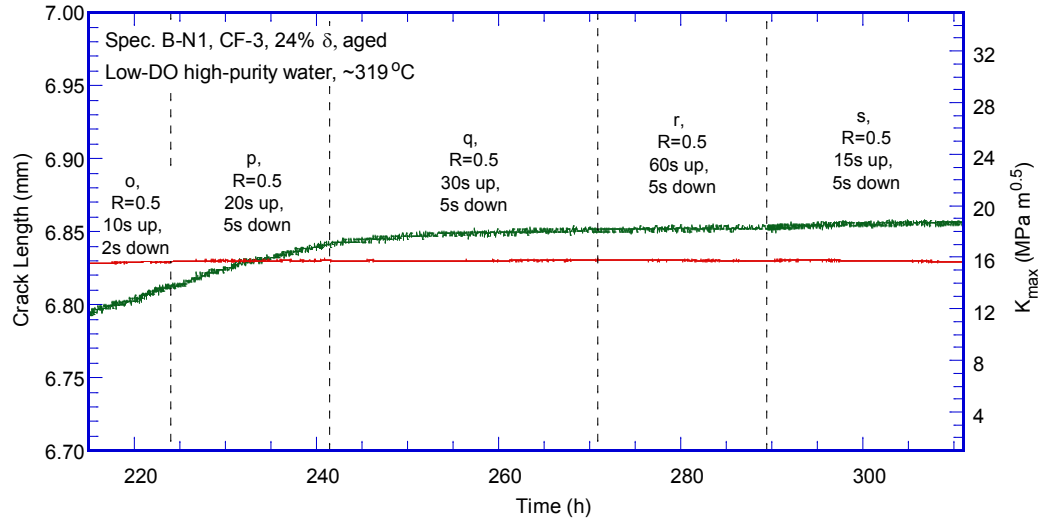


(e)

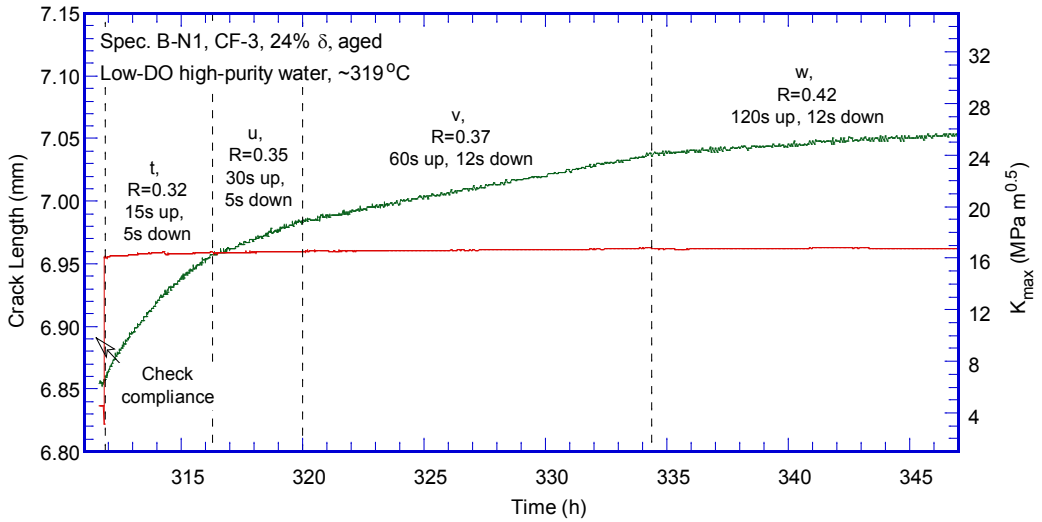


Figure 27. (Contd.)

(f)

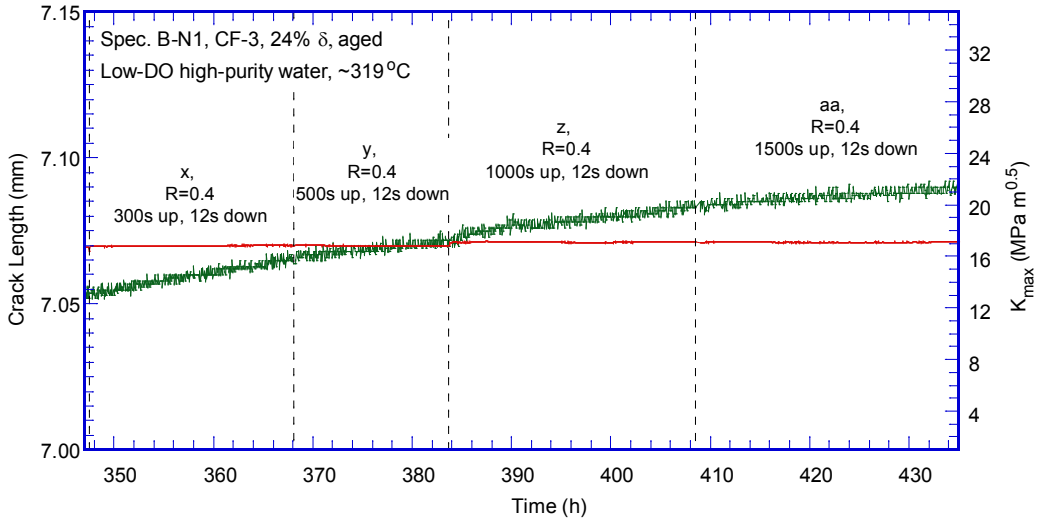


(g)

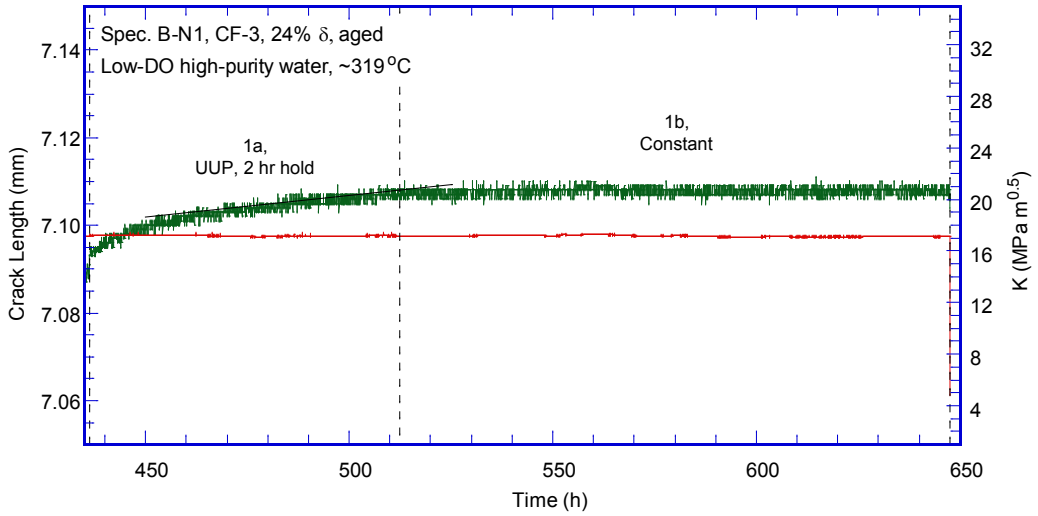


Figure 27. (Contd.)

After the environmentally assisted cracking was stabilized, the test was set to a constant stress intensity factor (~17 MPa $m^{1/2}$) with PPU every 2 hr. Following a short period of rapid growth, a CGR about 2.7 x $10^{-11}$ m/s was measured over 16-μm crack extension. Without PPU, the observed CGR dropped more than two orders of magnitude under a near constant-K condition. Limited by the test time, the CGR test was terminated after 135 hr with just 1-μm crack extension.

Fracture toughness J-R curve test

The fracture toughness J-R curve test was performed in the same PWR water environment. The test was conducted at a constant strain rate of 0.43 μm/s, and the crack extension was measured with the DCPD method. Before each DCPD measurement, the stress was allowed to relax for 30 s at a constant displacement. The obtained J-R curve is shown in Fig. 29. The estimated J

value at 0.2 mm offset line is about 170 kJ/m$^2$. Note that the J-R curve data cannot be validated for this test because the requirements of the crack straightness and $J_{max}$ were not met.

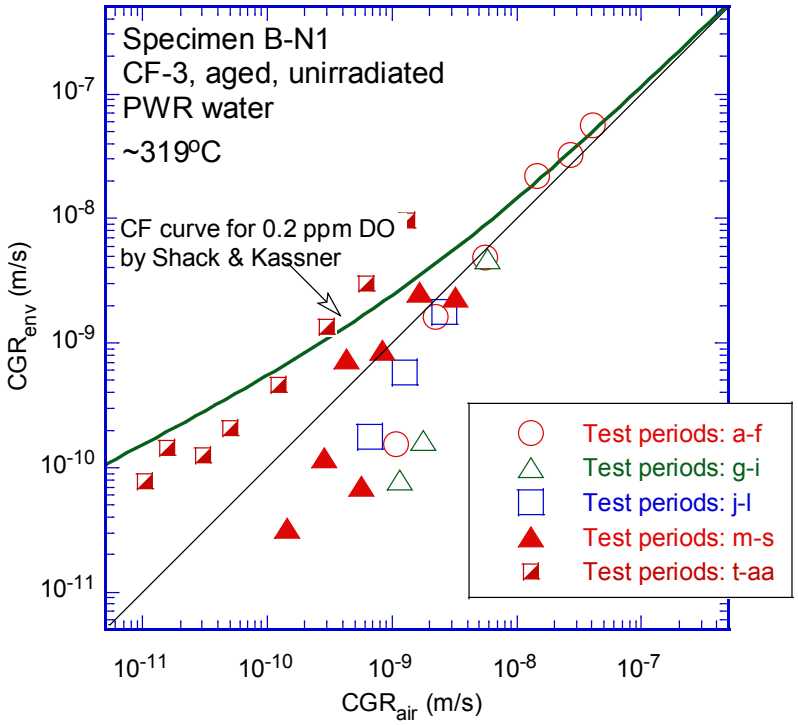


Figure 28. Cyclic CGRs of specimen B-N1.

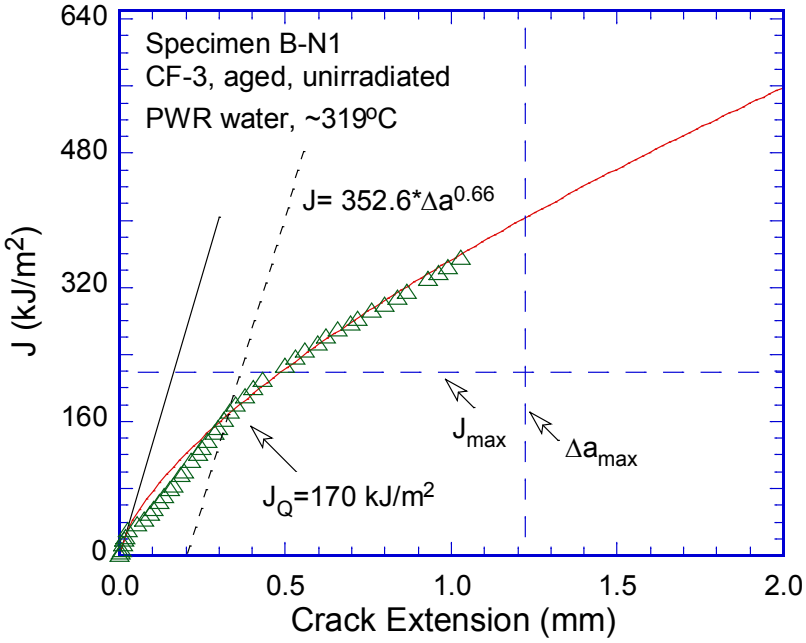


Figure 29. The J-R curve for specimen B-N1.

Fractographic examination

After the JR test, the sample was broken open at room temperature in air. The fracture surface of the tested sample was examined with SEM. Figure 30 is a global view of the entire fracture surface of the CGR and JR test regions. The crack front of the CGR test is quite straight, indicating a well-controlled loading condition. Figure 31 shows more details of the fracture along the central line of the specimen. The CGR test region shows a transganular morphology, and the JR test region is a ductile dimple fracture. A significant crack extension can be seen during the JR test, which is consistent with the low fracture resistance observed in this sample. In the CGR test region, the initial fracture close to the machined notch is characterized by coarse ledges resulting from fatigue fracture (Fig. 32), while at the later stage of the CGR test, the fracture surface is smoother (Fig. 33). Details of ductile dimple fracture in the JR test region can be seen in Fig. 34.

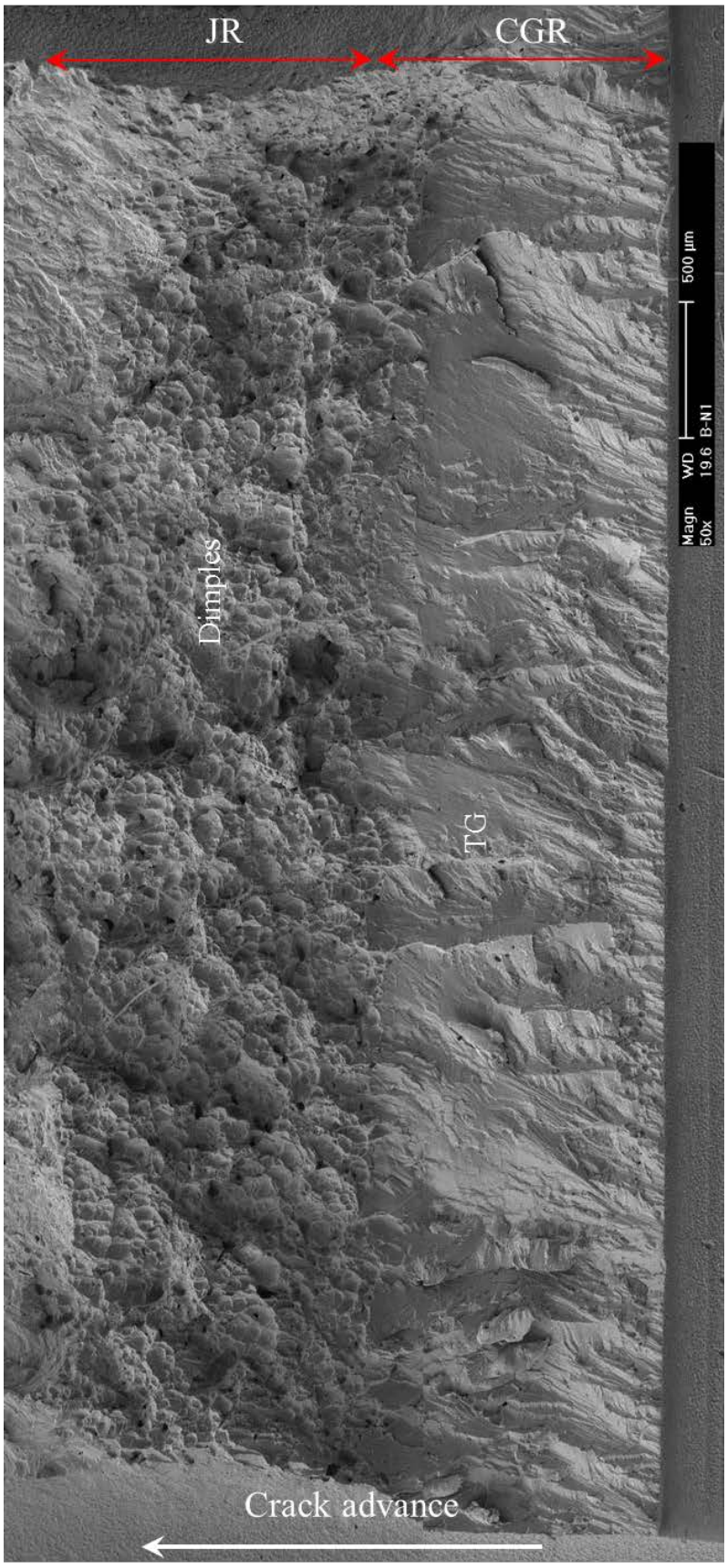


Figure 30. Fracture surface of specimen B-N1 tested in PWR water.

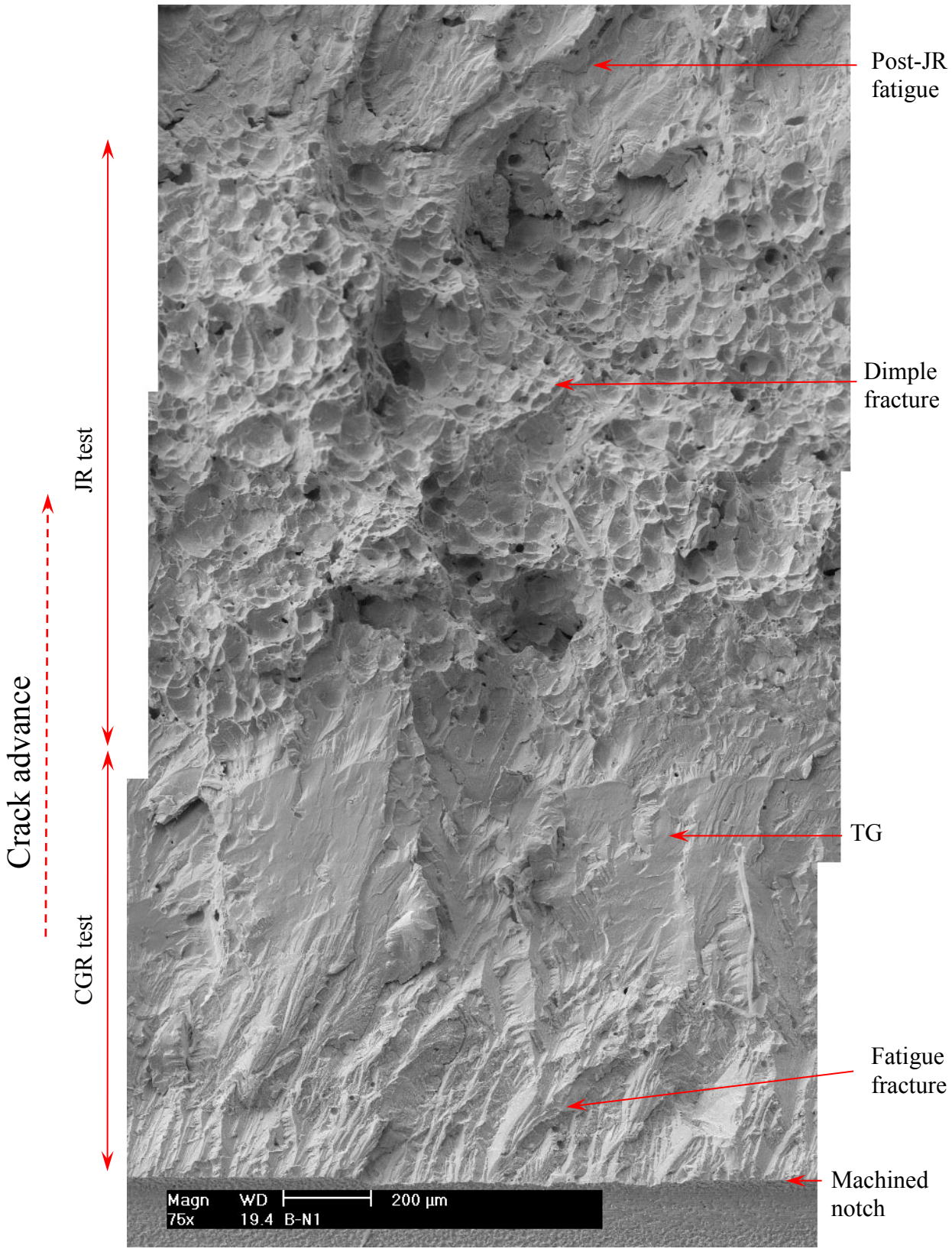


Figure 31. Fracture surface of specimen B-N1 along the sample central line.

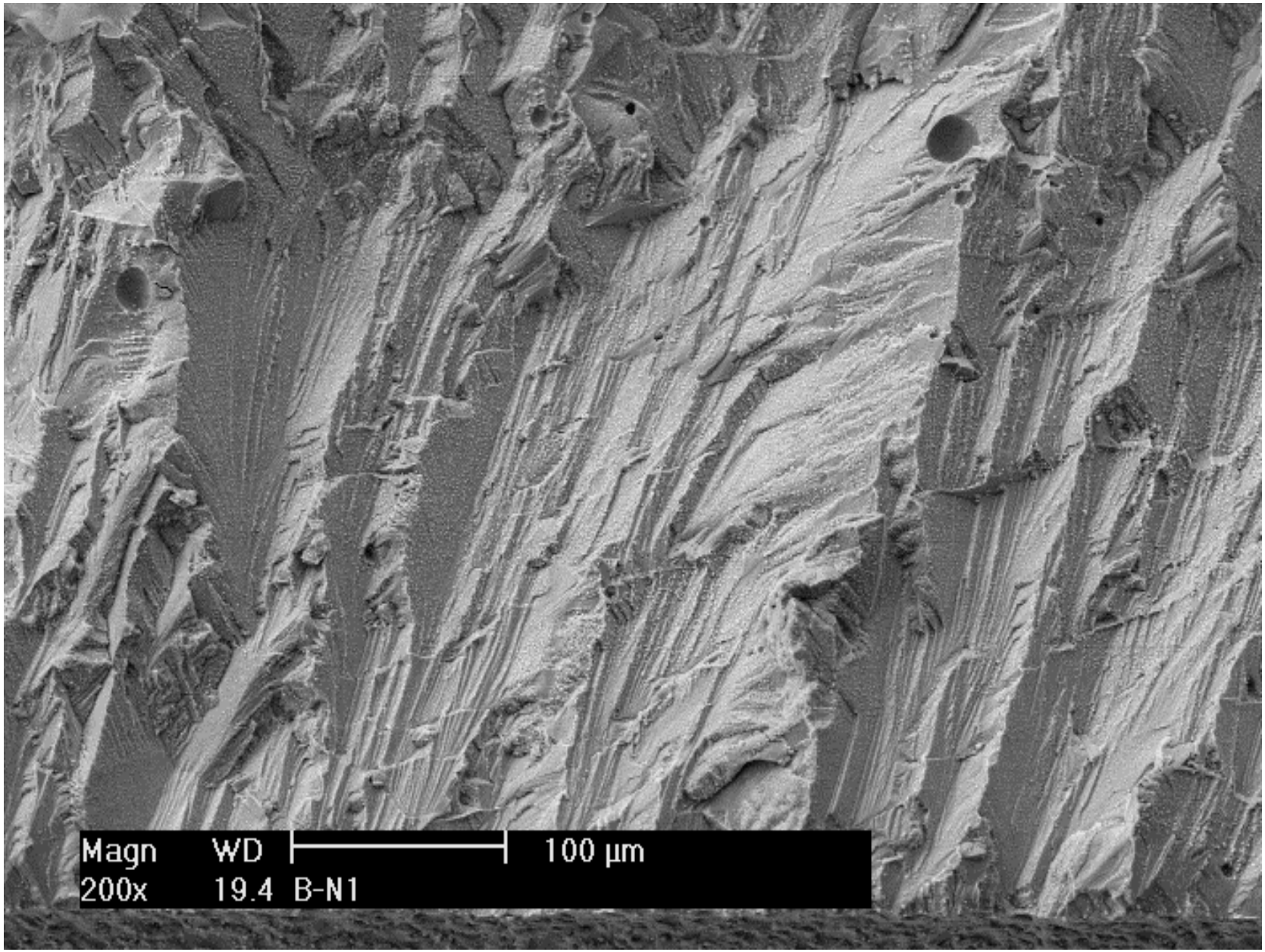


Figure 32. Transgranular fracture in specimen B-N1 at the beginning of the precracking. Crack propagation from bottom to top.

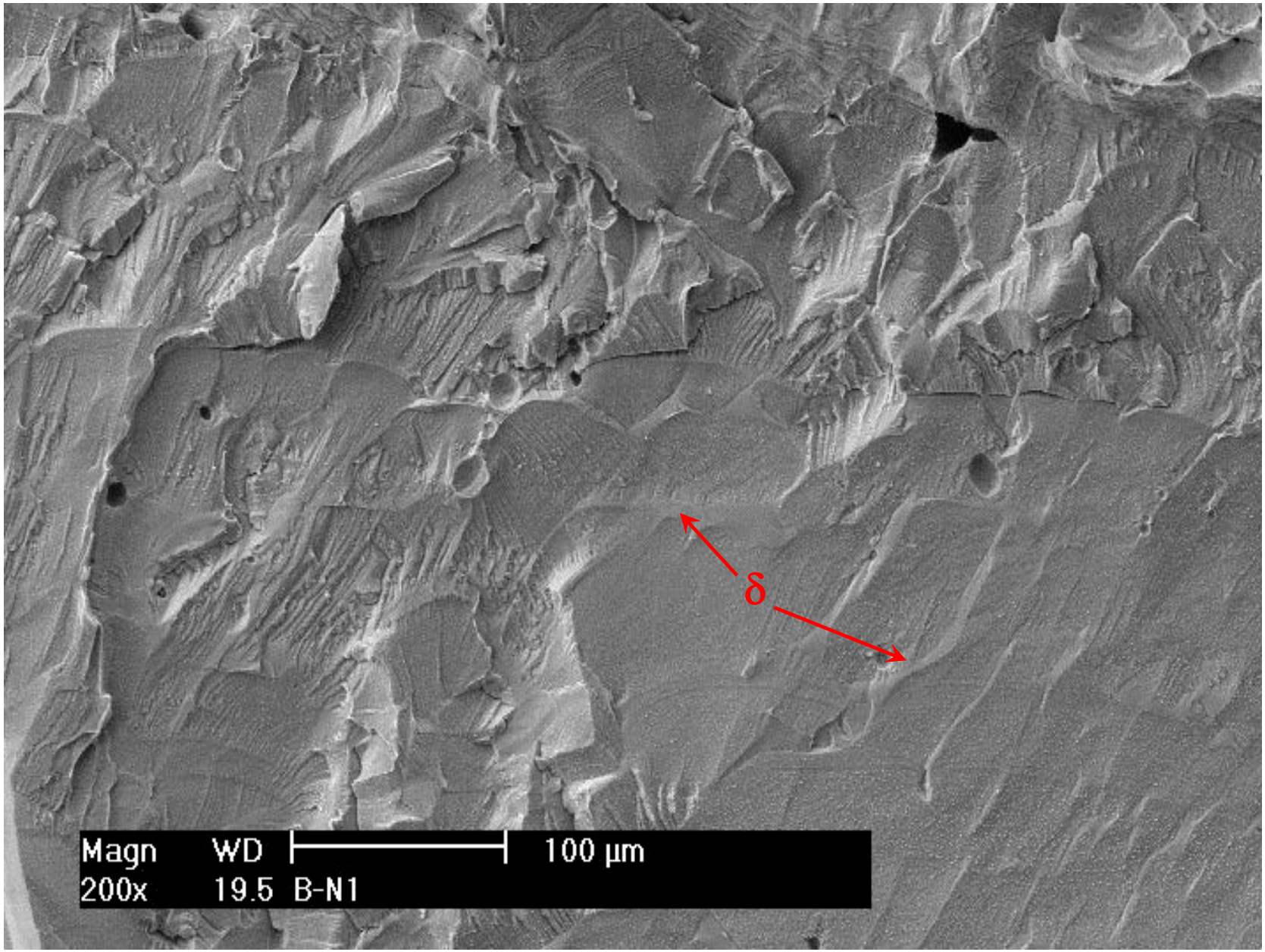


Figure 33. Transgranular fracture in specimen B-N1 at the end of the precracking. Crack propagation from bottom to top.

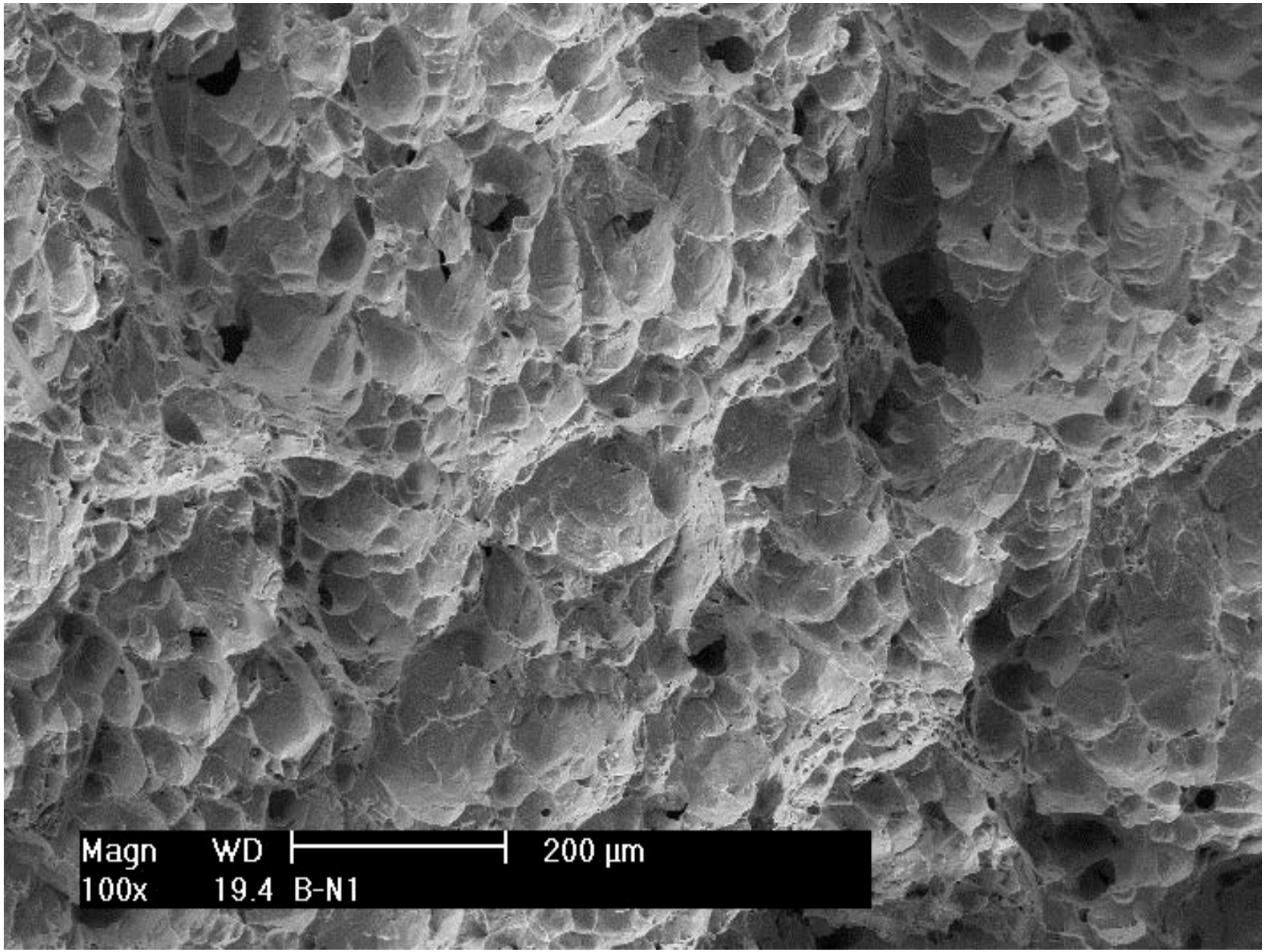


Figure 34. Ductile dimple fracture in the JR test region of specimen B-N1. Crack propagation from bottom to top.

*3.1.2.2 Irradiated specimen B-1 tested in PWR water*

Crack growth rate test

Specimen B-1 was a 0.08-dpa thermally aged CF-3 CASS with ~24% ferrite. This sample was obtained from the same heat (Heat 69) as specimens A-1 and A-2. The thermal aging condition was 400°C and 10,000 hr. The objective was to compare the results with those of the unaged CF-3 at the same dose level. The CGR test conditions and results are summarized in Table 8, and a crack-length history plot is shown in Fig. 35.

The test was started with fatigue pre-cracking at a maximum stress intensity factor of ~18 MPa $m^{1/2}$ and a load ratio of 0.3. A triangular waveform was used with a frequency of 1 Hz. Upon successful crack initiation, the maximum stress intensity factor was lowered to prepare for transitioning. In the following test periods, the load ratio and rise time were increased slowly to stimulate environmentally enhanced cracking. Despite the effort, the measured CGRs fell well below the fatigue growth rate line. A more aggressive loading condition was applied to re-activate the fatigue crack. Following that, repeated attempts (test periods *e-j*, *k-q*, and *r-af*) were made to induce environmental enhanced cracking. However, no elevated CGRs could be maintained. It appears that cracking cannot be sustained with a load ratio higher than 0.4 and a stress intensity factor less than 19 MPa $m^{1/2}$ in this sample. Environmentally enhanced cracking was only observed after increasing the stress intensity factor to about 22 MPa $m^{1/2}$. At this stress intensity, the measured CGR by the end of the cyclic test (period *ao*) was a factor of three higher than the fatigue crack growth rate in air. Subsequently, the test was set at constant load with PPU every 2 hr in test period *1*. A CGR of $2.8 \times 10^{-11}$ m/s was obtained at a stress intensity factor of 22 MPa $m^{1/2}$.

Table 8. CGR test of specimen B-1 (0.08-dpa aged CF-3 with 24% δ ferrite) in PWR water.[a]

| Test Period | Test Time, h | Test Temp., °C | Load Ratio | Rise Time, s | Return Time, s | Hold Time, s | Kmax, MPa $m^{1/2}$ | ΔK, MPa $m^{1/2}$ | CGR in Env., m/s | CGR in Air, m/s | Crack Length, mm |
|---|---|---|---|---|---|---|---|---|---|---|---|
| Start | 0.52 | | | | | | | | | | 6.019 |
| a | 3.0 | 319 | 0.27 | 0.38 | 0.38 | 0.12 | 17.6 | 12.8 | 7.88E-08 | 6.55E-08 | 6.250 |
| b | 6.7 | 320 | 0.39 | 0.35 | 0.35 | 0.15 | 17.0 | 10.4 | 4.11E-08 | 4.06E-08 | 6.442 |
| c | 10.5 | 320 | 0.50 | 0.64 | 0.64 | 0.36 | 15.8 | 7.9 | 2.75E-09 | 9.97E-09 | 6.460 |
| d | 20.1 | 320 | 0.45 | 1.32 | 1.32 | 0.68 | 15.9 | 8.8 | 3.63E-10 | 6.50E-09 | 6.466 |
| e | 23.3 | 320 | 0.27 | 0.37 | 0.37 | 0.13 | 17.9 | 13.1 | 5.89E-08 | 7.29E-08 | 6.698 |
| f | 25.4 | 320 | 0.27 | 0.36 | 0.36 | 0.14 | 17.1 | 12.4 | 4.86E-08 | 6.25E-08 | 6.822 |
| g | 27.8 | 320 | 0.38 | 0.34 | 0.34 | 0.16 | 16.8 | 10.4 | 2.77E-08 | 4.22E-08 | 6.905 |
| h | 32.2 | 320 | 0.38 | 0.66 | 0.66 | 0.34 | 16.3 | 10.1 | 8.33E-09 | 1.93E-08 | 6.950 |
| i | 44.2 | 319 | 0.44 | 3.20 | 3.20 | 1.80 | 16.2 | 9.2 | 2.63E-10 | 3.07E-09 | 6.955 |
| j | 47.5 | 320 | 0.38 | 1.32 | 1.32 | 0.68 | 16.2 | 10.0 | 7.00E-10 | 9.49E-09 | 6.958 |
| k[b] | 52.3 | 320 | 0.37 | 0.67 | 0.67 | 0.33 | 17.1 | 10.8 | 1.01E-08 | 2.32E-08 | 7.000 |
| l | 59.1 | 320 | 0.37 | 3.36 | 1.34 | 1.64 | 17.2 | 10.9 | 4.05E-09 | 4.80E-09 | 7.048 |
| m | 69 | 320 | 0.37 | 6.71 | 1.34 | 3.29 | 17.4 | 11.0 | 2.24E-09 | 2.48E-09 | 7.092 |
| n | 82.8 | 320 | 0.42 | 13.0 | 3.25 | 6.99 | 17.3 | 10.1 | 3.18E-10 | 1.01E-09 | 7.102 |
| o | 95.2 | 320 | 0.36 | 13.4 | 3.35 | 6.60 | 17.3 | 11.0 | 4.09E-11 | 1.23E-09 | 7.104 |
| p | 105 | 320 | 0.36 | 6.73 | 3.37 | 3.27 | 17.5 | 11.2 | 1.01E-10 | 2.59E-09 | 7.107 |
| q | 116.8 | 320 | 0.36 | 13.6 | 3.40 | 6.41 | 17.8 | 11.5 | 9.16E-11 | 1.40E-09 | 7.107 |
| r | 124.2 | 320 | 0.36 | 1.36 | 1.36 | 0.64 | 18.0 | 11.5 | 3.85E-09 | 1.43E-08 | 7.142 |
| s | 130.6 | 320 | 0.36 | 3.39 | 1.36 | 1.61 | 18.1 | 11.6 | 2.66E-09 | 5.86E-09 | 7.171 |
| t | 142.5 | 320 | 0.36 | 6.77 | 1.35 | 3.23 | 18.2 | 11.7 | 1.21E-09 | 3.00E-09 | 7.201 |
| u | 145.9 | 319 | 0.35 | 13.5 | 3.38 | 6.46 | 18.1 | 11.7 | 9.45E-11 | 1.49E-09 | 7.202 |
| v | 164.7 | 319 | 0.35 | 13.6 | 3.40 | 6.40 | 18.3 | 11.9 | 1.23E-10 | 1.56E-09 | 7.207 |
| w | 170 | 319 | 0.35 | 10.2 | 3.40 | 4.80 | 18.4 | 11.9 | 1.53E-10 | 2.09E-09 | 7.208 |
| x | 188.7 | 319 | 0.35 | 10.2 | 3.42 | 4.75 | 18.9 | 12.3 | 1.39E-09 | 2.28E-09 | 7.251 |
| y | 199 | 319 | 0.35 | 20.5 | 3.42 | 9.51 | 18.9 | 12.3 | 7.57E-10 | 1.15E-09 | 7.265 |
| z | 238 | 319 | 0.35 | 41.0 | 3.41 | 19.0 | 19.1 | 12.3 | 2.14E-10 | 5.88E-10 | 7.287 |
| aa | 284.5 | 319 | 0.36 | 81.8 | 8.18 | 38.2 | 19.3 | 12.4 | 2.61E-10 | 3.00E-10 | 7.318 |
| ab | 356.3 | 319 | 0.35 | 204.4 | 8.18 | 95.6 | 19.2 | 12.4 | 4.36E-11 | 1.20E-10 | 7.325 |
| ac | 442.2 | 318 | 0.35 | 413.0 | 8.26 | 187.0 | 19.9 | 12.9 | 2.88E-11 | 6.65E-11 | 7.331 |
| ad | 501.5 | 319 | 0.35 | 693.0 | 8.32 | 307.0 | 20.2 | 13.2 | 1.41E-11 | 4.26E-11 | 7.334 |
| ae | 527.8 | 318 | 0.46 | 78.0 | 7.80 | 42.0 | 19.9 | 10.8 | 5.94E-12 | 2.23E-10 | 7.336 |
| af | 574.5 | 318 | 0.45 | 39.4 | 7.88 | 20.6 | 20.6 | 11.3 | 2.11E-10 | 4.98E-10 | 7.356 |
| ag | 644.4 | 318 | 0.45 | 78.8 | 7.88 | 41.2 | 20.6 | 11.2 | negligible | 2.48E-10 | 7.355 |
| ah | 648 | 318 | 0.29 | 3.97 | 3.97 | 1.03 | 22.5 | 15.9 | 2.93E-08 | 1.30E-08 | 7.477 |
| ai | 650 | 318 | 0.34 | 11.7 | 3.89 | 3.32 | 22.3 | 14.7 | 7.43E-09 | 3.61E-09 | 7.509 |
| aj | 653.2 | 318 | 0.41 | 22.6 | 3.76 | 7.43 | 21.5 | 12.8 | 2.97E-09 | 1.27E-09 | 7.532 |
| ak | 671.3 | 318 | 0.39 | 45.8 | 9.16 | 14.2 | 22.6 | 13.8 | 1.02E-09 | 7.91E-10 | 7.577 |
| al | 693.8 | 318 | 0.39 | 91.5 | 9.15 | 28.5 | 22.8 | 14.0 | 7.29E-10 | 4.09E-10 | 7.618 |
| am | 717 | 318 | 0.46 | 194.0 | 7.76 | 106.0 | 22.1 | 11.9 | 4.90E-10 | 1.22E-10 | 7.644 |
| an | 747.7 | 319 | 0.46 | 387.7 | 7.75 | 212.3 | 22.0 | 11.9 | 1.66E-10 | 6.16E-11 | 7.655 |
| ao | 788.7 | 319 | 0.46 | 645.4 | 7.74 | 354.6 | 22.1 | 11.9 | 1.20E-10 | 3.71E-11 | 7.667 |
| 1 | 837.5 | 318 | 0.40 | 12 | 12 | 7200 | 22.1 | 13.3 | 2.81E-11 | 4.42E-12 | 7.675 |

[a] Simulated PWR water with 2 ppm Li and 1000 ppm B. Conductivity ~20 μS/cm.

[b] The CGR value was obtained from the later part of the test period.

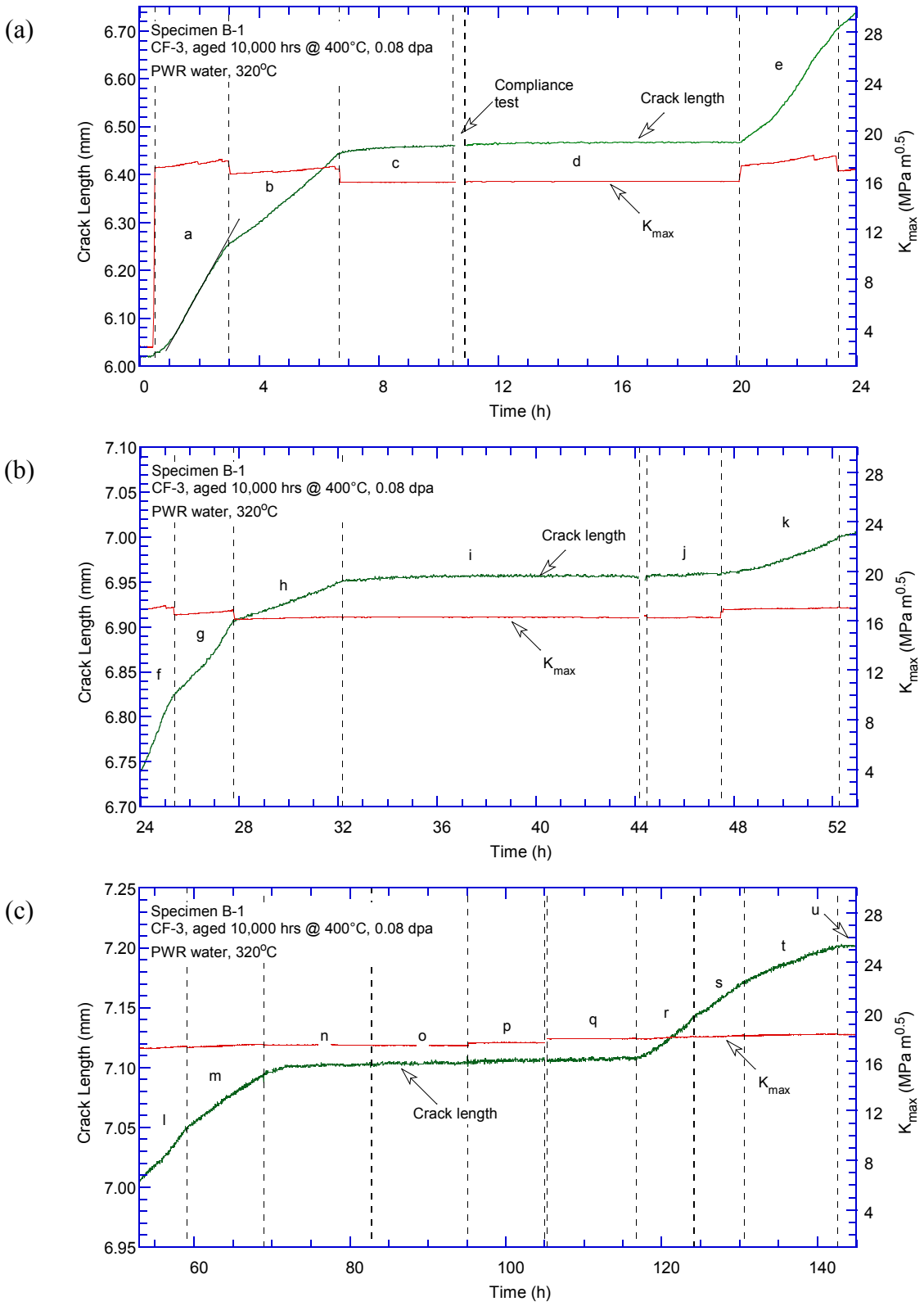


Figure 35. Crack-length-vs.-time plot for specimen B-1 (0.08-dpa aged CF-3 with 24% ferrite) in PWR water: test periods (a) a-e, (b) f-k, (c) l-u, (d) v-y, (e) z-ac, (f) ad-ag, (g) ah-al, and (h) am-1.

(d)

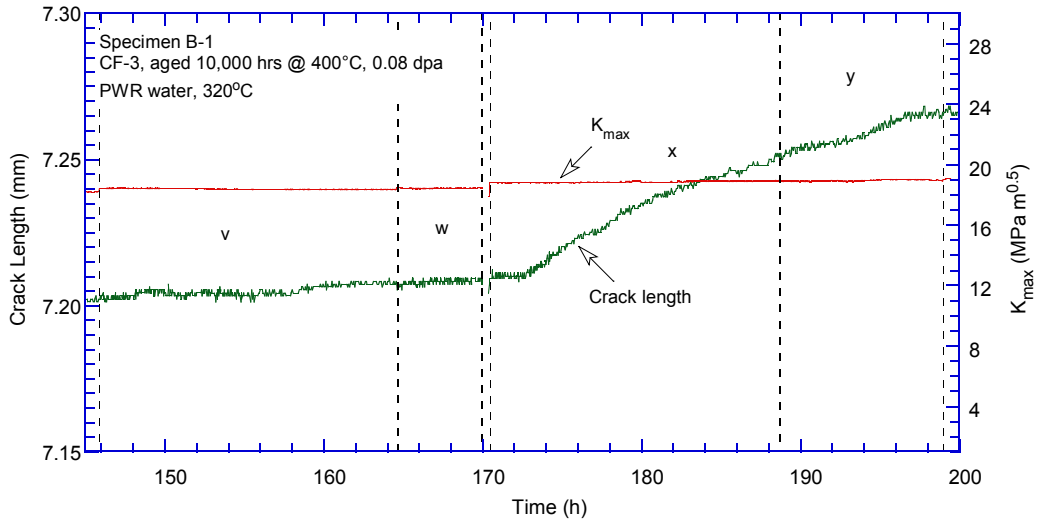


(e)

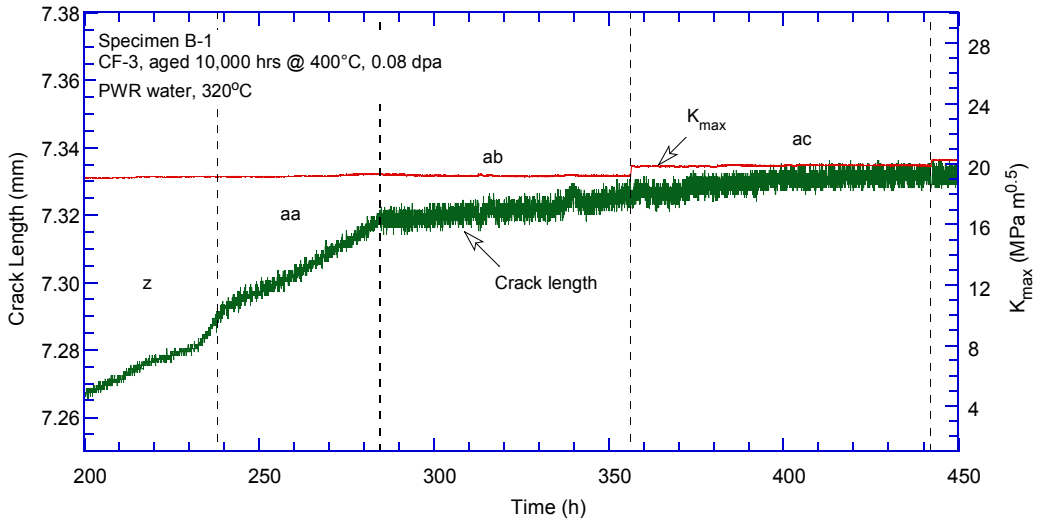


(f)

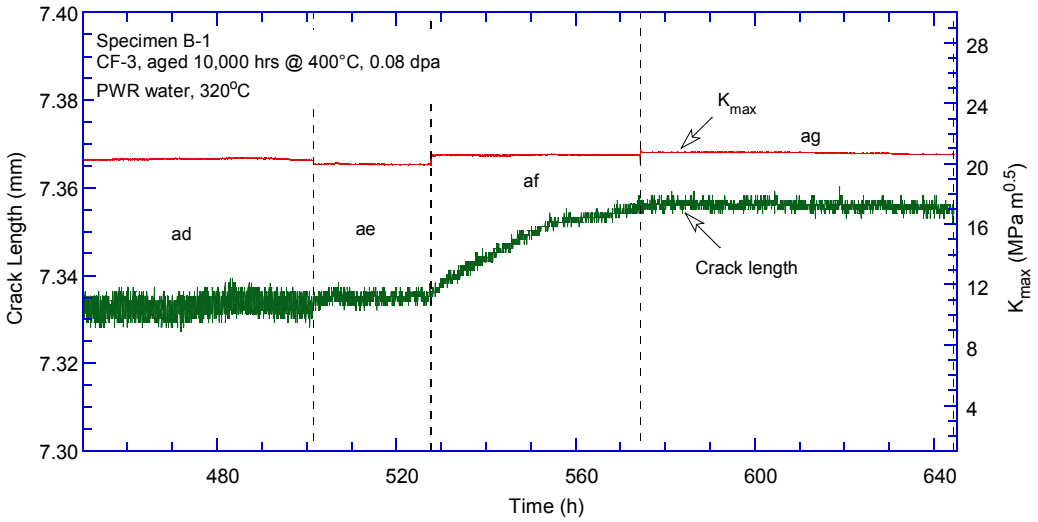


Figure 35. (Contd.)

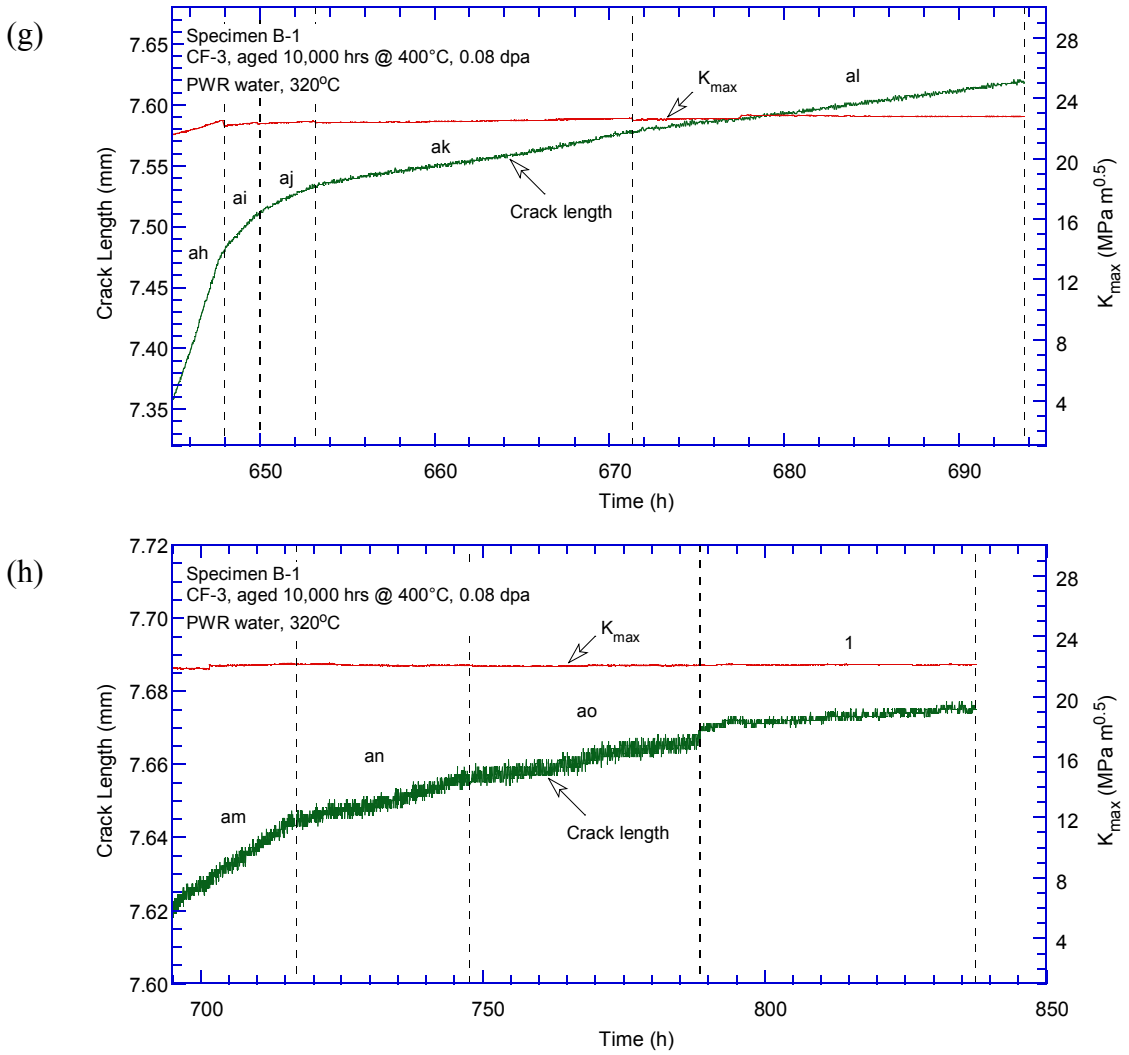


Figure 35. (Contd.)

The cyclic CGRs with a significant crack extension (defined as >10 μm) from this sample are plotted in Fig. 36 along with the corrosion fatigue curve for unirradiated SSs. No elevated corrosion fatigue response can be seen for this material despite its thermal aging condition. Comparing Figs. 14 and 36, we found the corrosion fatigue behaviors of unaged and aged CF-3 to be similar in PWR water. It seems that a combination of irradiation damage and thermal aging does not increase cracking susceptibility of CF-3 at 0.08 dpa, as would be expected.

All SCC CGRs obtained from specimens A-N1, A-1, A-2, B-N1, and B-1 are shown in Fig. 37. The open and closed symbols are for the unaged and thermally aged CF-3, and the blue and red symbols are for the unirradiated and irradiated specimens, respectively. The data points are all well below the NUREG-0313 curve, as expected in such low-corrosion-potential environments. No obvious difference can be seen between the unirradiated and irradiated specimens. The SCC CGRs of the unaged CF-3 (specimens A-1 and A-2) are also similar for the low-DO high-purity water and PWR water environments. The thermally aged specimen (B-1) has a slightly lower

CGR than that of unaged CF-3. However, given the large scatter of the SCC CGR data, this difference is considered insignificant.

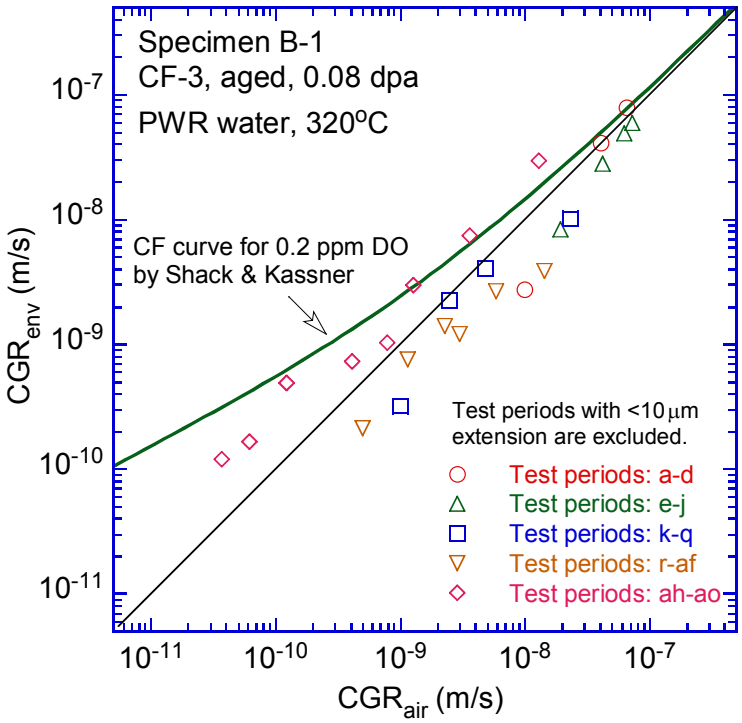


Figure 36. Cyclic CGRs of specimen B-1.

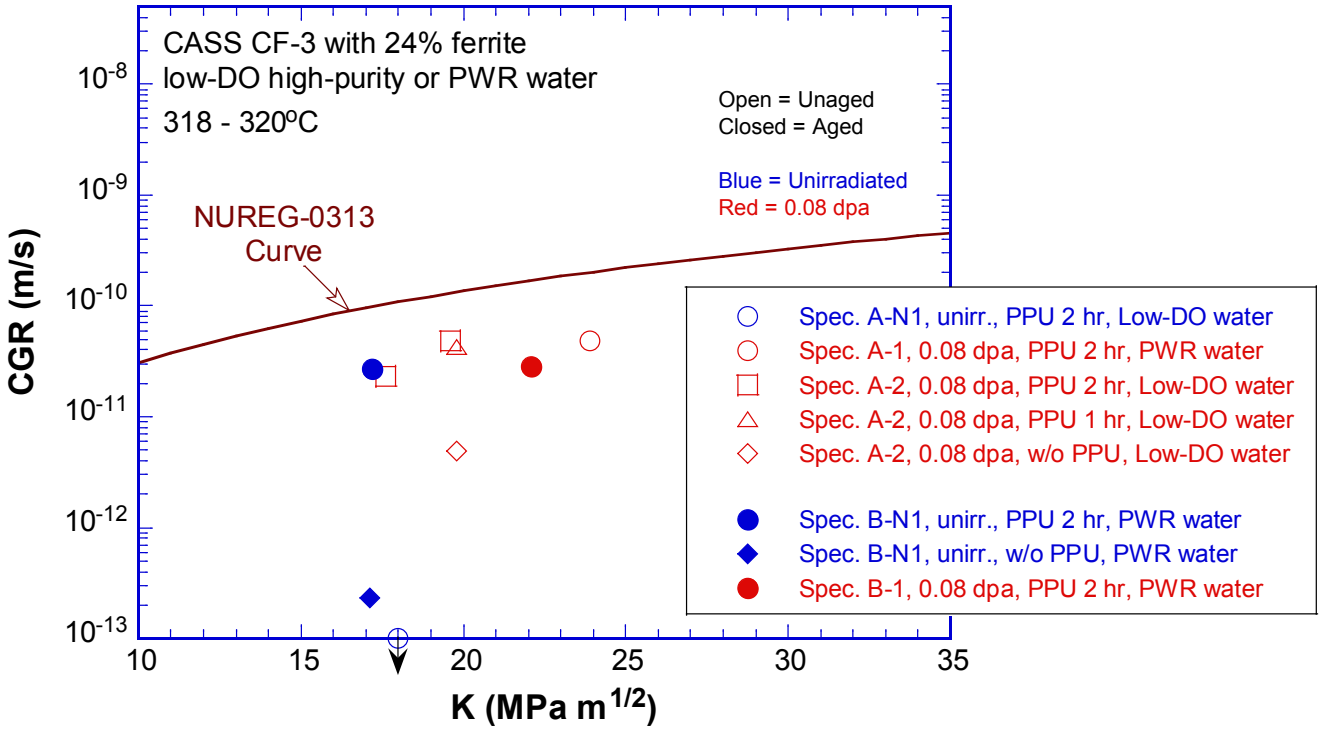


Figure 37. SCC CGRs of unaged and thermally aged CF-3 with 24% ferrite.

Fracture toughness J-R curve test

After the CGR test, a fracture toughness J-R curve test was conducted on the same sample at 320°C in PWR water. The obtained J-R curve is shown in Fig. 38. A power-law fitting of the JR data gives a relationship of $J = 362\Delta a^{0.85}$. The estimated J value is about 116kJ/m$^2$ at the 0.2-mm offset line. The J-R curve data cannot be validated with the ASTM standard because both measurements of the initial and final crack size did not meet the requirements. The data points above the $J_{max}$ limit were also used in the analysis.

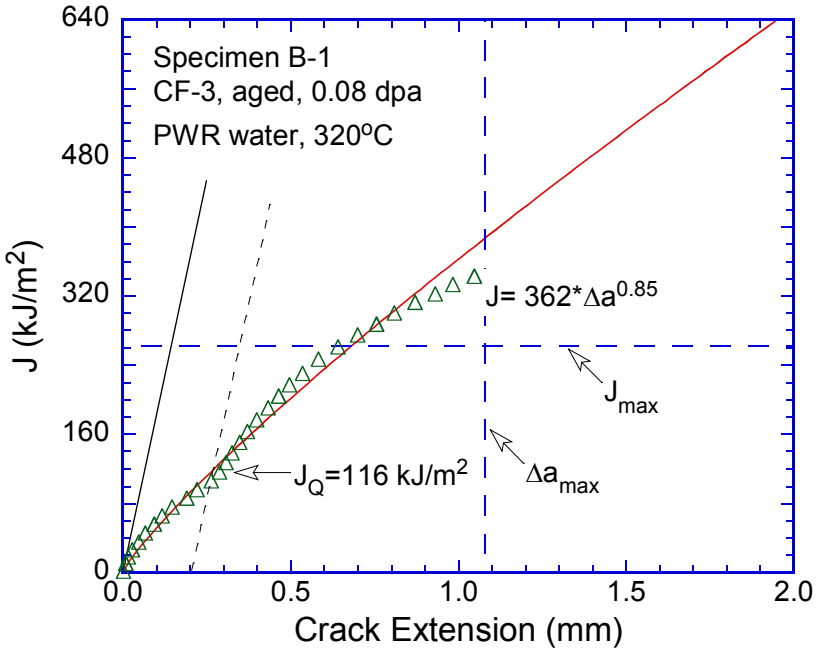


Figure 38. The J-R curve for specimen B-1.

Fractographic examination

Fractographic analysis of specimen B-1 was carried out with replicas, and Fig. 39 shows the entire fracture surface. Transgranular cleavage-like cracking is the dominant fracture morphology in the CGR test region. The overall crack extension for the CGR test is a little more on one side of the sample than the other, leading to a slightly skewed crack front. Figure 40 shows an enlarged view of the fracture surface along the sample central line. The CGR and JR test regions can be clearly distinguished by their appearance. The CGR region is relatively flat, and the JR region indicates heavily deformed ductile tearing. Note that air bubbles trapped in the replica are more excessive in the JR test region, a rough and dimpled fracture surface, than the flat CGR test region. Casting dendrite morphology with ferrite cores was seen at the end of the CGR test.

Cleavage-like morphology dominated the fatigue pre-cracking region, as shown in Fig. 41. Deformation steps are clearly visible on the fracture surface. With the advance of the crack, an area with delta ferrite at dendrite cores started to appear (Fig. 42). Compared with the surrounding austenitic phase, fewer deformation steps can be seen within the ferrite phase, as shown in Fig. 43.

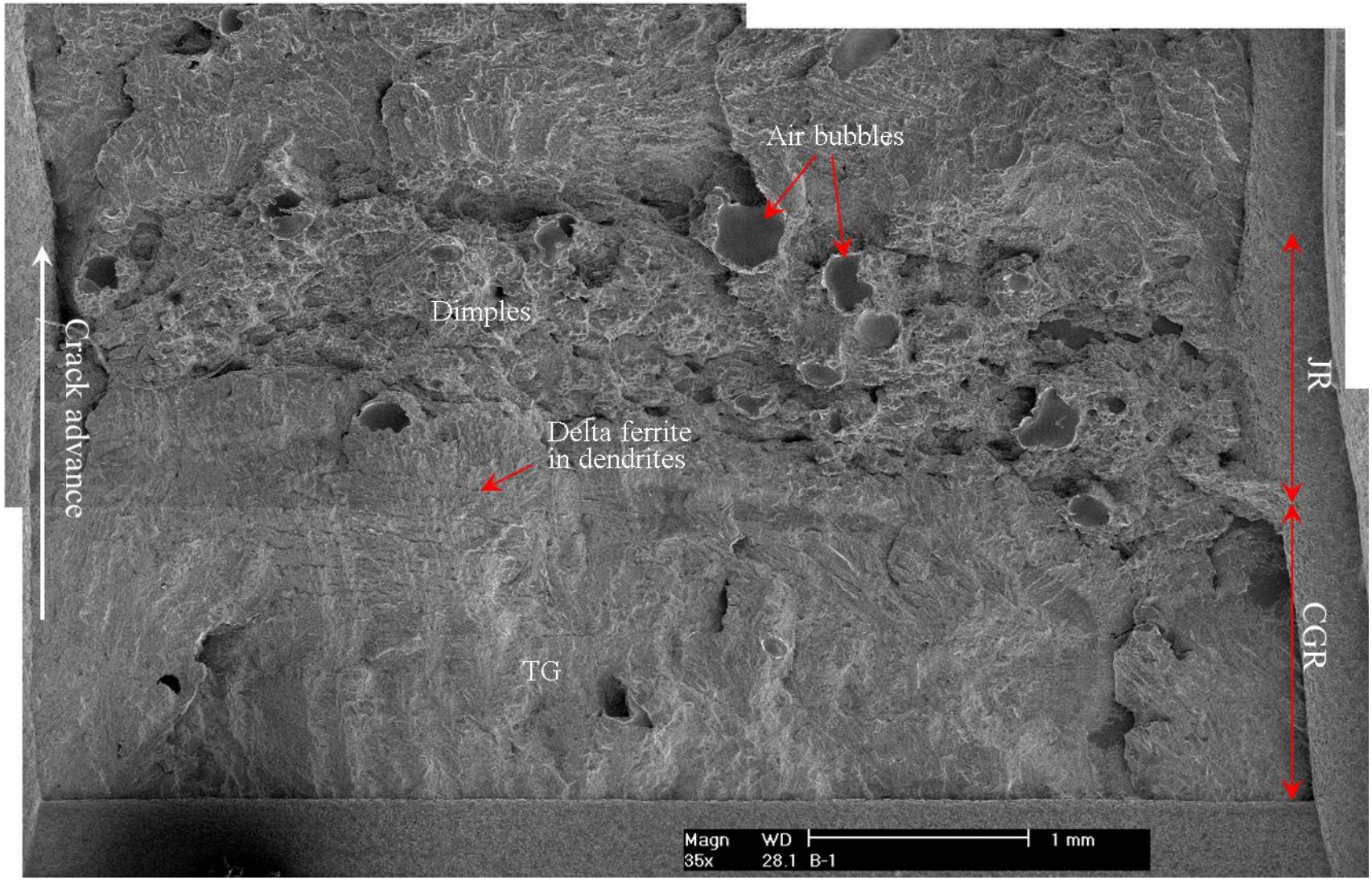


Figure 39. Fracture surface of specimen B-1 tested in PWR water.

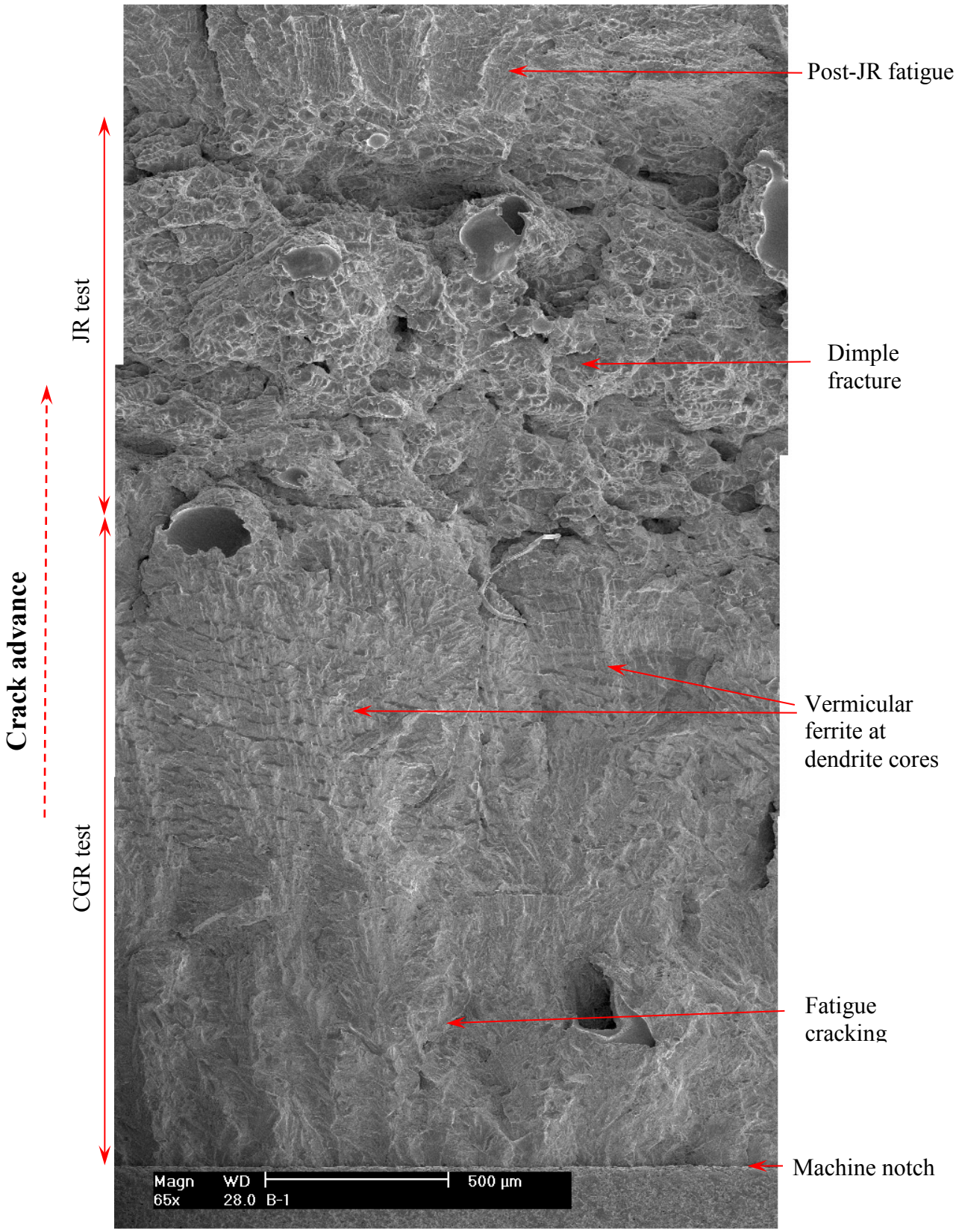


Figure 40. Fracture surface of specimen B-1 along the sample central line.

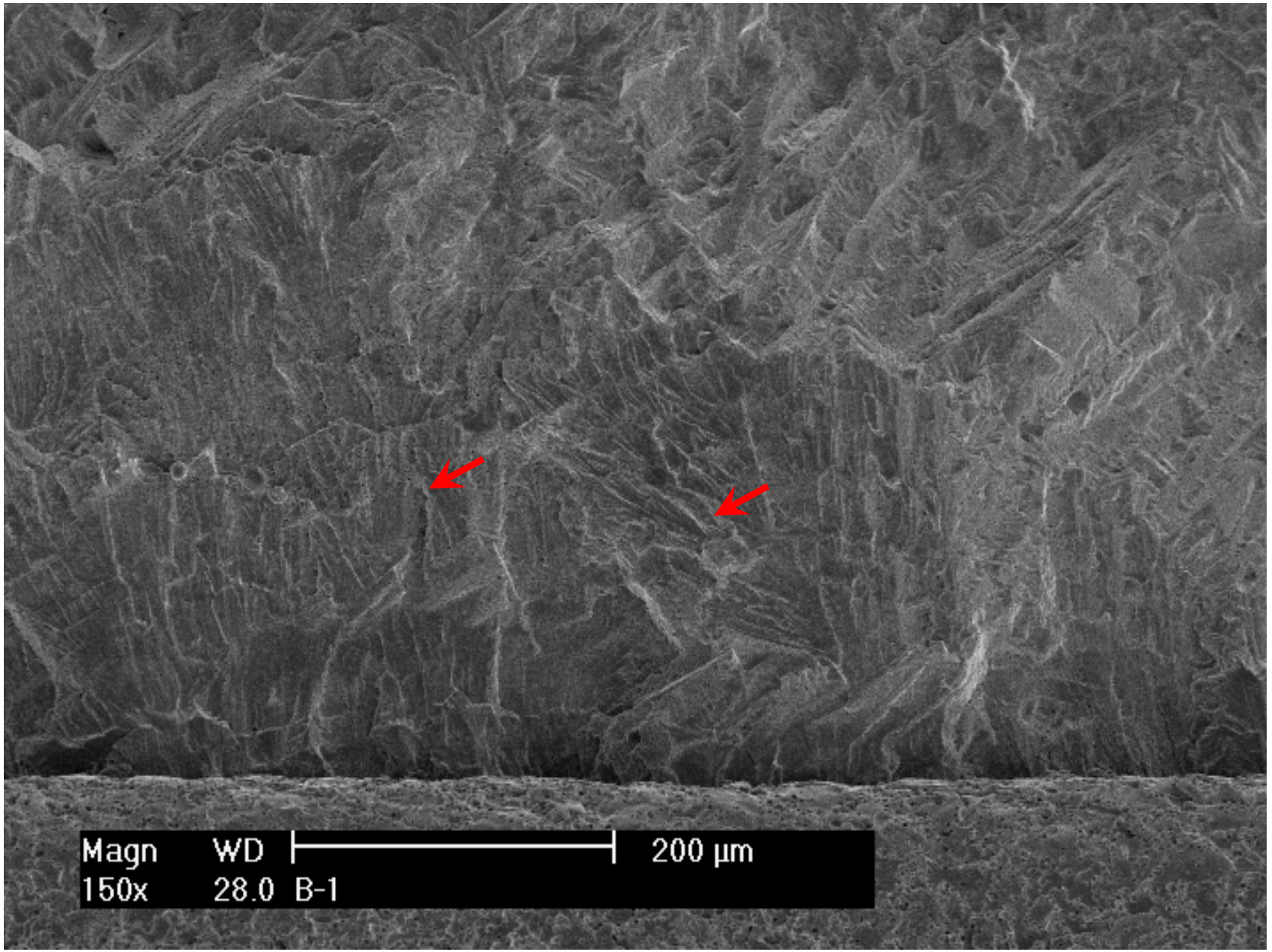


Figure 41. Deformation steps in the pre-cracking region of specimen B-1. Crack propagation from bottom to top.

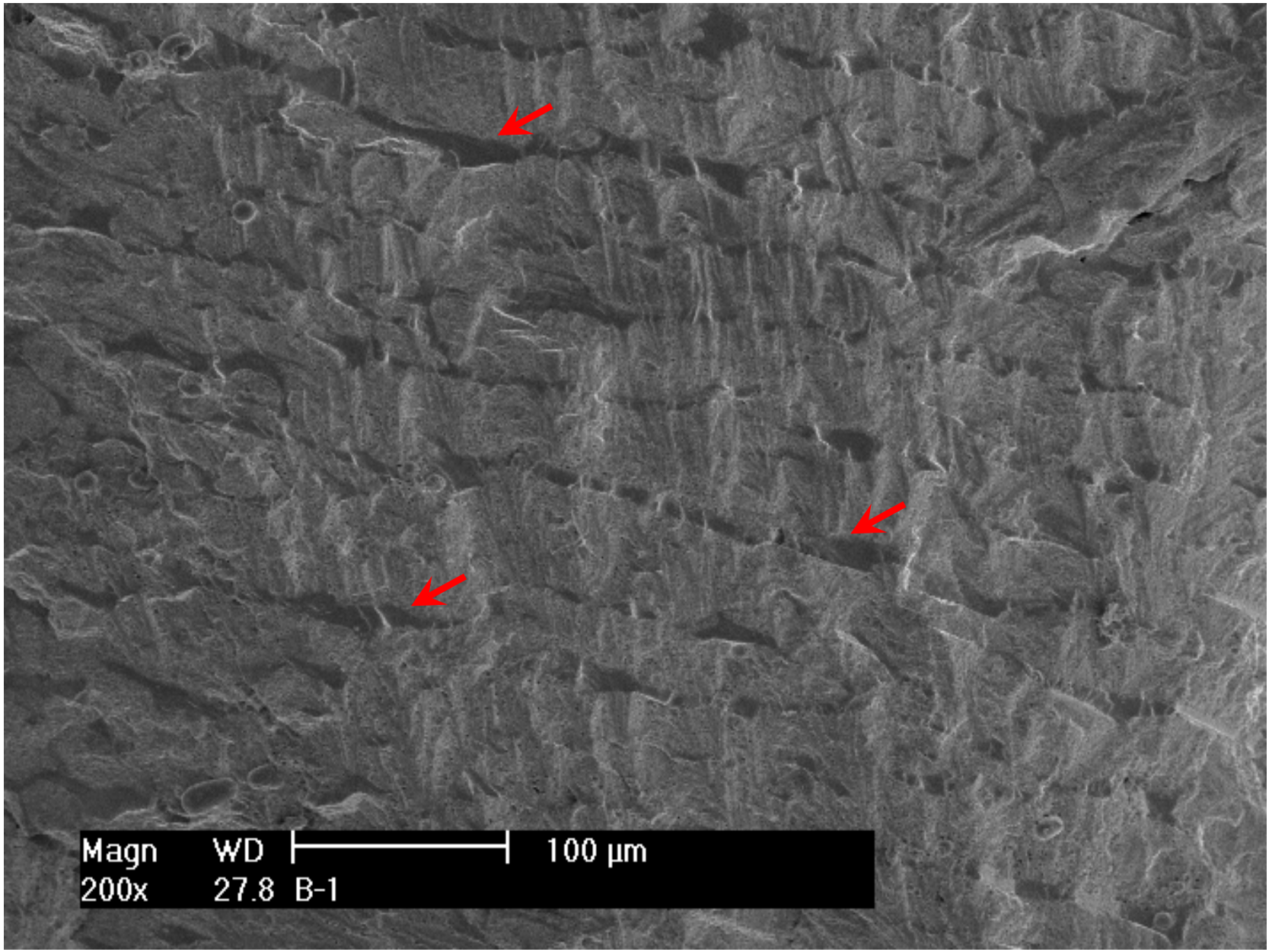


Figure 42. Delta ferrite at dendrite cores in specimen B-1. Crack propagation from bottom to top.

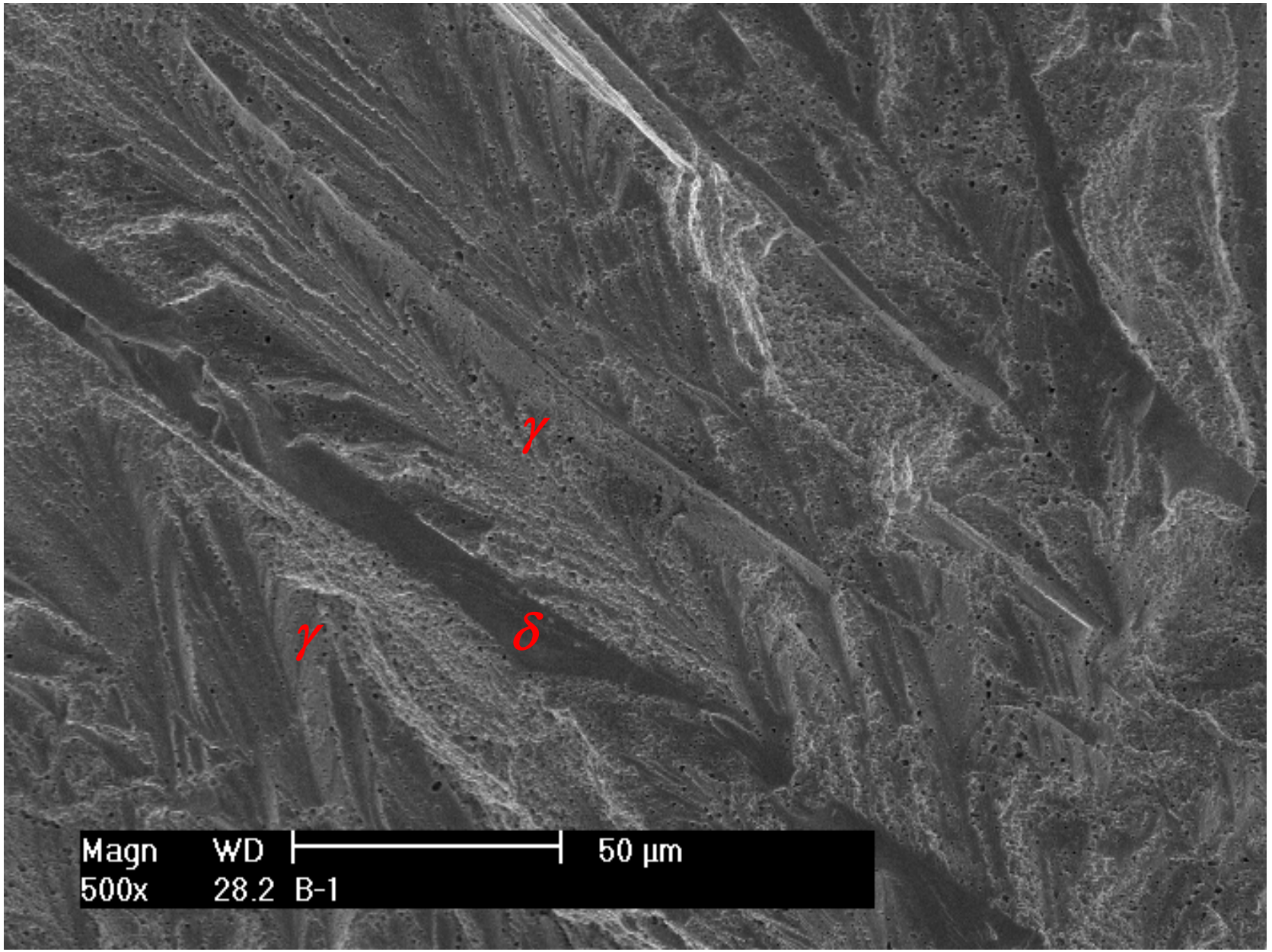


Figure 43. Fracture surface of specimen B-1 showing that delta ferrite is surrounded by heavily deformed austenite phase. Crack propagation from bottom to top.

## 3.2 CF-8 Cast Stainless Steel

### *3.2.1 Unaged CF-8 CASS*

#### *3.2.1.1 Unirradiated specimen E-N1 tested in low-DO high-purity water*

Crack growth rate test

Specimen E-N1 was an unirradiated control sample tested in low-DO high-purity water. The material was an unaged CF-8 with ~23% ferrite. The objective of the test was to compare with the test of unaged CF-3 (specimen A-N1) and to provide a baseline for the irradiated tests on CF-8 CASS. The CGR test conditions and results of this sample are summarized in Table 9, and a crack-length history plot is shown in Fig. 44.

Table 9. CGR test of specimen E-N1 (unirradiated, unaged CF-8 with 23% δ ferrite) in low-DO high-purity water.

| Test Period | Test Time, h | Test Temp., °C | Load Ratio | Rise Time, s | Return Time, s | Hold Time, s | Kmax, MPa $m^{1/2}$ | ΔK, MPa $m^{1/2}$ | CGR in Env., m/s | CGR in Air m/s | Crack Length, mm |
|---|---|---|---|---|---|---|---|---|---|---|---|
| Start | 0.2 | | | | | | | | | | 5.967 |
| a [a] | 2.7 | 319 | 0.21 | 0.36 | 0.36 | 0.14 | 15.2 | 12.0 | 8.06E-08 | 5.05E-08 | 6.172 |
| b | 3.9 | 319 | 0.21 | 0.35 | 0.35 | 0.15 | 14.1 | 11.1 | 4.98E-08 | 4.05E-08 | 6.248 |
| c | 9.2 | 319 | 0.32 | 0.33 | 0.33 | 0.17 | 13.3 | 9.1 | 1.67E-10 | 2.54E-08 | 6.252 |
| d | 92.3 - 94.2 | 319 | 0.24 | 0.35 | 0.35 | 0.15 | 13.6 | 10.4 | 5.84E-11 | 3.43E-08 | 6.250 |
| e [a] | 97.7 | 319 | 0.20 | 0.36 | 0.36 | 0.14 | 14.6 | 11.7 | 1.45E-08 | 4.68E-08 | 6.296 |
| f | 100.8 | 320 | 0.30 | 0.35 | 0.35 | 0.15 | 15.3 | 10.7 | 9.76E-09 | 4.10E-08 | 6.342 |
| g | 116.2 - 119.6 | 320 | 0.20 | 0.36 | 0.36 | 0.14 | 16.1 | 13.0 | 5.54E-08 | 6.45E-08 | 6.567 |
| h | 124.2 | 320 | 0.40 | 0.33 | 0.33 | 0.17 | 16.0 | 9.6 | 2.41E-09 | 3.36E-08 | 6.595 |
| i | 140.4 - 148.5 | 319 | 0.32 | 0.35 | 0.35 | 0.15 | 16.4 | 11.2 | 2.19E-10 | 4.84E-08 | 6.596 |
| j | 165.1 - 165.8 | 319 | 0.36 | 0.27 | 0.27 | 0.23 | 15.9 | 10.1 | 6.28E-08 | 4.61E-08 | 6.643 |
| k1 | 167.1 - 170.1 | 319 | 0.43 | 0.52 | 0.52 | 0.48 | 16.4 | 9.3 | 2.36E-09 | 1.97E-08 | 6.693 |
| k2 | 170.5 - 174.1 | 319 | 0.42 | 0.53 | 0.53 | 0.47 | 17.1 | 9.9 | 2.14E-08 | 2.35E-08 | 6.766 |
| l [a] | 191.6 | 319 | 0.50 | 1.22 | 1.22 | 1.28 | 17.2 | 8.6 | 9.12E-09 | 6.91E-09 | 6.823 |
| m | 213 | 319 | 0.56 | 2.27 | 2.27 | 2.73 | 17.0 | 7.6 | 1.59E-09 | 2.56E-09 | 6.854 |
| n [a] | 233.7 | 319 | 0.60 | 6.43 | 2.14 | 8.57 | 17.1 | 6.8 | 6.00E-10 | 6.77E-10 | 6.865 |
| o | 260.3 | 319 | 0.59 | 12.9 | 2.15 | 17.1 | 16.9 | 6.9 | 1.13E-11 | 3.43E-10 | 6.867 |
| p | 284.4 | 319 | 0.54 | 13.7 | 2.29 | 16.3 | 16.9 | 7.7 | 4.19E-10 | 4.49E-10 | 6.880 |
| q | 309.2 | 319 | 0.54 | 27.6 | 2.30 | 32.4 | 17.2 | 7.8 | 4.07E-10 | 2.35E-10 | 6.896 |
| r | 333 | 319 | 0.54 | 55.4 | 2.31 | 64.6 | 17.2 | 7.9 | 4.44E-10 | 1.22E-10 | 6.912 |
| s | 358.4 | 319 | 0.53 | 139.1 | 5.56 | 160.9 | 17.2 | 8.0 | 2.88E-10 | 5.00E-11 | 6.923 |
| t | 404.4 | 319 | 0.54 | 232.2 | 5.57 | 267.8 | 17.6 | 8.1 | 2.97E-10 | 3.11E-11 | 6.945 |
| u | 429.1 | 320 | 0.53 | 464.2 | 5.57 | 535.8 | 17.4 | 8.1 | 7.04E-11 | 1.55E-11 | 6.949 |
| 1a | 553.3 | 319 | 0.55 | 12 | 12 | 7200 | 17.5 | 7.9 | 1.43E-11 | 9.27E-13 | 6.959 |
| 1b | 718.7 | 320 | 1 | - | - | - | 17.5 | 0.3 | 8.09E-12 | - | 6.962 |

[a] The CGR value was obtained from the later part of the test period.

Fatigue precracking was started with a triangle waveform at 1 Hz and a load ratio of ~0.2. A CGR close to the fatigue growth rate in air was readily established at a $K_{max}$ of ~15.2 MPa $m^{1/2}$. No stable crack growth could be maintained with a lower $K_{max}$ in the following test periods. After the machine compliance was confirmed, the crack was advanced for 500 μm at 16-17 MPa $m^{1/2}$. Eventually, environmentally assisted cracking started to appear in test periods *p* and *q*. With further increases in load ratio and rise time, environmental enhancement was stabilized between test periods *r* and *u*. The cyclic CGRs obtained from this sample are shown in Fig. 45 along with the corrosion fatigue curve for SSs in low-DO water. It is clear that the corrosion fatigue response of the unaged CF-8 is comparable to that of the wrought SSs in low-DO water.

After the cyclic CGR test, the test was set to a constant load with PPU every 2 hr. A SCC CGR of 1.4 x $10^{-11}$ m/s was obtained over 10-μm crack extension. This CGR was much higher than that observed in the unirradiated CF-3 CASS (specimen A-N1). After the PPU was removed, the CGR decreased to about 7.8 x $10^{-12}$ m/s, which was also much higher than that of the unirradiated CF-3 CASS.

(a)

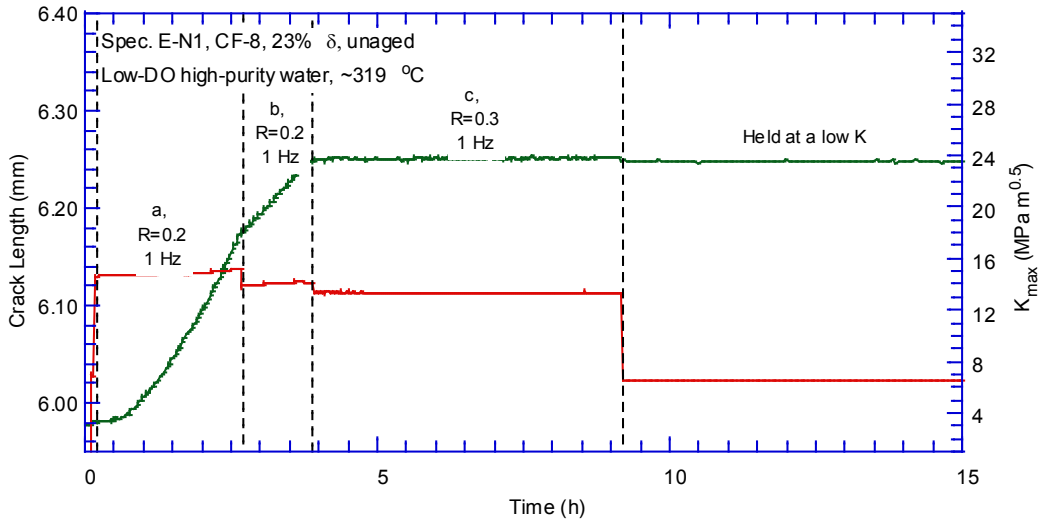


Figure 44. Crack-length-vs.-time plot for specimen E-N1 (unirradiated, unaged CF-8 with 23% ferrite): test periods (a) a-c, (b) d-f, (c) g-i, (d) j-m, (e) n-q, (f) r-u, and (g) 1a-1b.

(b)

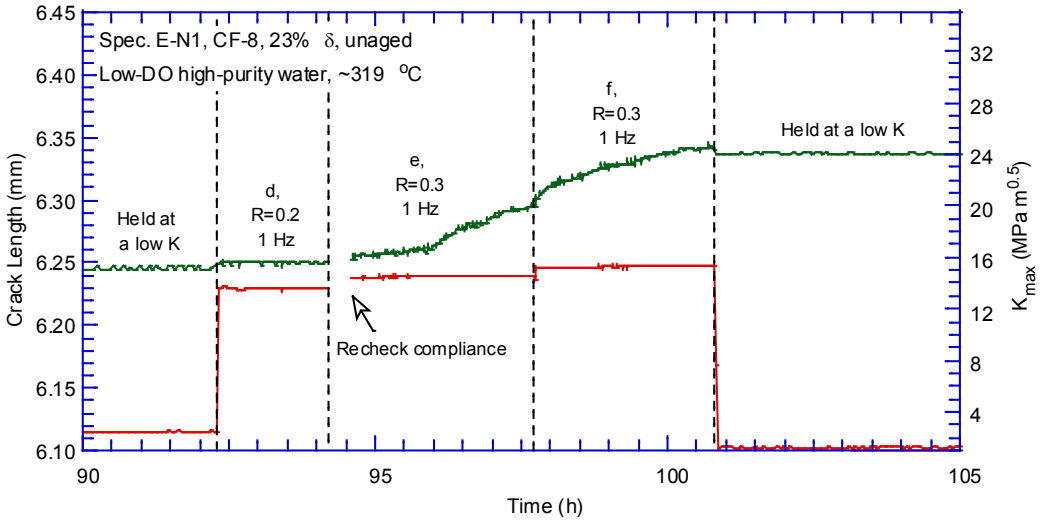


(c)

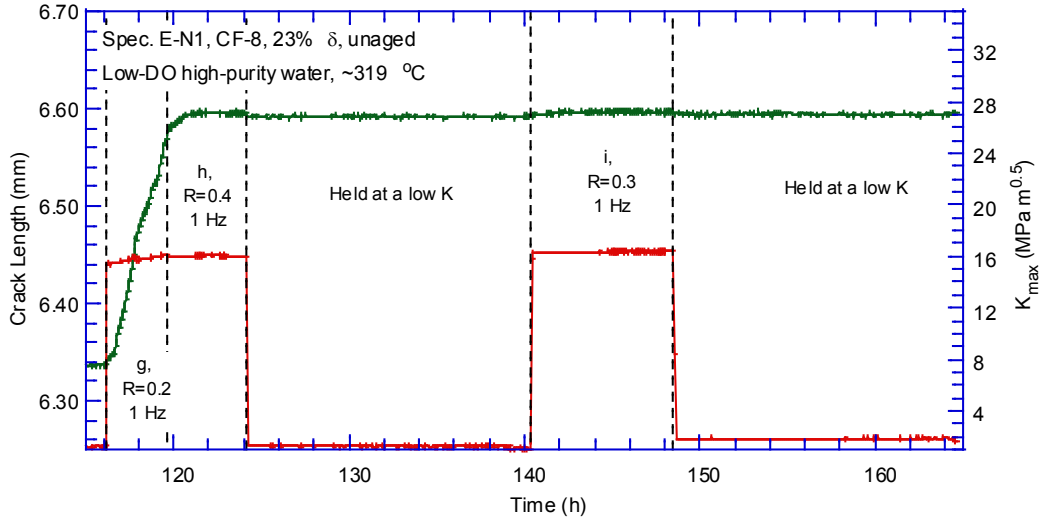


(d)

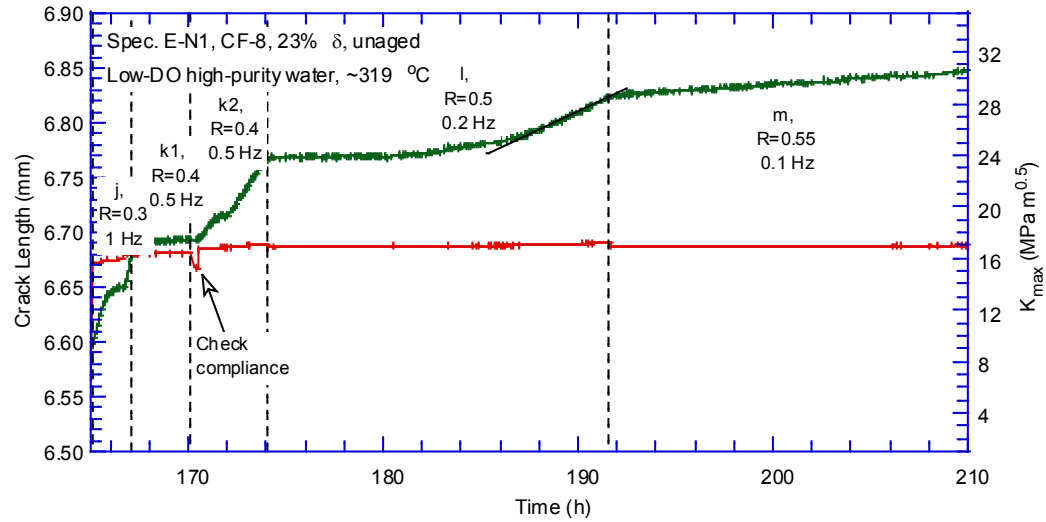


Figure 44. (Contd.)

(e)

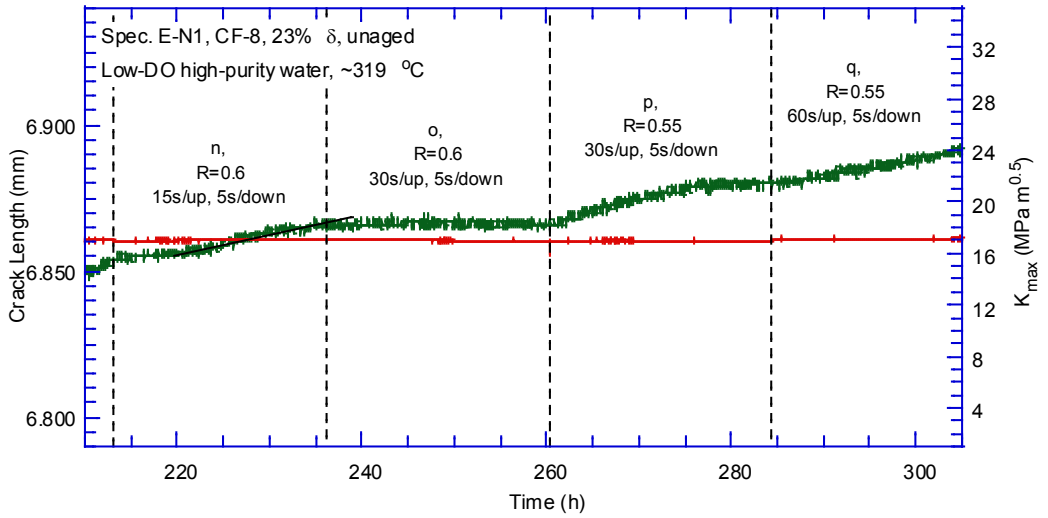


(f)

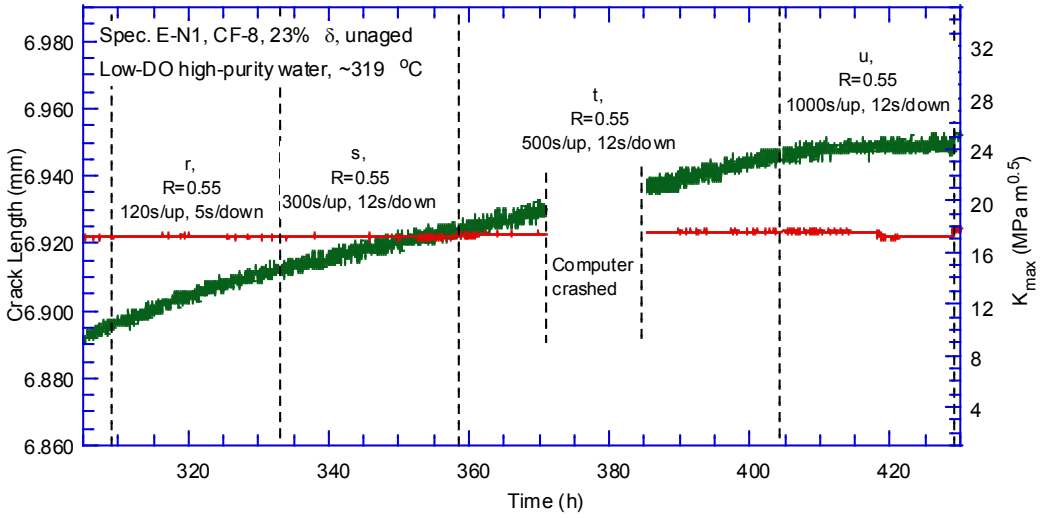


(g)

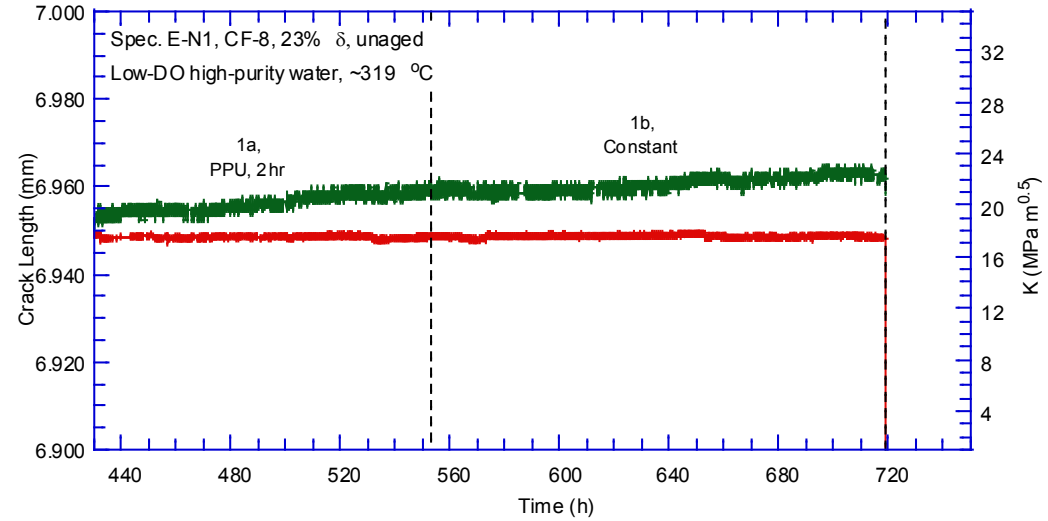


Figure 44. (Contd.)

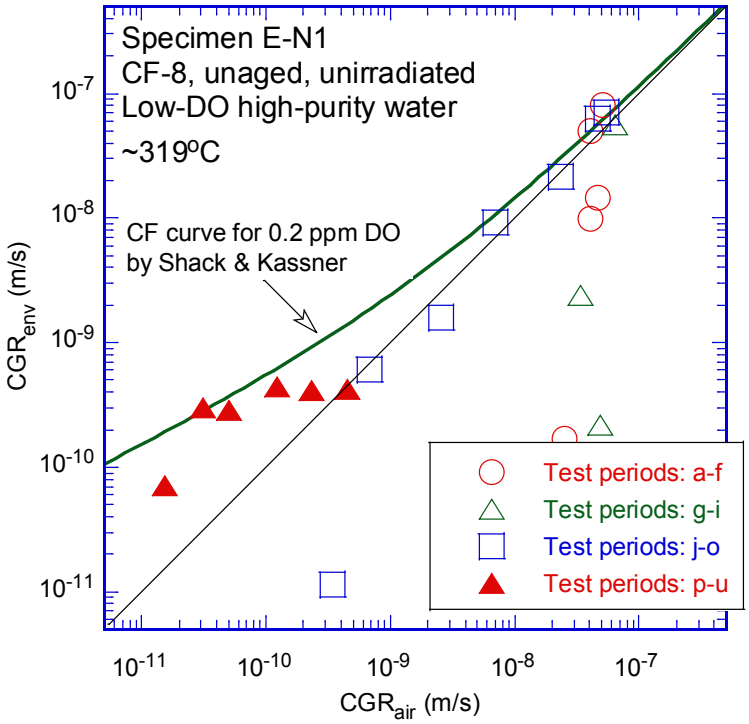


Figure 45. Cyclic CGRs of specimen E-N1.

Fracture toughness J-R curve test

Following the CGR test, a fracture toughness J-R curve test was performed on this sample in the same low-DO high-purity water environment. The test was conducted at a constant strain rate of 0.43 μm/s, and the crack extension was measured with the DCPD method. Before each DCPD measurement, the stress was allowed to relax at a constant displacement for 30 s. Due to the low flow stress and high ductility, significant plastic flow was observed in this sample during the J-R curve test. Very little crack extension was obtained before the maximum cross-head displacement was reached (limited by the load train inside the autoclave and the total range of LVDT). Consequently, no data point was available in the qualified range above the 0.2-mm offset line for a power-law curve fit (see Fig. 46). The J value measured at the end of the test was ~500 kJ/m$^2$. A J value greater than 700 kJ/m$^2$ was estimated by extrapolating the available data points to the 0.2-mm offset line. It is clear the fracture toughness of this sample is much higher than the measurement capacity of the 1/4T-CT specimen.

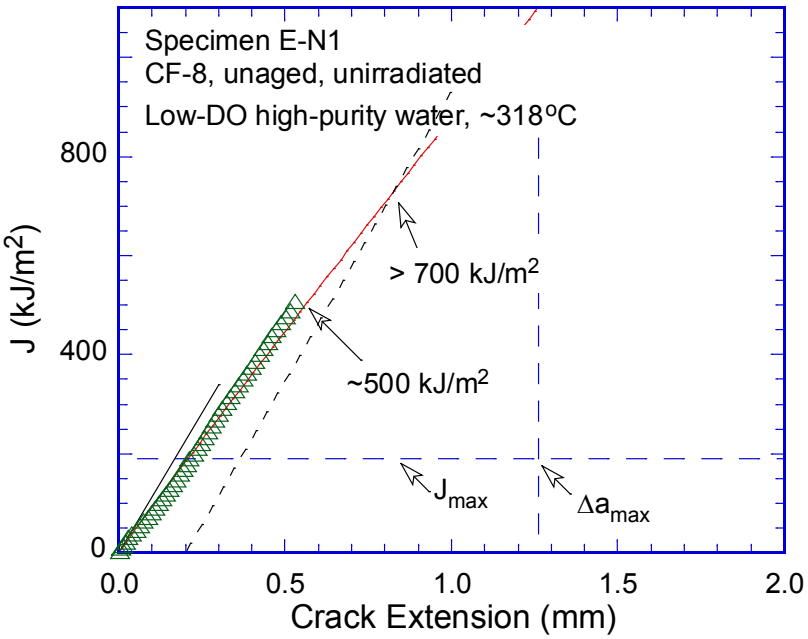


Figure 46. J-R curve data of specimen E-N1.

Fractographic examination

A fractographic analysis of the tested sample was carried out after the sample was broken open at room temperature in air. Figure 47 shows the entire fracture surface of the CGR and JR tests. The crack front of the CGR test is not very straight in this test, and the crack extension is smaller on one side of the sample than the other. Transgranular cracking and ductile dimples are the dominant morphologies for the CGR and JR test regions, respectively. For the CGR test region, heavy deformation ledges resulting from fatigue loading can be seen close to the machined notch (Fig. 48). Fractured δ ferrites with little plastic deformation are more evident at the later stage of the CGR test (Fig. 49). The brittle fracture is not visible during the JR test, and ductile dimples are the main fracture morphology in the JR test region (Fig. 50). Only a narrow band of JR test region can be seen on the fracture surface, which is consistent with the high ductility observed in this sample.

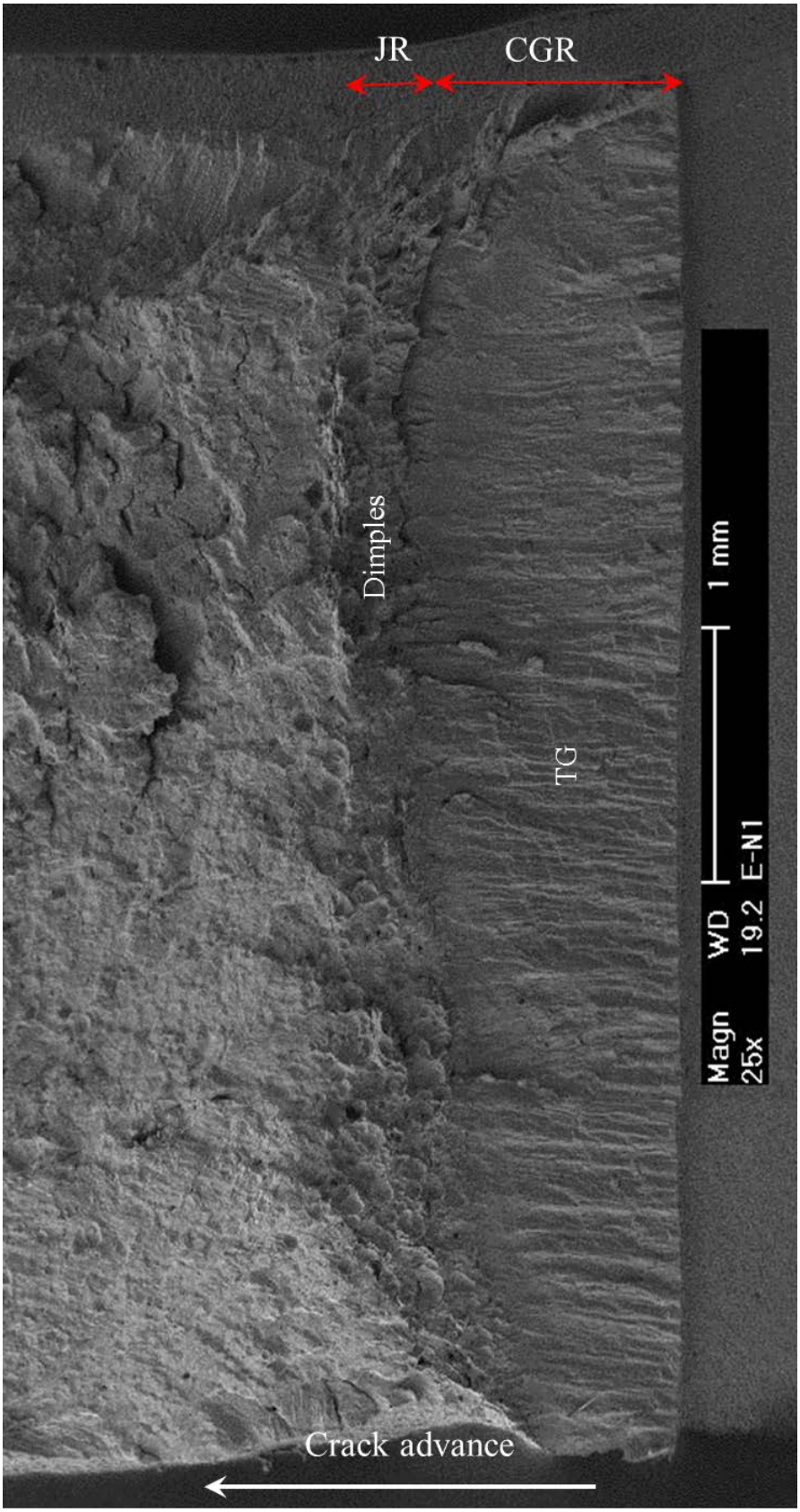


Figure 47. Fracture surface of specimen E-N1 tested in low-DO high-purity water.

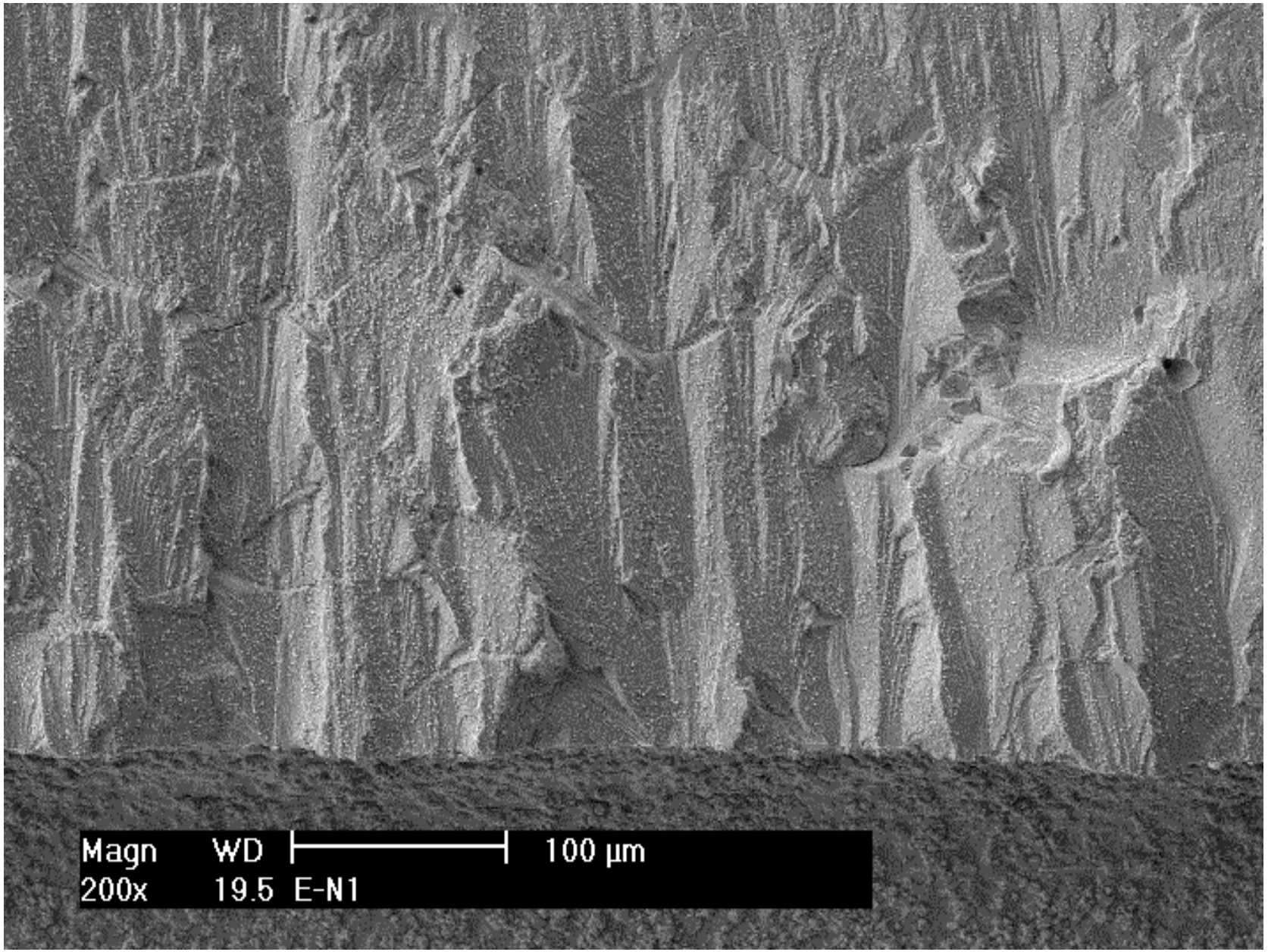


Figure 48. Transgranular fracture at the beginning of the precracking for specimen E-N1. Crack propagation from bottom to top.

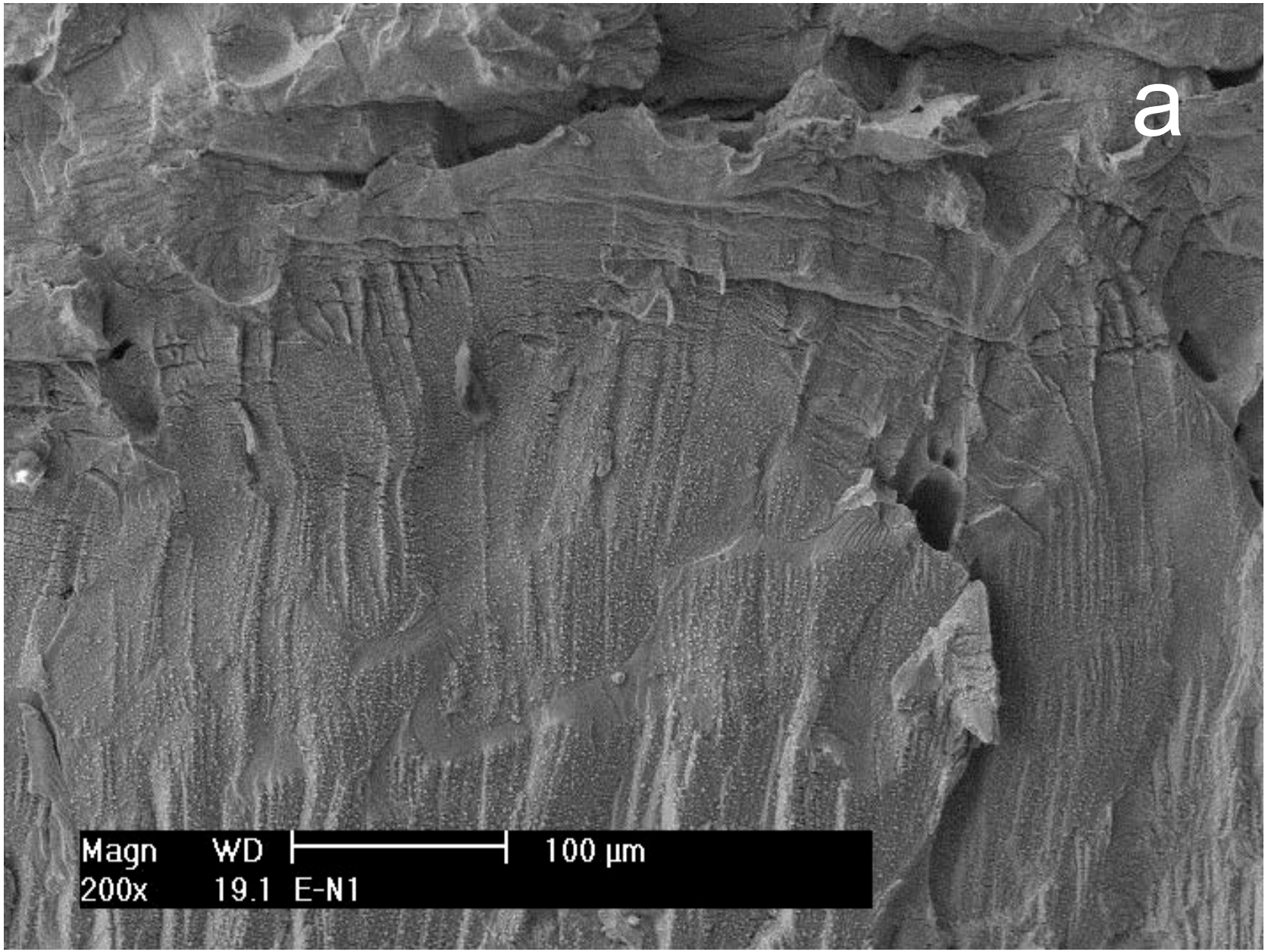


Figure 49. Transgranular fracture at the end of the CGR test for specimen E-N1. Crack propagation from bottom to top.

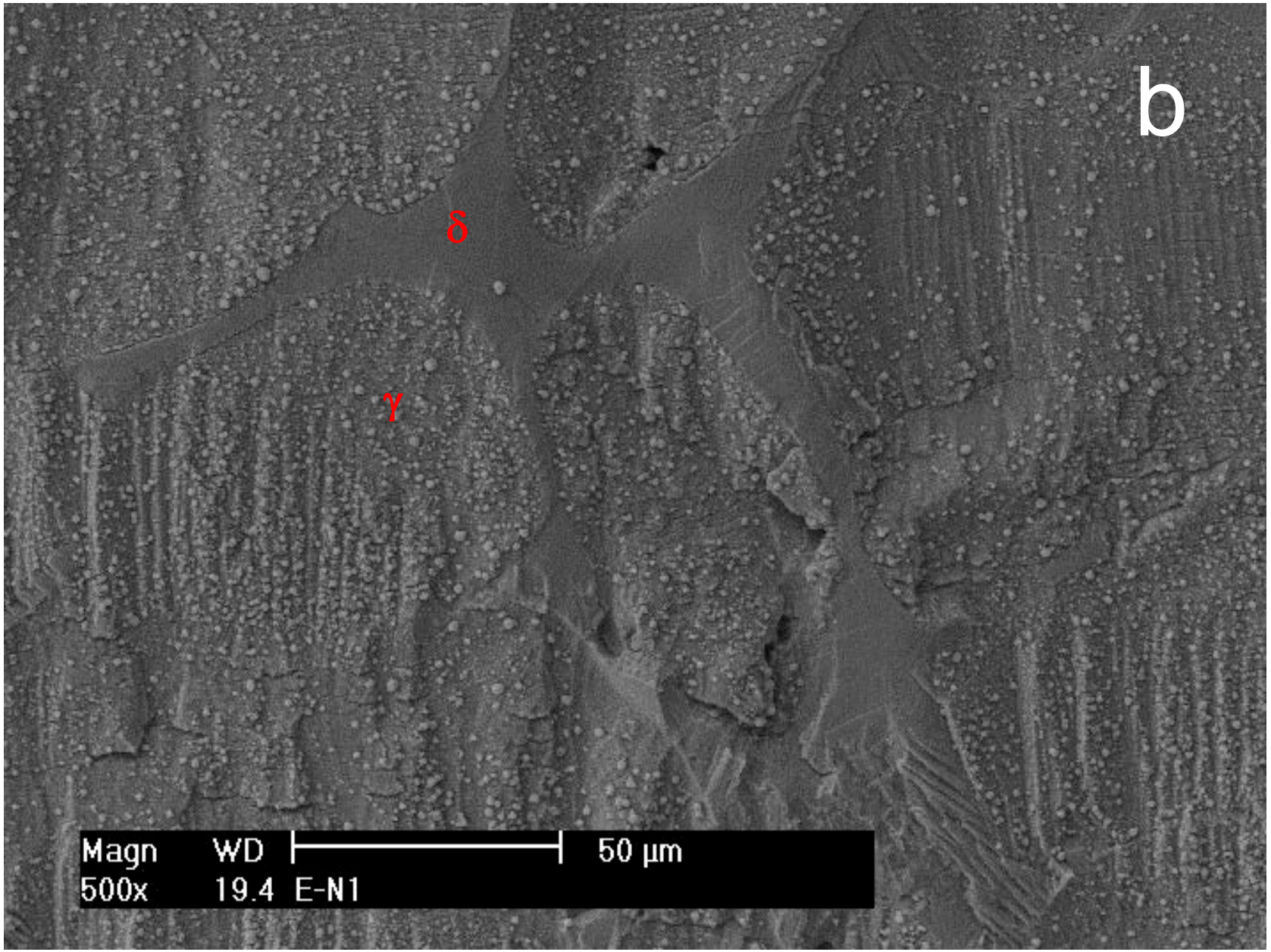


Figure 49. (Contd.)

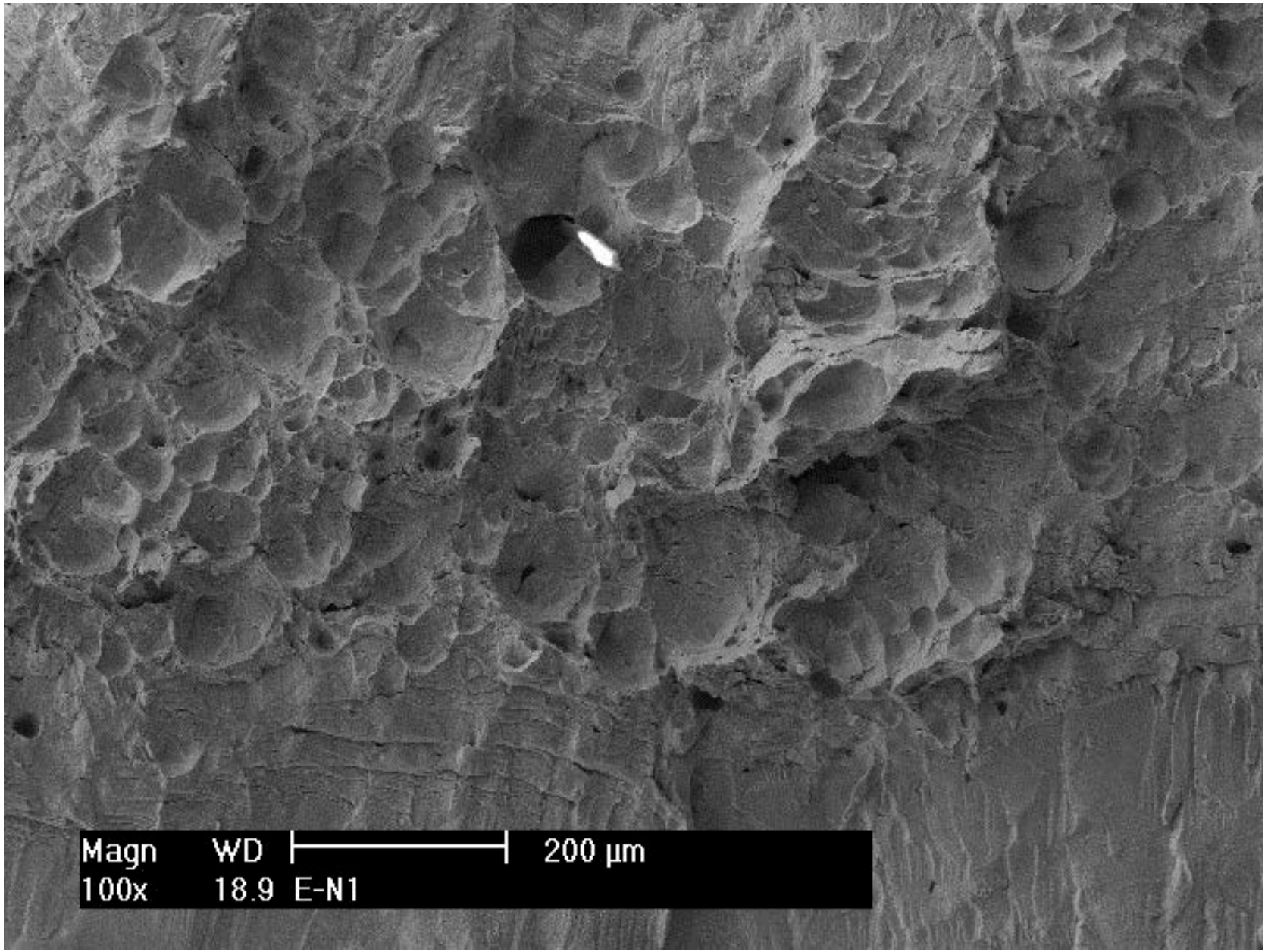


Figure 50. Ductile dimple fracture in the JR test region of specimen E-N1. Crack propagation from bottom to top.

*3.2.1.2 Irradiated specimen E-1 tested in low-DO high-purity water*

Crack growth rate test

Specimen E-1, an unaged CF-8 CASS (Heat 68) irradiated to 0.08 dpa, was tested in low-DO high-purity water at 320°C. This sample contained ~23% ferrite, similar to that of CF-3 in this study. The objective was to compare the results with those from thermally aged CF-8 at the same dose. The CGR test conditions and results are summarized in Table 10, and a crack-length history plot is shown in Fig. 51.

Table 10. CGR test of specimen E-1 (0.08-dpa unaged CF-8 with 23% δ ferrite) in low-DO high-purity water.

| Test Period | Test Time, h | Test Temp., °C | Load Ratio | Rise Time, s | Return Time, s | Hold Time, s | Kmax, MPa $m^{1/2}$ | ΔK, MPa $m^{1/2}$ | CGR in Env., m/s | CGR in Air m/s | Crack Length, mm |
|---|---|---|---|---|---|---|---|---|---|---|---|
| Start | 1.3 | | | | | | | | | | 6.001 |
| a | 3.0 | 320 | 0.20 | 0.44 | 0.44 | 0.06 | 17.4 | 13.9 | 6.98E-08 | 6.70E-08 | 6.153 |
| b | 6.6 | 319 | 0.30 | 0.43 | 0.43 | 0.07 | 16.4 | 11.5 | 2.26E-08 | 4.15E-08 | 6.294 |
| c1 | 15.6 | 319 | 0.30 | 0.85 | 0.85 | 0.15 | 15.5 | 10.8 | 4.03E-09 | 1.73E-08 | 6.360 |
| c2 | 18.3 | 319 | 0.30 | 0.85 | 0.85 | 0.15 | 15.7 | 11.0 | 1.57E-08 | 1.83E-08 | 6.421 |
| c3 | 21.7 | 319 | 0.30 | 0.85 | 0.85 | 0.15 | 16.3 | 11.4 | 2.54E-08 | 2.04E-08 | 6.552 |
| d | 25.3 | 319 | 0.30 | 0.84 | 0.84 | 0.16 | 15.5 | 10.9 | 1.50E-08 | 1.76E-08 | 6.629 |
| e1 | 36.5 | 319 | 0.40 | 0.81 | 0.81 | 0.19 | 14.5 | 8.7 | 9.26E-10 | 9.81E-09 | 6.650 |
| e2 | 45.5 | 319 | 0.40 | 0.81 | 0.81 | 0.19 | 14.6 | 8.8 | 2.68E-09 | 1.01E-08 | 6.682 |
| e3 | 50.5 | 319 | 0.40 | 0.81 | 0.81 | 0.19 | 14.5 | 8.8 | 6.48E-09 | 1.00E-08 | 6.733 |
| e4 | 53.8 | 319 | 0.40 | 0.81 | 0.81 | 0.19 | 14.9 | 8.9 | 1.59E-08 | 1.08E-08 | 6.805 |
| f | 59.6 | 319 | 0.50 | 1.54 | 1.54 | 0.46 | 14.7 | 7.4 | 5.31E-09 | 3.28E-09 | 6.852 |
| g | 73 | 319 | 0.50 | 3.84 | 3.84 | 1.16 | 14.7 | 7.4 | 2.09E-09 | 1.32E-09 | 6.891 |
| h | 96.7 | 319 | 0.50 | 11.5 | 3.83 | 3.52 | 14.4 | 7.3 | 4.26E-10 | 4.20E-10 | 6.913 |
| i | 125.1 | 320 | 0.55 | 22.4 | 3.73 | 7.62 | 14.4 | 6.5 | negligible | 1.60E-10 | 6.911 |
| j | 144.6 | 319 | 0.44 | 23.5 | 3.91 | 6.54 | 14.4 | 8.0 | 2.41E-10 | 2.72E-10 | 6.925 |
| k | 152.2 | 320 | 0.45 | 11.8 | 3.92 | 3.25 | 14.8 | 8.2 | 1.68E-09 | 5.76E-10 | 6.951 |
| l | 167.4 | 319 | 0.49 | 23.0 | 3.83 | 7.01 | 14.8 | 7.5 | 6.61E-10 | 2.28E-10 | 6.973 |
| m | 181.7 | 320 | 0.49 | 46.0 | 9.19 | 14.0 | 14.7 | 7.5 | 3.64E-10 | 1.15E-10 | 6.988 |
| n | 217.5 | 320 | 0.49 | 92.0 | 9.20 | 28.0 | 14.7 | 7.5 | 1.97E-10 | 5.87E-11 | 7.004 |
| o | 262.6 | 320 | 0.49 | 229.8 | 9.19 | 70.2 | 14.7 | 7.5 | 1.01E-10 | 2.35E-11 | 7.018 |
| p | 320.5 | 320 | 0.49 | 459.7 | 9.19 | 140.3 | 14.8 | 7.6 | 1.04E-10 | 1.20E-11 | 7.032 |
| q | 360 | 321 | 0.49 | 765.3 | 9.18 | 234.7 | 14.9 | 7.6 | 8.40E-11 | 7.20E-12 | 7.041 |
| 1 | 431.8 | 321 | 0.45 | 12 | 12 | 7200 | 14.9 | 8.2 | 1.80E-11 | 9.53E-13 | 7.051 |
| 2 | 578.4 | 320 | 0.45 | 12 | 12 | 7200 | 16.8 | 9.3 | 2.71E-11 | 1.43E-12 | 7.073 |

Fatigue pre-cracking was started with a triangular waveform at a maximum stress intensity factor of ~17.5 MPa $m^{1/2}$, load ratio of 0.2, and frequency of 1 Hz. After about 300-μm crack extension, the load ratio was increased to 0.3, and the maximum stress intensity factor was decreased to ~15.5 MPa $m^{1/2}$. The measured CGR gradually increased in test period *c* after a short period of sluggish growth, and the final CGR was about 2.0 x $10^{-8}$ m/s. The rise time and load ratio were increased further in the subsequent test periods, and environmentally enhanced cracking started to appear at the end of test period *e*. In the following test periods, the maximum stress intensity factor was decreased to ~14-15 MPa $m^{1/2}$. Environmental enhancement appears

to have been readily established in this sample at a fairly low stress intensity level with a load ratio below 0.5. By the end of test period *q*, the measured CGR was more than one order of magnitude higher than the fatigue growth rate in air. All cyclic CGRs of this sample are plotted in Fig. 52. The corrosion fatigue curve for unirradiated SSs still bounds all data points from this sample. However, compared to the cyclic CGRs of CF-3 (specimens A-1, A-2, and B-1), the CF-8 sample shows a slightly lower sensitivity to corrosion fatigue.

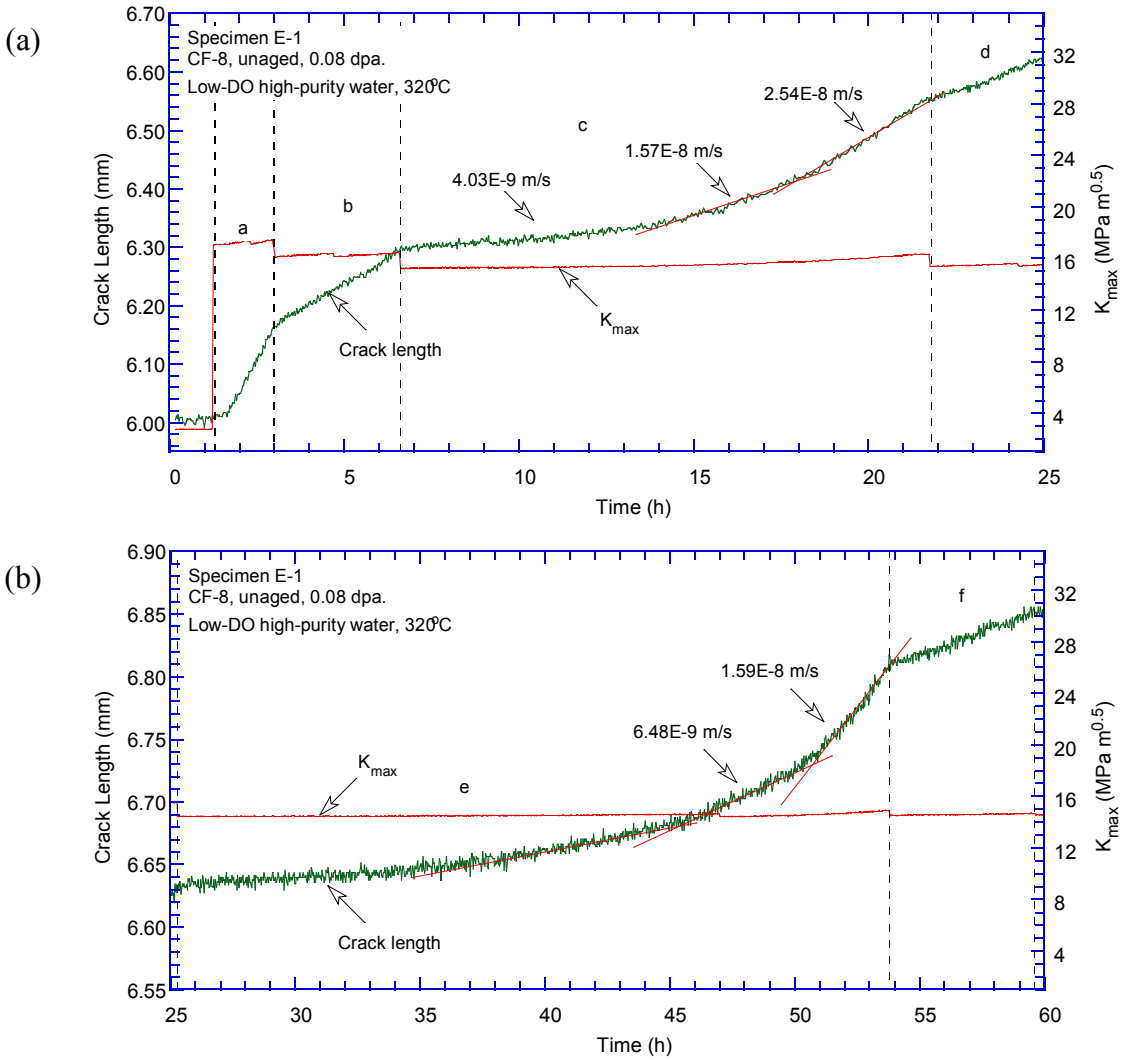


Figure 51. Crack-length-vs.-time plot for specimen E-1 (0.08-dpa unaged CF-8 with 23% ferrite): test periods (a) a-d, (b) e-f, (c) g-j, (d) k-o, and (e) p-2.

(c)

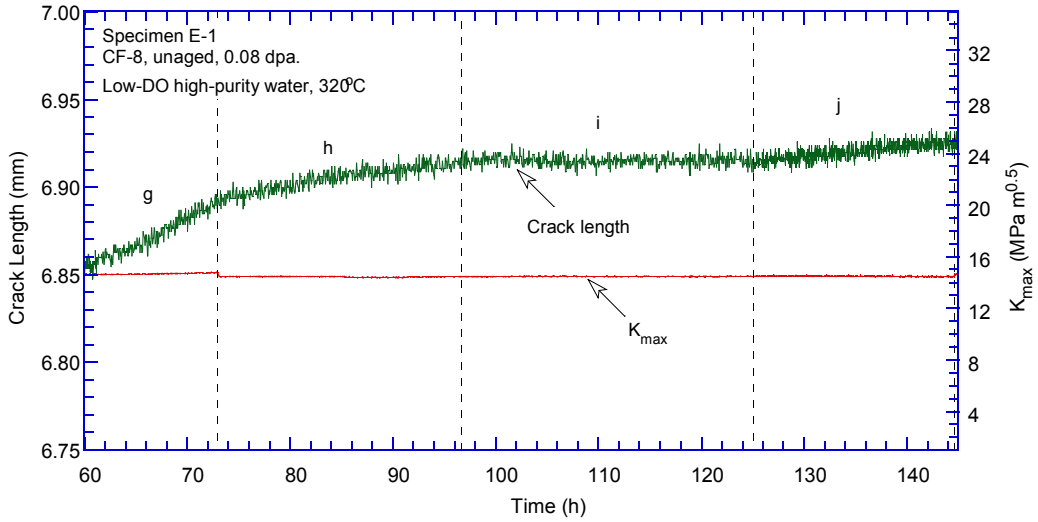


(d)

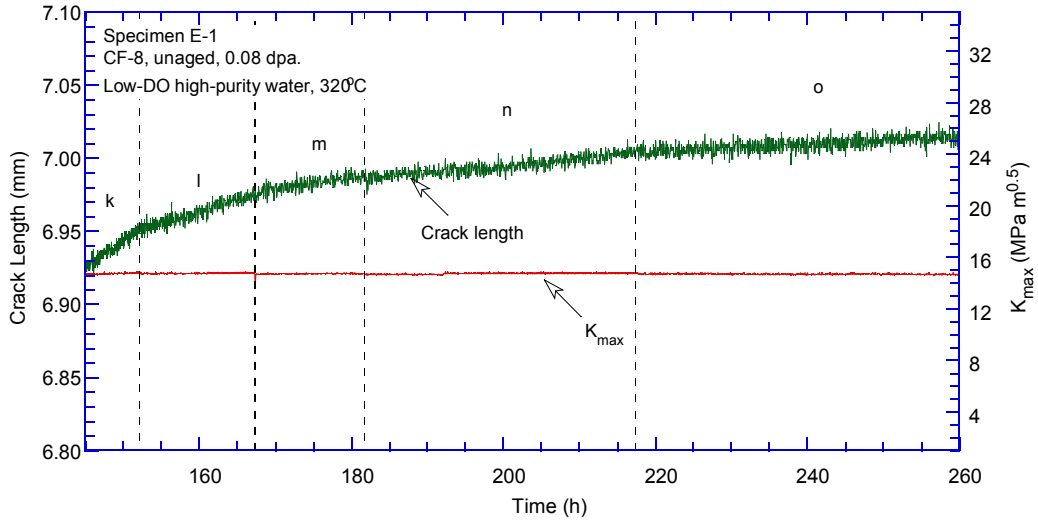


(e)

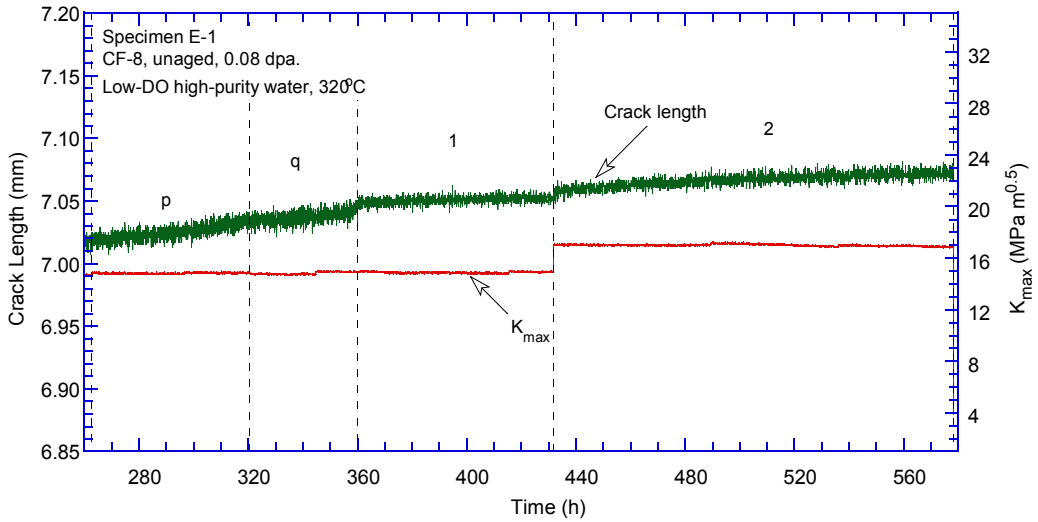


Figure 51. (Contd.)

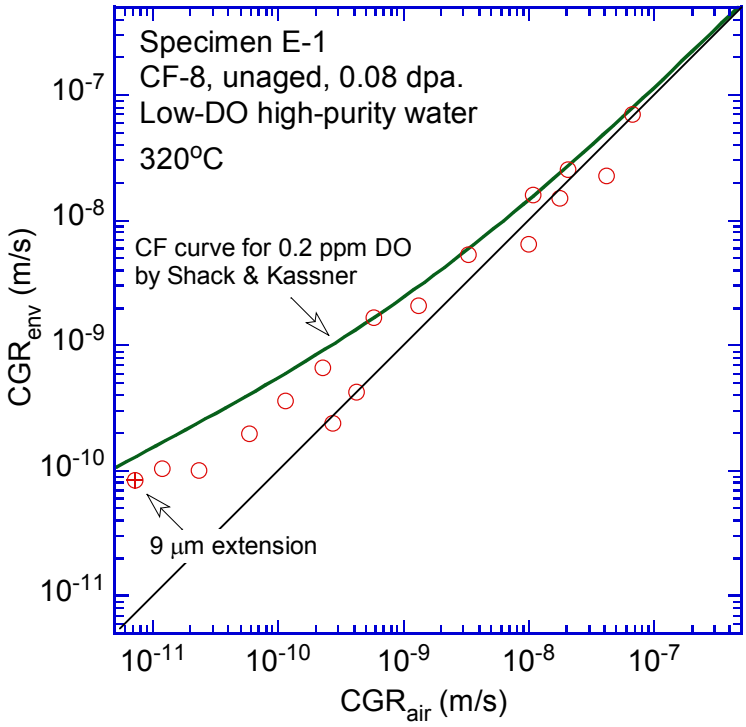


Figure 52. Cyclic CGRs of specimen E-1.

Following the pre-cracking, the test was set at constant load with PPU every 2 hr. The stress intensity factor was about 15 MPa $m^{1/2}$. A SCC CGR of 1.8 x $10^{-11}$ m/s was measured over a 10-μm crack extension. The stress intensity level was increased to ~17 MPa $m^{1/2}$ with PPU every 2 hr for another SCC CGR measurement. A CGR of 2.7 x $10^{-11}$ m/s was recorded over a 22-μm crack extension.

Fracture toughness J-R curve test

A fracture toughness J-R curve test was performed on the sample after the CGR test. The J-R data are plotted in Fig. 53, and a power-law fitting gives rise to a resistance curve of $J = 359\Delta a^{0.57}$. The J value at the 0.2-mm offset line is 183 kJ/$m^2$ for this sample. The crack extension was heavily curved in this sample, and the J-R curve data could not be validated per the ASTM standard. Four of the nine measurements of the final crack size were above the limit, and the $J_{max}$ requirement was also ignored in the analysis.

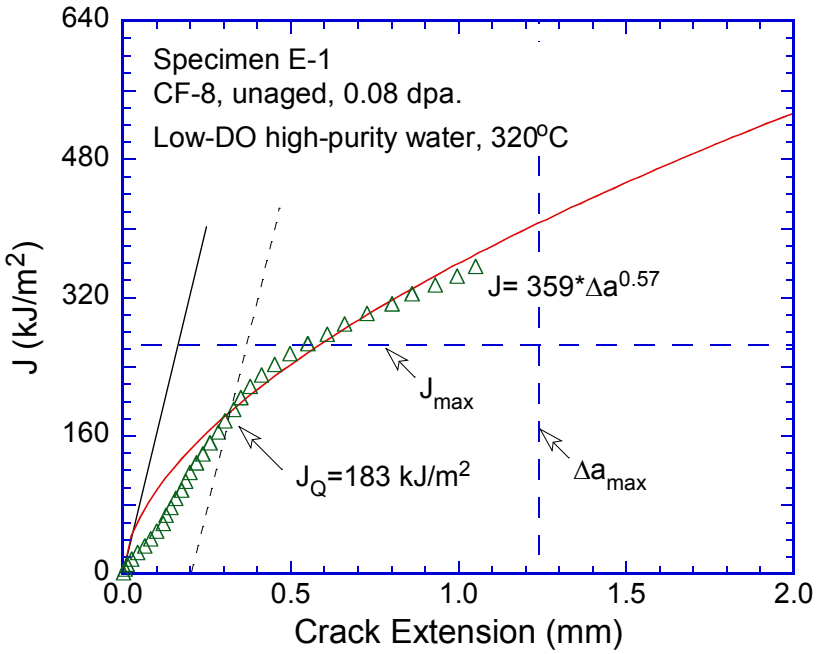


Figure 53. The J-R curve of specimen E-1.

Fractographic examination

Figure 54 shows the entire fracture surface of specimen E-1. Different stages of the test can be clearly identified. The CGR crack front is not straight, and the crack extension on the right side of the sample is significantly less. Transgranular cleavage-like cracking is the dominant morphology close to the machine notch in the pre-cracking region. As the CGR test progressed, casting microstructure became more evident. Vermicular ferrites at the cores of casting dendrites were clearly visible.

Figure 55 is an enlarged view of the fracture surface along the sample central line. Cleavage-like morphology dominates the fatigue pre-cracking region. Large deformation steps can be seen in the early stage of the test (Fig. 56). With the advance of the crack, the fracture surface became smoother, and deformation steps less pronounced. As shown in Fig. 57, deformation steps can still be seen in the austenite but are much less evident in the ferrite. At the end of the CGR test, the fracture surface became completely flat in both the ferrite and austenite (Fig. 58). Beyond the CGR test region, the fracture morphology changed to ductile dimples (Fig. 59), suggesting a heavy plastic deformation leading to a ductile fracture.

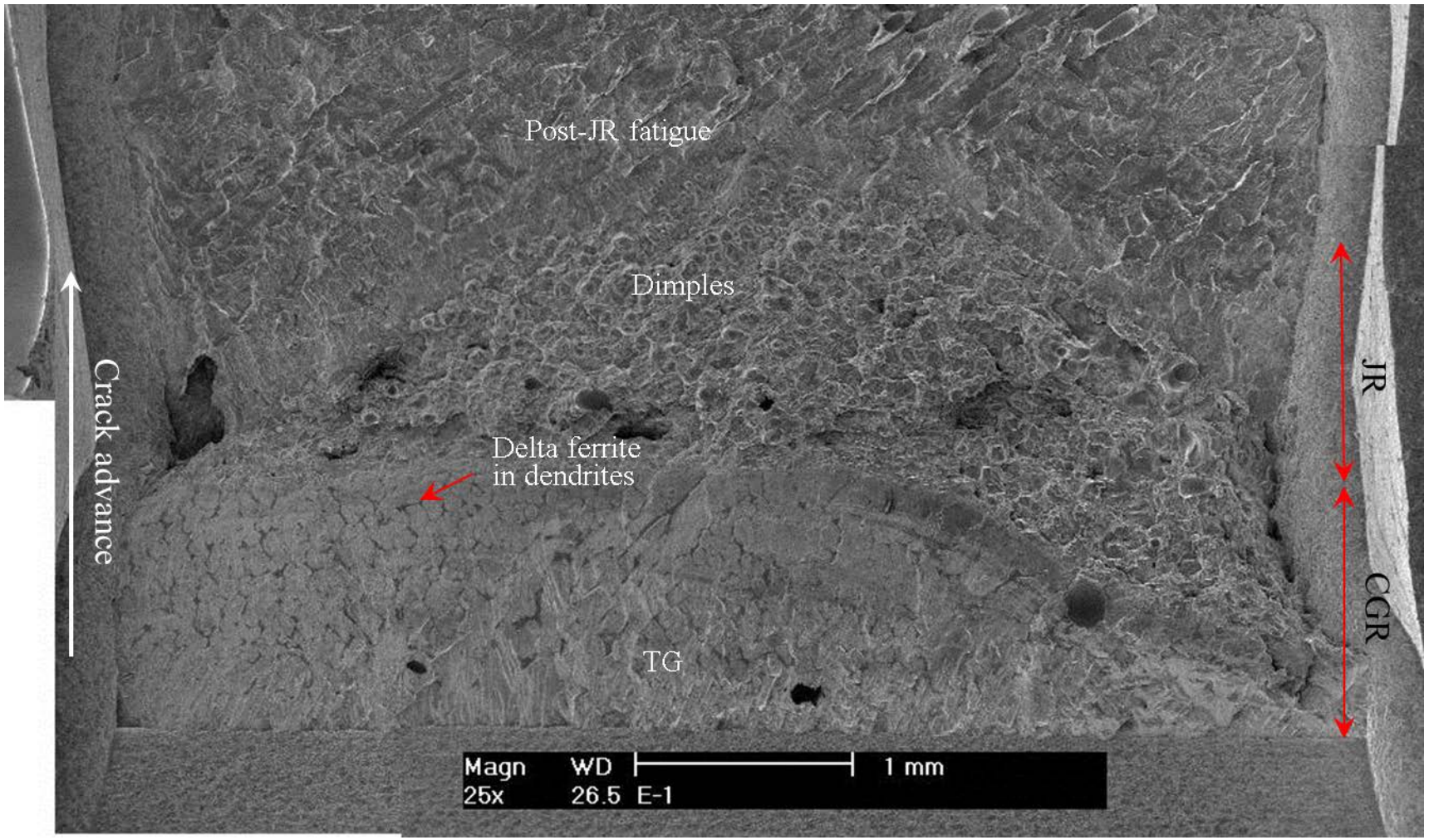


Figure 54. Fracture surface of specimen E-1 tested in low-DO high-purity water.

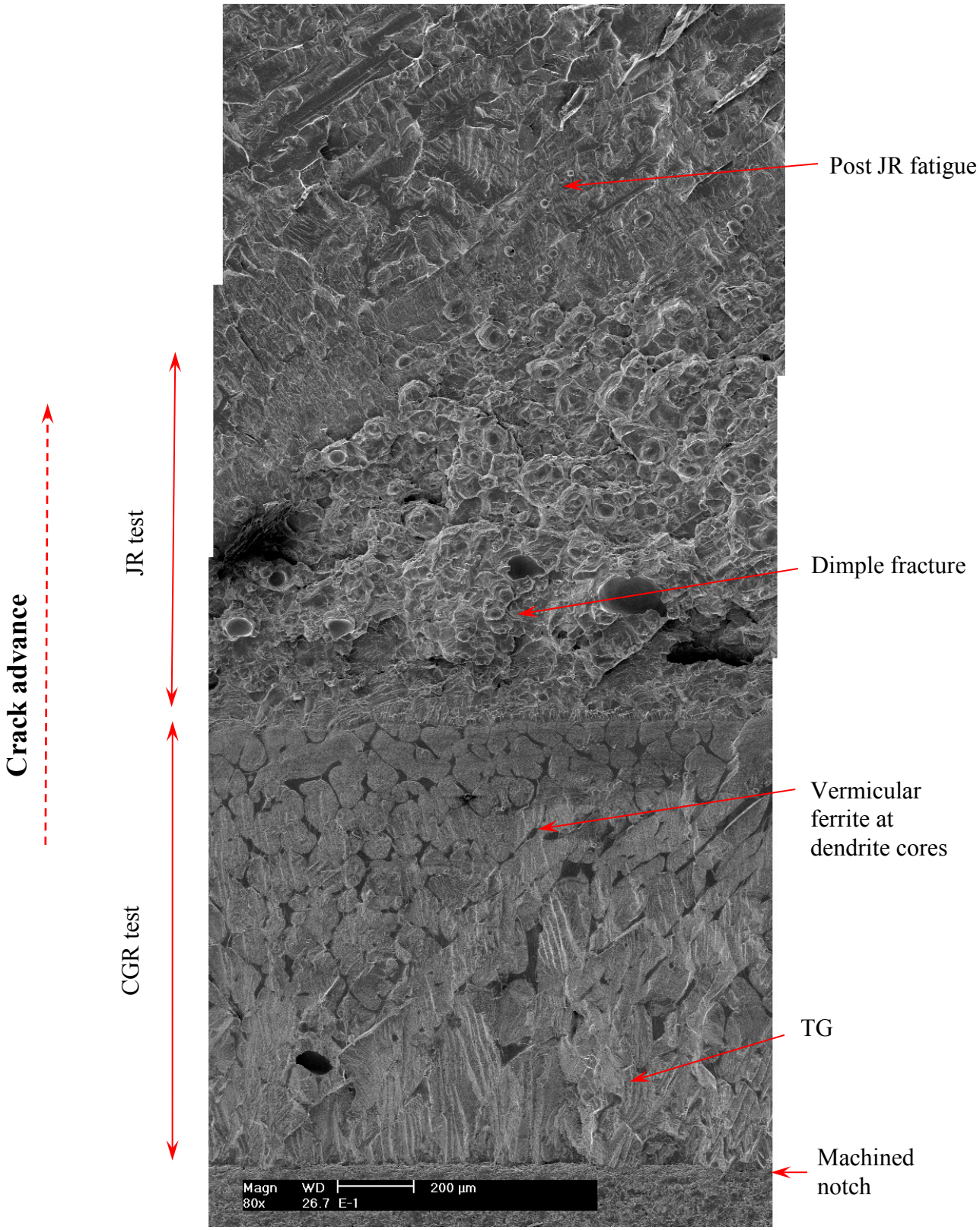


Figure 55. Fracture surface of specimen E-1 along the sample central line.

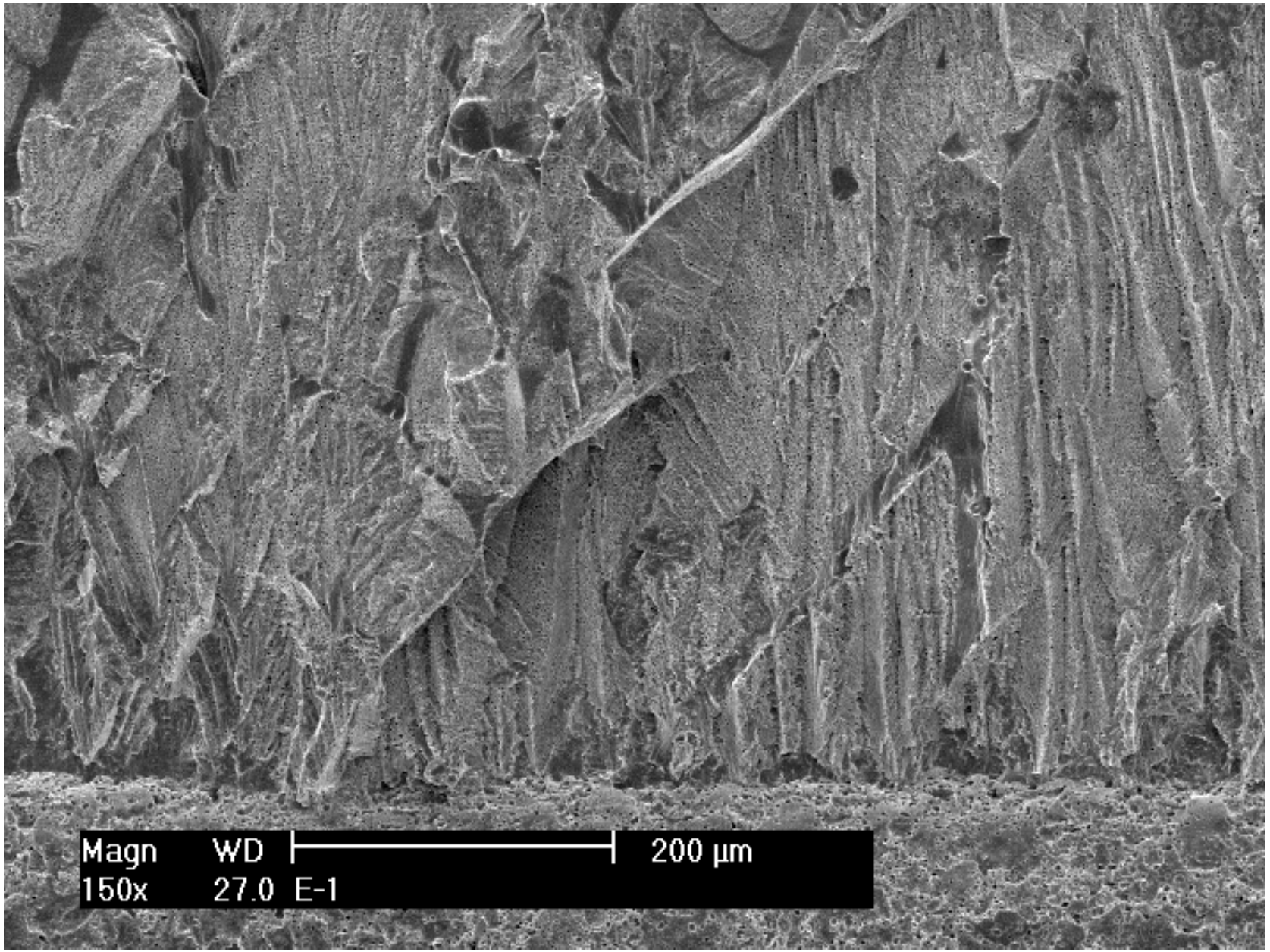


Figure 56. Cleavage-like cracking at the beginning of the CGR test of specimen E-1. Crack propagation from bottom to top.

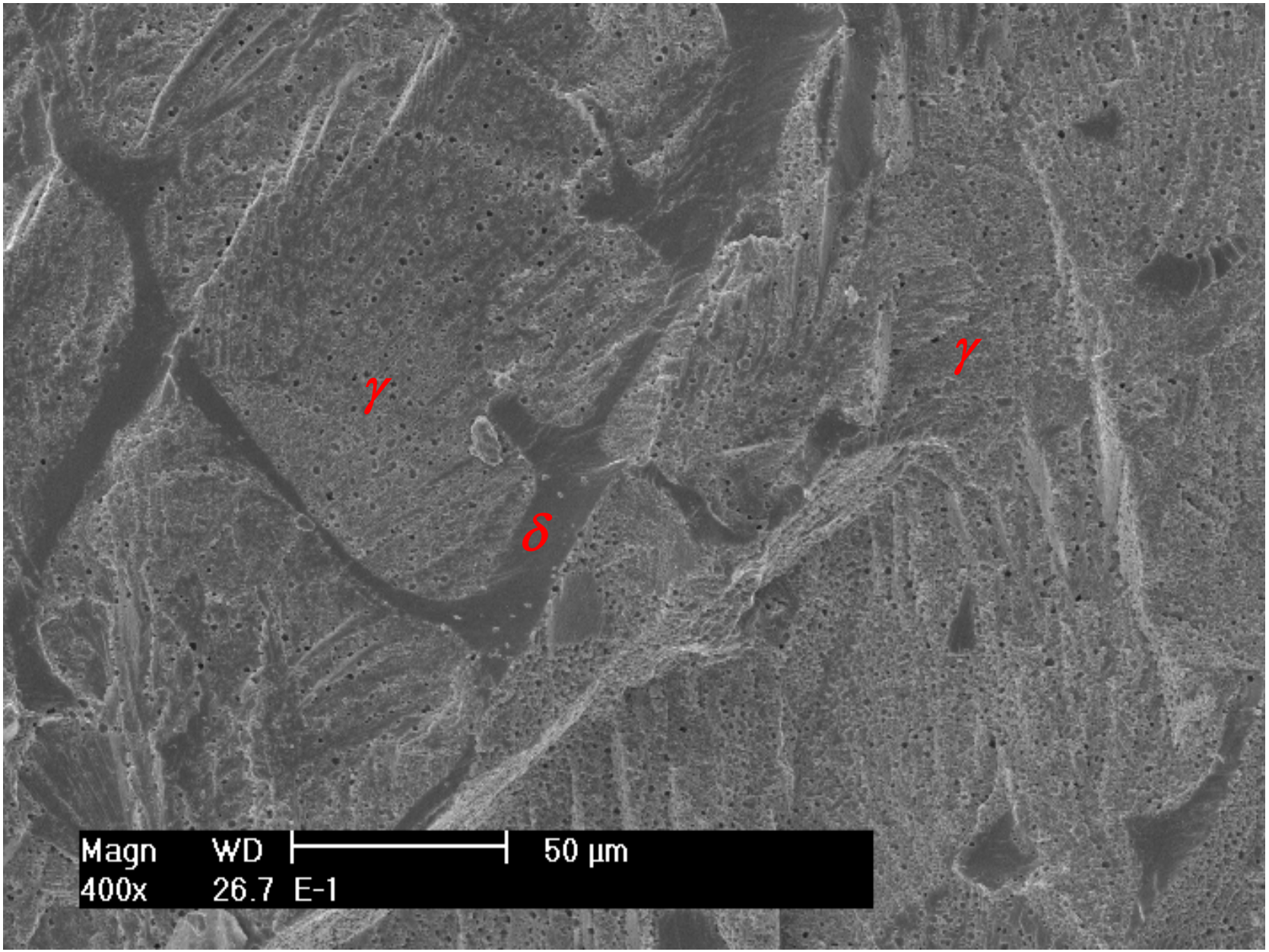


Figure 57. Cyclic CGR test region of specimen E-1. Crack propagation from bottom to top.

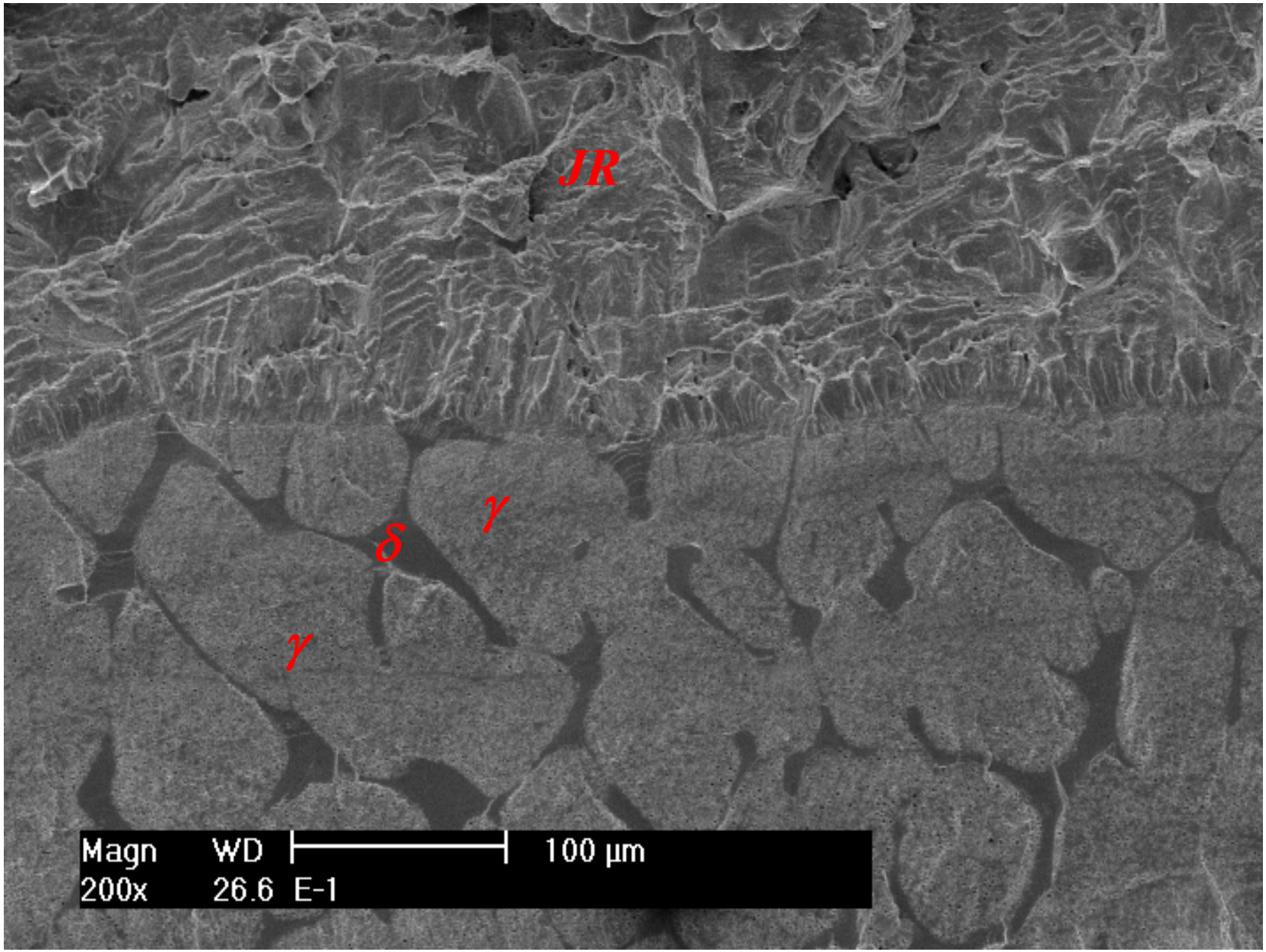


Figure 58. Smooth fracture surface at the end of the CGR test in specimen E-1. Crack propagation from bottom to top.

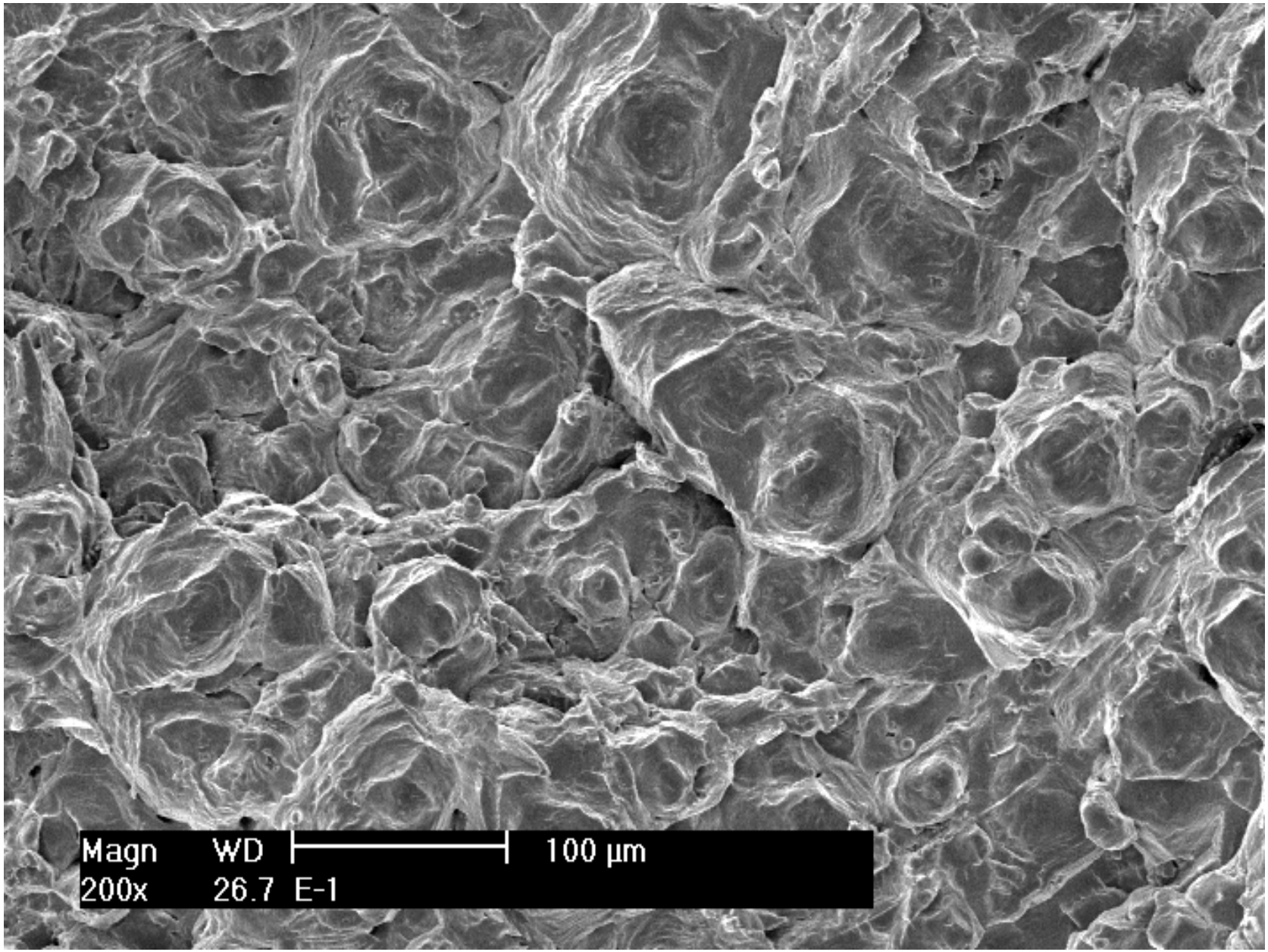


Figure 59. Ductile dimple fracture in the J-R test region of specimen E-1. Crack propagation from bottom to top.

*3.2.2 Thermally Aged CF-8 CASS*

*3.2.2.1 Unirradiated specimen F-N1 tested in low-DO high-purity water*

Crack growth rate test

Specimen F-N1 was an unirradiated control sample tested in low-DO high-purity water. The material was a thermally aged CF-8 with ~23% ferrite. The objective of the test was to compare it with the test of the irradiated thermally aged CF-8 CASS. The CGR test conditions and results of this sample are summarized in Table 11, and a crack-length history plot is shown in Fig. 60.

Fatigue precracking was started with a triangle waveform of 1 Hz and a load ratio of ~0.2 at a maximum stress intensity factor of ~15.5 MPa $m^{1/2}$. After an initial slow growth period, a CGR slightly below the fatigue growth rate in air was obtained. After about 200-μm crack extension, the load ratio and rise time were slowly increased to induce environmentally enhanced cracking. The environmental effect became evident in test period *n* with a load ratio of ~0.5. In the following test periods, the elevated CGR was stabilized with the further increases in rise time. Figure 61 shows all cyclic CGRs obtained from this sample along with the corrosion fatigue curve for SSs in high-purity water with 0.2 ppm DO. Similar to the unaged CF-8, the thermally aged CF-8 showed a good corrosion fatigue response in the low-DO high-purity water.

Table 11. Crack growth rates of specimen F-N1 (unirradiated, aged CF-8 with 23% δ ferrite) in a low-DO high-purity water environment.

| Test Period | Test time, h | Test Temp., °C | Load Ratio | Rise Time, s | Return Time, s | Hold Time, s | Kmax, MPa $m^{1/2}$ | ΔK, MPa $m^{1/2}$ | CGR in Env., m/s | CGR in Air m/s | Crack Length, mm |
|---|---|---|---|---|---|---|---|---|---|---|---|
| Start | 1.3 | | | | | | | | | | 5.983 |
| a [a] | 4.9 | 319 | 0.19 | 0.40 | 0.40 | 0.10 | 15.5 | 12.4 | 4.82E-08 | 5.13E-08 | 6.178 |
| b | 11.9 | 319 | 0.29 | 0.76 | 0.76 | 0.24 | 15.5 | 10.9 | 1.56E-08 | 1.97E-08 | 6.332 |
| c | 23.3 | 319 | 0.40 | 3.65 | 3.65 | 1.35 | 15.3 | 9.2 | 4.15E-10 | 2.63E-09 | 6.341 |
| d | 46.8 | 319 | 0.41 | 1.45 | 1.45 | 0.55 | 15.1 | 9.0 | 8.54E-11 | 6.10E-09 | 6.345 |
| e [a] | 51.4 | 319 | 0.35 | 0.75 | 0.75 | 0.25 | 15.5 | 10.1 | 1.16E-08 | 1.66E-08 | 6.385 |
| f | 54.5 | 319 | 0.40 | 1.46 | 1.46 | 0.54 | 15.5 | 9.3 | 3.19E-09 | 6.82E-09 | 6.398 |
| g | 73.8 | 319 | 0.40 | 3.63 | 1.45 | 1.37 | 15.3 | 9.2 | 3.66E-10 | 2.61E-09 | 6.415 |
| h | 98.5 | 319 | 0.40 | 7.27 | 1.45 | 2.73 | 15.4 | 9.2 | 1.72E-10 | 1.33E-09 | 6.423 |
| i | 119.2 | 318 | 0.40 | 3.64 | 1.45 | 1.36 | 15.9 | 9.5 | 2.45E-09 | 2.93E-09 | 6.514 |
| j | 142.6 | 319 | 0.40 | 7.25 | 1.45 | 2.75 | 16.1 | 9.7 | 1.68E-09 | 1.55E-09 | 6.604 |
| k | 171.8 | 319 | 0.45 | 14.2 | 3.54 | 5.85 | 16.3 | 9.0 | 5.53E-10 | 6.50E-10 | 6.645 |
| l | 195.3 | 319 | 0.50 | 41.3 | 8.27 | 18.7 | 16.3 | 8.2 | 2.41E-11 | 1.74E-10 | 6.647 |
| m [a] | 244.7 | 319 | 0.47 | 41.8 | 8.37 | 18.2 | 16.2 | 8.5 | 1.05E-10 | 1.93E-10 | 6.654 |
| n | 287 | 319 | 0.50 | 103.5 | 8.28 | 46.5 | 16.6 | 8.3 | 1.57E-10 | 7.27E-11 | 6.671 |
| o | 310.5 | 319 | 0.49 | 207.4 | 8.30 | 92.6 | 16.5 | 8.4 | 8.22E-11 | 3.70E-11 | 6.675 |
| p | 343.1 | 319 | 0.49 | 347.2 | 8.33 | 152.8 | 16.6 | 8.5 | 8.02E-11 | 2.33E-11 | 6.684 |
| q | 382.6 | 319 | 0.49 | 692.2 | 8.31 | 307.8 | 16.5 | 8.4 | 3.54E-11 | 1.13E-11 | 6.688 |
| 1a | 478.4 | 318 | 0.50 | 12 | 12 | 7200 | 16.5 | 8.3 | 1.23E-11 | 1.03E-12 | 6.696 |
| 1b | 621.5 | 319 | 1 | - | - | - | 16.5 | - | 1.17E-11 | - | 6.702 |

[a] The CGR value was obtained from the later part of the test period.

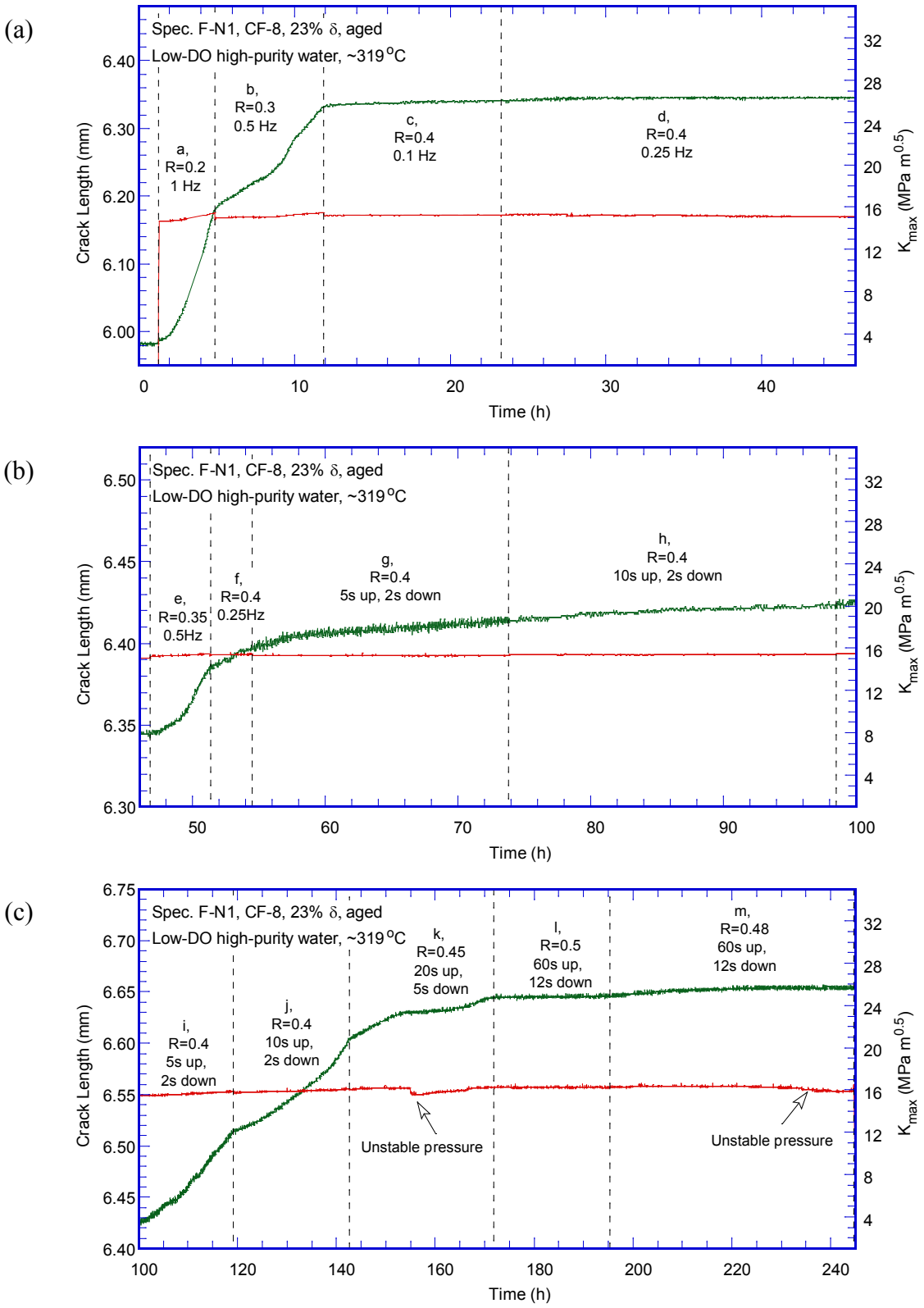


Figure 60. Crack-length-vs.-time plot for specimen F-N1 (unirradiated, aged CF-8 with 23% ferrite): test periods (a) a-d, (b) e-h, (c) i-m, (d) n-q, and (e) 1a-1b.

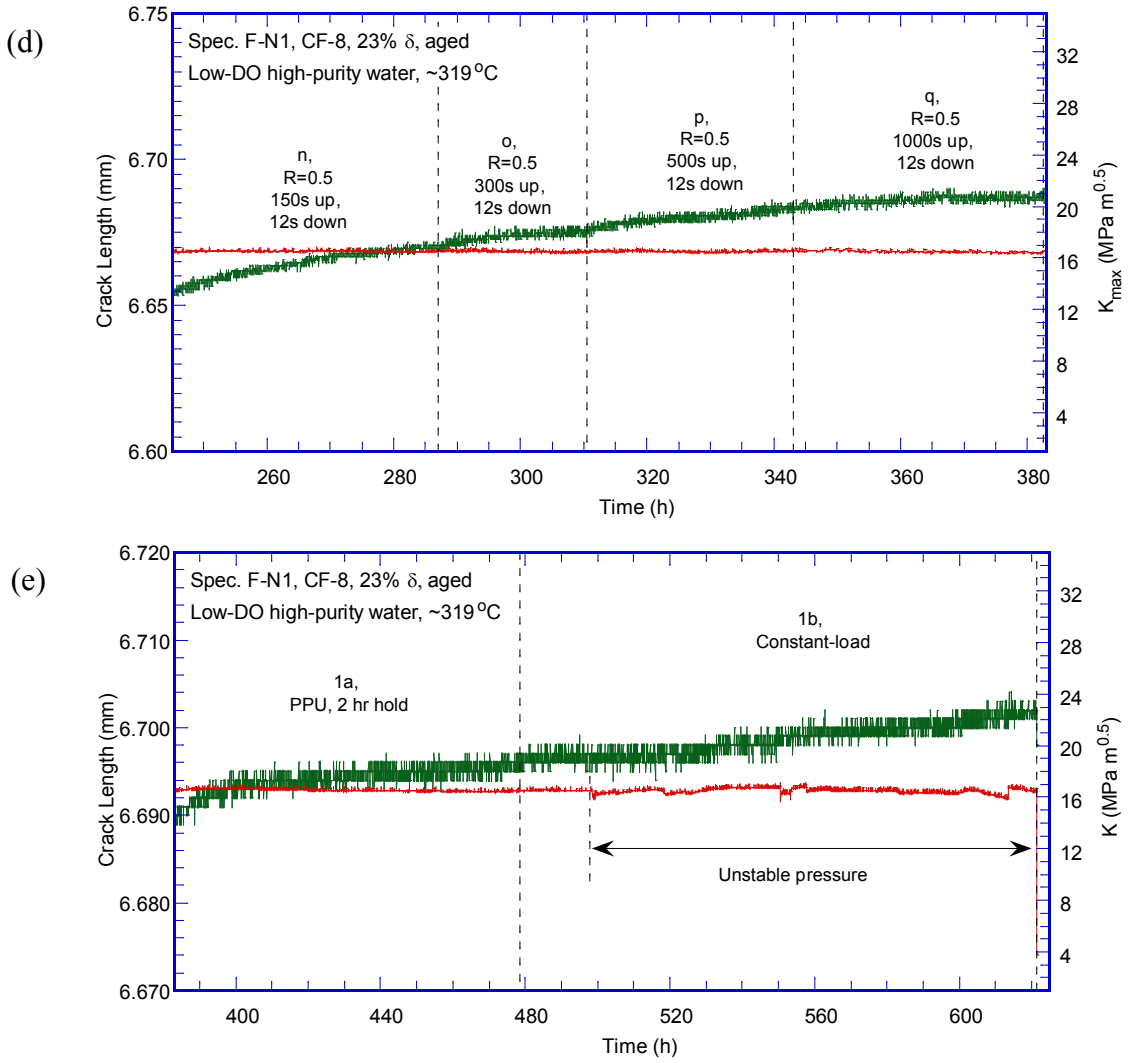


Figure 60. (Contd.)

After more than ~700-µm crack extension under cyclic loading, the test was transitioned to a constant load with PPU every 2 hr (test period *1a*). Under this condition, a CGR of $1.2 \times 10^{-11}$ m/s was obtained at ~16.5 MPa $m^{1/2}$ after an initial short period of rapid growth. Next, the PPU was removed, and the test was held at a near constant-K condition (~16.5 MPa $m^{1/2}$) for a total of ~140 hr (test period *1b*). Unlike the other tests conducted under low-corrosion-potential environments, the measured CGRs with and without PPU were almost identical in this test. This growth rate under a constant K was unexpectedly high, suggesting a dynamic loading condition during this test period. Note that the autoclave pressure was unstable during the test period *1b* and several large pressure drops (>60 psig) were detected. Consequently, the applied stress intensity factor fluctuated in this test period (as shown in Fig. 60e). This dynamic loading condition may be responsible for the relatively high SCC CGR observed in this sample.

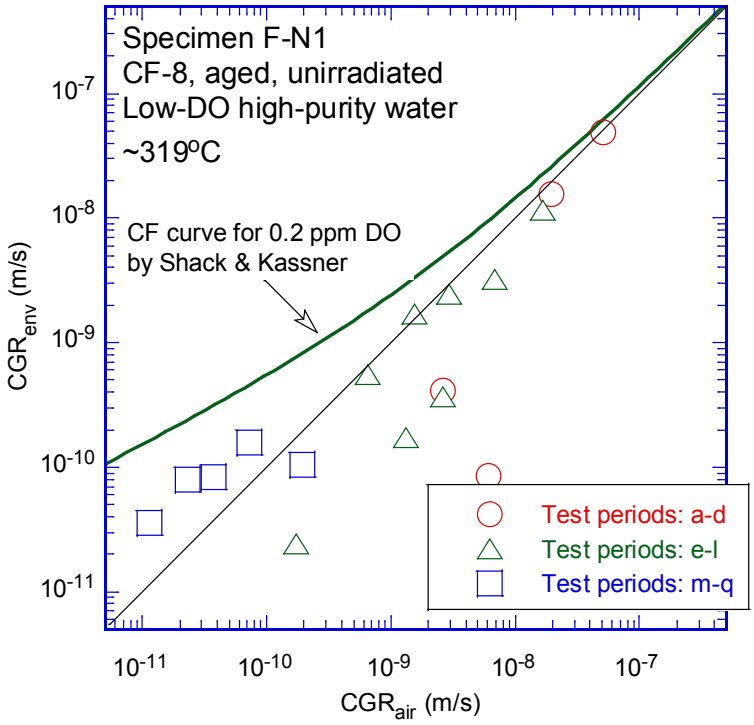


Figure 61. Cyclic CGRs of specimen F-N1.

Fracture toughness J-R curve test

After the CGR test, a fracture toughness J-R curve test was performed on the sample in the same low-DO high-purity water environment. The test was conducted with a constant extension rate of 0.43 μm/s. During the test, the loading was interrupted periodically to measure the crack extension by DCPD. The obtained J-R curve is shown in Fig. 62. The estimated J value at the 0.2-mm offset line is about 220 kJ/m$^2$. This fracture toughness value is significantly lower than that of the unaged CF-8, suggesting a strong thermal aging effect in this sample. Note that the J-R curve data cannot be validated for this test since the requirements of the crack front straightness and $J_{max}$ were violated.

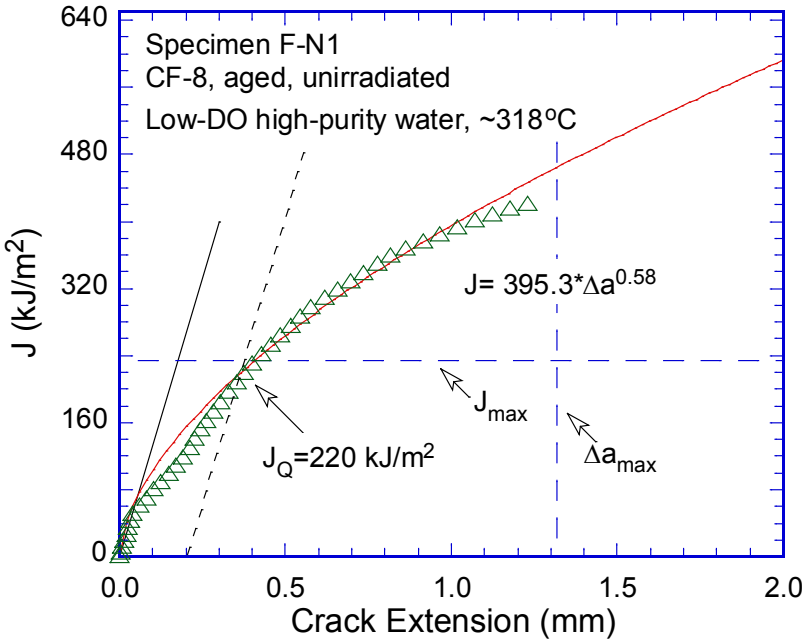


Figure 62. The J-R curve of specimen F-N1.

Fractographic examination

The tested sample was broken open under cyclic loading at room temperature in air. Figure 63 shows the entire fracture surface of the CGR and JR tests. The crack front of the CGR test was quite straight, indicating a well-controlled test condition. While the fracture surface of the CGR test region shows a TG morphology, the failure mode of the JR test region is ductile. More details of the fracture morphologies can be seen in Fig. 64 along the sample central line. At the beginning of the precracking, heavy deformation ledges resulting from fatigue loading can be seen on the fracture surface (Fig. 65a). As the crack advances deeper and environmental enhancement starts to appear, the fracture surface becomes flat. At the end of the CGR test, most δ ferrites appear to fracture in a brittle fashion with little plastic deformation (Fig. 65b). Figure 66 shows the details of the transition area from the CGR to JR tests. Some brittle morphology can be seen at the very beginning of the JR test. Beyond the initial 30-50 μm, the crack advances in a ductile tearing mode, and ductile dimples resulting from microvoid coalescence become the dominant morphology (Fig. 67).

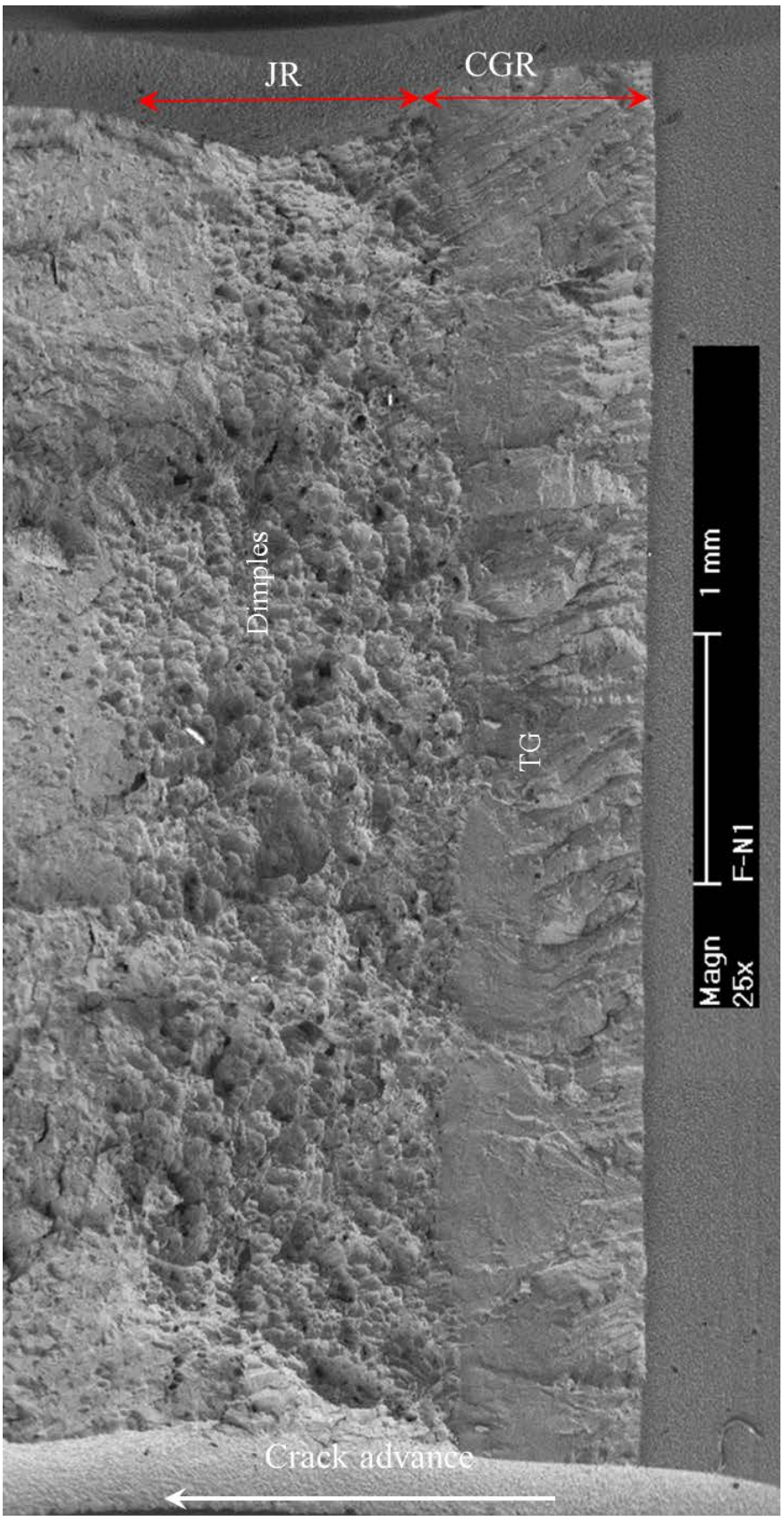


Figure 63. Fracture surface of specimen F-N1 tested in low-DO high-purity water.

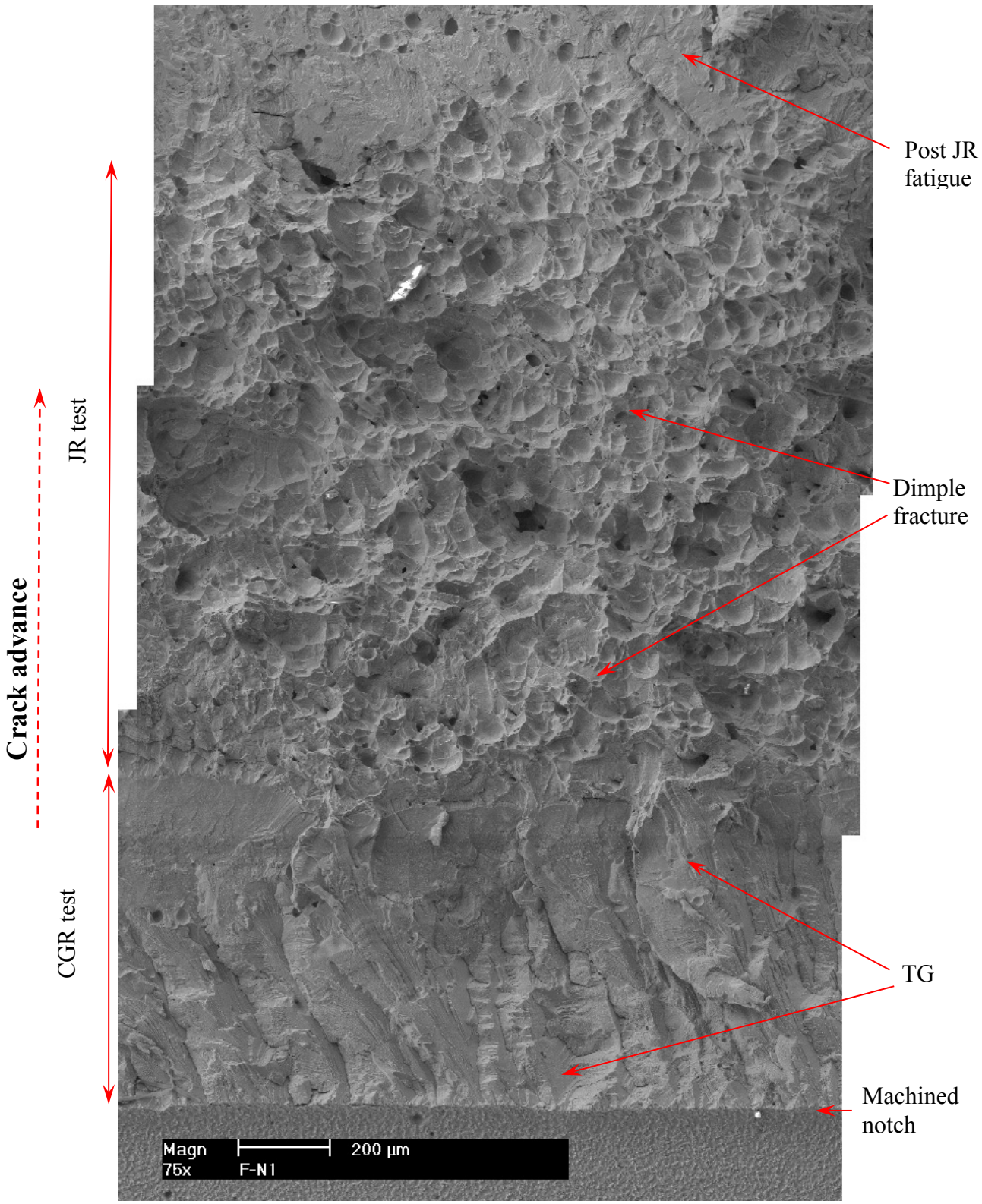


Figure 64. Fracture surface of specimen F-N1 along the sample central line.

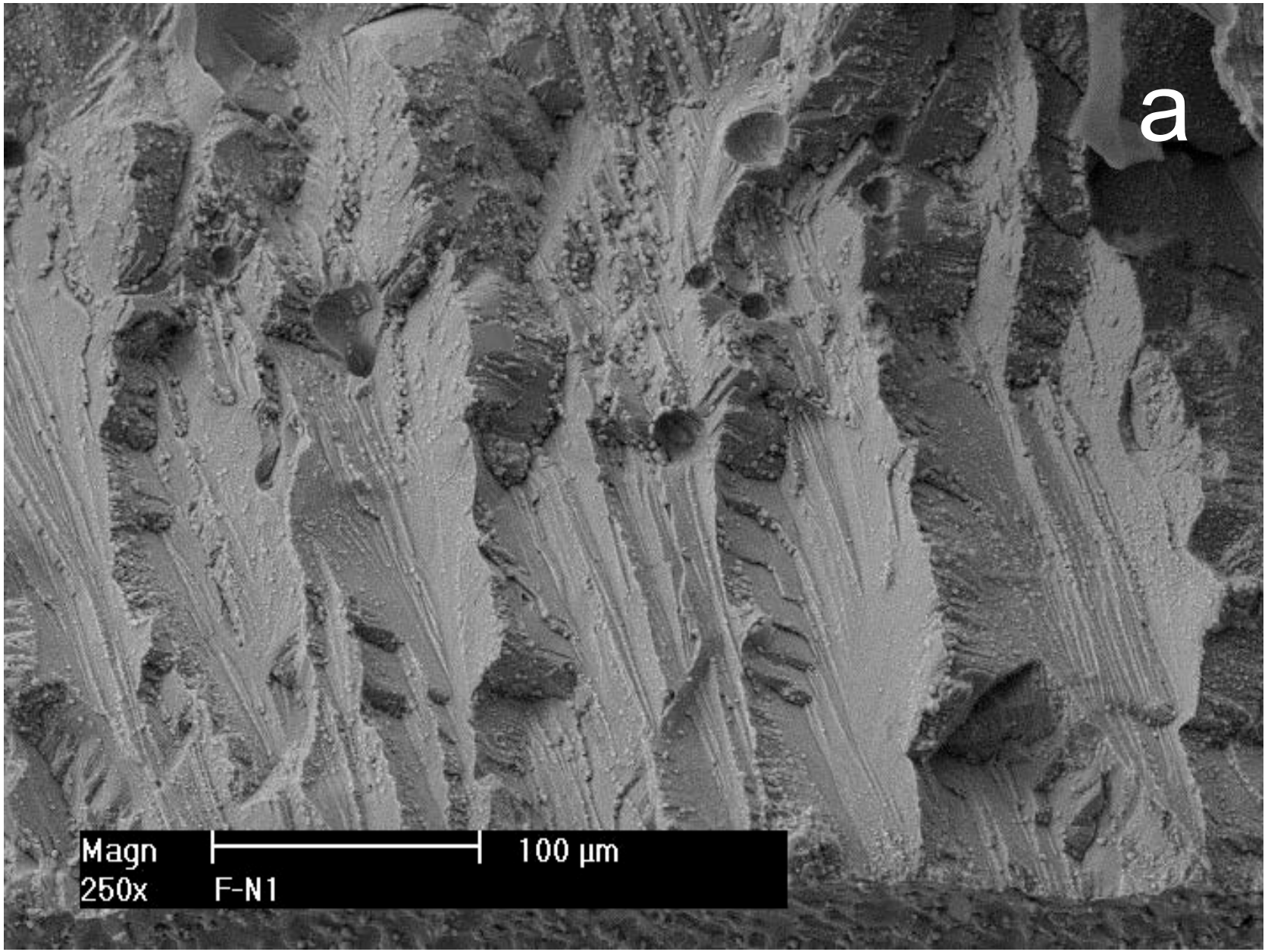


Figure 65. Transgranular fracture in the CGR test of specimen F-N1: (a) in the precracking region and (b) at the end of CGR test. Crack advance direction from bottom to top.

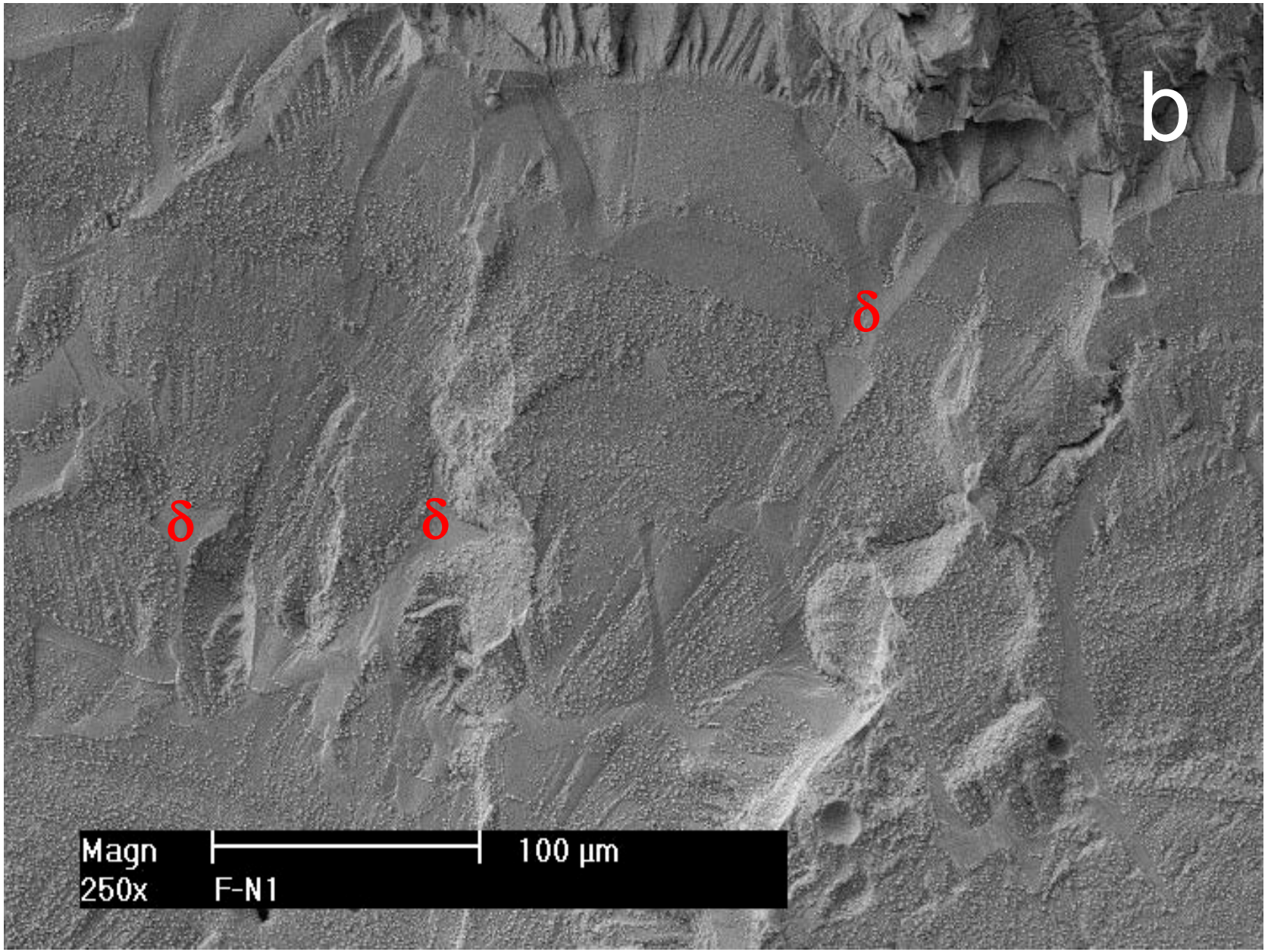


Figure 65. (Contd.)

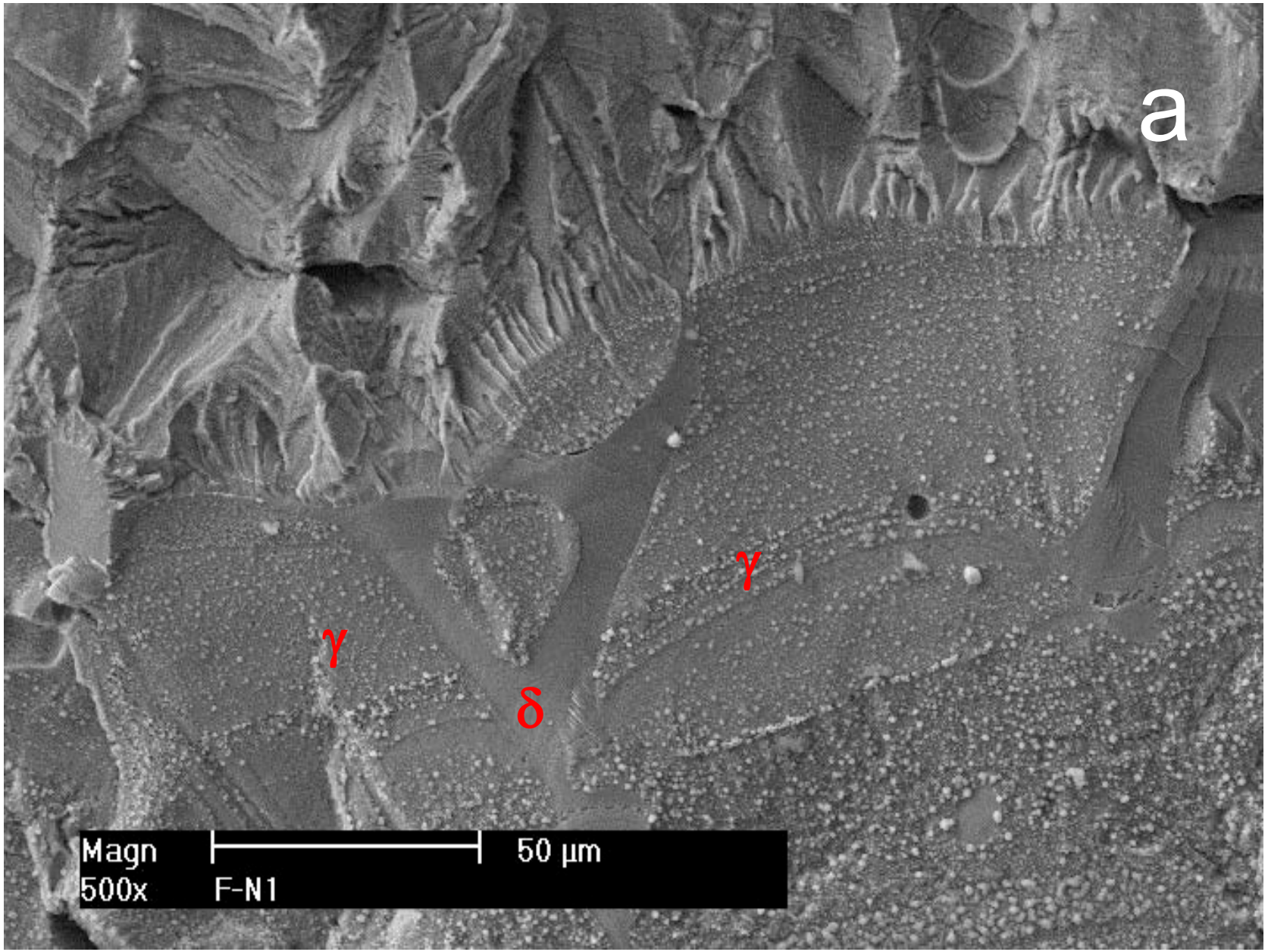


Figure 66. Transition region from CGR to J-R curve tests of specimen F-N1. Crack advance direction from bottom to top.

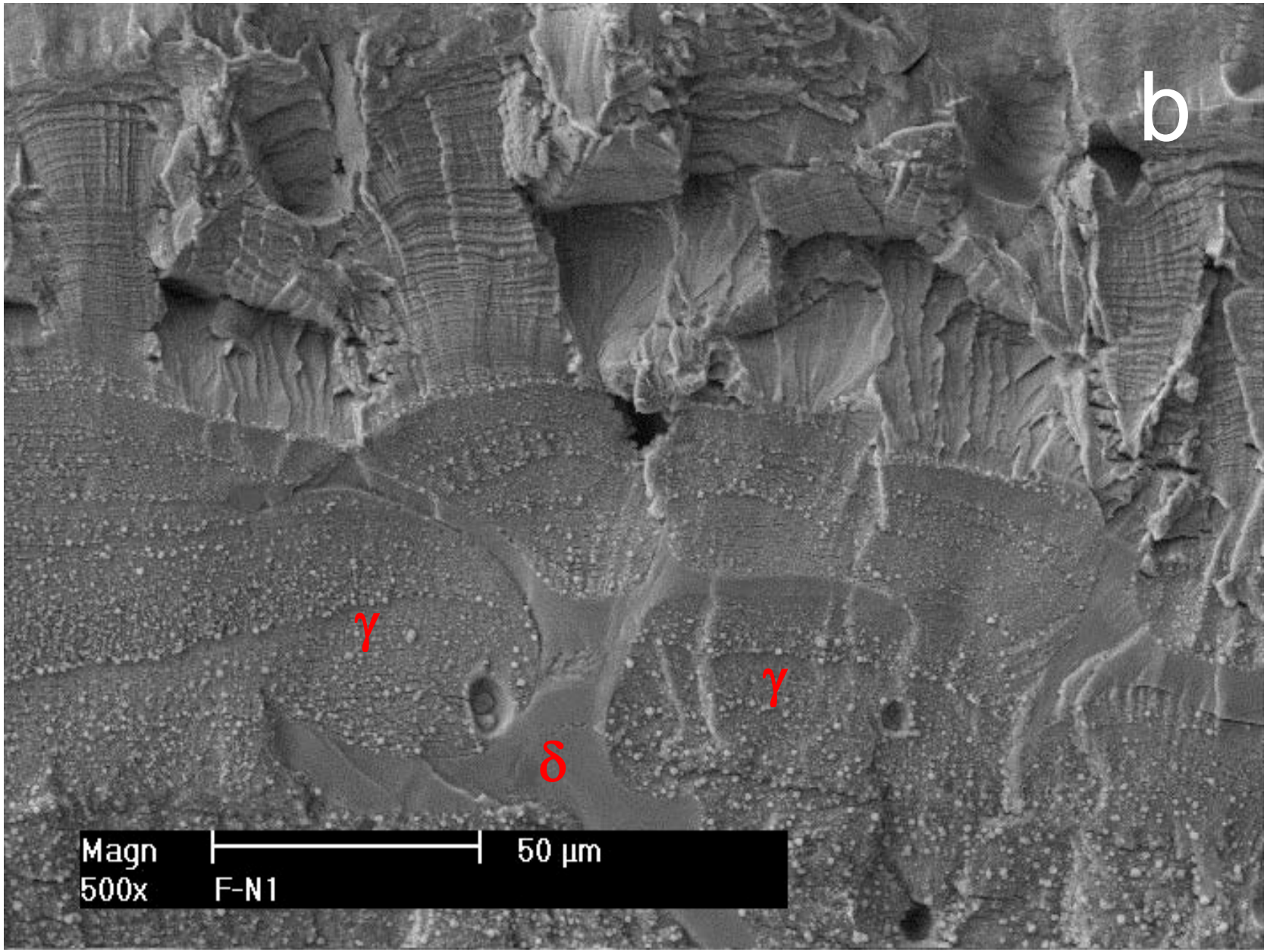


Figure 66. (Contd.)

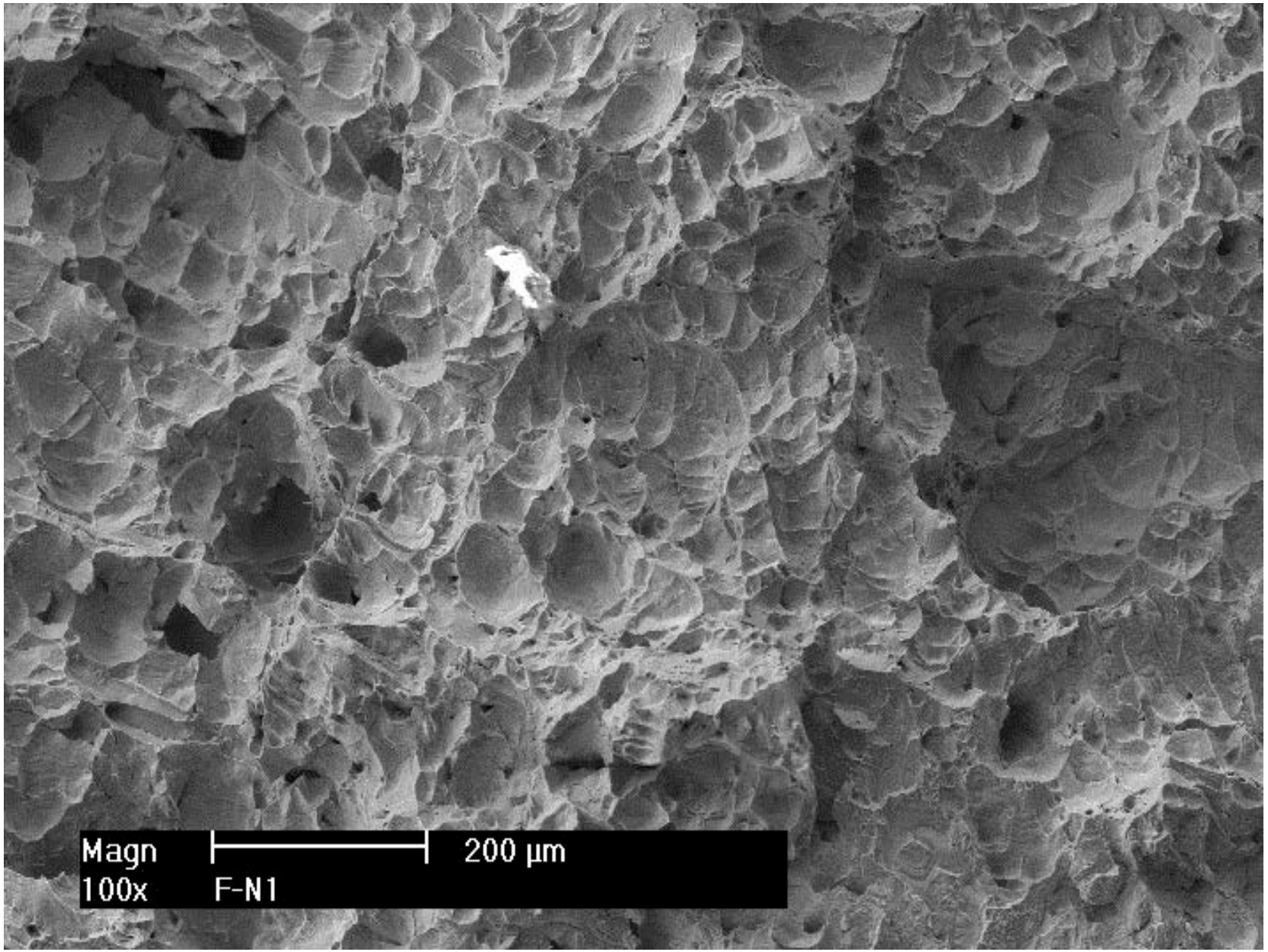


Figure 67. Ductile dimple fracture in the JR test region of specimen F-N1. Crack advance direction from bottom to top.

*3.2.2.2 Irradiated specimen F-1 tested in low-DO high-purity water*

Crack growth rate test

Specimen F-1 was a CF-8 CASS with 23% ferrite cut from the same heat as specimen E-1 (Heat 68). The specimen was thermally aged at 400°C for 10,000 hr prior to irradiation. This specimen was also tested in low-DO high-purity water at 320°C. The CGR test conditions and results are summarized in Table 12, and a crack-length history plot is shown in Fig. 68.

The test was started with fatigue pre-cracking at a maximum stress intensity factor of ~17 MPa $m^{1/2}$, load ratio of 0.2, and frequency of 1 Hz. Using a triangular waveform, the crack was advanced for about 500 μm with gradually increased load ratio. After a saw-tooth waveform was introduced in test period *g*, environmentally enhanced cracking started to appear. In the following test periods, the maximum stress intensity factor was maintained at ~16 MPa $m^{1/2}$ while the load ratio and rise time were gradually increased. A significant degree of environmental enhancement was readily established in this sample, similar to that observed in unaged CF-8 (specimen E-1). By the end of the cyclic CGR test, the measured CGR in water was about a factor of seven higher than that of the fatigue growth rate. All cyclic CGRs obtained from this sample are plotted in Fig. 69. The corrosion fatigue curve for unirradiated SSs still bounds the data points of the aged CF-8 CASS.

After the cyclic CGR test, the test was set at constant load with PPU every 2 hr. A SCC CGR of 2.69 x $10^{-11}$ m/s was measured at a stress intensity factor of 16 MPa $m^{1/2}$ (Fig. 70). This growth rate is about a factor of three lower than the NUREG-0313 curve, and is very similar to that obtained from the unaged CF-8 CASS (specimen E-1).

Table 12. Crack growth rates of specimen F-1 (0.08-dpa aged CF-8 with 23% δ ferrite) in a low-DO high-purity water environment.

| Test Period | Test time, h | Test Temp., °C | Load Ratio | Rise Time, s | Return Time, s | Hold Time, s | Kmax, MPa $m^{1/2}$ | ΔK, MPa $m^{1/2}$ | CGR in Env., m/s | CGR in Air m/s | Crack Length, mm |
|---|---|---|---|---|---|---|---|---|---|---|---|
| Start | 0.4 | | | | | | | | | | 6.038 |
| a | 2.0 | 319 | 0.20 | 0.45 | 0.45 | 0.05 | 17.3 | 13.8 | 6.84E-08 | 6.51E-08 | 6.196 |
| b | 3.9 | 319 | 0.30 | 0.44 | 0.44 | 0.06 | 16.4 | 11.4 | 4.28E-08 | 4.04E-08 | 6.323 |
| c | 5.7 | 319 | 0.40 | 0.42 | 0.42 | 0.08 | 15.4 | 9.2 | 1.11E-08 | 2.29E-08 | 6.358 |
| d | 8.2 | 319 | 0.40 | 0.84 | 0.84 | 0.16 | 15.4 | 9.3 | 6.40E-09 | 1.16E-08 | 6.382 |
| e | 11.7 | 319 | 0.35 | 0.85 | 0.85 | 0.15 | 15.6 | 10.1 | 1.13E-08 | 1.46E-08 | 6.440 |
| f | 24.2 | 319 | 0.35 | 4.25 | 4.25 | 0.75 | 15.6 | 10.1 | 3.20E-09 | 2.94E-09 | 6.505 |
| g | 36.7 | 319 | 0.35 | 10.2 | 4.25 | 1.81 | 15.7 | 10.2 | 2.06E-09 | 1.25E-09 | 6.561 |
| h | 49.4 | 319 | 0.40 | 16.8 | 4.19 | 3.25 | 15.6 | 9.4 | 1.36E-09 | 6.18E-10 | 6.601 |
| i | 76.8 | 319 | 0.39 | 33.5 | 10.05 | 6.5 | 15.8 | 9.6 | 7.62E-10 | 3.22E-10 | 6.650 |
| j | 120.9 | 319 | 0.39 | 83.6 | 10.04 | 16.4 | 15.7 | 9.6 | 3.05E-10 | 1.30E-10 | 6.685 |
| k | 168 | 319 | 0.44 | 247.6 | 9.91 | 52.4 | 15.8 | 8.9 | 1.69E-10 | 3.64E-11 | 6.708 |
| l | 224 | 319 | 0.44 | 495.0 | 9.90 | 105.0 | 16.0 | 8.9 | 8.94E-11 | 1.84E-11 | 6.723 |
| m | 290.3 | 320 | 0.44 | 824.9 | 9.90 | 175.1 | 16.0 | 9.0 | 7.17E-11 | 1.11E-11 | 6.735 |
| l | 359.3 | 318 | 0.45 | 12 | 12 | 7200 | 16.0 | 8.8 | 2.69E-11 | 1.20E-12 | 6.749 |

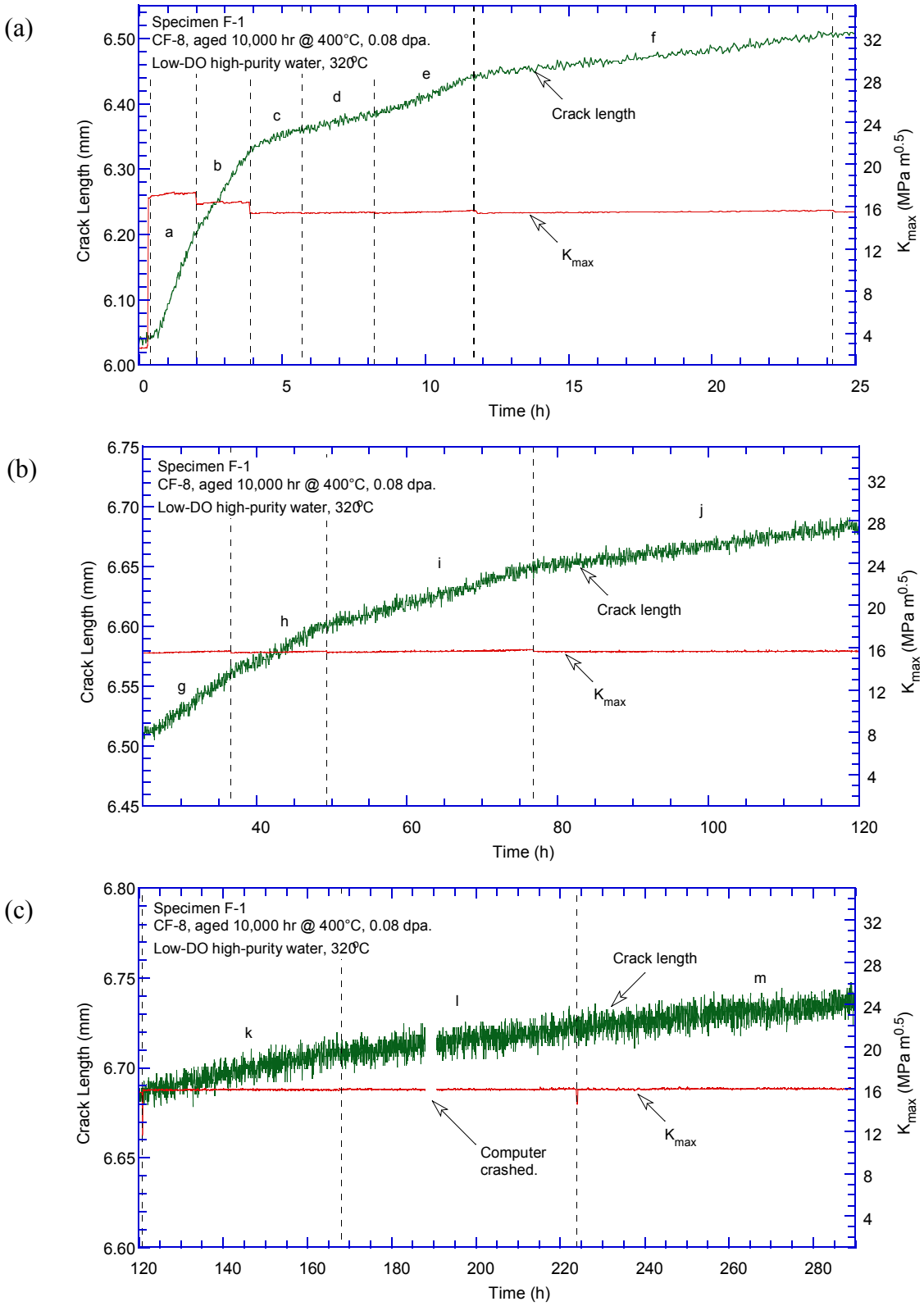


Figure 68. Crack-length-vs.-time plot for specimen F-1 (0.08-dpa aged CF-8 with 23% ferrite): test periods (a) a-f, (b) g-j, (c) k-m, and (d) 1.

(d)

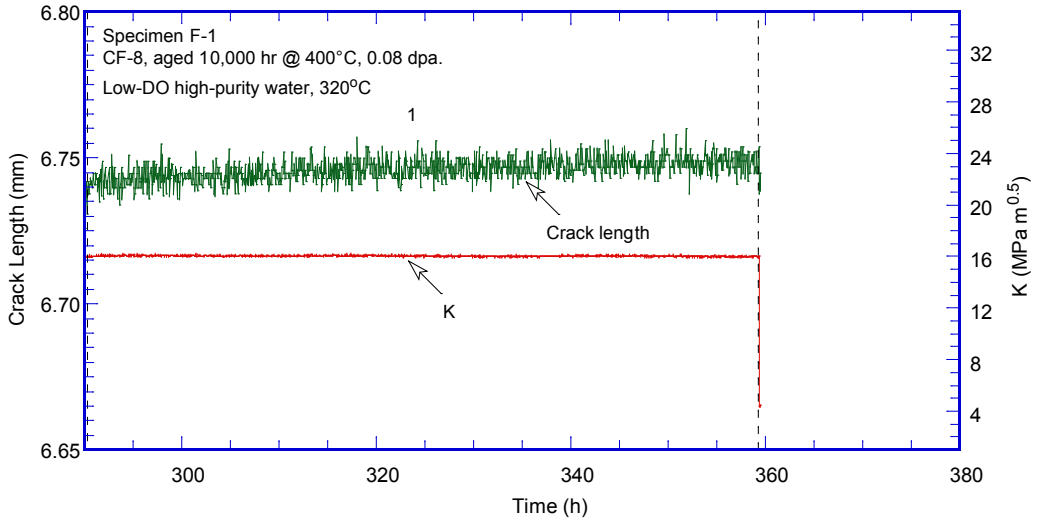


Figure 68. (Contd.)

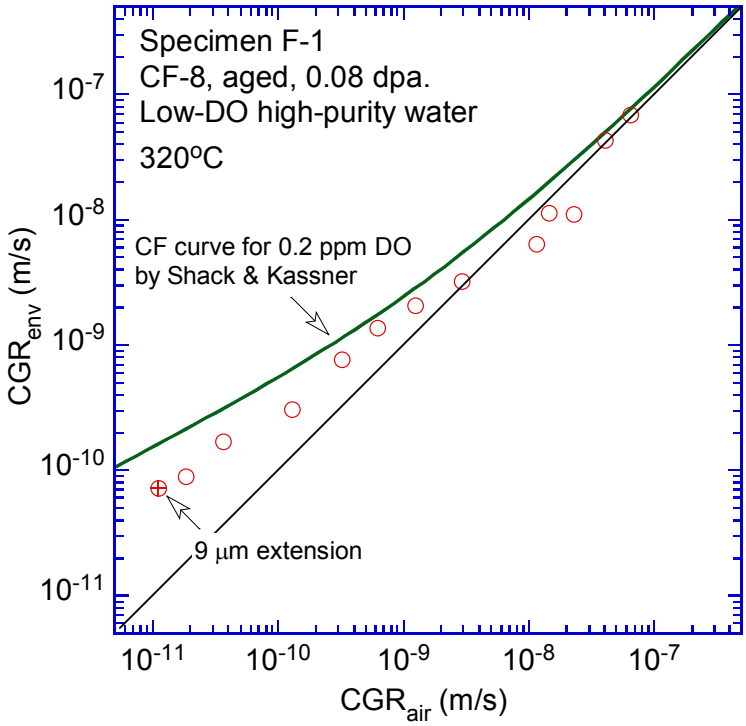


Figure 69. Cyclic CGRs of specimen F-1.

Fracture toughness J-R curve test

Following the CGR test, a fracture toughness J-R curve test was performed on the same sample in the test environment. Figure 71 shows the obtained data, and a power-law fitting gives rise to a J-R curve of $J = 372\Delta a^{0.62}$. The estimated J value at the 0.2-mm offset line is 171 kJ/m$^2$. Note that the J-R curve data cannot be validated because one of the nine measurements of the final

crack size did not meet the requirements. Some J values used in the analysis were also above the limit for this sample.

Fractographic examination

Replicas of the fracture surface of specimen F-1 were examined with SEM. As shown in Figs. 72 and 73, transgranular cleavage-like cracking is the main fracture mode during the pre-cracking stage. Deformation steps are clearly visible next to the machine notch. As the crack advances, the fracture surface became increasingly smoother, suggesting the crack had propagated in a progressively more brittle fashion (Fig. 74). Also, as shown in Fig. 75, deformation steps seem to develop in the austenitic phase surrounding the ferritic phase at dendrite cores. Deformation ledges are seen less often within the ferrite. Finally, after the CGR test, the fracture surface became completely ductile. The sample was fractured by ductile tearing in the J-R curve test (Fig. 76).

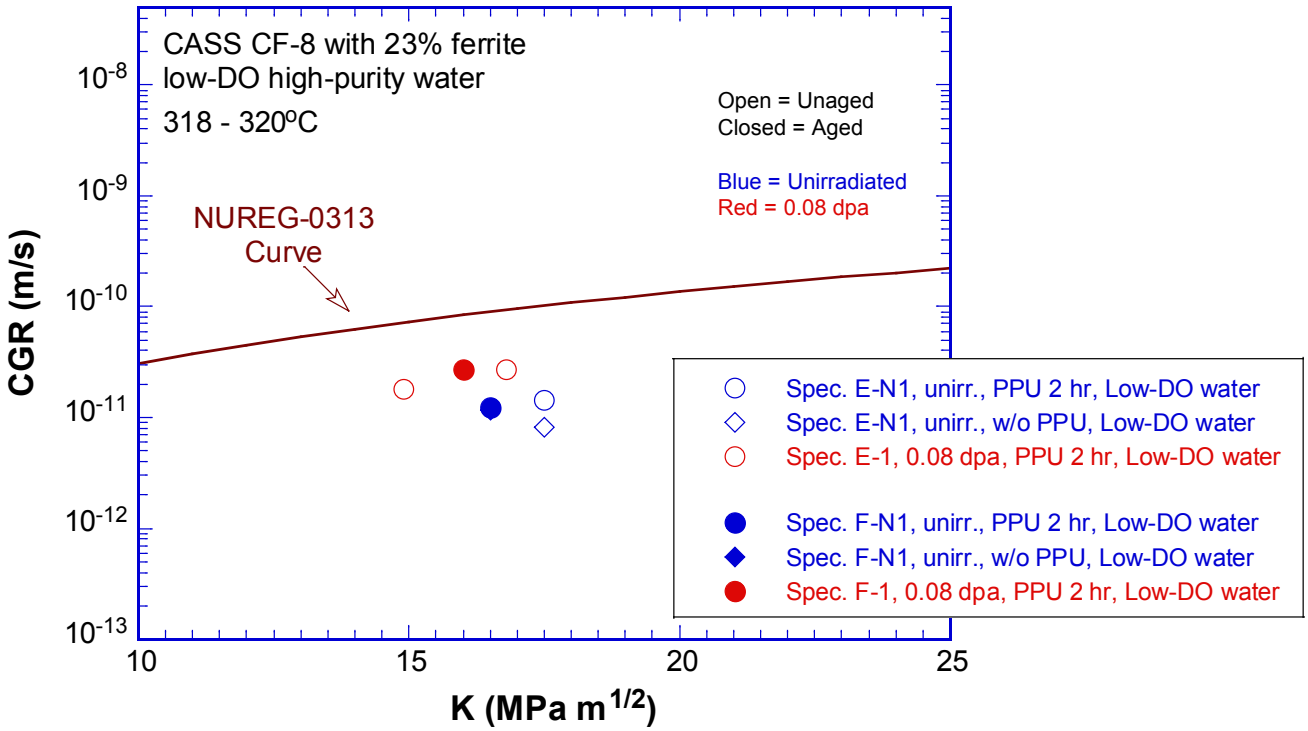


Figure 70. SCC CGRs of unaged and aged CF-8 CASS with 23% ferrite.

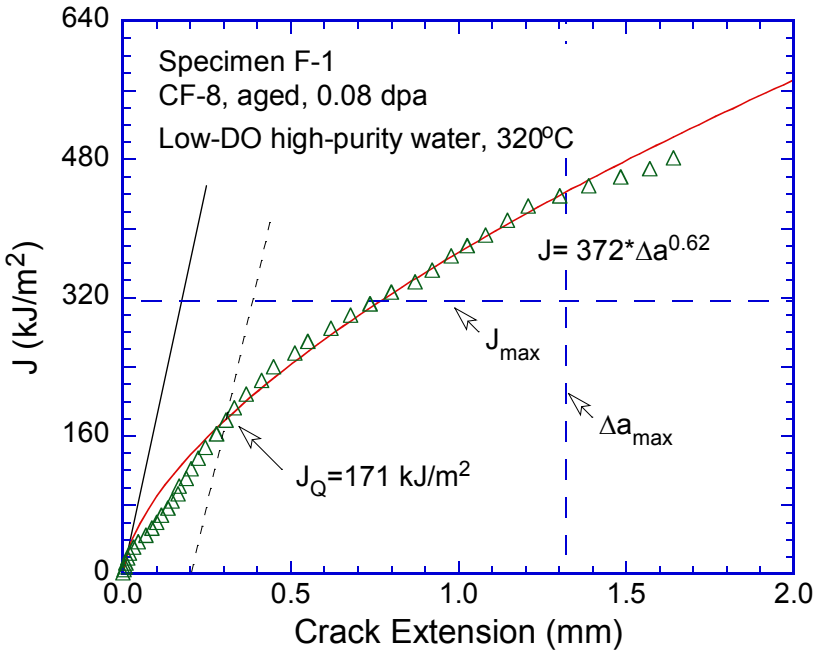


Figure 71. The J-R curve of specimen F-1.

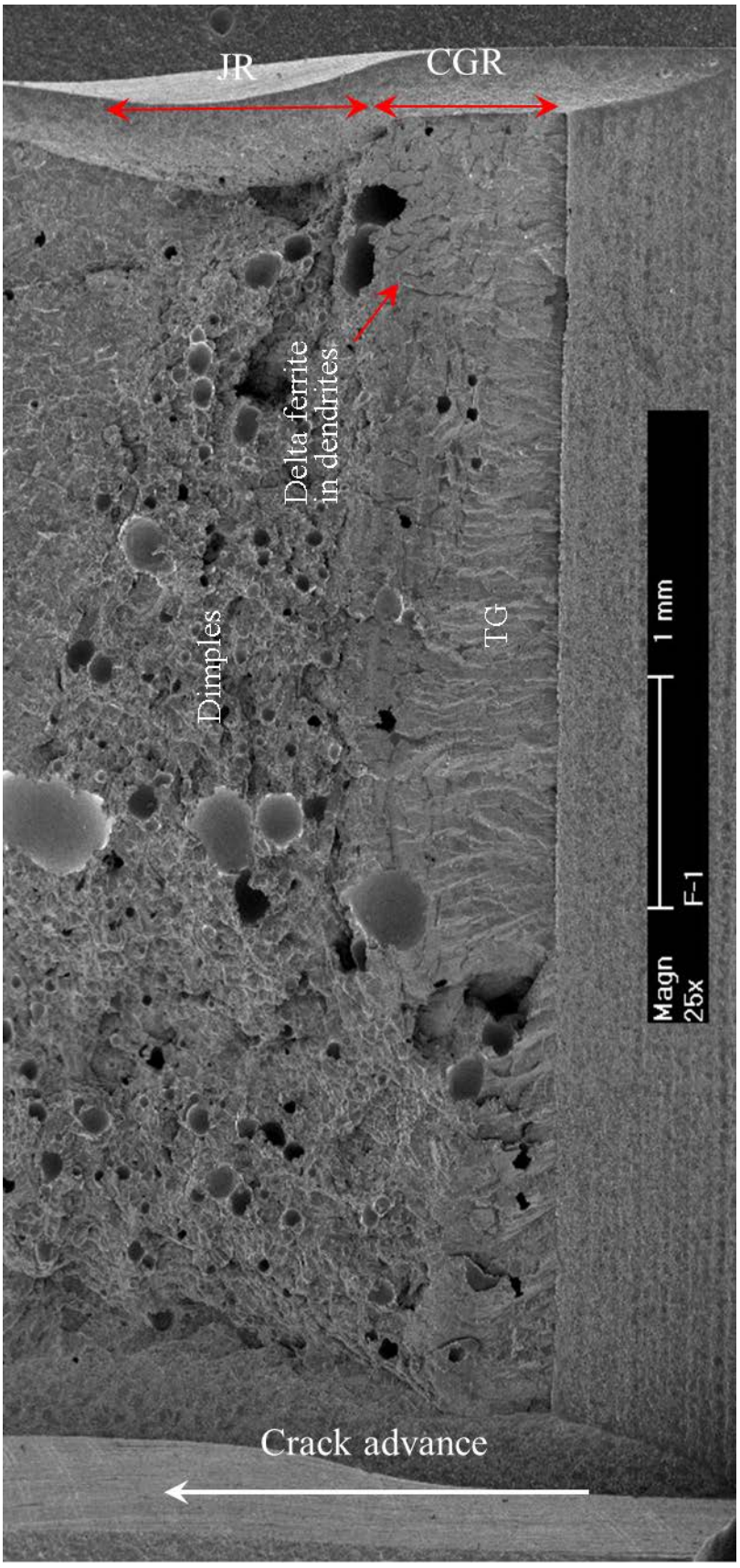


Figure 72. Fracture surface of specimen F-1 tested in low-DO high-purity water.

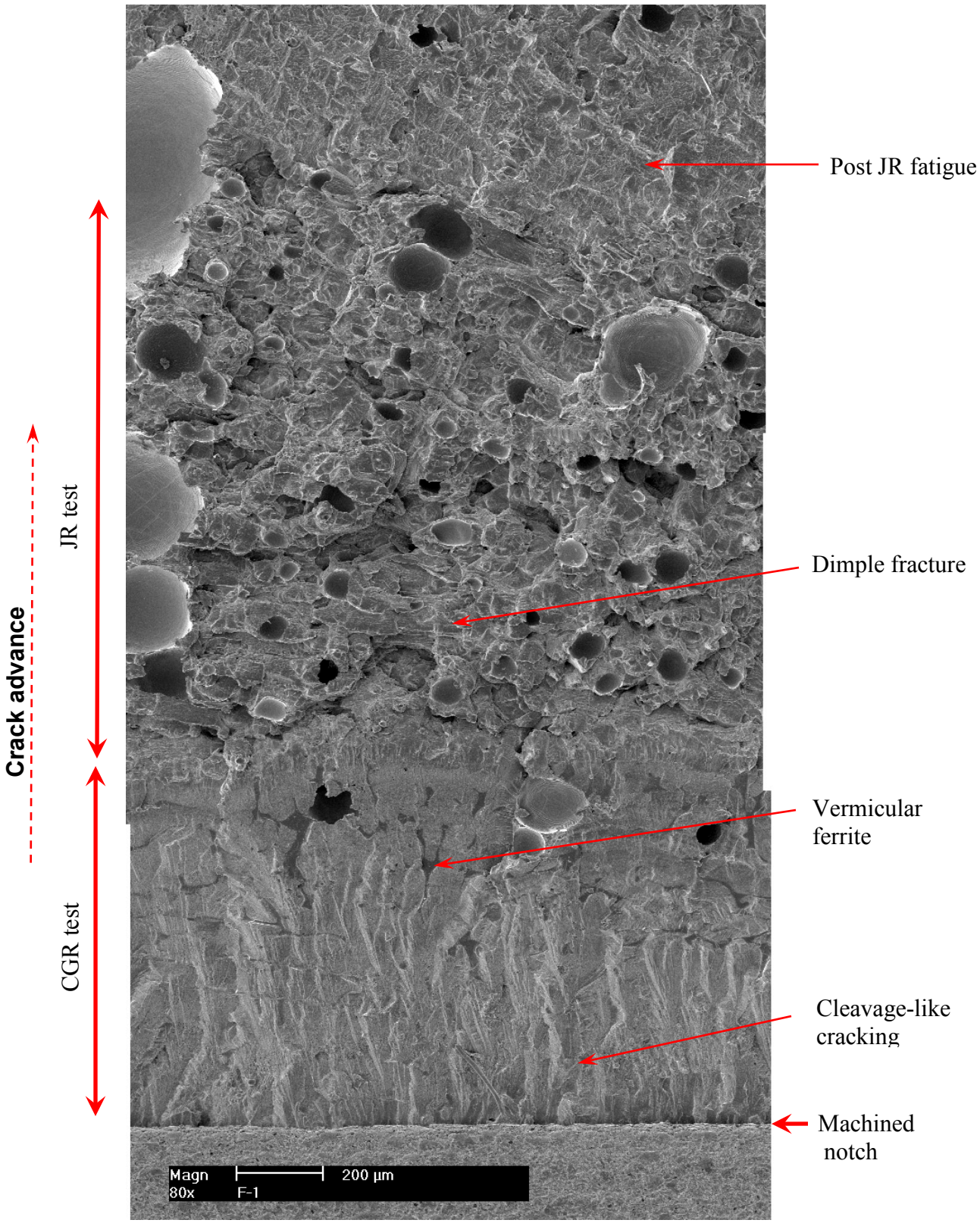


Figure 73. Fracture surface of specimen F-1 along the sample central line.

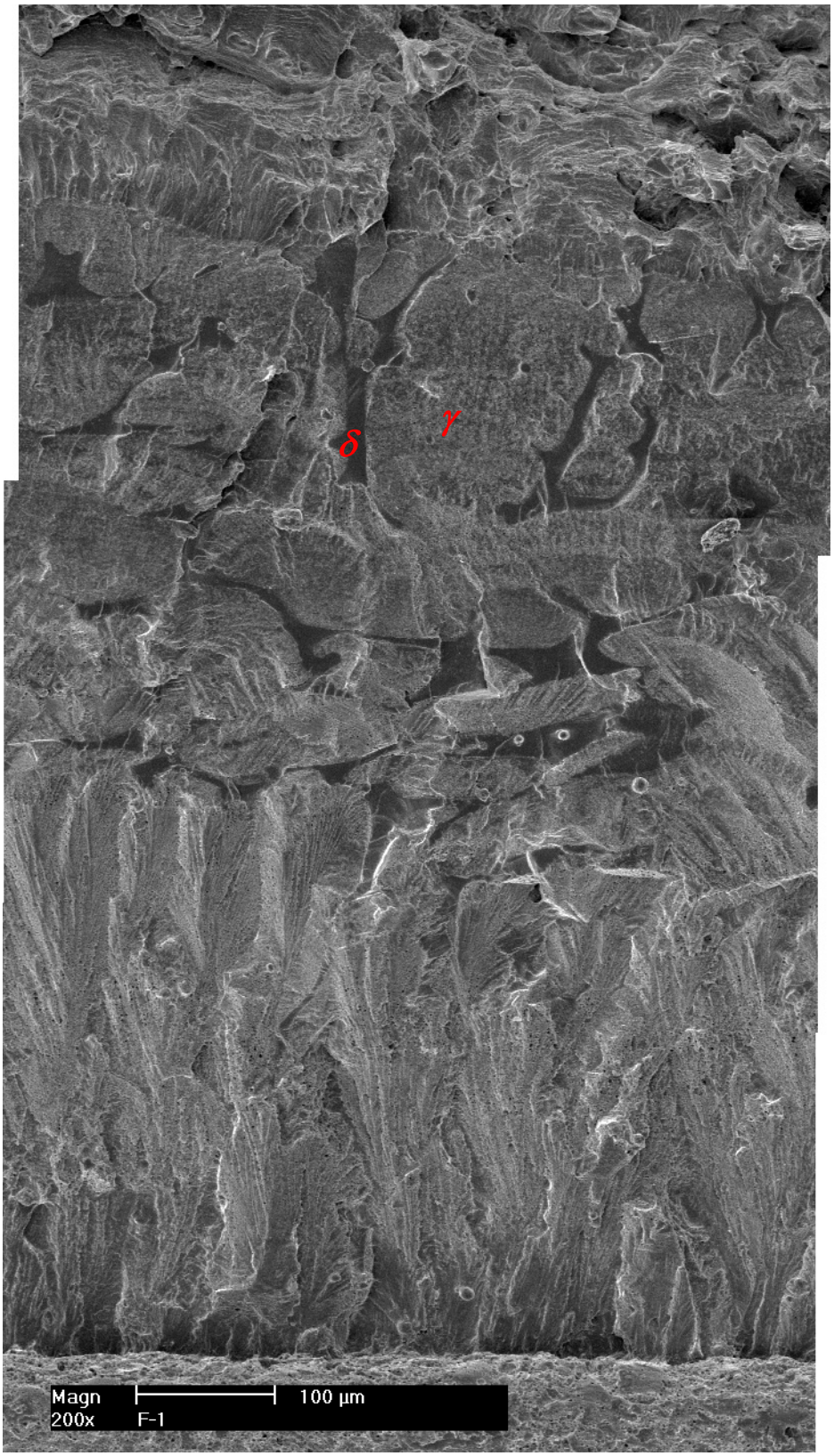


Figure 74. Fracture surface of the CGR region in specimen F-1. Crack propagation from bottom to top.

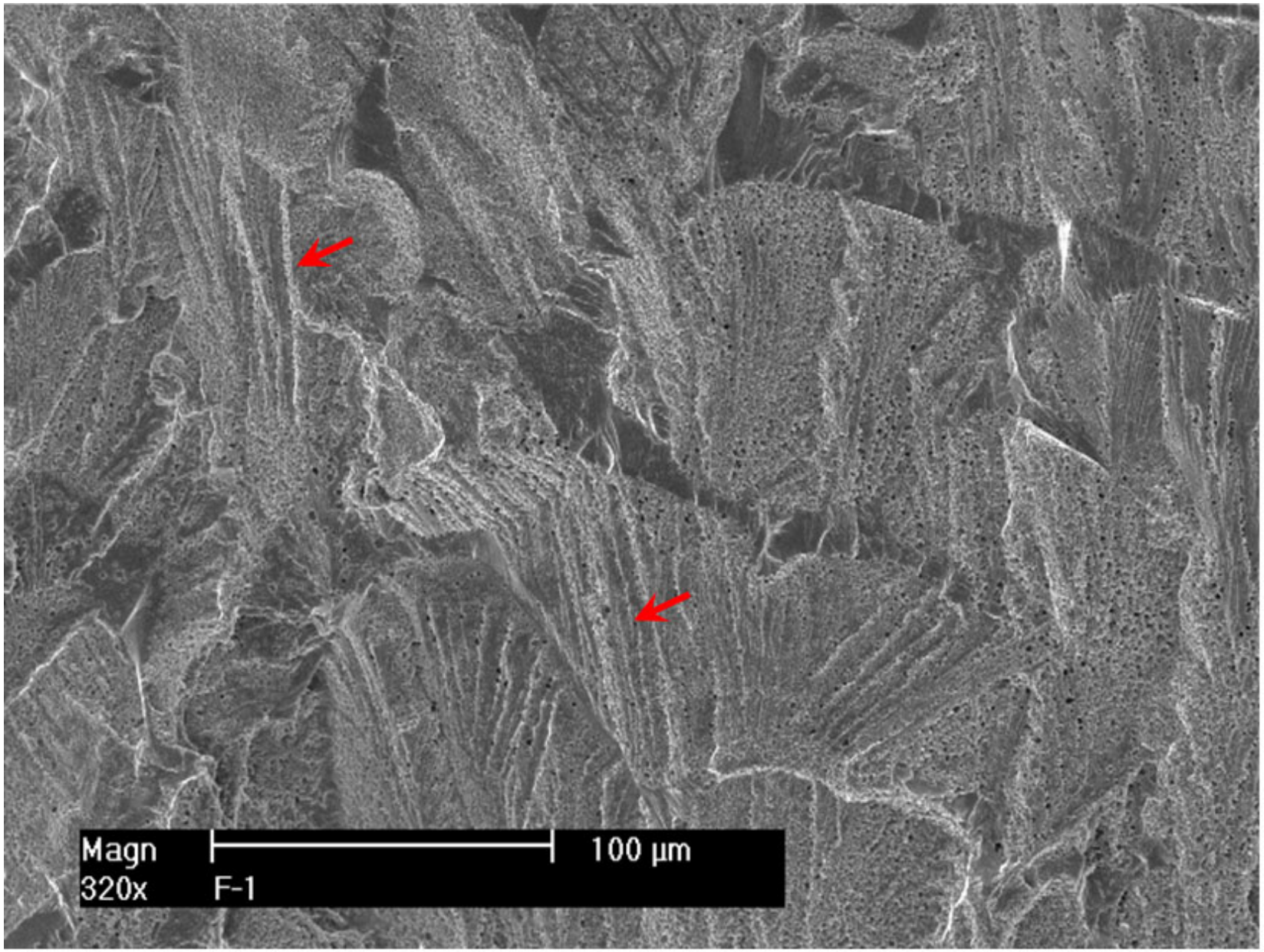


Figure 75. Deformation steps in austenite grain around ferrite phase in the CGR test region of specimen F-1. Crack propagation from bottom to top.

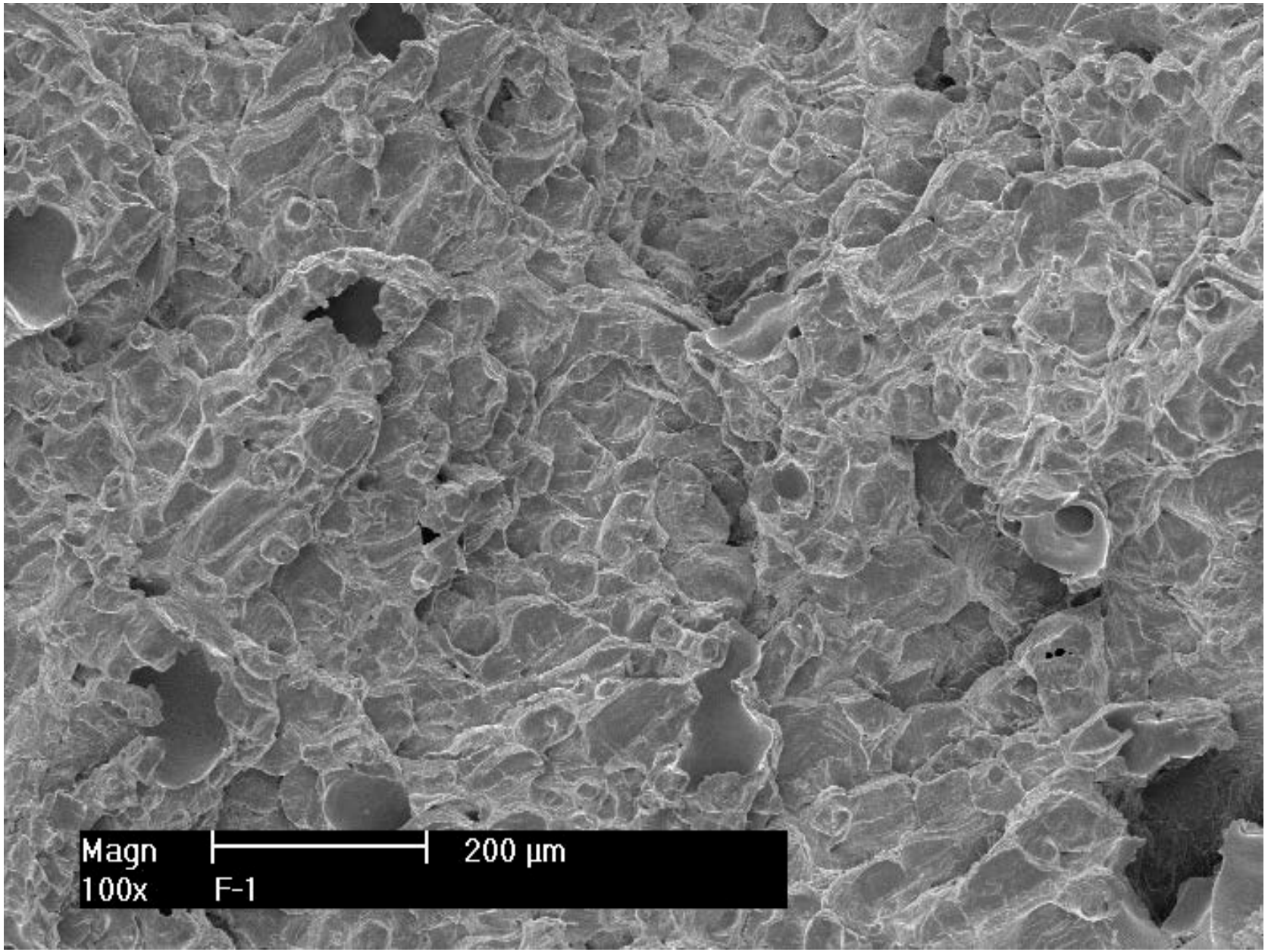


Figure 76. Dimple fracture in the JR test region of specimen F-1. Crack propagation from bottom to top.

## 3.3 CF-8M Stainless Steel

### *3.3.1 Unaged CF-8M CASS*

Crack growth rate test

Specimen I-1 was an unaged CF-8M CASS with 28% ferrite (Heat 75) irradiated to 0.08 dpa. The specimen was tested in a low-DO high-purity water environment at 320°C. The objective was to compare the test results with those of its thermally aged equivalent. The CGR test conditions and results are summarized in Table 13, and a crack-length history plot is shown in Fig. 77.

Fatigue pre-cracking was started with a triangular waveform at a maximum stress intensity factor of ~14 MPa $m^{1/2}$, a load ratio of 0.2, and frequency of 2 Hz. After the crack was initiated from the notch, several test periods with an increasing rise time and load ratio were carried out to stimulate environmentally assisted cracking. Two repeated attempts were made until environmental enhancement started to appear in test period *n*. In the following test periods, the enhancement was stabilized successfully at a maximum stress intensity factor of ~15.5 MPa $m^{1/2}$. Before the test was set at constant load, a hydraulic pump tripped. Consequently, the actuator of the test system was switched off automatically. To eliminate any possible overloading effect, additional test periods (from *s* to *ac*) were added after the system was recovered to repeat the transition. Under a similar loading condition, a similar degree of environmental enhancement was re-established in test period *x* and became stabilized in the following test periods. By the end of test period *ac*, the measured CGR was more than a factor of 10 higher than the fatigue crack growth rate curve in air.

All cyclic CGRs obtained from this sample are plotted in Fig. 78. The data points are close to and sometime higher than the corrosion fatigue curve for unirradiated SSs. It appears that this CF-8M CASS is more susceptible to cracking compared to CF-3 and CF-8. The test was then set at constant load with PPU every 2 hr. A CGR of $1.27 \times 10^{-11}$ m/s was recorded at ~18 MPa $m^{1/2}$ over 26-μm crack extension. This SCC CGR is still significantly lower than the NUREG-0313 curve.

Table 13. Crack growth rates of specimen I-1 (0.08-dpa unaged CF-8M with 28% δ ferrite) in a low-DO high-purity water environment.

| Test Period | Test Time, h | Test Temp., °C | Load Ratio | Rise Time, s | Return Time, s | Hold Time, s | Kmax, MPa $m^{1/2}$ | ΔK, MPa $m^{1/2}$ | CGR in Env., m/s | CGR in Air, m/s | Crack Length, mm |
|---|---|---|---|---|---|---|---|---|---|---|---|
| Start | 0.9 | | | | | | | | | | 5.977 |
| a[a] | 3.11 | 319 | 0.23 | 0.21 | 0.21 | 0.04 | 14.3 | 11.0 | 5.09E-08 | 6.72E-08 | 6.127 |
| b | 5.0 | 319 | 0.36 | 0.20 | 0.20 | 0.05 | 12.7 | 8.1 | 2.74E-09 | 3.02E-08 | 6.134 |
| c | 6.5 | 319 | 0.33 | 0.21 | 0.21 | 0.04 | 14.2 | 9.6 | 4.10E-08 | 4.87E-08 | 6.225 |
| d | 9.8 | 319 | 0.43 | 0.40 | 0.40 | 0.10 | 14.2 | 8.1 | 1.27E-08 | 1.61E-08 | 6.285 |
| e | 23.9 | 319 | 0.53 | 0.76 | 0.76 | 0.24 | 14.2 | 6.6 | 1.47E-09 | 4.79E-09 | 6.315 |
| f | 26.5 | 319 | 0.49 | 0.78 | 0.78 | 0.22 | 14.1 | 7.3 | 8.93E-10 | 6.14E-09 | 6.316 |
| g | 28.6 | 319 | 0.30 | 0.83 | 0.83 | 0.17 | 14.7 | 10.2 | 2.38E-08 | 1.47E-08 | 6.371 |
| h | 31.4 | 319 | 0.40 | 0.81 | 0.81 | 0.19 | 14.8 | 8.8 | 1.48E-08 | 1.04E-08 | 6.434 |
| i | 37 | 320 | 0.45 | 1.98 | 1.98 | 0.52 | 14.8 | 8.1 | 3.91E-09 | 3.33E-09 | 6.463 |
| j | 47.9 | 319 | 0.45 | 3.94 | 3.94 | 1.06 | 14.8 | 8.1 | 1.89E-09 | 1.67E-09 | 6.495 |
| k | 56.7 | 320 | 0.45 | 7.88 | 3.94 | 2.12 | 14.8 | 8.1 | 1.19E-09 | 8.46E-10 | 6.513 |
| l | 72.8 | 319 | 0.45 | 15.8 | 3.94 | 4.24 | 14.8 | 8.1 | 5.61E-10 | 4.27E-10 | 6.534 |
| m | 104.5 | 319 | 0.45 | 23.6 | 3.94 | 6.37 | 14.8 | 8.2 | 2.28E-10 | 2.87E-10 | 6.551 |
| n[a] | 153.1 | 319 | 0.45 | 47.2 | 3.94 | 12.8 | 14.9 | 8.2 | 3.09E-10 | 1.46E-10 | 6.578 |
| o | 176.2 | 320 | 0.45 | 94.5 | 9.45 | 25.5 | 15.0 | 8.3 | 3.71E-10 | 7.47E-11 | 6.605 |
| p[a] | 240 | 319 | 0.50 | 231.1 | 9.24 | 68.9 | 15.1 | 7.5 | 3.17E-10 | 2.38E-11 | 6.634 |
| q | 335.4 | 320 | 0.50 | 461.4 | 9.23 | 138.6 | 15.0 | 7.6 | 1.49E-10 | 1.21E-11 | 6.676 |
| r | 363.8 | 320 | 0.51 | 768.0 | 9.22 | 232.0 | 15.3 | 7.6 | 1.95E-10 | 7.30E-12 | 6.690 |
| Hydraulic pump trip | | | | | | | | | | | |
| s1 | 394.3-410.3 | 320 | 0.49 | 231.5 | 9.26 | 68.5 | 15.2 | 7.8 | 4.67E-10 | 2.63E-11 | 6.726 |
| s2 | 433.6 | 320 | 0.49 | 231.5 | 9.26 | 68.5 | 15.2 | 7.8 | 1.35E-09 | 2.63E-11 | 6.726 |
| t | 440 | 320 | 0.48 | 463.4 | 9.27 | 136.6 | 15.1 | 7.9 | 3.16E-12 | 1.34E-11 | 6.731 |
| u | 505.6 | 319 | 0.48 | 464.4 | 9.29 | 135.6 | 15.2 | 7.9 | 3.76E-11 | 1.38E-11 | 6.740 |
| v | 530 | 319 | 0.49 | 116.5 | 9.32 | 33.5 | 15.7 | 8.1 | 1.44E-11 | 5.80E-11 | 6.740 |
| w | 532 | 319 | 0.29 | 8.32 | 4.16 | 1.68 | 16.5 | 11.7 | 1.12E-08 | 2.23E-09 | 6.787 |
| x | 538.7 | 319 | 0.39 | 24.2 | 4.04 | 5.76 | 16.5 | 10.0 | 1.52E-09 | 5.16E-10 | 6.813 |
| y | 559.3 | 320 | 0.50 | 46.6 | 9.33 | 13.4 | 16.5 | 8.3 | 2.81E-10 | 1.63E-10 | 6.831 |
| z | 601.7 | 319 | 0.48 | 93.5 | 9.35 | 26.5 | 16.3 | 8.5 | 8.88E-11 | 8.41E-11 | 6.845 |
| aa | 630.7 | 319 | 0.49 | 236.6 | 9.47 | 63.4 | 17.7 | 9.0 | 3.90E-10 | 4.17E-11 | 6.877 |
| ab | 672.7 | 319 | 0.49 | 473.0 | 9.46 | 127.0 | 17.7 | 9.1 | 2.37E-10 | 2.11E-11 | 6.902 |
| ac | 696.6 | 319 | 0.49 | 787.7 | 9.45 | 212.3 | 17.7 | 9.1 | 1.55E-10 | 1.26E-11 | 6.909 |
| 1 | 821.9 | 319 | 0.50 | 12 | 12 | 7200 | 17.9 | 8.9 | 1.89E-11 | 1.33E-12 | 6.925 |

[a] The CGR value was obtained from the later part of the test periods.

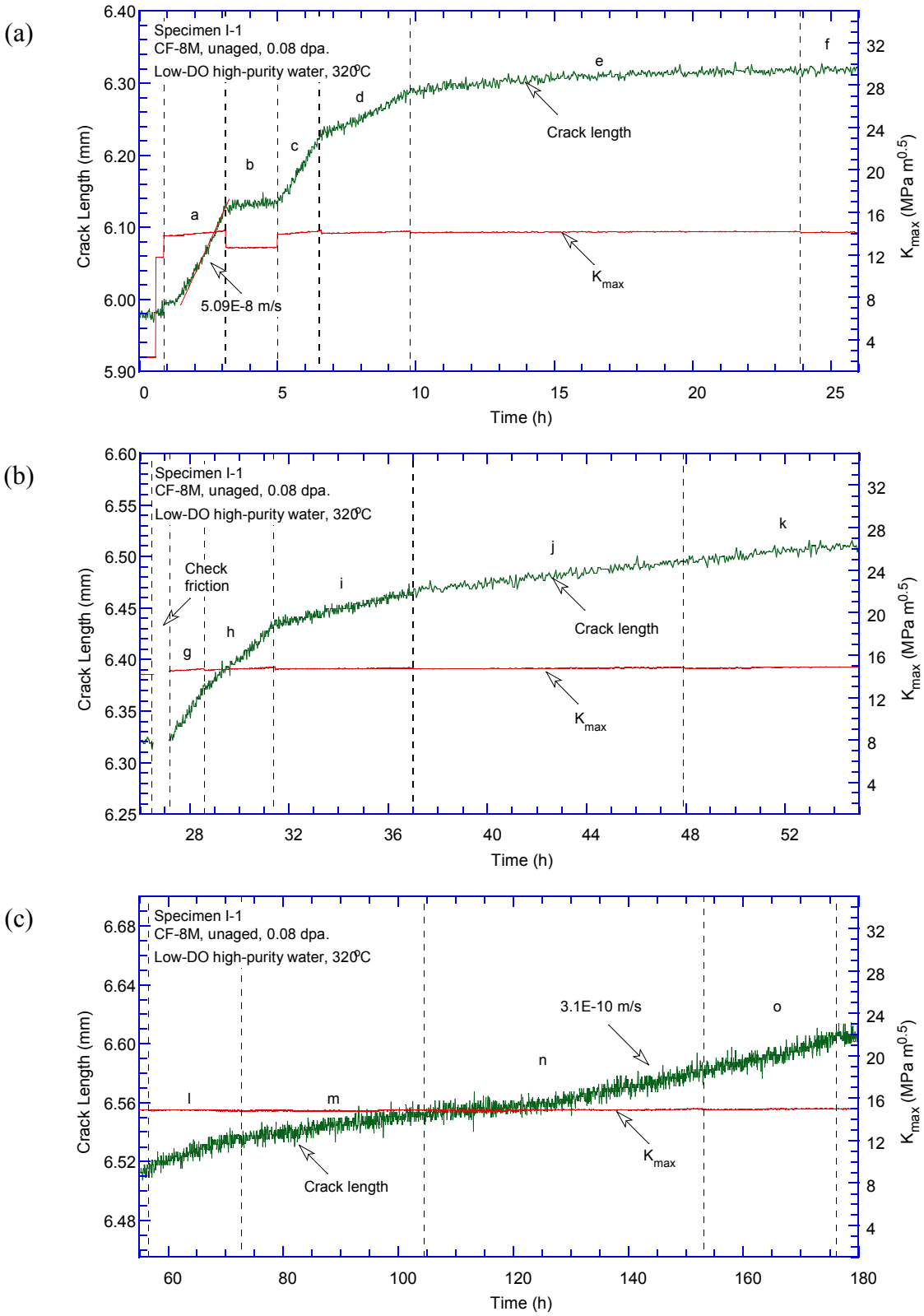


Figure 77. Crack-length-vs.-time plot for specimen I-1 (0.08-dpa unaged CF-8M with 28% ferrite): test periods (a) a-f, (b) g-k, (c) l-o, (d) p-r, (e) s-v, (f) w-z, (g) aa-ac, and (h) 1.

(d)

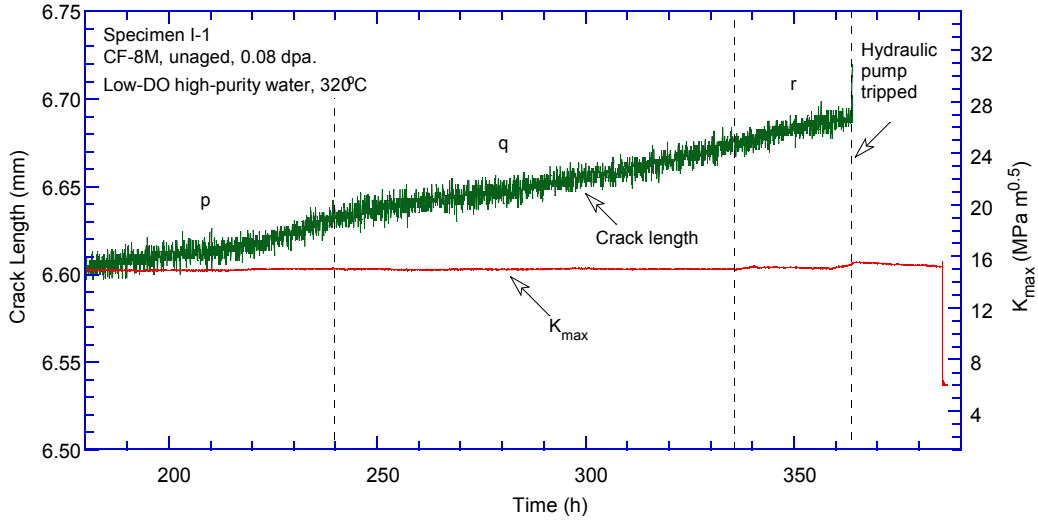


(e)

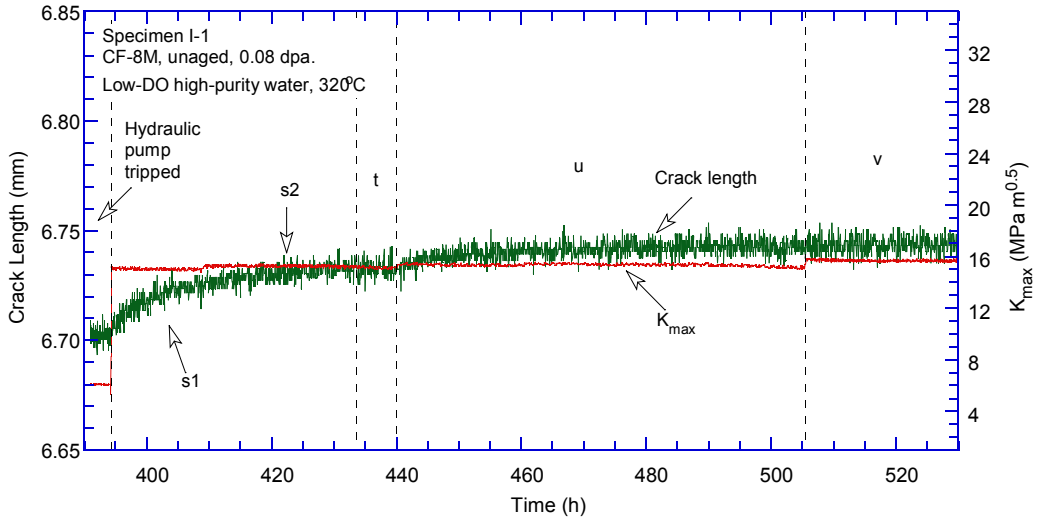


(f)

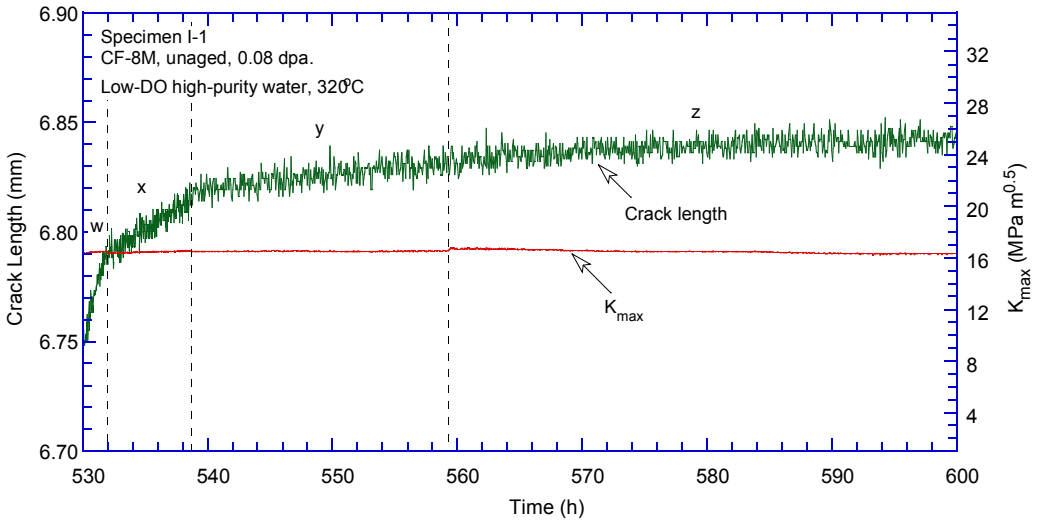


Figure 77. (Contd.)

(g)

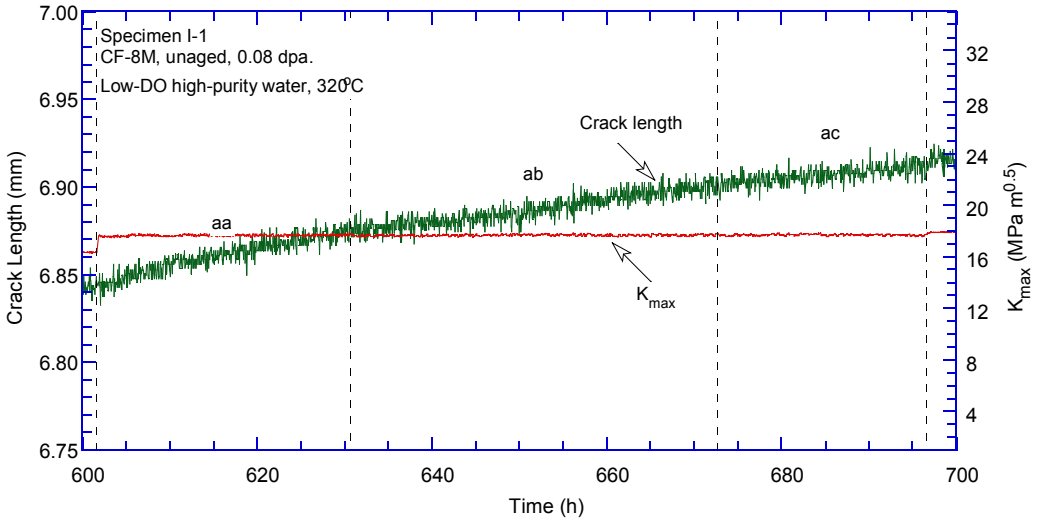


(h)

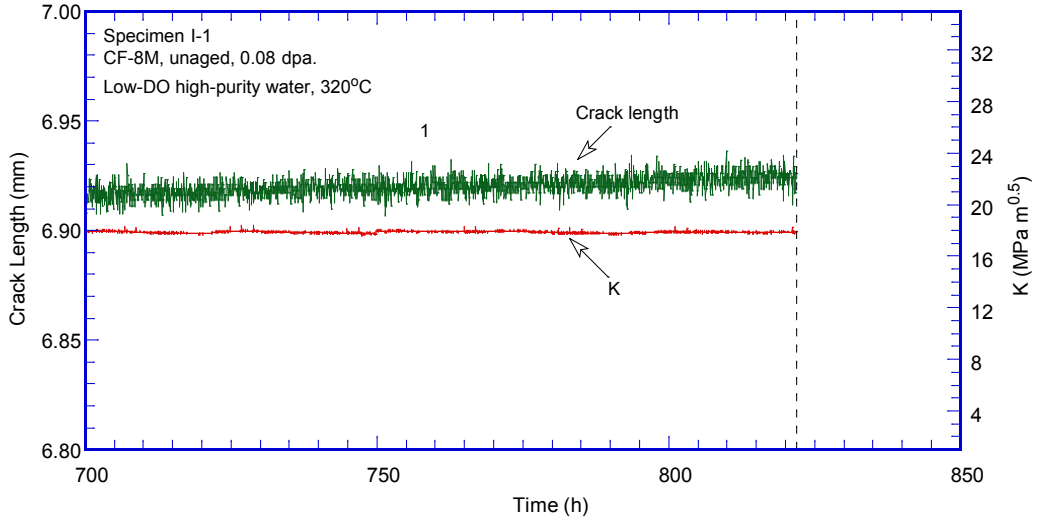


Figure 77. (Contd.)

Fracture toughness J-R curve test

After the CGR test, a fracture toughness J-R curve test was performed on the same sample in the test environment. The obtained J and crack extension results are plotted in Fig. 79. A power-law fitting shows a J-R correlation of $J = 336\Delta a^{0.66}$. The J value at the 0.2-mm offset line is about 145 kJ/m$^2$. Note that the J-R curve data cannot be validated because one of the nine measurements of the final crack size was above the limit. Some data points above the $J_{max}$ were also used in the analysis.

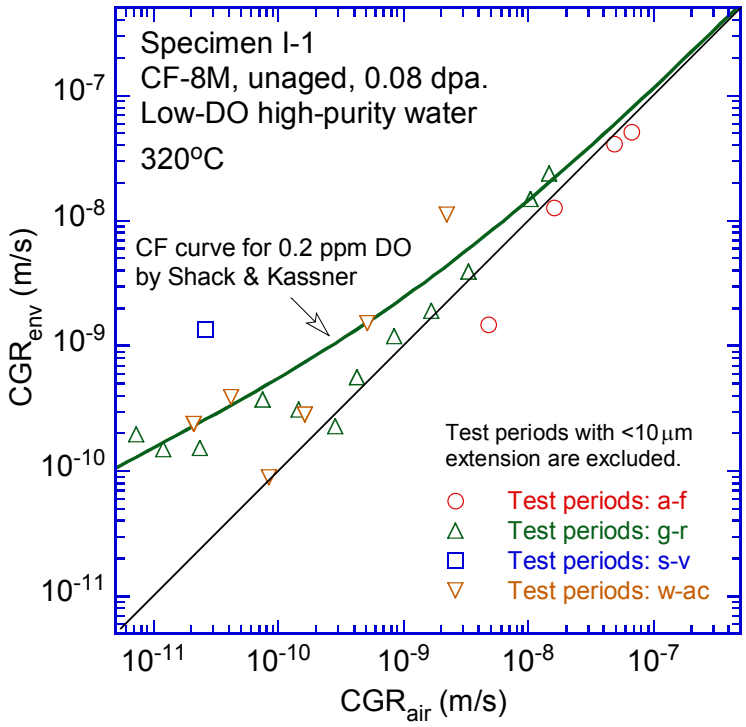


Figure 78. Cyclic CGRs of specimen I-1.

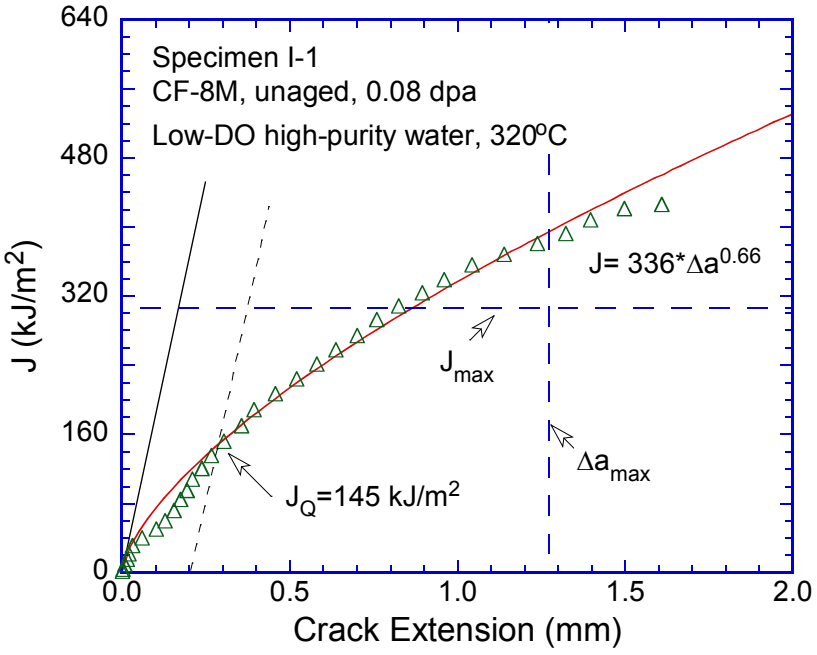


Figure 79. The J-R curve of specimen I-1.

Fractographic examination

Following the J-R curve test, cyclic loading was applied at room temperature in an air atmosphere to break the remaining ligament. Figure 80 shows the fracture surface of specimen I-1. The crack front is relatively straight, indicating a well-controlled loading condition during the CGR test. The CGR region is flat, which shows a clear contrast from the heavily deformed plastic region in the JR test. Multiple secondary cracks perpendicular to the fracture surface can also be seen in the CGR test region. Figure 81 shows an enlarged view of the sample central line. Transgranular cleavage-like cracking can be seen at the beginning of the CGR test. With the advance of the crack, cleavage-like cracking became less pronounced and the vermicular ferrite that formed at the core of casting dendrites started to appear (Fig. 82). At the end of the CGR test, little deformation steps can be seen on the fracture surface (Fig. 83). In the JR test region, the fracture was a ductile dimple morphology, suggesting heavy plastic deformation prior to fracture (Fig. 84).

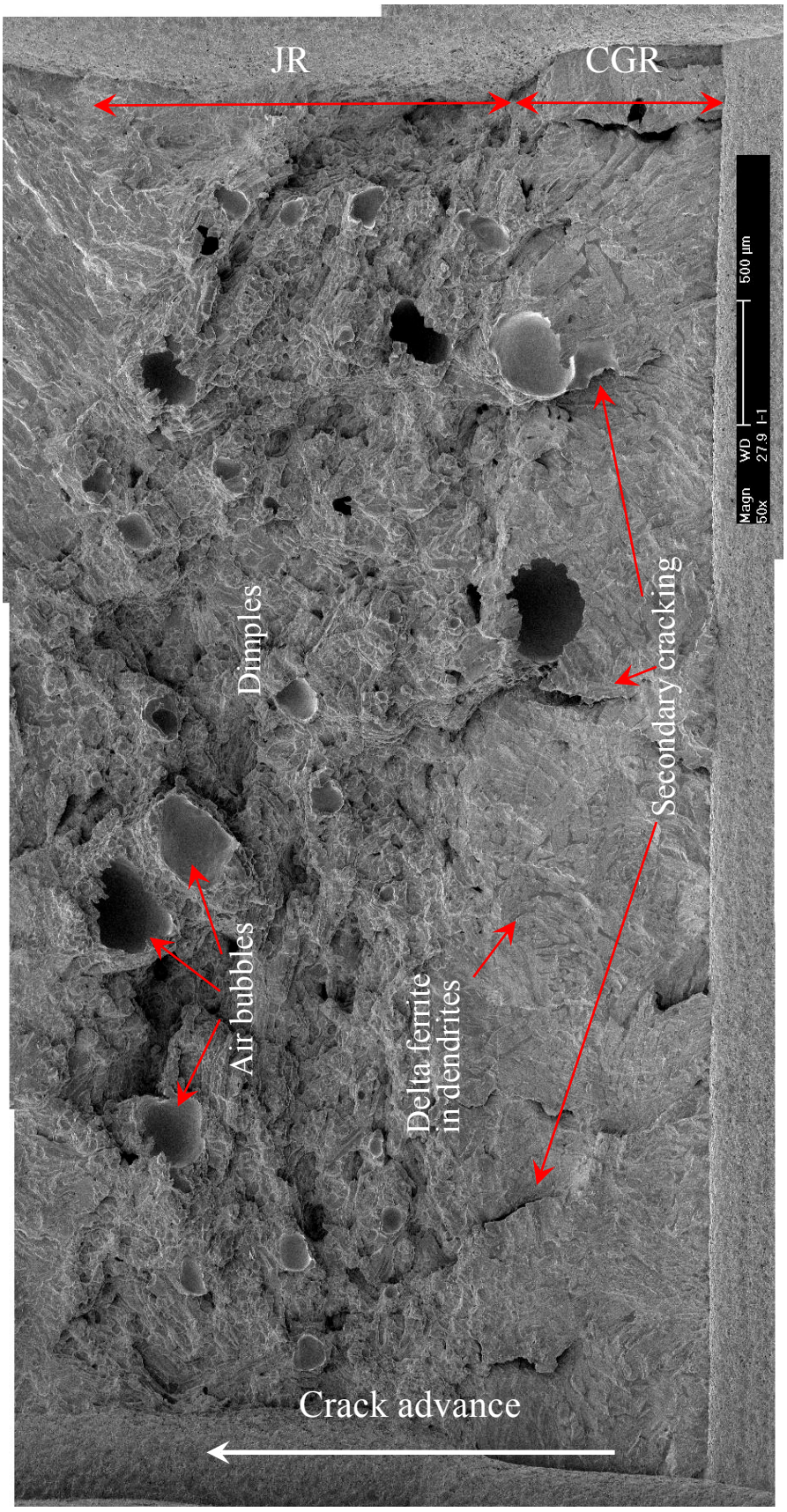


Figure 80. Fracture surface of specimen I-1 tested in low-DO high-purity water.

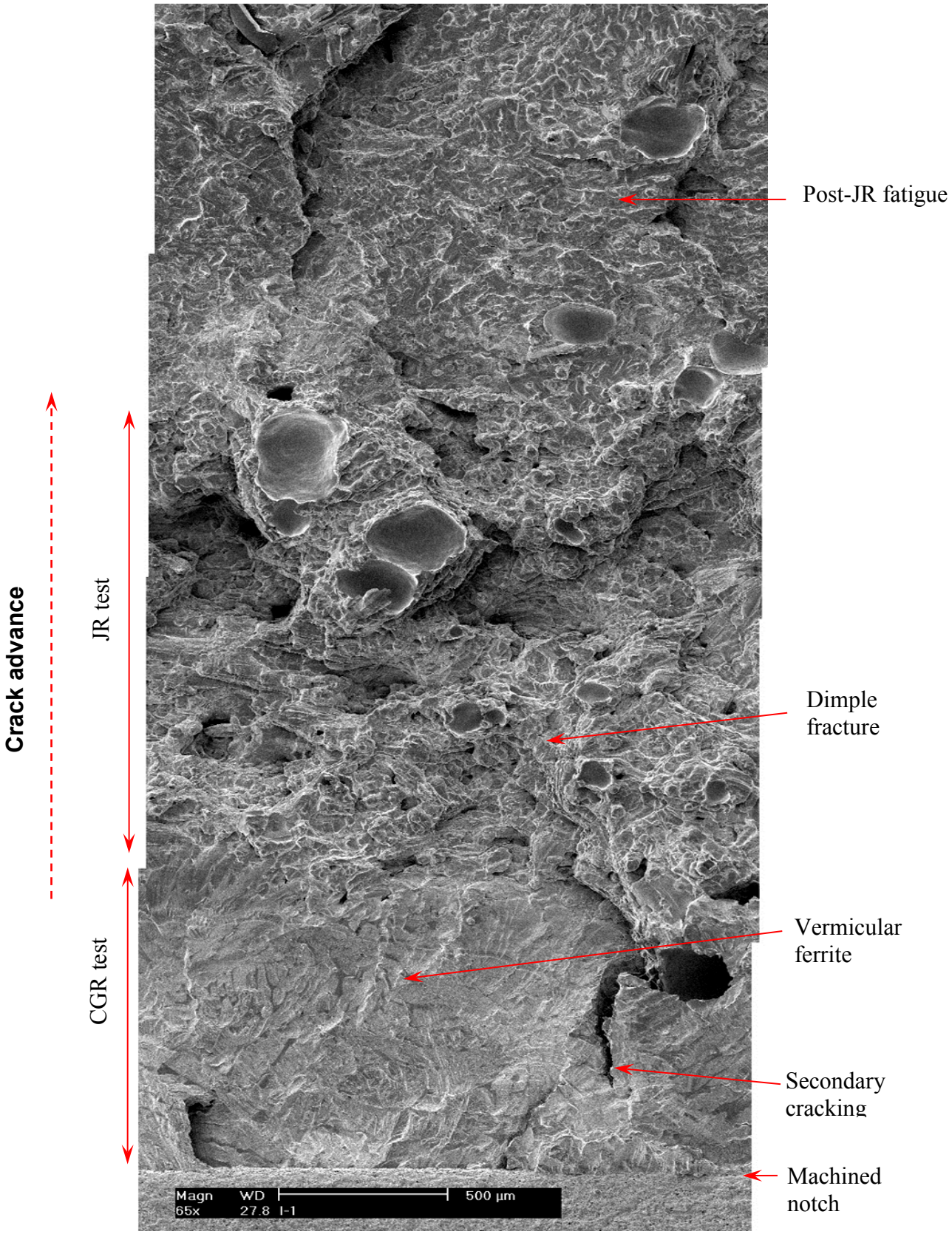


Figure 81. Fracture surface of specimen I-1 along the sample central line.

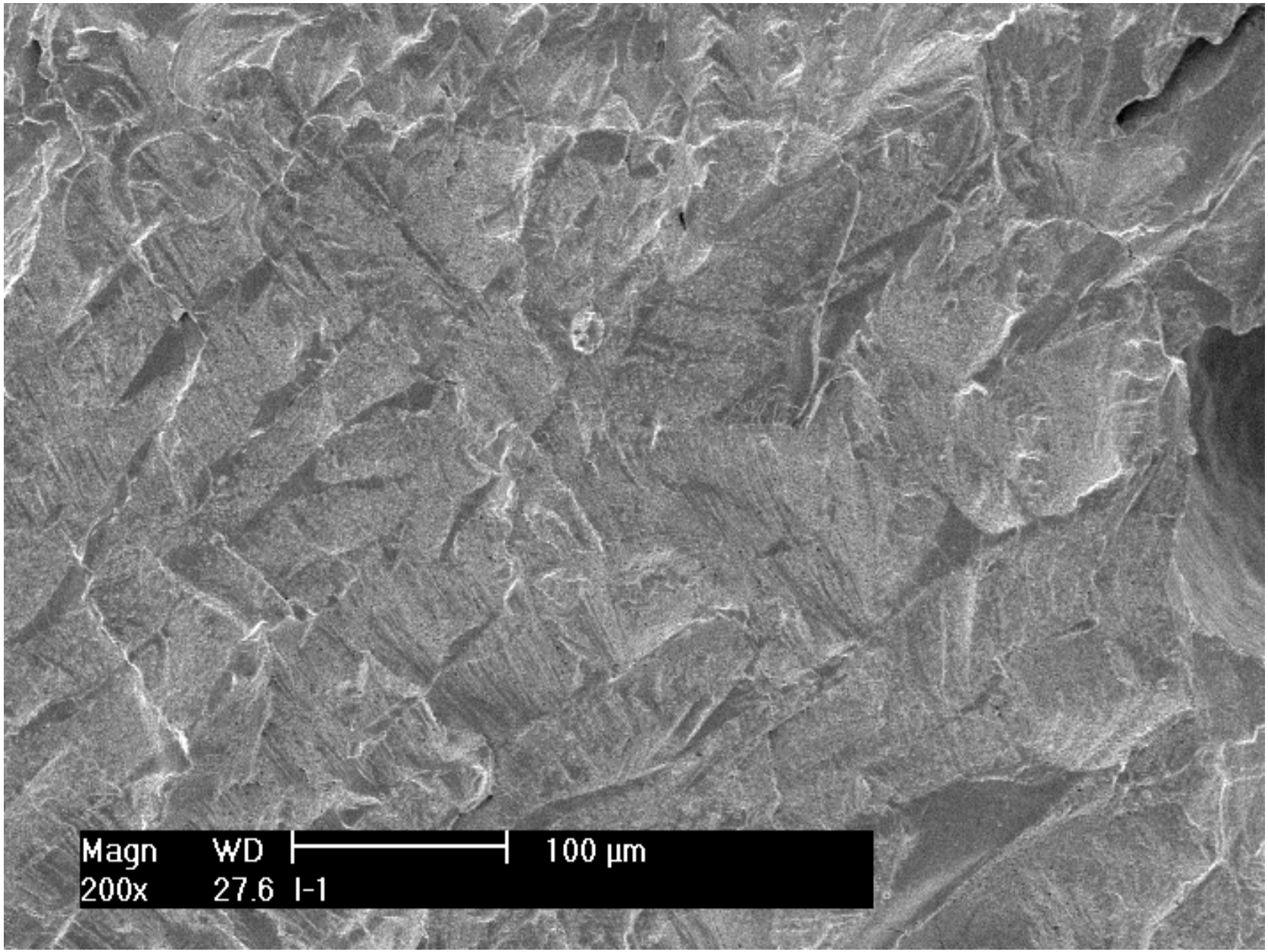


Figure 82. Precracking region in the CGR test of specimen I-1. Crack propagation from bottom to top.

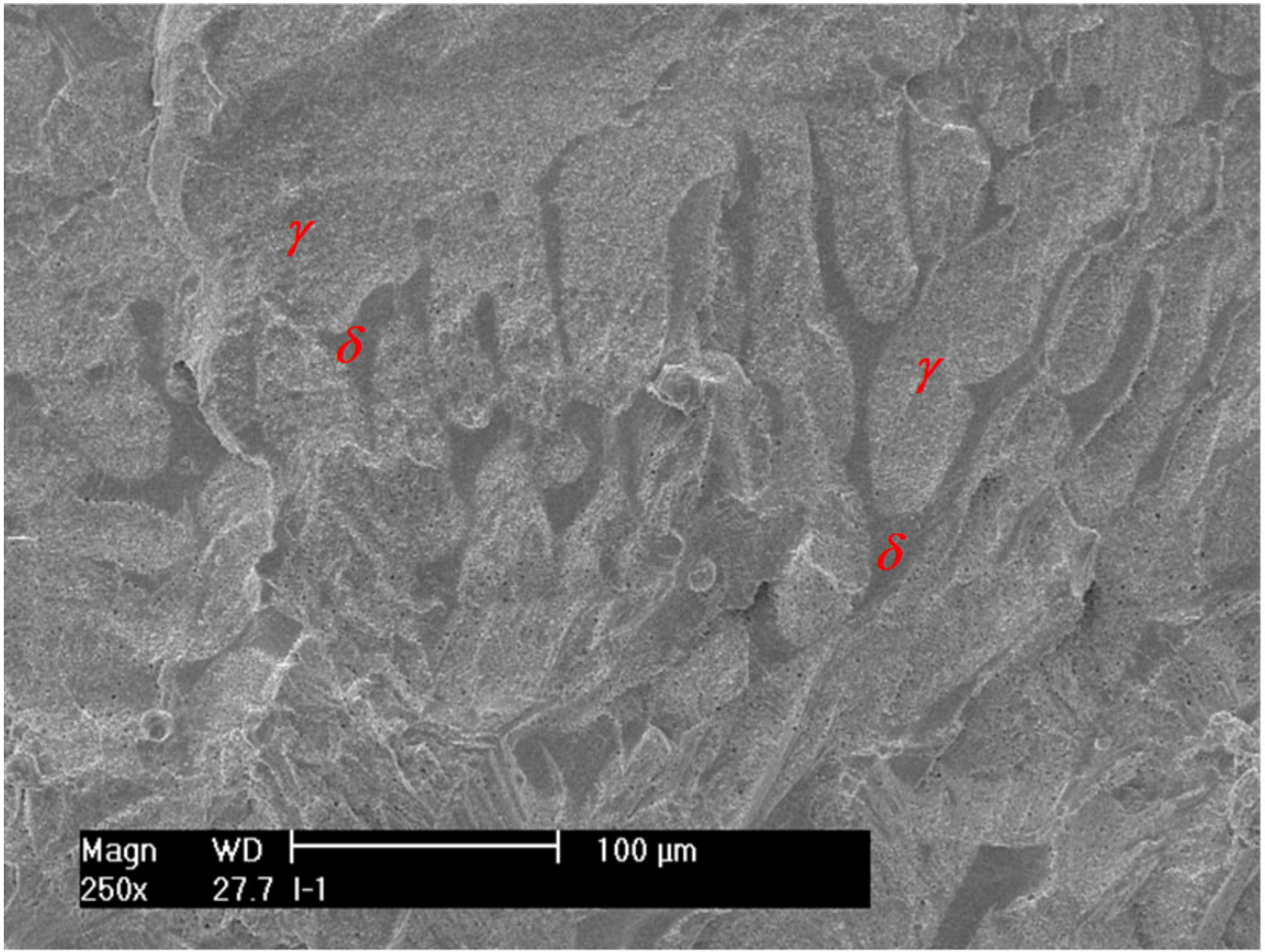


Figure 83. Fracture surface at the end of CGR test of specimen I-1. Crack propagation from bottom to top.

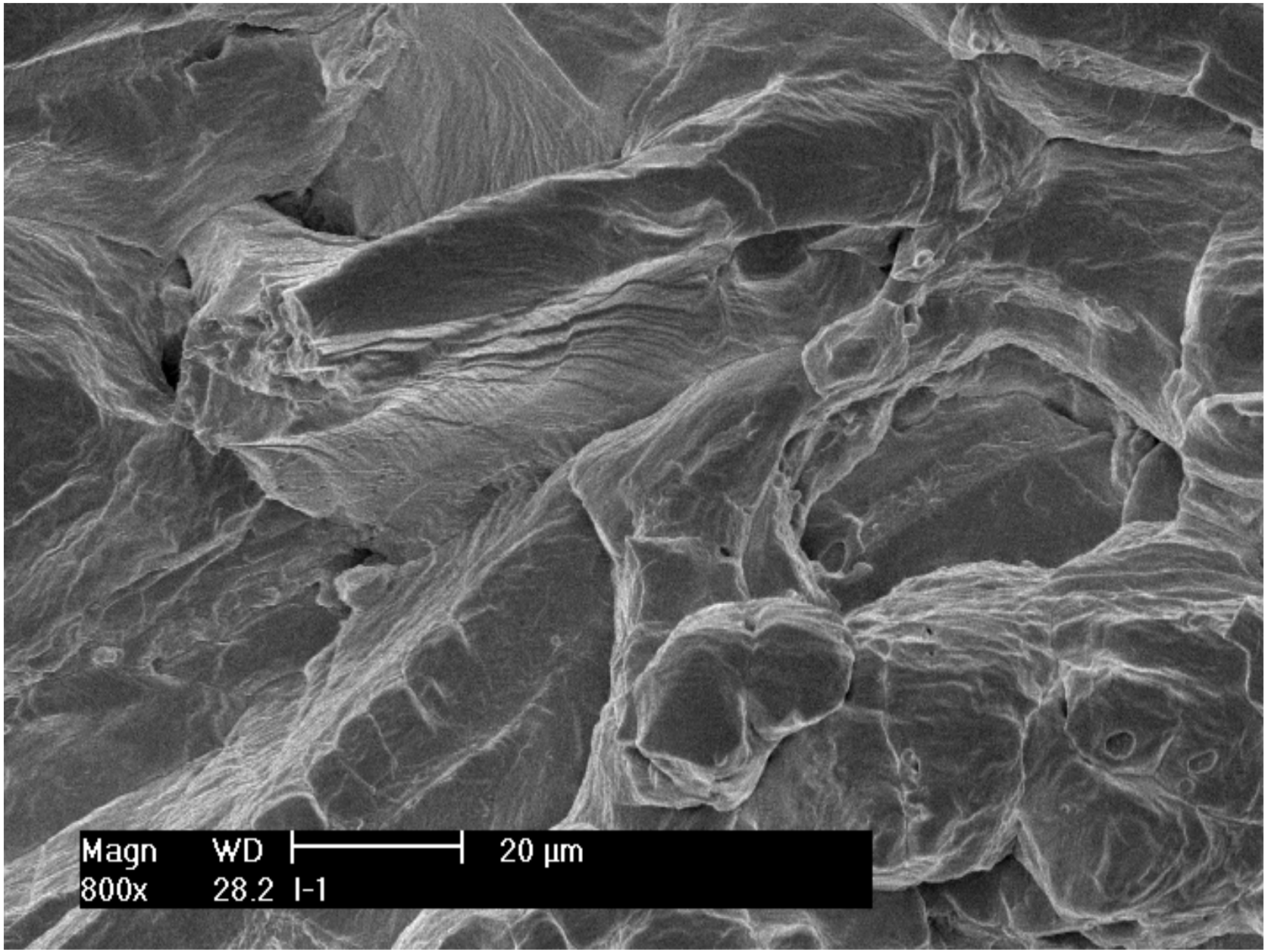


Figure 84. Heavily deformed microstructure in the JR test region of specimen I-1.

*3.3.2 Thermally Aged CF-8M CASS*

Crack growth rate test

Specimen J-1 was the thermally aged version of specimen I-1, a CF-8M CASS with 28% ferrite. The sample was aged at 400°C for 10,000 hr and then irradiated to 0.08 dpa. The test was performed in the low-DO high-purity water at 320°C. The objective was to compare the results with those of the unaged CF-8M at the same dose. The CGR test conditions and results are summarized in Table 14, and a crack-length history plot is shown in Fig. 85.

Table 14. Crack growth rates of specimen J-1 (0.08-dpa aged CF-8M with 28% δ ferrite) in a low-DO high-purity water environment.

| Test Period | Test Time, h | Test Temp., °C | Load Ratio | Rise Time, s | Return Time, s | Hold Time, s | Kmax, MPa $m^{1/2}$ | ΔK, MPa $m^{1/2}$ | CGR in Env., m/s | CGR in Air, m/s | Crack Length, mm |
|---|---|---|---|---|---|---|---|---|---|---|---|
| Start | 0.4 | | | | | | | | | | 5.970 |
| a | 2.2 | 320 | 0.20 | 0.22 | 0.22 | 0.03 | 14.2 | 11.3 | 6.53E-09 | 6.82E-08 | 5.990 |
| b | 3.6 | 320 | 0.20 | 0.22 | 0.22 | 0.03 | 16.6 | 13.2 | 5.35E-08 | 1.13E-07 | 6.111 |
| c | 6.3 | 320 | 0.30 | 0.43 | 0.43 | 0.07 | 15.5 | 10.8 | 1.57E-08 | 3.37E-08 | 6.183 |
| d | 8.6 | 320 | 0.30 | 0.21 | 0.21 | 0.04 | 14.5 | 10.1 | 9.37E-09 | 5.43E-08 | 6.217 |
| e | 23.8 | 320 | 0.30 | 4.29 | 4.29 | 0.71 | 14.4 | 10.0 | 2.97E-10 | 2.67E-09 | 6.225 |
| f | 25.3 | 320 | 0.30 | 0.22 | 0.22 | 0.03 | 15.9 | 11.1 | 7.02E-08 | 7.34E-08 | 6.381 |
| g [a] | 28.7 | 320 | 0.30 | 0.43 | 0.43 | 0.07 | 15.0 | 10.4 | 2.98E-08 | 3.05E-08 | 6.494 |
| h | 33.5 | 320 | 0.40 | 0.83 | 0.83 | 0.17 | 15.1 | 9.0 | 1.24E-08 | 1.08E-08 | 6.587 |
| i | 37.1 | 320 | 0.45 | 1.64 | 1.64 | 0.36 | 15.1 | 8.2 | 6.15E-09 | 4.31E-09 | 6.620 |
| j | 48.5 | 320 | 0.52 | 3.98 | 3.98 | 1.02 | 15.0 | 7.2 | 6.21E-10 | 1.20E-09 | 6.632 |
| k [a] | 51.5 | 320 | 0.45 | 0.82 | 0.82 | 0.18 | 15.2 | 8.3 | 1.20E-08 | 8.81E-09 | 6.669 |
| l | 54.9 | 320 | 0.50 | 1.60 | 1.60 | 0.40 | 15.1 | 7.5 | 4.29E-09 | 3.41E-09 | 6.692 |
| m | 61.7 | 320 | 0.50 | 4.00 | 4.00 | 1.00 | 15.1 | 7.6 | 1.80E-09 | 1.39E-09 | 6.709 |
| n | 72.2 | 320 | 0.55 | 7.82 | 3.91 | 2.18 | 15.0 | 6.8 | 2.40E-10 | 5.15E-10 | 6.715 |
| o | 80.8 | 320 | 0.50 | 7.99 | 3.99 | 2.01 | 15.2 | 7.5 | 9.35E-10 | 6.91E-10 | 6.731 |
| p | 103.7 | 319 | 0.50 | 24.0 | 9.60 | 5.99 | 15.3 | 7.7 | 5.52E-10 | 2.41E-10 | 6.758 |
| q | 125.6 | 320 | 0.50 | 47.9 | 9.59 | 12.1 | 15.5 | 7.7 | 6.71E-10 | 1.23E-10 | 6.794 |
| r | 147.8 | 319 | 0.55 | 93.9 | 9.39 | 26.1 | 15.6 | 7.0 | 4.36E-10 | 4.81E-11 | 6.819 |
| s | 176.2 | 319 | 0.60 | 228.8 | 9.15 | 71.2 | 15.6 | 6.3 | 1.59E-10 | 1.44E-11 | 6.833 |
| t | 216.7 | 319 | 0.60 | 381.2 | 9.15 | 118.8 | 15.6 | 6.3 | 1.80E-10 | 8.77E-12 | 6.853 |
| u | 249.4 | 319 | 0.60 | 762.8 | 9.15 | 237.2 | 15.8 | 6.4 | 1.32E-10 | 4.47E-12 | 6.864 |
| 1-a | 317.5 | 319 | 0.60 | 12 | 12 | 7200 | 15.5 | 6.2 | 1.79E-11 | 4.39E-13 | 6.874 |
| 1-b | 365.2 | 319 | 0.60 | 12 | 12 | 3600 | 15.6 | 6.3 | 2.47E-11 | 8.97E-13 | 6.878 |
| 2-a [a] | 416.7 | 319 | 0.60 | 12 | 12 | 7200 | 19.0 | 7.6 | 5.51E-11 | 8.49E-13 | 6.899 |
| 2-b | 466 | 320 | 0.60 | 12 | 12 | 3600 | 18.9 | 7.6 | 6.42E-11 | 1.68E-12 | 6.910 |
| 2-c | 503.9 | 320 | 1 | - | - | - | 18.9 | - | 2.02E-12 | - | 6.911 |

[a] The CGR value was obtained from the later part of the test periods.

Fatigue pre-cracking was carried out with a maximum stress intensity factor of 14-15 MPa $m^{1/2}$, a load ratio of 0.2-0.3, and frequency of 2 Hz. After about 600-μm crack extension, a stable crack growth was obtained in test period *h,* and the measured CGRs were very close to the fatigue line. Next, both the rise time and load ratio were gradually increased to promote environmentally enhanced cracking, and an elevated CGR became evident in test period *r*. Additional increases in rise time and load ratio produced a further environmental enhancement. By the end of test period *u*, the measured CGR was a factor of 25 higher than the fatigue growth

rate. Figure 86 shows the cyclic CGRs obtained from this sample. The corrosion fatigue behavior of this thermally aged specimen seems to be similar to that of its unaged counterpart. Both of the CF-8M specimens show a higher degree of sensitivity to environmentally enhanced cracking than the CF-3 and CF-8 CASS used in this study.

After pre-cracking, the test was set at constant load with PPU every 2 hr in test period *1-a*. A CGR of 1.8 x $10^{-11}$ m/s was recorded at a stress intensity factor of 15.5 MPa $m^{1/2}$. With a shorter holding time (PPU every 1 hr), a slightly higher CGR (2.5 x $10^{-11}$ m/s) was obtained at the same stress intensity level. Next, the constant-load CGR (with PPUs) was measured at a higher stress intensity level (~19 MPa $m^{1/2}$). A slightly higher CGR was once again observed with a shorter holding time (2-hr PPU in period *2-a* and 1-hr PPU in period *2-b*). When the PPU was removed in test period *2-c*, the CGR became much lower. Constrained by test time, the CGR test was concluded after 10-μm crack extension.

Figure 87 shows the SCC CGRs obtained from the unaged and aged CF-8M CASS in this study. The CGR values are all well below the NUREG-0313 disposition curve, as expected at this dose and ECP level. The unaged CF-8M may have performed slightly better than the aged sample. However, given the inherent uncertainty of CGR measurements, the difference in SCC CGRs of the aged and unaged CF-8M is insignificant.

(a)

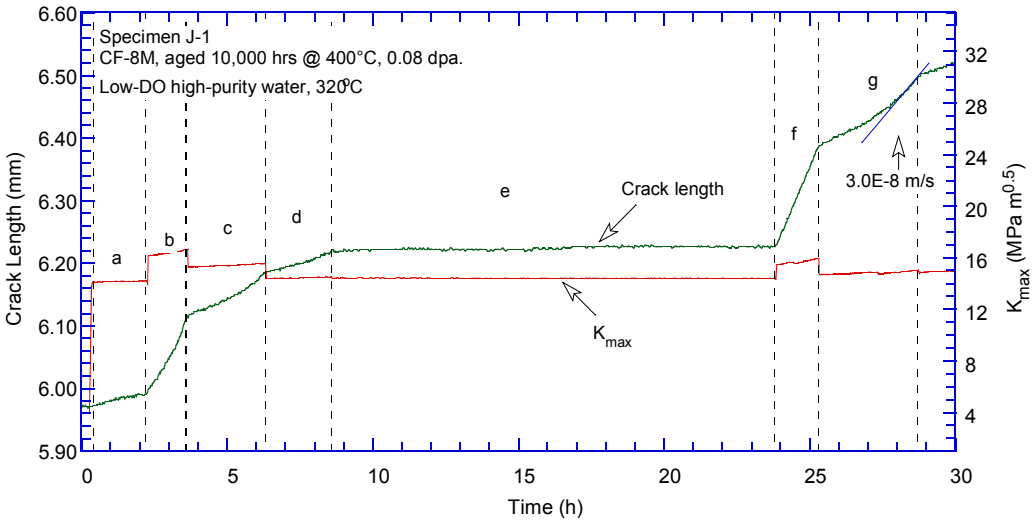


Figure 85. Crack-length-vs.-time plot for specimen J-1 (0.08-dpa aged CF-8M with 28% ferrite): test periods (a) a-g, (b) h-n, (c) o-r, (d) s-u, (e) 1a-1b, and (f) 2a-2c.

(b)

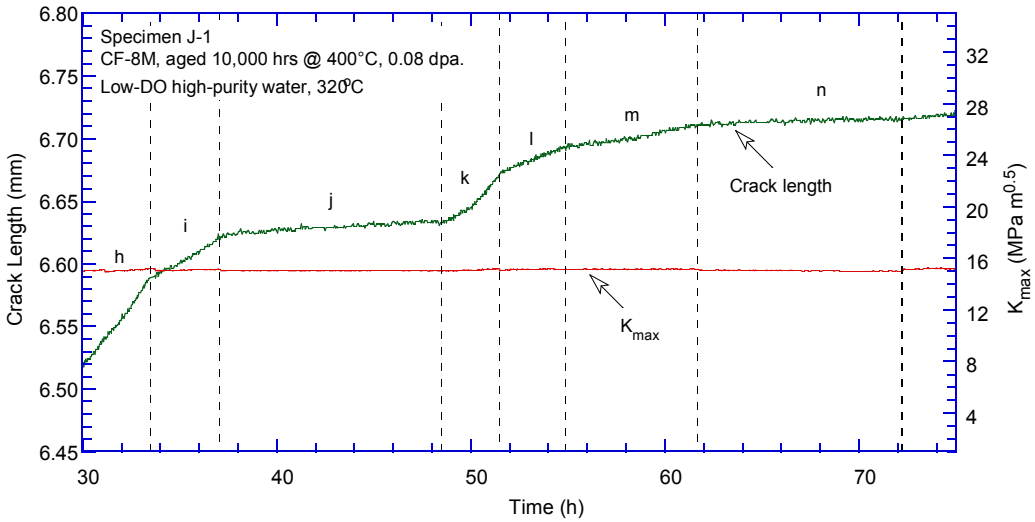


(c)

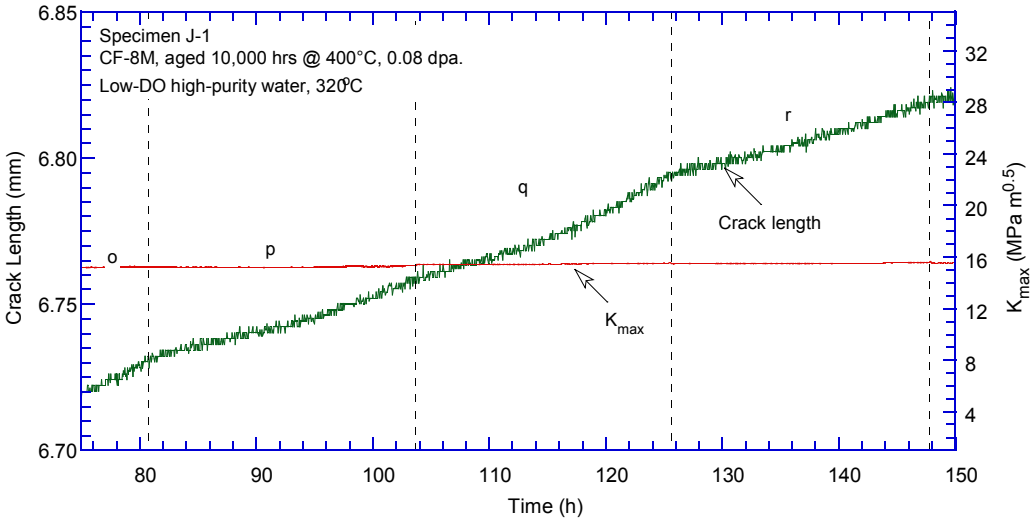


(d)

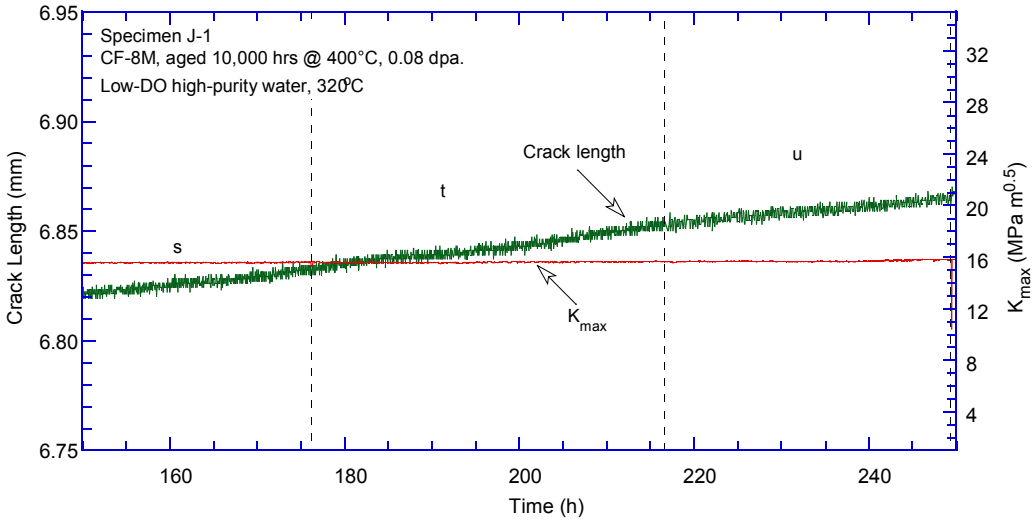


Figure 85. (Contd.)

(e)

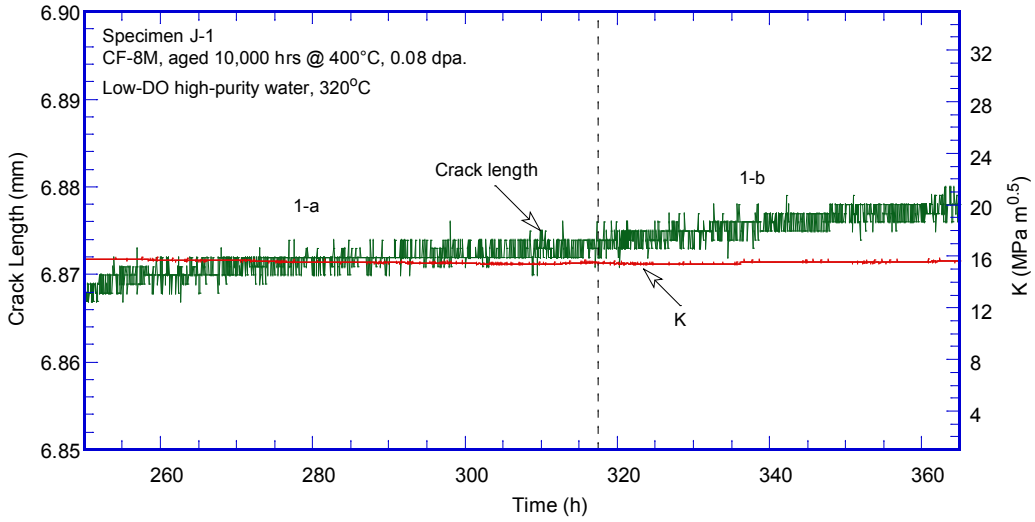


(f)

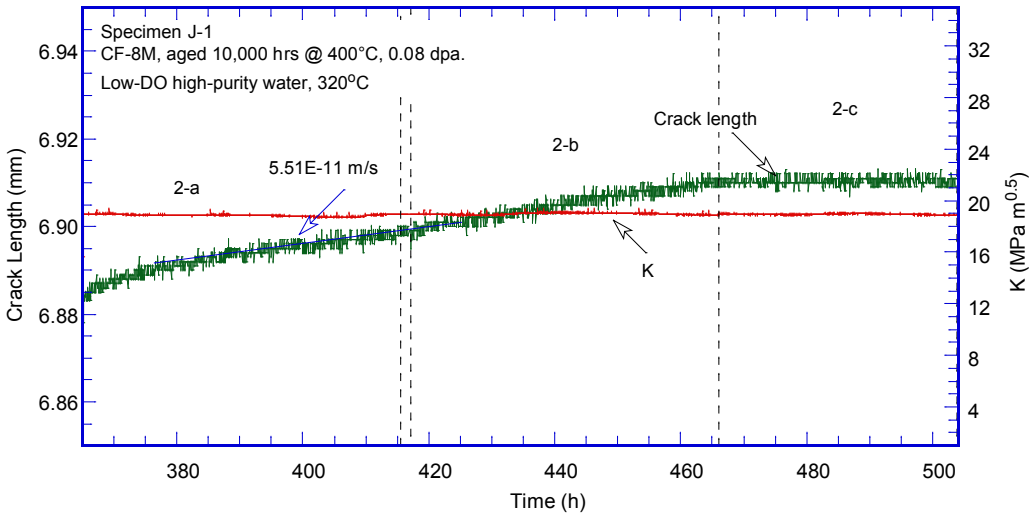


Figure 85. (Contd.)

Fracture toughness J-R curve test

After the CGR test, a fracture toughness J-R curve test was carried out on the same sample in the test environment. The J and crack extension results are shown in Fig. 88. A power-law fitting of the data shows a JR relationship of $J = 259\Delta a^{0.64}$, which yields a J value of 106 kJ/m$^2$ at the 0.2-mm offset line. All J values obtained in this sample were below the $J_{max}$ limit. However, one of the nine measurements of the final crack size still exceeded the limit. Thus, the J-R curve cannot be validated.

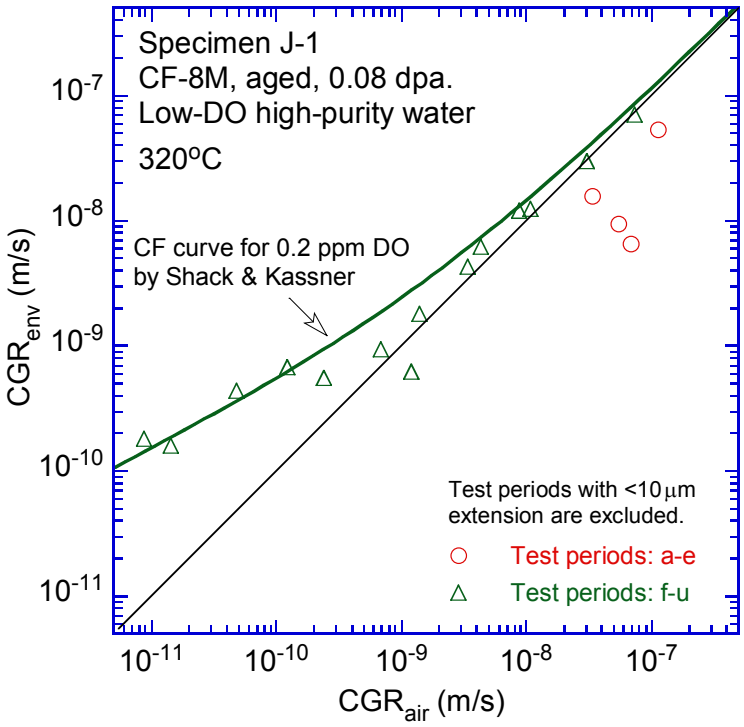


Figure 86. Cyclic CGRs of specimen J-1.

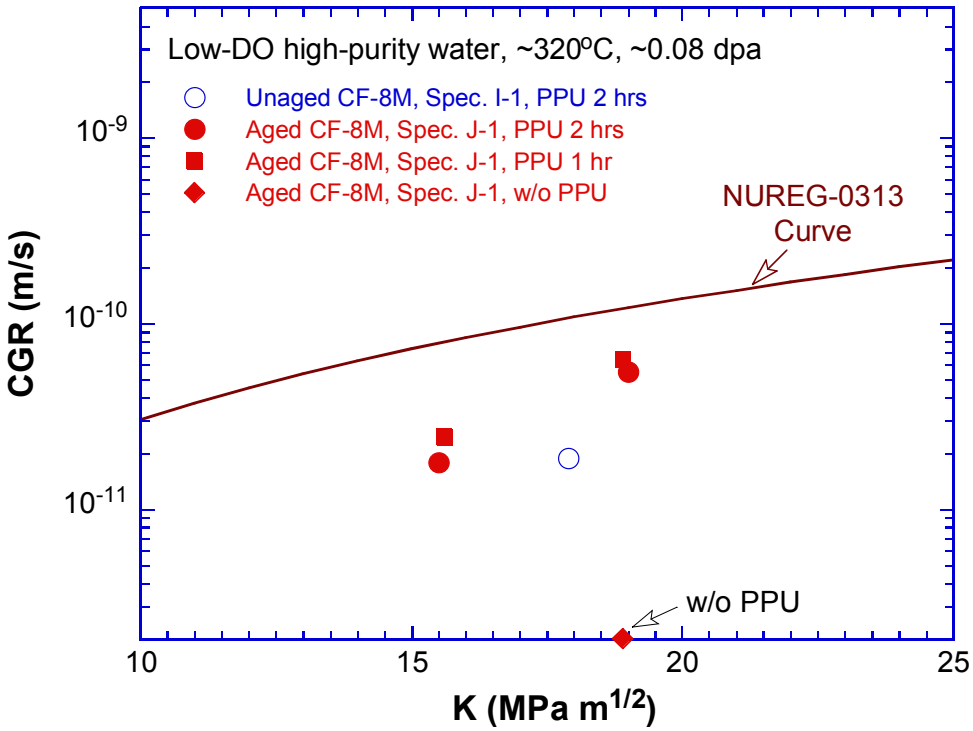


Figure 87. SCC CGRs of unaged and aged CF-8M CASS, irradiated to 0.08 dpa.

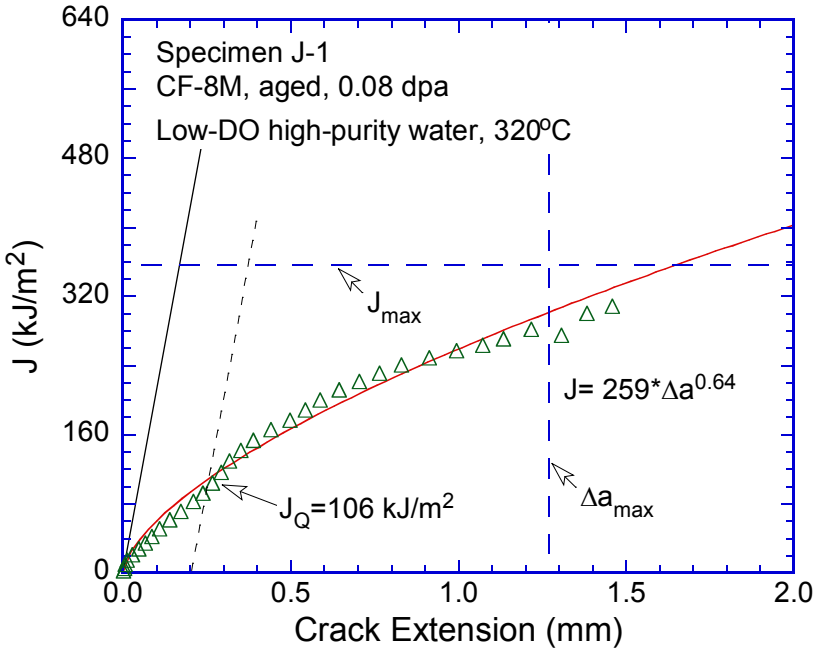


Figure 88. The J-R curve of specimen J-1.

Fractographic examination

The fracture surface of specimen J-1 was examined with replicas. Figure 89 shows the entire fracture surface. Two distinct fracture regions, CGR and JR test areas, can be clearly identified. The crack front of the CGR test is straight, indicating a well-controlled loading condition during the test. The CGR region is relatively flat and shows a clear contrast from the heavily deformed JR test region. Similar to the unaged CF-8M (specimen I-1), secondary cracks can be seen on the fracture surface.

Figure 90 shows an enlarged view of the fracture surface along the sample central line. Ferrite phase at the casting dendrite cores can be seen throughout the entire CGR region. Transgranular cleavage-like cracking is clearly visible in the pre-cracking region, as shown in Fig. 91. As the crack advances, deformation steps became less pronounced in some areas, and little plastic deformation could be seen within the ferrites phase compared to the surrounding austenite phase (Fig. 92). In some other areas, however, cleavage-like cracking remained the dominant fracture mode (Fig. 93). In the JR test region, the fracture morphology was mostly ductile dimples, suggesting heavy plastic flow during the JR test. In some areas, fracture occurred along the ferrite core of the columnar dendrites, as shown in Fig. 94.

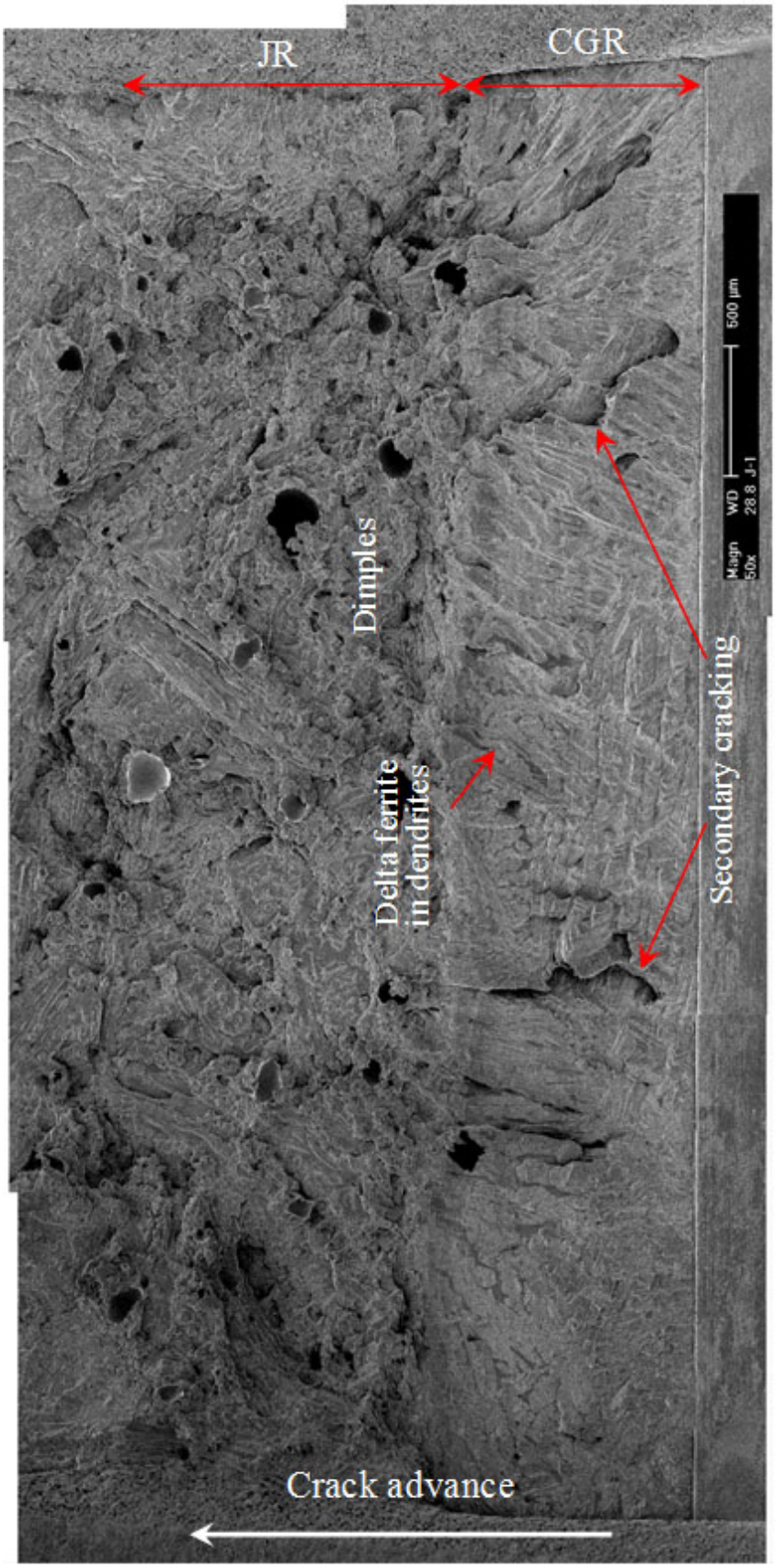


Figure 89. Fracture surface of specimen J-1 tested in low-DO high-purity water.

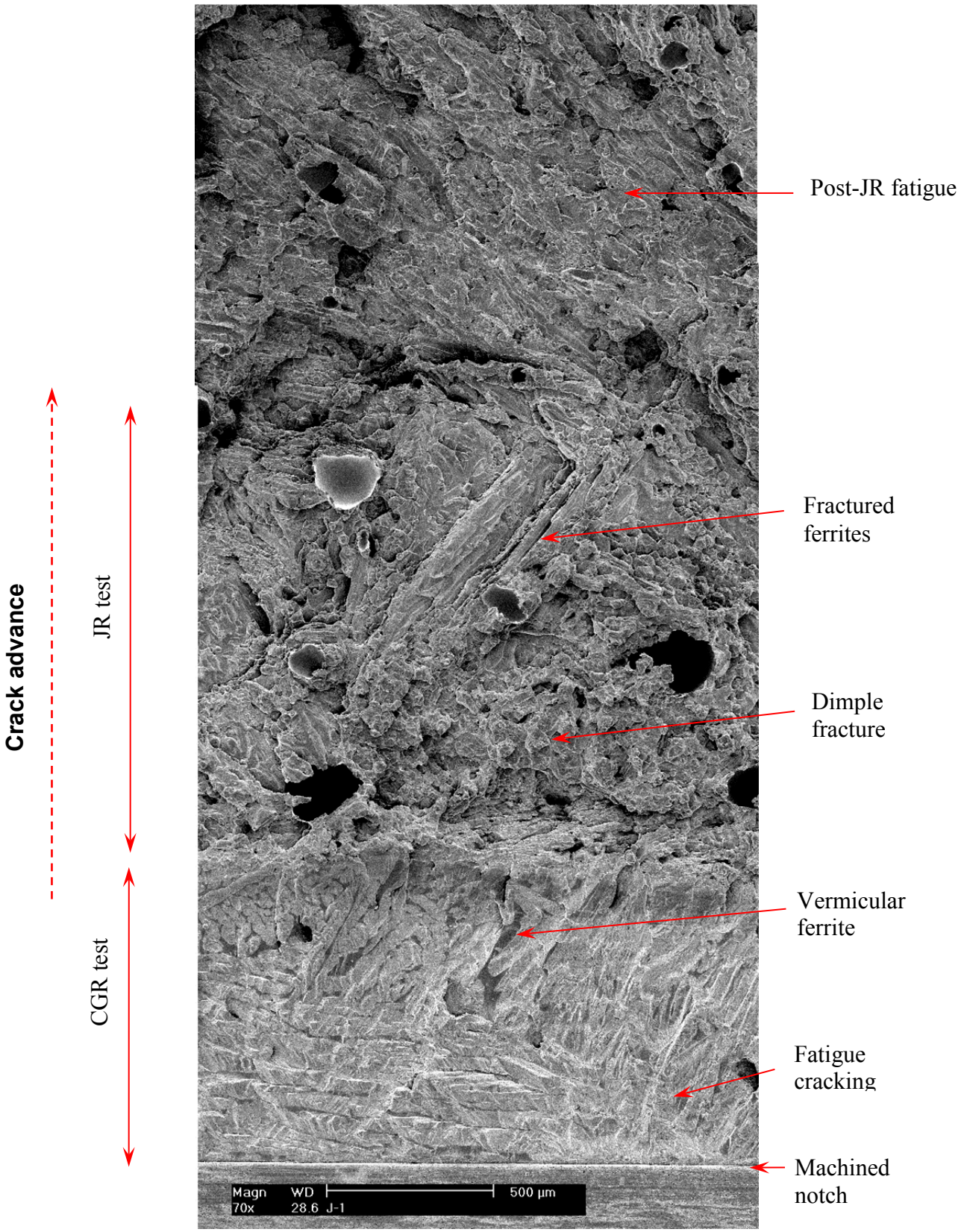


Figure 90. Fracture surface of specimen J-1 along the sample central line.

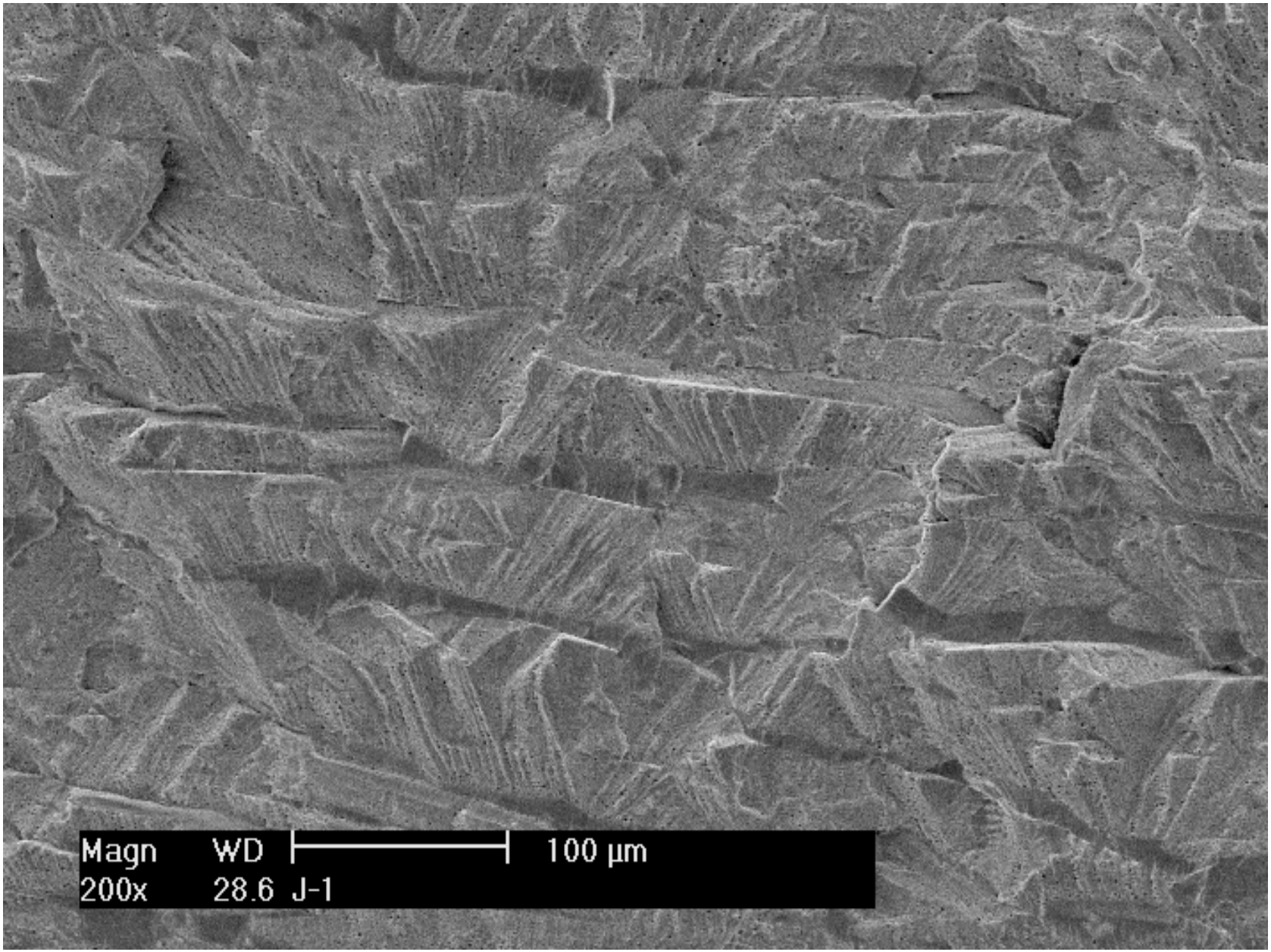


Figure 91. Precracking region of specimen J-1. Crack propagation from bottom to top.

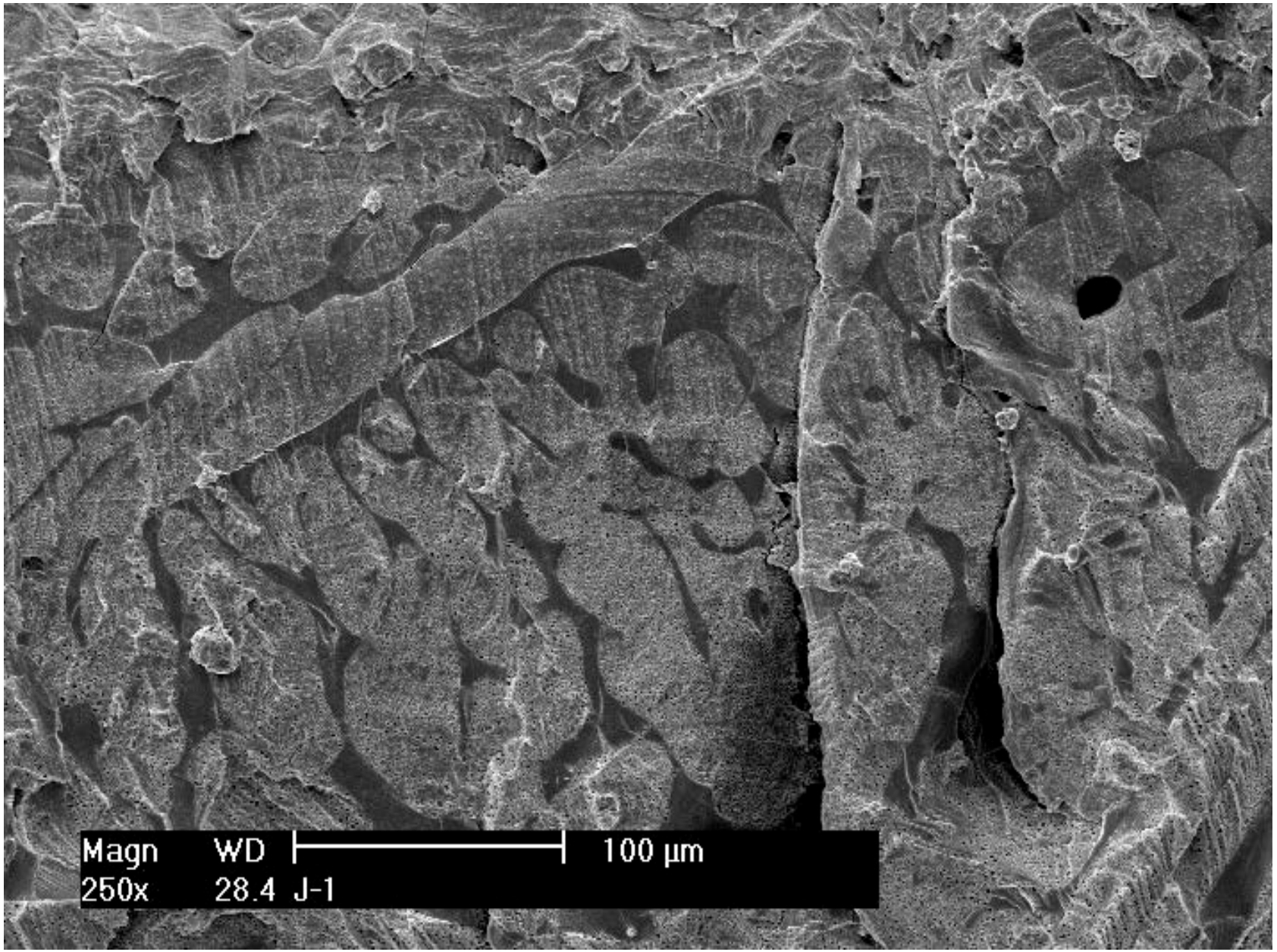


Figure 92. Ferrite microstructure at the end of CGR test of specimen J-1. Crack propagation from bottom to top.

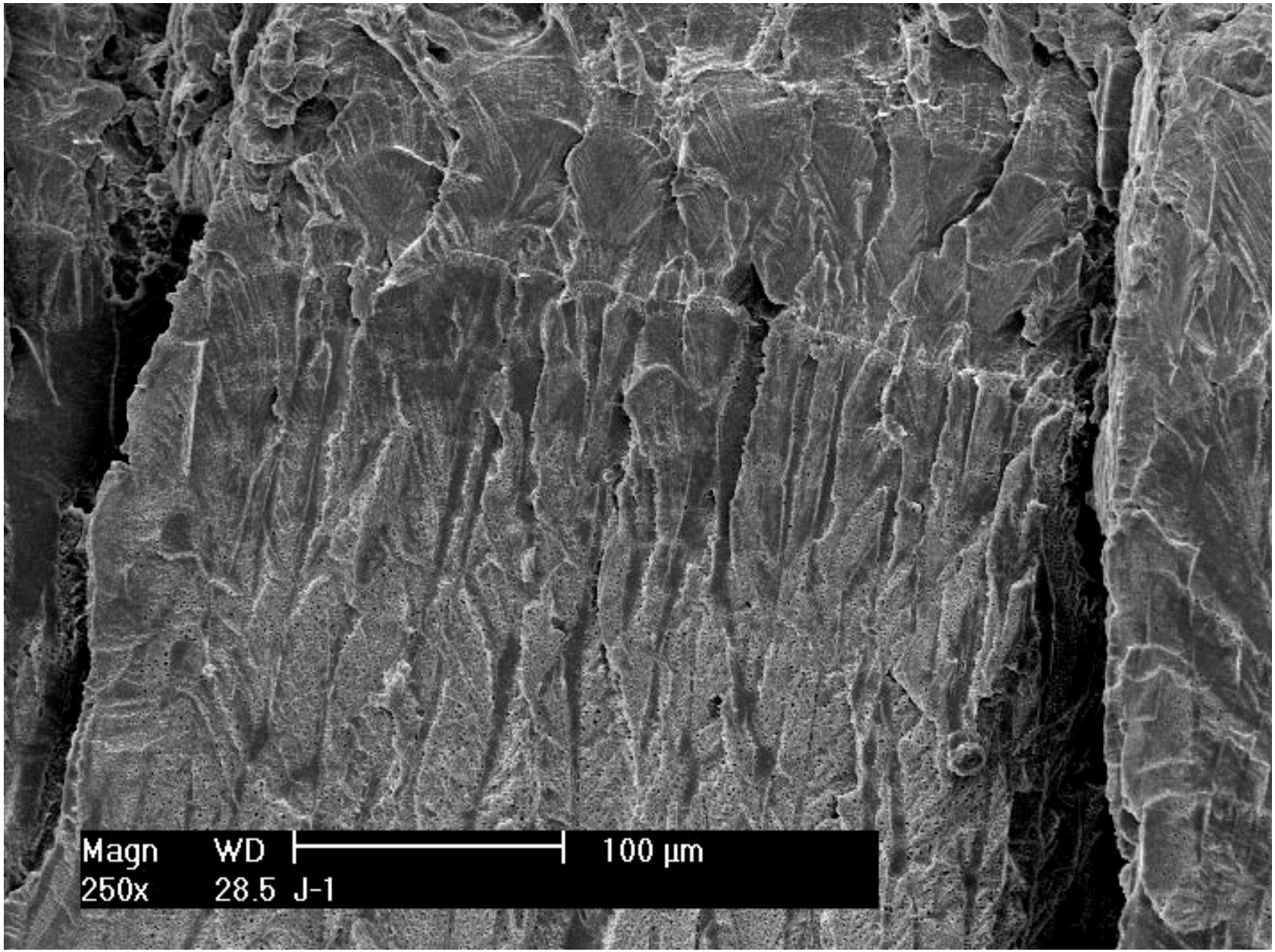


Figure 93. Cleavage-like fracture at the end of CGR test of specimen J-1. Crack propagation from bottom to top.

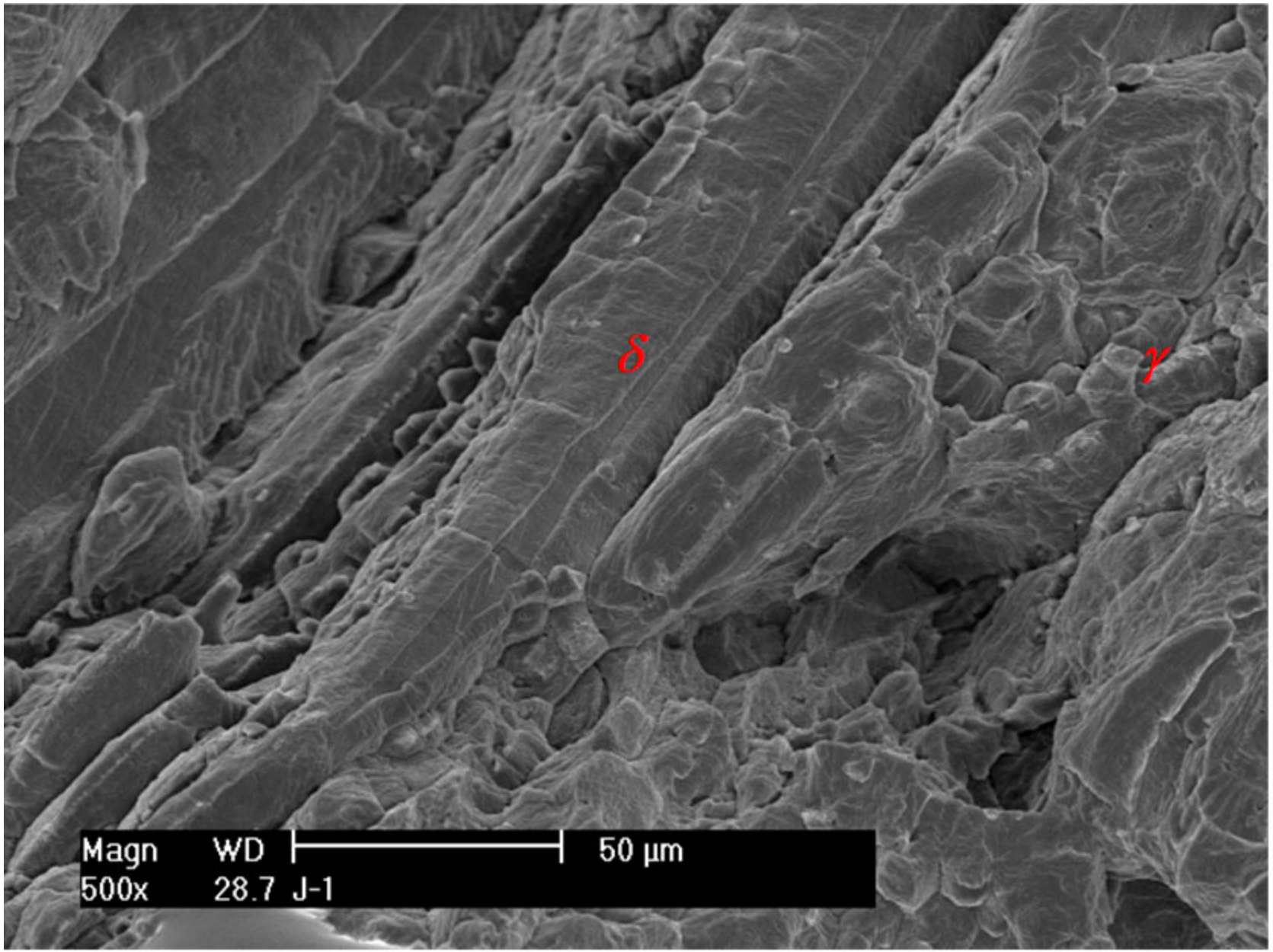


Figure 94. Fracture along ferrite at dendrite core in the JR test region of specimen J-1. Crack propagation from bottom to top.

## 4. DISCUSSION

Eleven unirradiated and irradiated 1/4T-CT specimens prepared from as-received and thermally aged CASS materials were tested in either low-DO high-purity water or simulated PWR water at ~320°C. These specimens were fabricated from CF-3, CF-8, and CF-8M CASS with high ferrite contents (more than ~23%). Seven of the specimens were irradiated to 0.08 dpa in the Halden reactor. Thermal aging of the CASS samples was conducted at 400°C for 10,000 hr prior to the irradiation. This thermal aging treatment had been shown to yield a high degree of embrittlement in a previous study.[4,39] Crack growth rate tests were performed on the specimens in low-corrosion-potential environments. Cyclic and constant-load CGR tests were carried out at several stress intensity factors to assess the susceptibility of these materials to environmentally assisted cracking. The SCC CGRs obtained from the present study are summarized in Table 15.

Table 15. CGR test results at ~320°C for CASS specimens with high ferrite contents.

| Material | Ferrite Content | Thermal Aging | Dose (dpa) | Sample ID | Test Environment | SCC CGR [a] | |
|---|---|---|---|---|---|---|---|
| | | | | | | **K** (MPa $m^{1/2}$) | **CGR** (m/s) |
| CF-3 | 24% | Unaged | - | A-N1 | Low-DO high-purity | 18.0 | Negligible |
| | | | 0.08 | A-1 | PWR | 23.9 | 4.8E-11 |
| | | | 0.08 | A-2 | Low-DO high-purity | 17.6 | 2.3E-11 |
| | | | | | | 19.6 | 4.9E-11 |
| | | | | | | 19.8 | 4.9E-12 (w/o PPU) |
| | | | | | | 19.8 | 4.3E-11 |
| | | Aged | - | B-N1 | PWR | 17.2 | 2.7E-11 |
| | | | | | | 17.1 | 2.3E-13 (w/o PPU) |
| | | | 0.08 | B-1 | PWR | 22.1 | 2.8E-11 |
| CF-8 | 23% | Unaged | - | E-N1 | Low-DO high-purity | 17.5 | 1.4E-11 |
| | | | | | | 17.5 | 8.1E-12 (w/o PPU) |
| | | | 0.08 | E-1 | Low-DO high-purity | 14.9 | 1.8E-11 |
| | | | | | | 16.8 | 2.7E-11 |
| | | Aged | - | F-N1 | Low-DO high-purity | 16.5 | 1.2E-11 |
| | | | | | | 16.5 | 1.2E-11 (w/o PPU) |
| | | | 0.08 | F-1 | Low-DO high-purity | 16.0 | 2.7E-11 |
| CF-8M | 28% | Unaged | 0.08 | I-1 | Low-DO high-purity | 17.9 | 1.9E-11 |
| | | Aged | 0.08 | J-1 | Low-DO high-purity | 15.5 | 1.8E-11 |
| | | | | | | 15.6 | 2.5E-11 |
| | | | | | | 19.0 | 5.5E-11 |
| | | | | | | 18.9 | 6.4E-11 |
| | | | | | | 18.9 | 2.0E-12 (w/o PPU) |

[a] Unless otherwise noted, SCC CGRs were measured under constant loads with PPU every 1 or 2 hours.

Fracture toughness J-R curve tests were also performed in the current study in the test environments at ~320°C with environmentally enhanced starter cracks. Table 16 shows the J-R curve results along with some previous unirradiated results obtained in air at ~290°C. The parameters *C* and *n* in the table are the fitting coefficients of the power-law relationship of J =

$C\Delta a^n$. The J value at the 0.2-mm offset line ($J_Q$) is reported for each test. Note that the unirradiated specimens tested in air were 1T-CT samples, larger than the specimens used in the current study (1/4T-CT). No crack growth rate results in water were available for the 1T-CT specimens. Experimental details of the previous unirradiated tests in air can be found in references [22, 39].

Table 16. Fracture toughness JR test results for CASS with high ferrite contents.

| Material [a] | Ferrite content | Thermal aging | Sample Size | Test Env. [b] | Test Temp. [b] (°C) | Unirradiated | | | Irradiated (0.08 dpa) | | |
|---|---|---|---|---|---|---|---|---|---|---|---|
| | | | | | | C | n | $J_Q$ (kJ/m$^2$) | C | n | $J_Q$ (kJ/m$^2$) |
| CF-3 | 24% | Unaged | 1/4T | Water | ~320 | 536 | 0.68 | 320 | 430 | 0.64 | 204 |
| | | | 1T | Air | ~290 | 756 | 0.31 | 700 | - | - | - |
| | | Aged | 1/4T | Water | ~320 | 353 | 0.66 | 170 | 362 | 0.85 | 116 |
| | | | 1T | Air | ~290 | 296 | 0.51 | 167 | - | - | - |
| CF-8 | 23% | Unaged | 1/4T | Water | ~320 | - | - | > 500 [c] | 359 | 0.57 | 183 |
| | | | 1T | Air | ~290 | 783 | 0.27 | 753 | - | - | - |
| | | Aged | 1/4T | Water | ~320 | 395 | 0.58 | 220 | 372 | 0.62 | 171 |
| | | | 1T | Air | ~290 | 396 | 0.51 | 242 | - | - | - |
| CF-8M | 28% | Unaged | 1/4T | Water | ~320 | - | - | - | 336 | 0.66 | 145 |
| | | | 1T | Air | ~290 | 583 | 0.45 | 437 | - | - | - |
| | | Aged | 1/4T | Water | ~320 | - | - | - | 259 | 0.64 | 106 |
| | | | 1T | Air | ~290 | 274 | 0.46 | 156 | - | - | - |

[a] Irradiated unaged and aged materials were exposed to the irradiation temperature (~315°C) for approximately 4320 hr. The aging parameter P defined in reference [40] is 1.66, 1.82, and 2.07 for Material CF-3, CF-8, and CF-8M, respectively. Thus, the extent of embrittlement caused by the reactor temperature is negligible during the course of the irradiation.

[b] All 1/4T-CT specimens were tested in low-corrosion-potential water environments at ~320°C in the current study. All 1T-CT specimens were tested in an air atmosphere at ~290°C in a previous study (NUREG/CR 4744, No.7).

[c] The last data point measured at the end of the test. A J value of ~700 kJ/m$^2$ was estimated by extrapolating the available data to the 0.2-mm offset line.

## 4.1 Cyclic Crack Growth Rates

Cyclic CGR data obtained from the unaged and aged CASS specimens were analyzed based on a superposition model previously developed by Shack and Kassner.[38] By assuming that the environmental contribution to cyclic CGR is related to fatigue crack growth rate in air, Shack and Kassner determined the corrosion fatigue curves of unirradiated wrought and CASS SSs in high-purity water containing 0.2 ppm and 8 ppm DO. Using the corrosion fatigue curve of 0.2 ppm DO as a reference, the best fit curves for each data set of the CASS specimens are compared. For the CF-3 specimens with 24% ferrite (Fig. 95a), the five fitting curves are all bounded by the line of 0.2-ppm DO, regardless of their irradiation, thermal aging, or test conditions. This observation suggests that irradiation does not increase the cracking susceptibility of CF-3 at this dose level. The relatively low environmental enhancement in the CF-3 can be attributed to the beneficial effect of ferrite in CASS. Several authors have reported a better SCC resistance for CASS than wrought SSs in aqueous environments.[15,16]

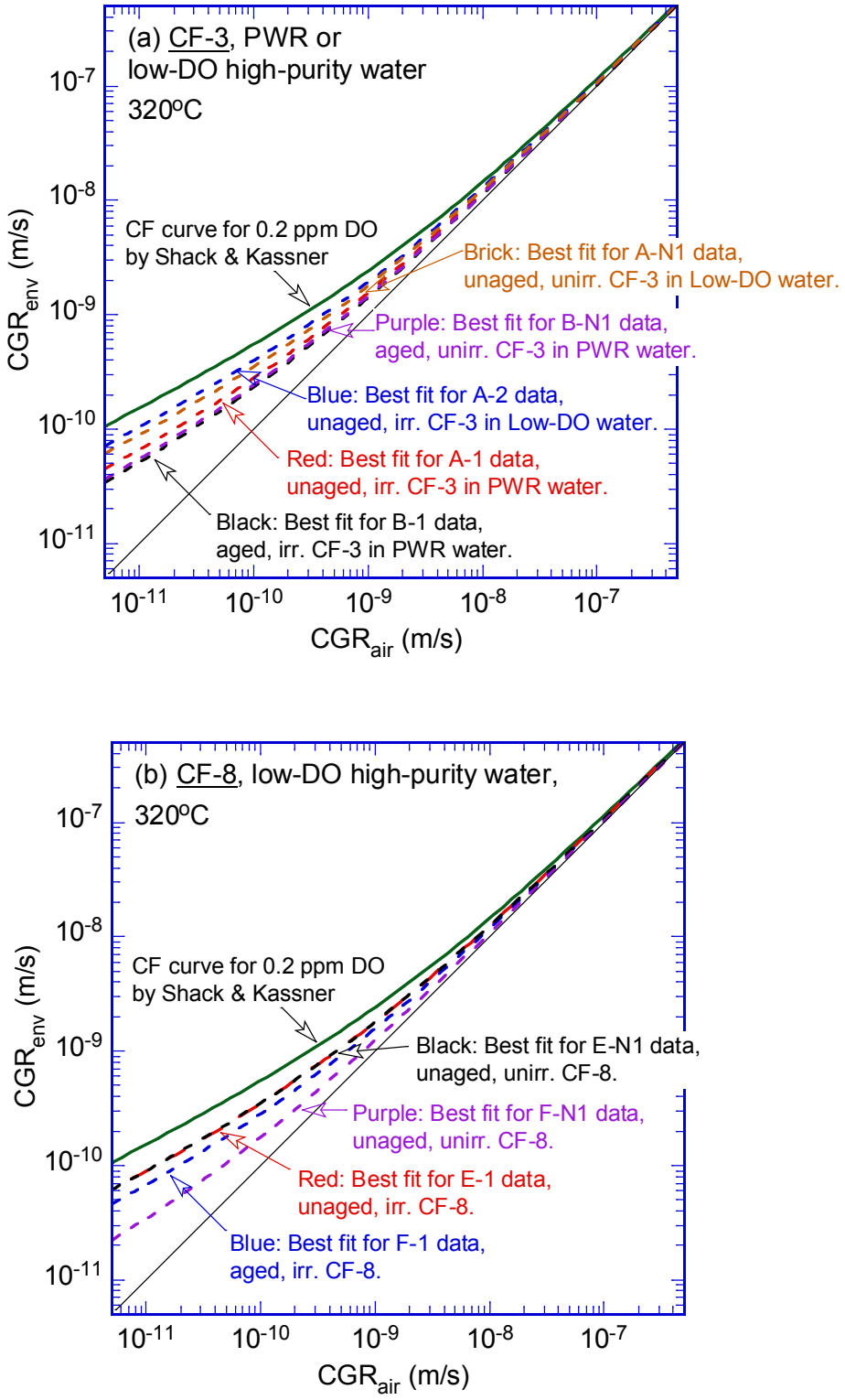


Figure 95. Best-fit curves of cyclic CGRs at 0.08-dpa dose: (a) unaged and aged CF-3, (b) unaged and aged CF-8, and (c) unaged and aged CF-8M.

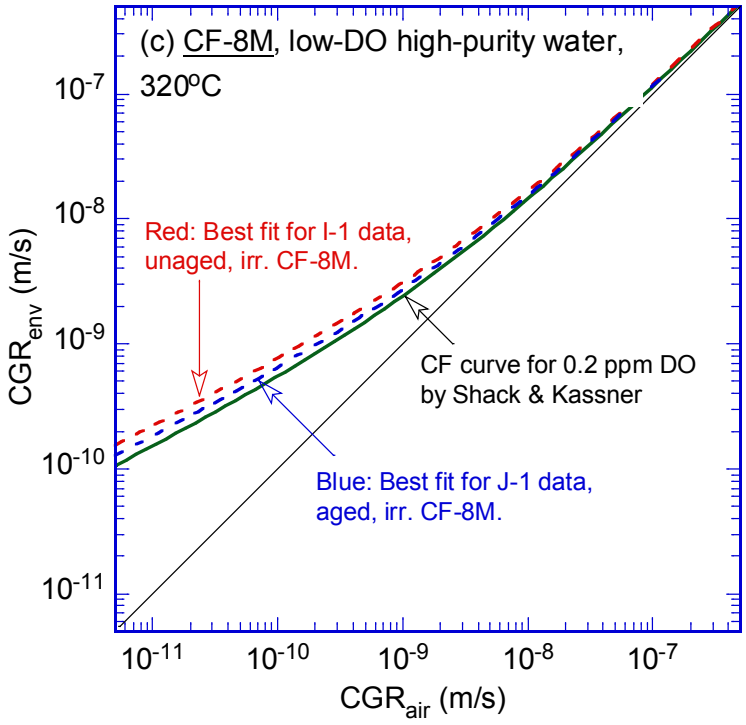


Figure 95. (Contd.)

As shown in Fig. 95b, the best fit curves of unaged and thermally aged CF-8 are also below the bounding line. The similar behaviors between CF-3 and CF-8 suggest that the difference in carbon content does not have a significant impact on corrosion fatigue behavior in low-DO high-purity or PWR water. For the CF-8M however, the fitting curves are slightly higher than the corrosion fatigue curve, as shown in Fig. 95c. Obviously, the CF-8M samples are more susceptible to environmentally assisted cracking under the current test conditions. Figure 96 shows the fitting coefficient "A" (in $CGR_{env} = A \cdot CGR_{air}^{0.5}$) for each data set obtained in the current study. While the fitting coefficients for CF-3 and CF-8 are similar, the values for CF-8M are much higher. Based on the current data, the corrosion fatigue growth rate of CF-8M is a factor of two to three higher than that of CF-3 and CF-8.

As shown in Fig. 96, the cyclic CGRs of thermally aged CASS are generally lower than those of unaged CASS, except for the unirradiated CF-3 where different test environments (PWR vs. low-DO water) were used in the different tests. The different cracking responses between the unaged and aged CASS suggest a better corrosion fatigue performance of the latter. However, given the large scatter in the CGR data, the observed differences between aged and unaged CASS may not be statistically significant. Nonetheless, the current study clearly shows that the corrosion fatigue behavior is similar between unaged and aged CASS in low-corrosion-potential environments. This observation contrasts with the results of unirradiated CASS tested in high-DO water environments. The cyclic CGRs of thermally aged CASS were found to be one order of magnitude higher than those of unaged alloys in high-DO water (>1 ppm).[38] The mechanism leading to similar cyclic CGRs between unaged and aged CASS in low-DO environments needs to be better understood.

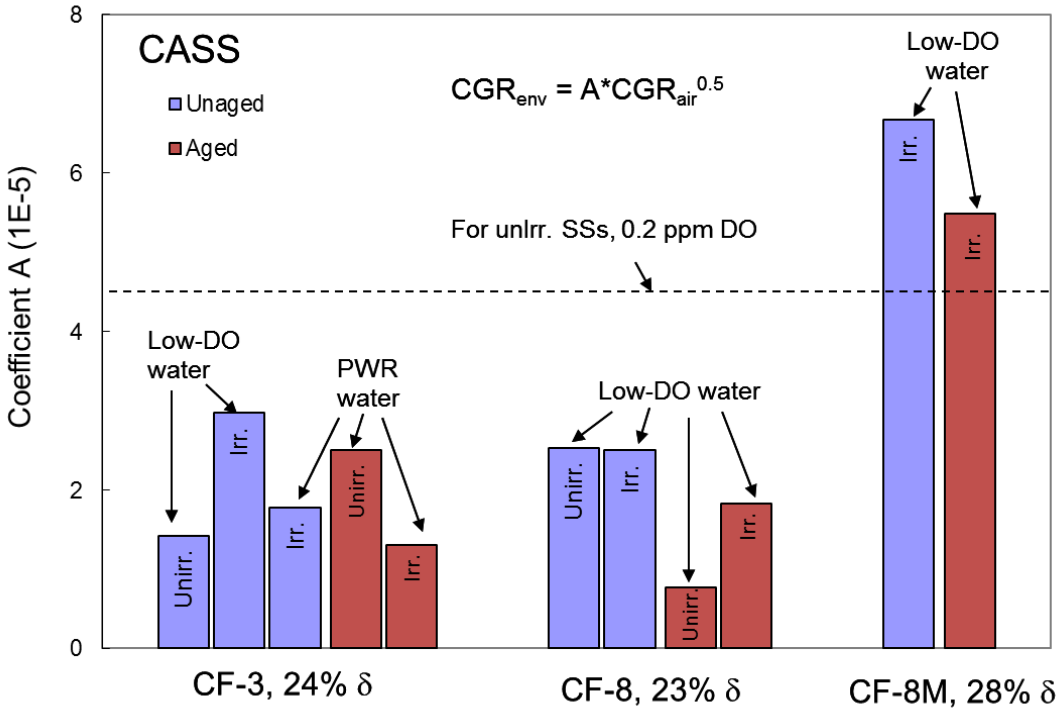


Figure 96. Fitting coefficient A for the corrosion fatigue superposition model.

### 4.2 Constant-load Crack Growth Rates

All constant-load CGRs obtained with or without PPU are plotted in Fig. 97. The open symbols represent the unaged CASS, and the closed symbols, their thermally aged counterparts. All data points are well below the NUREG-0313 line, and moderate CGRs in the range of $10^{-11}$ m/s are mainly obtained under loading conditions with PPU. Without PPU, the measured CGRs (the square symbols in Fig. 97) are much lower, except for the test on the unirradiated and thermally aged CF-8, where a dynamic loading condition resulting from pressure fluctuation was present. An accurate determination of the low growth rate exhibited by these CASS samples would require much longer test times than possible in the current study. In general, the tested CASS specimens show good SCC resistance, and neutron irradiation up to 0.08 dpa does not appear to elevate their cracking susceptibility significantly in the PWR and low-DO high-purity water environments.

The unaged and aged data sets, regardless of their grades, irradiation, and test conditions, are fitted to a power-law expression with an exponent of 2.16 (same as the NUREG-0313 curve). As shown in Fig. 97, the fitting curve of the aged CASS is just slightly higher (<20%) than that of the unaged CASS. However, given the large scatter of the data sets and the inherent uncertainty in short-duration CGR tests like these, the difference is statistically insignificant. Thus, thermal aging does not appear to affect the cracking susceptibility of the CASS specimens in the low-DO high-purity and PWR water. This lack of sensitivity to thermal aging history is consistent with that observed in cyclic CGR tests.

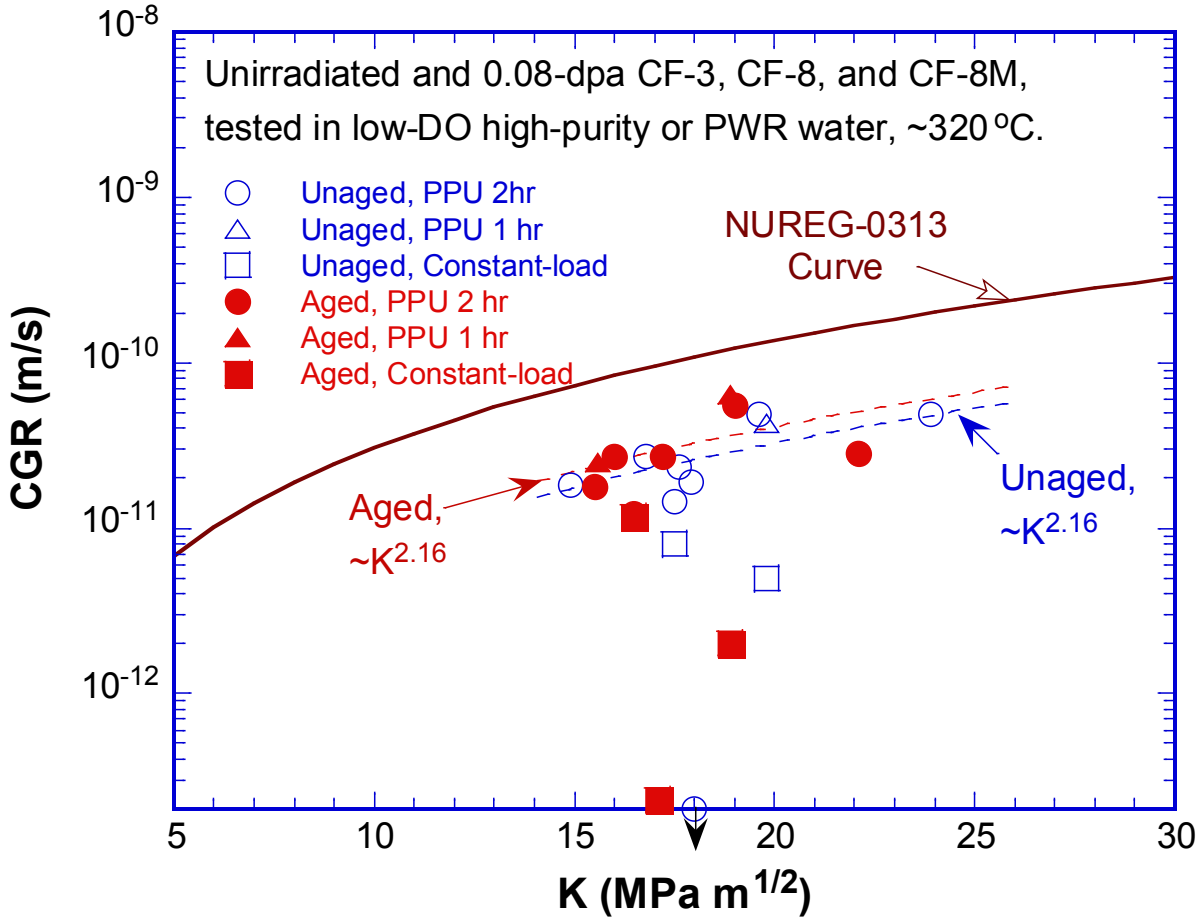


Figure 97. Constant-load CGRs of the low-dose CASS with more than 23% ferrite in low-DO high-purity and PWR water environments.

A low susceptibility to IASCC is expected for CASS owing to the beneficial effects of ferrite. It has been shown that unirradiated CASS samples are more resistant to SCC than wrought SSs in high-DO water.[15,16] The superior SCC performance of the duplex microstructure may arise from the deformation behavior of the ferrite phase. Ferrite is more difficult to deform plastically compared with austenite under the same stress level. Using a nano-indentation measurement, Wang et al.[42] showed that the hardness of ferrite phase is higher than that of austenite phase in CF-8. Furthermore, the austenite is also more noble than the ferrite in corrosion potential measurements of single-phase alloys. By delaying the development of heavy plastic deformation in ferrite phase, a slip-dissolution mechanism could be hindered, to some extent, in a duplex microstructure. Our fractographic examinations support this hypothesis. As shown in the micrographs of the CGR test regions (e.g., Figs. 18, 25, 43, 49, 57, 74, 75, 83, and 91), little plastic deformation can be seen within the ferrite phase. In contrast, the surrounding austenite grains are often heavily deformed. If this mechanism is correct, the beneficial effect of ferrite could be diminished, in principle, by thermal aging or irradiation embrittlement. A deteriorated fracture resistance of the ferrite grains would accelerate the development of plastic strain in the surrounding austenite phase. In fact, elevated SCC CGRs have been observed in a thermally aged CF-8M at ~2.4 dpa.[31] This observation suggests that the beneficial effect of a duplex

microstructure may be eliminated or greatly reduced by neutron exposure to a sufficiently high fluence level.

### 4.3 Fracture Toughness

Figure 98 shows all fracture toughness values (J at 0.2 mm offset) obtained from the current study. The blue and brick color bars are for the unirradiated and irradiated CASS specimens, respectively. Note that the J value for the unirradiated and unaged CF-8 is an estimated minimum (see Section 3.2.2.1 for details). Fracture toughness results of unirradiated CF-8M tested in air from Ref. [39] are also included in Fig. 98 (green bars). Neutron irradiation, even at such a low dose (0.08 dpa), has a significant impact on the fracture toughness of CASS. The extent of irradiation embrittlement is much greater for unaged than aged specimens. After irradiation, the fracture toughness values of unaged CASS are significantly lower than the original unirradiated values. For aged CASS, fracture toughness is also reduced by 20-30% after irradiation. Since the comparison tests were performed in identical environments for CF-3 and CF-8, the differences between unirradiated and irradiated JR results can only be attributed to neutron irradiation. For the CF-8M, no unirradiated control tests were carried out in water at ~320°C. Thus, we cannot rule out a potential effect of test environment on the fracture toughness. However, given the good SCC resistance observed in the CGR tests, it is unlikely that that test environment had a significant contribution to the loss of toughness in irradiated tests. In addition, the fractographic examinations showed that both irradiated and unirradiated specimens had similar fracture morphology (ductile dimples) in JR test regions, suggesting an insignificant role of the test environment in the irradiated J-R curve tests. Thus, the differences between unirradiated and irradiated JR results for CF-8M are also likely due to the neutron irradiation.

Because the deterioration in fracture toughness developed more rapidly with neutron irradiation in unaged CASS, the difference in fracture toughness between unaged and aged specimens was reduced after irradiation. As shown in Fig. 98, the drastically different fracture toughness values between unaged and aged specimens (blue and green bars) are lessened after irradiation (brick bars). This change suggests a dominant role of neutron irradiation (compared to thermal aging) in promoting embrittlement in CASS. The rapidly developed irradiation effect in unaged materials may also explain the inconsistent observations between the current study and the previous work discussed in the last section. Shack and Kassner reported that thermal aging can considerably decrease the cracking resistance of unirradiated CASS in high-DO high-purity water.[38] However, in our study, both corrosion fatigue and SCC of irradiated CASS seem to be insensitive to thermal aging history (e.g., Figs. 96 and 97). There is no doubt that neutron irradiation had introduced detrimental effects in both unaged and aged materials, but not necessarily at the same rate. It is possible that the unaged microstructure deteriorated more quickly than did the aged microstructure at the current dose level. Consequently, the cracking behavior between the aged and unaged specimens became similar after irradiation.

While the irradiation damage seems to be a dominant factor for embrittlement, a combined effect of thermal aging and irradiation damage does reduce the fracture resistance of CASS further. As shown in Fig. 98, the fracture toughness values of irradiated and aged specimens are

approximately 50 kJ/m$^2$ lower than those of unirradiated and aged specimens. The decline of fracture resistance in thermally aged CASS samples at such low dose level is unexpected, and points toward an interaction between thermal aging and irradiation embrittlement. More important, these results show that the kinetics of thermal aging embrittlement could be altered by irradiation, as could the saturation state (i.e., the lower bound of fracture toughness). This finding suggests that the conservatism assumed for thermal aging embrittlement needs to be examined closely under neutron irradiation. The current result does not show, however, how the ferrite content affects the extent of embrittlement. The samples tested in this study are all high-ferrite-content CASS materials. If only the changes in ferrite contribute to the embrittlement, the combined effect of thermal aging and irradiation damage should vary with the initial ferrite content. Additional tests on specimens with lower ferrite contents are needed to understand the precise role of ferrite in the combined effect of thermal aging and neutron irradiation.

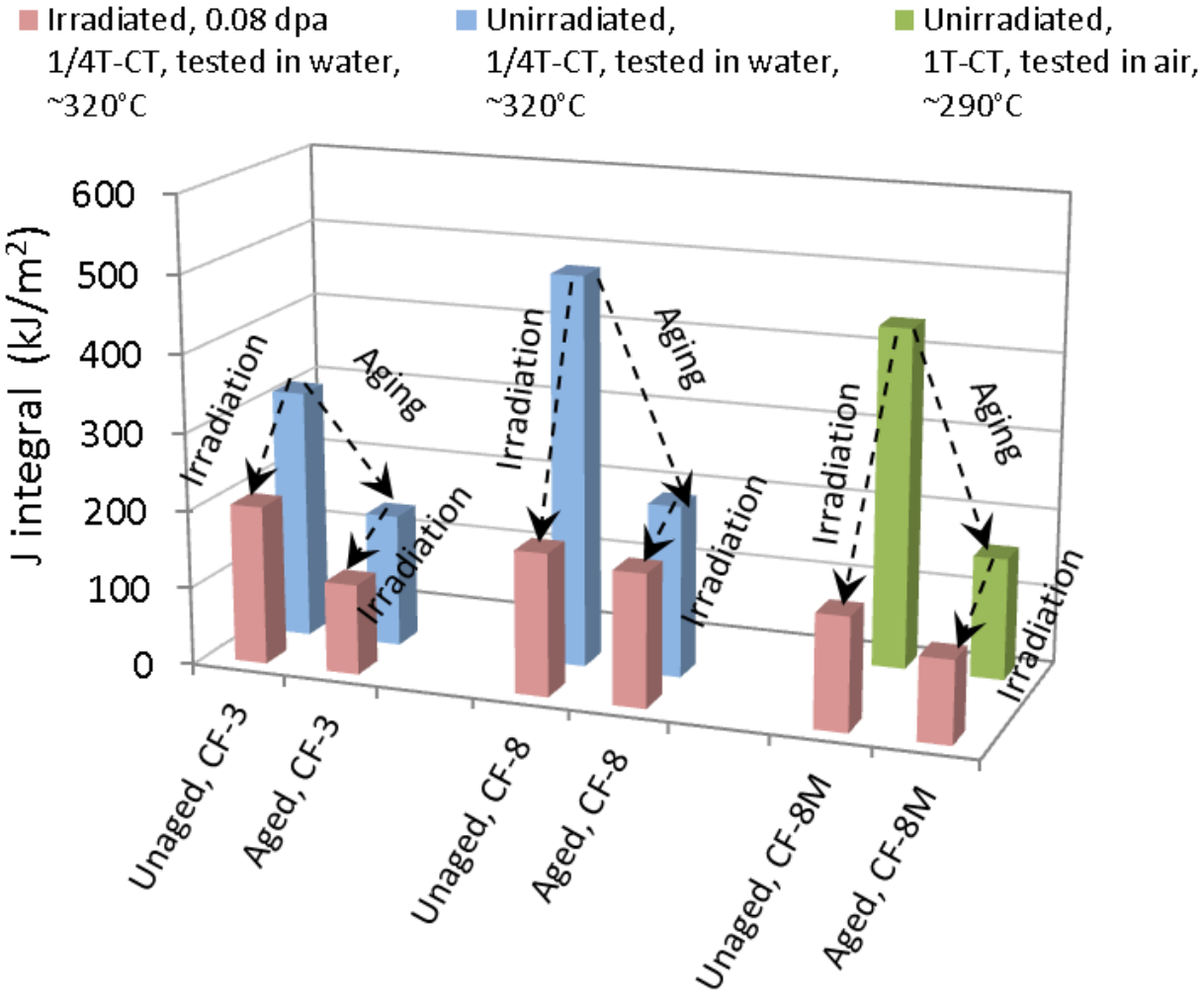


Figure 98. Fracture toughness values of unirradiated and irradiated CASS in unaged and aged conditions. Note that most of the results are from 1/4T-CT specimens tested at ~320°C in water environments. The unirradiated results for CF-8M CASS are from 1T-CT specimens tested at ~290°C in an air atmosphere.

The mechanisms of CASS thermal embrittlement are well understood. [17-20] A miscibility gap in the Fe-Cr phase diagram gives rise to a spinodal decomposition of two ferrite phases, a Fe-rich $\alpha$ phase and a Cr-rich $\alpha$' phase. The $\alpha$' phase has a slightly different lattice parameter from the matrix and, thus, strengthens the ferrite grains and causes the embrittlement. The redistribution of Cr within ferrite phase is accompanied by the rearrangement of other alloying elements, which can lead to additional nucleation and growth of precipitates within the ferrite phase or at the ferrite-austenite boundaries. Thus, carbides and Ni-rich G-phase are also found to be the main contributors to the thermal aging embrittlement of CASS. Under neutron irradiation, the kinetics of these embrittlement mechanisms may be affected.[43] The natural miscibility gap could be widened, and new temperature-dependent wavelengths could be developed. While no irradiation microstructural work has been carried out in the current study, the mechanical test results suggest that an accelerated microstructural evolution occurs under neutron irradiation, and the initial microstructures of CASS may be a key factor for the evolution of irradiation microstructure. Detailed microstructural examinations of irradiation defects, precipitations, segregations, and phase stability in the ferrite phase and at austenite-ferrite boundaries would be helpful to explain the combined effect of thermal aging and irradiation embrittlement.

## 5. SUMMARY

Crack growth rate and fracture toughness J-R curve tests have been conducted on CF-3, CF-8, and CF-8M CASS with high ferrite content (>23%). The samples were irradiated in the Halden test reactor to a low dose of 0.08 dpa. Both as-received and thermally aged specimens were included to show the combined effect of thermal aging and irradiation embrittlement. The CGR tests were conducted on irradiated and unirradiated control samples in low-DO high-purity water or PWR water at 320°C. Following the CGR tests, fracture toughness J-R curve tests were performed on the same samples in the test environments.

Cyclic CGRs and constant-load CGRs were obtained to evaluate the corrosion fatigue and SCC resistance of the CASS specimens. In cyclic CGR tests, environmentally enhanced cracking was more difficult to establish in the CASS specimens than in wrought SSs. In SCC CGR tests, only moderate CGRs in the range of $10^{-11}$ m/s were recorded in the CASS specimens, regardless of their thermal aging history or irradiation conditions. In general, the CASS materials showed good resistance to both corrosion fatigue and SCC before irradiation and at 0.08 dpa. Transgranular cleavage-like cracking was the dominant fracture mode during the CGR tests, and the ferrite phase was often deformed to a lesser extent than the surrounding austenite phase. This observation supports the hypothesis that the beneficial effect of ferrite arises, in part, from the high plastic deformation stress in ferrite phase.

All CASS specimens tested in this study failed in a ductile dimple mode during the fracture toughness J-R curve tests. Neutron irradiation had a significant impact on the fracture toughness of CASS. At 0.08 dpa, the fracture toughness values of unaged specimens were significantly lower than the initial unirradiated values. An additional 20-30% reduction in fracture toughness was also observed for thermally aged specimens after irradiation. The combined effect of thermal aging and irradiation damage can reduce the fracture resistance of CASS to a higher extent than any one of them can achieve alone. These results indicate that neutron irradiation can affect not only the kinetics of thermal aging embrittlement, but also the saturation state (i.e., lower bound values of fracture toughness). For this reason, the effects of neutron irradiation should be considered when the degree of thermal aging embrittlement is evaluated for CASS components.

## 6. REFERENCES


1. U.S. NRC, "Expert Panel Report on Proactive Materials Degradation Assessment," NUREG/CR-6923, 2006.
2. Blair, M., and T. L. Steven, *Steel Castings Handbook,* Sixth Edition, Steel Founders' Society of America and ASM International, 1995.
3. ASTM International, "Standard Specification for Castings, Austenitic, for Pressure-Containing Parts," A351/A351M-10, Annual Book of ASTM Standards, 2012.
4. Chopra, O. K., and A. Sather, "Initial Assessment of the Mechanisms and Significance of Low-Temperature Embrittlement of Cast Stainless Steels in LWR Systems," NUREG/CR-5385, ANL-89/17, 1990.
5. Mills, W. J., "Fracture Toughness of Type 304 and 316 Stainless Steels and Their Welds," International Materials Reviews, **4,** No. 2 (1997): 45.
6. Leger, M. T., "Predicting and Evaluating Ferrite Content in Austenitic Stainless Steel Castings," *Stainless Steel Castings*, ASTM STP 756 (1982): 105-125.
7. Aubrey, L. S., P. F. Wieser, W. J. Pollard, and E. A. Schoefer. "Ferrite Measurement and Control in Cast Duplex Stainless Steel," in *Stainless Steel Castings*, ASTM STP 756 (1982): 126-164.
8. Schaeffler, A. L., "Constitution Diagram for Stainless Steel Weld Metal," Metal Progress, **56,** No. 11 (1949): 680-680B.
9. Hull, F. C., "Delta Ferrite and Martensite Formation in Stainless Steels," Welding Journal, **52** (1973): 183.
10. Long, C. J., and W. T. DeLong, "Ferrite Content of Austenitic Stainless Steel Weld Metal," Welding Journal, **52** (1973): 281.
11. Olson, D. L., "Prediction of Austenitic Weld Metal Microstructure and Properties," Welding Journal, **64,** No. 10 (1985): 281.
12. ASTM International, "Standard Practice for Steel Casting, Austenitic Alloy, Estimating Ferrite Content Thereof," A800/A800M-10, Annual Book of ASTM Standards, 2012.
13. Beck, F. H., E. A. Schoefer, J. W. Flowers, and M. G. Fontana, "New Cast High-Strength Alloy Grades by Structure Control," in *Advances in the Technology of Stainless Steels and Related Alloys*, ASTM STP 369, 1965.
14. Floreen, S., and H. W. Hayden, "The Influence of Austenite and Ferrite on the Mechanical Properties of Two-phase Stainless Steels Having Microduplex Structures," ASM Transactions Quarterly, **61,** No. 3 (1968): 489-499.
15. Beck, F. H., J. Juppenlatz, and P. F. Wieser, "Effects of Ferrite and Sensitization on Intergranular and Stress Corrosion Behavior of Cast Stainless Steels," in *Stress Corrosion - New Approaches*, H. L. Craig, Jr., ed., ASTM STP 610, 1976.
16. Hughes, N. R., W. L. Clarke, and D. E. Delwiche, "Intergranular Stress-Corrosion Cracking Resistance of Austenitic Stainless Steel Castings," in *Stainless Steel Castings*, V. G. Behal and A. S. Melilli, eds., ASTM STP 756, 1982.
17. Fisher, R. M, E. J. Dulis, and K. G. Carroll, "Identification of the Precipitate Accompanying 885F Embrittlement in Chromium Steels," Transactions of AIME, **197** No. 5 (1953): 690–695.

18. Grobner, P. J., "The 885°F (475°C) Embrittlement of Ferritic Stainless Steels," Metallurgical and Materials Transactions B, **4**, No. 1 (1973): 251-260.
19. Nichol, T. J., A. Datta, and G. Aggen, "Embrittlement of Ferritic Stainless Steels," Metallurgical and Materials Transactions A, **11**, No. 4 (1980): 573-585.
20. Trautwein, A., and W. Gysel, "Influence of Long-time Aging of CF8 and CF8M Cast Steel at Temperatures Between 300 and 500°C on Impact Toughness and Structural Properties," in *Stainless Steel Castings*, ASTM STP 756 (1982): 165-189.
21. Andresen, P. L., F. P. Ford, K. Gott, R. L. Jones, P. M. Scott, T. Shoji, R. W. Staehle, and R. L. Tapping, "Expert Panel Report on Proactive Materials Degradation Assessment (PMDA)," NUREG/CR-6923, BNL-NUREG-77111-2006, 2007.
22. Chopra, O. K., and A. Sather, "Initial Assessment of the Mechanisms and Significance of Low-Temperature Embrittlement of Cast Stainless Steels in LWR Systems," NUREG/CR-5385, ANL-89/17, 1990.
23. Hiser, A. L., "Tensile and J-R Curve Characterization of Thermally Aged Cast Stainless Steels," NUREG/CR-5024, MEA-2229, 1988.
24. Solomon, H. D., and T. M. Devine, "Influence of Microstructure on the Mechanical Properties and Localized Corrosion of a Duplex Stainless Steel," ASTM STP 672 (1979): 430-461.
25. Chung, H. M., and O. K. Chopra, "Kinetics and Mechanism of Thermal Aging Embrittlement of Duplex Stainless Steels," Proc. 3rd Intl. Symp. on Environmental Degradation of Materials in Nuclear Power Systems -- Water Reactors, Metallurgical Society, 1987.
26. Chung, H. M., and T. R. Leax, "Embrittlement of Laboratory and Reactor Aged CF3, CF8, and CF8M Duplex Stainless Steels," Materials Science and Technology, **6**, No. 3 (1990): 249-262.
27. Leax, T. R., S. S. Brenner, and J. A. Spitznagel, "Atom Probe Examination of Thermally Aged CF8M Cast Stainless Steel," Metallurgical and Materials Transactions A, **23**, No. 10 (1992): 2725-2736.
28. Hamaoka, T., A. Nomoto, K. Nishida, K. Dohi, and N. Soneda, "Effects of Aging Temperature on G-phase Precipitation and Ferrite-Phase Decomposition in Duplex Stainless Steel," Philosophical Magazine, **92,** No. 22 (2012) 2716-2732.
29. Averback, R. S., "Atomic Displacement Processes in Irradiated Metals," Journal Nuclear Materials, **216** (1994): 49.
30. Wollenberger, H., "Phase Transformations under Irradiation," Journal Nuclear Materials, **216** (1994) 63.
31. Chopra, O. K., and W. J. Shack, "Crack Growth Rates and Fracture Toughness of Irradiated Austenitic Stainless Steels in BWR Environments," NUREG/CR-6960, ANL-06/58, 2008.
32. Mills, W. J., "Fracture Toughness of Irradiated Stainless Steel Alloys," Nuclear Technology, **82**, No. 3 (1988): 290-303.
33. Karlsen, T. M., "ANL Fabrication Report of Irradiation Capsules," OECD Halden Reactor Project, 2009.

34. Andresen, P. L., F. P. Ford, S. M. Murphy, and J. M. Perks, "State of Knowledge of Radiation Effects on Environmental Cracking in Light Water Reactor Core Materials," Proc. 4th Intl. Symp. on Environmental Degradation of Materials in Nuclear Power Systems -- Water Reactors, NACE, Houston, TX, pp. 1.83-1.121, 1990.
35. ASTM International, "Standard Test Method for Measurement of Fracture Toughness," E1802-08a, Annual Book of ASTM Standards, 2008.
36. Hazelton, W. S., and W. H. Koo, "Technical Report on Material Selection and Processing Guidelines for BWR Coolant Pressure Boundary Piping," NUREG-0313, Rev. 2, 1988.
37. James, L. A., and D. P. Jones, "Fatigue Crack Growth Correlation for Austenitic Stainless Steels in Air," In Predictive Capabilities in Environmentally Assisted Cracking, PVP Vol. 99, ASME, pp. 363-414, 1985.
38. Shack, W. J., and T. F. Kassner, "Review of Environmental Effects on Fatigue Crack Growth of Austenitic Stainless Steels," NUREG/CR-6176, 1994.
39. Chopra, O. K., "Long-Term Embrittlement of Cast Duplex Stainless Steels in LWR Systems," NUREG/CR-4744, ANL-93/11, 1993.
40. Chopra, O. K., "Estimation of Fracture Toughness of Cast Stainless Steels during Thermal Aging in LWR Systems," NUREG/CR-4513, Rev. 1, ANL-93/22, 1994.
41. Kassner, T. F., W. E. Ruther, and W. K. Soppet, "Mitigation of Stress Corrosion Cracking of AISI 304 Stainless Steel by Organic Species at Low Concentrations in Oxygenated Water," Corrosion, **90** (1990): 489.
42. Wang, Z., F. Xue, J. Jiang, W. Ti, and W. Yu, "Experimental Evaluation of Temper Aging Embrittlement of Cast Austenitic Stainless Steel from PWR," Engineering Failure Analysis, **18** (2011): 403.
43. Garner, F. A., J. M. McCathy, K. C., Russell, and J. J. Hoyt, "Spinodal-like Decomposition of Fe-35Ni and Fe-Cr-35Ni Alloys during Irradiation and Thermal Aging," Journal Nuclear Materials**, 205** (1993): 411.

NRC FORM 335
(12-2010)
NRCMD 3.7

U.S. NUCLEAR REGULATORY COMMISSION

# BIBLIOGRAPHIC DATA SHEET

*(See instructions on the reverse)*

1. REPORT NUMBER
(Assigned by NRC, Add Vol., Supp., Rev., and Addendum Numbers, if any.)

NUREG/CR-7184
ANL-12/56

2. TITLE AND SUBTITLE

Crack Growth Rate and Fracture Toughness Tests on Irradiated Cast Stainless Steels

3. DATE REPORT PUBLISHED

| MONTH | YEAR |
|---|---|
| July | 2015 |

4. FIN OR GRANT NUMBER

V6454

5. AUTHOR(S)

Y. Chen, B. Alexandreanu, and K. Natesan

6. TYPE OF REPORT

Technical

7. PERIOD COVERED (Inclusive Dates)

8. PERFORMING ORGANIZATION - NAME AND ADDRESS (If NRC, provide Division, Office or Region, U. S. Nuclear Regulatory Commission, and mailing address; if contractor, provide name and mailing address.)

Argonne National Laboratory
9700 South CASS Avenue
Argonne, IL 60439

9. SPONSORING ORGANIZATION - NAME AND ADDRESS (If NRC, type "Same as above", if contractor, provide NRC Division, Office or Region, U. S. Nuclear Regulatory Commission, and mailing address.)

Division of Engineering
Office of Nuclear Regulatory Research
U.S. Nuclear Regulatory Commission
Washington, DC 20555-0001

10. SUPPLEMENTARY NOTES

A. S. Rao, NRC Project Manager

11. ABSTRACT (200 words or less)

Cast austenitic stainless steel, which has a ferrite-austenite duplex microstructure, is used in the cooling system of light water reactors for components with complex shapes, such as pump casings, valve bodies, and coolant piping. In the present study, crack growth rate and fracture toughness J-R curve tests were performed on irradiated cast stainless steels and unirradiated control samples in low-corrosion-potential environments (high-purity water with low dissolved oxygen or simulated pressurized water reactor) at 320°C. Both as-received and thermally aged materials were included to investigate the combined effect of thermal aging and irradiation embrittlement on the fracture behavior of cast stainless steels. The samples were irradiated to approximately 0.08 dpa at the Halden reactor. Good resistance to corrosion fatigue and stress corrosion cracking was observed for all cast stainless steel specimens. Thermal aging had little effect on the crack growth behavior at 0.08 dpa. Cleavage-like fracture was the dominant cracking morphology during the crack growth rate tests, and the ferrite phase was deformed to a lesser extent compared with the surrounding austenite phase. The fracture toughness results showed a dominant effect of neutron irradiation, and the fracture resistances were decreased considerably for all cast specimens regardless of their thermal aging. The reduction in fracture toughness was more significant in the unaged than thermally aged specimens. Nonetheless, the fracture toughness values of thermally aged specimens were 20-30% lower than their unaged counterparts, suggesting a combined effect of thermal aging and neutron irradiation in cast stainless steel.

12. KEY WORDS/DESCRIPTORS (List words or phrases that will assist researchers in locating the report.)

Cast austenitic stainless steel, thermal aging embrittlement, irradiation embrittlement, environmentally assisted cracking, stress corrosion cracking, crack growth rate, fracture toughness

13. AVAILABILITY STATEMENT

unlimited

14. SECURITY CLASSIFICATION

*(This Page)*
unclassified

*(This Report)*
unclassified

15. NUMBER OF PAGES

16. PRICE


Federal Recycling Program


**UNITED STATES**
**NUCLEAR REGULATORY COMMISSION**
WASHINGTON, DC 20555-0001

OFFICIAL BUSINESS

NUREG/CR-7184

# Crack Growth Rate and Fracture Toughness Tests on Irradiated Cast Stainless Steels

July 2015